DECIPHERING ANTIGEN RECOGNITION BY LYMPHOCYTE RECEPTORS

INSIGHTS FROM T-CELL RECEPTORS AND ANTIBODIES

Anna Gesine Huhn

Lincoln College

University of Oxford

A dissertation submitted for the degree of

Doctor of Philosophy

Hilary 2024

"Alle wichtigen Entscheidungen müssen auf der Basis lückenhafter Daten getroffen werden."

"All important decisions must be made on the basis of incomplete data."

— Mariana Leky, *Die Herrenausstatterin*

ABSTRACT

The adaptive immune system is composed of specialised cells that detect and respond to foreign pathogens. T cells and B cells, the main coordinators of this immune response, present lymphocyte antigen receptors on their cell surface that can bind to antigens of foreign pathogens. Lymphocyte antigen receptors encompasses the T-cell receptor (TCR) on the surface of T cells, which bind peptide antigens presented by MHC complexes (peptide-MHC) on the surface of cells. The second type of antigen receptors are immunoglobulins, which either occur as surface expressed B-cell receptor (BCR) or secreted antibodies by B cells.

This thesis investigates how the biophysical properties of an interaction between antigen receptors and their antigen is translated into a functional cellular response. Specifically, the focus is on how the TCR discriminates between foreign and endogenous (self) antigens. In a second project the mechanism of antibody/antigen binding and its impact of antibody function is examined. This involved developing advanced SPR methods to measure ultra-low affinity interaction and bivalent binding. The affinity measurements are then compared with the functional responses the antigens evoke by measuring T-cell activation and the neutralisation potency of antibodies.

PROJECT 1: ANTIGEN DISCRIMINATION BY THE TCR T cells use their TCRs to discriminate between lower-affinity self and higher-affinity foreign antigens. Early studies on murine TCRs showed that TCRs are capable of perfectly discriminating between small difference in antigens. This means that antigens with a slight change in structure and binding affinity compared to the cognate, stimulatory antigen were unable to activate T cells, regardless of their concentration. The concept of perfect antigen discrimination cannot be reconciled with recent clinical evidence on T-cell off-target toxicity, and autoimmune responses. To understand this apparent discrepancy, this thesis revisits antigen discrimination by the TCR. The discrimination strength is quantified from previously published data and by remeasuring affinities of the OT-I-TCR to antigen variants. This analysis reveals that the discrimination strength is significantly lower than the current consensus, which means low-affinity antigens can induce an immune response when present at high concentrations. Though lower, TCRs still have enhanced discrimination compared to other surface ligand receptors. This thesis also reports the first affinity measurements of TCR binding naturally occurring self-peptide-MHCs at physiological temperatures.

PROJECT 2: BIVALENT ANTIBODY BINDING Antibodies carry two identical binding sites, which allow them to achieve strong binding to their antigen through bivalent binding and thus increase their neutralisation potency. Although antibodies bind bivalently, current methods to screen and optimise them rely on methods that measure monovalent binding. However monovalent binding parameters have failed to predict the neutralisation potency of antibodies. Interestingly, methods to measure bivalent binding using SPR are readily available but there are currently no mathematical models that can be used to analyse this bivalent data. This thesis presents a particle-based bivalent model that relies on stochastic-spatial simulations to analyse bivalent binding data. The model includes a new biophysical parameter, termed the 'molecular reach', that quantifies the maximum separation distance between two antigens that still allows a single antibody to bind them both simultaneously. The model is used to determine the binding kinetics of a panel of 80 antibodies isolated from COVID-19 patients that recognise the receptor-binding-domain (RBD) of SARS-CoV-2. This revealed that the molecular reach of an antibody is the strongest correlate of SARS-CoV-2 viral neutralisation. Using the bivalent binding parameters, the antibody concentrations required for viral neutralisation were predicted.

ACKNOWLEDGEMENTS

I would like to thank all those who, over the past five years, have put so much of their own time into helping me produce, write and examine this thesis.

Most importantly Omer, who conceptualised and guided me through my PhD projects, and who tolerated all the mistakes I made along the way. I have learned a lot from his exceptional ability to break down complex concepts into simple ideas. I could not be more grateful for all the opportunities he has given me.

Anton, who understands better than anyone else the experiments and hypotheses that led to the understanding we have of the adaptive immune system today, and who has acted as my living encyclopaedia throughout the writing process.

A PhD thesis is not a solitary task, and I owe particular thanks to the members of the Dushek lab, for the exchange of ideas, shared complaints and the necessary emotional support after failed experiments. Especially Misha, from whom I learnt all the laboratory techniques, and who, with unfailing kindness, helped me overcome any experimental obstacle.

A special thank you to my invaluable collaborators Sam Isaacson, Daniel Wilson and Dan Nissley, who generously shared their mathematical wisdom with me.

My thanks also goes to the Dunn School of Pathology for their financial and administrative support, especially during the COVID pandemic, and for fostering a social and supportive environment that encouraged collaboration and allowed me to meet outstanding scientists as fellow students, PIs and invited speakers.

I am indebted to the friends I made in Oxford, for their comradeship that kept me sane through the uncertainties of research and the isolation of the pandemic. As well as to my indisputably loyal friends overseas, never more than a telephone call away, for always helping me with the important decisions in life.

To my parents, whose stimulating discussions around the dining table encouraged my scientific curiosity from early on - I would not have achieved this without them. A special thank you to my mum during the writing phase, for her meticulous proofreading and spellchecking of this thesis and sending care packages full of gummy bears.

One third, and everything to come, to Oliver, in whose presence I found a home.

Finally, a big thank you to my examiners, Malcolm Sim and Katelyn Spillane, for the time they spent reading, discussing, rightfully criticising and approving my thesis. Their input has improved the thesis tremendously.

CONTENTS

LIST OF FIGURES

LIST OF TABLES

LIST OF ABBREVIATIONS

Ab	antibody
APC	antigen presenting cell
β_2m	β2-microglobulin
BCR	B-cell receptor
BRS	basic rich stretch motifs
CAR	chimeric antigen receptor
cTEC	cortical thymic epithelial cell
CDR	complementarity-determining region
DC	DoubleCatcher
EM	electron microscopy
ER	endoplasmic reticulum
Fab	fragment antigen-binding
Fc	fragment crystallizable
FDC	follicular dendritic cell
FRET	fluorescence resonance energy transfer
GCI	grating-coupled interferometry
GPCR	G-protein coupled receptor
Ig	immunoglobulin
IgA	immunoglobulin A
IgG	immunoglobulin G
IgM	immunoglobulin M
IgE	immunoglobulin E
IgD	immunoglobulin D
Ii	invariant chain
ITAM	immunoreceptor tyrosine-based activation motif

KP	kinetic proofreading
KS	kinetic segregation
MD	molecular dynamic
MHC	major histocompatibility complex
mTEC	medullary thymic epithelial cell
NMR	Nuclear Magnetic Resonance
NTR	non-catalytic tyrosine-phosphorylated receptor
ODE	ordinary differential equation
pMHC	peptide-MHC
RBD	receptor binding domain
PRR	proline-rich region
RSS	recombination signal sequences
RTK	receptor tyrosine kinase
RU	response unit
SEC	size exclusion chromatography
SLO	secondary lymphoid organ
SPR	Surface Plasmon Resonance
TAP	transporter associated with antigen processing
TCR	T-cell receptor
TdT	deoxynucleotidyl transferase
TMD	transmembrane domain
UPS	ubiquitin-proteasome system

1

INTRODUCTION

Cells sense and respond to their environment through expressing surface receptors that recognise extracellular ligands. Studying this recognition event can uncover how receptors decode and translate the information provided by the ligand to mediate a specific cellular response. The consensus is that the biophysical properties of the receptor/ligand interaction dictate the cellular response and that these properties are fully encoded in their atomic structure[1]. This concept is frequently used to rationally optimise therapeutic drugs. In the adaptive immune system, lymphocyte antigen receptors enable lymphocytes to detect foreign pathogens in the body. There are two types of lymphocyte antigen receptors: T-cell receptors (TCR) and immunoglobins. Immunoglobins can occur as either B-cell receptors or secreted by B cells as antibodies. These receptors bind specifically to structures on pathogens known as antigens. The recognition of foreign antigens is critical for the initiation of an effective immune response that leads to the elimination of the pathogen. Despite significant advancements, our understanding of how lymphocyte antigen receptors recognise their ligands remains incomplete. Intriguingly, biophysical properties of the ligand-receptor interaction, such as its strength or lifetime, appear to be inadequate to explain the cellular responses elicited by antigen receptors. This discrepancy poses a fundamental challenge in understanding the mechanism of lymphocyte activation. In this thesis, I will explore two main open questions concerning the recognition of antigens by TCRs and antibodies.

The first of these questions revolves around one of the crucial features of the TCR: its ability to recognise harmful foreign antigens while tolerating healthy self-antigens. It is unclear how this discrimination between foreign and self-antigens by the TCR is achieved with this level of accuracy in the periphery. This thesis will address this question by measuring the affinities and kinetics of TCR-antigen interactions. Surface Plasmon Resonance (SPR) is a method to study

protein interactions *in vitro* and is used throughout this thesis. The data is then used to test different models and challenge our current understanding of TCR antigen discrimination.

The second question addressed in this thesis concerns the functional effectiveness of antibodies. It is believed that the affinity of antibody-antigen interaction dictates their effectiveness in eliminating pathogens. However, when the affinity of the interaction is measured it does not correlate with the antibodies' functional effectiveness. This thesis hypothesises that the ability of antibodies to bind to multiple antigens simultaneously is crucial to understanding their functions. In other words bivalent binding increases their overall binding strength. This thesis presents a new model that quantifies bivalent binding from SPR binding data and successfully identifies the properties that determine antibody effectiveness.

Overall, this thesis shows that both these questions can be resolved with more quantitative and accurate measurements of binding properties. It proves that the function of lymphocyte antigen receptors is intricately connected to the biophysical properties of their antigen interactions. It establishes new SPR methods for the study of protein interactions and provides datasets for the use of other researchers. The work presented here has implications for basic science and clinical applications. Harnessing the unique antigen discrimination capabilities of T-cell receptors could optimize immunotherapeutic strategies, and deepen our understanding of autoimmune diseases. The improved understanding of antibody-antigen interactions can also help in optimising antibodies for therapy and enhancing vaccine development.

1.1 Chapter overview

CHAPTER 2: BACKGROUND. We will review the structure and function of TCRs and antibodies and introduce the main theories regarding TCR antigen discrimination.

CHAPTER 3: META-ANALYSIS OF ANTIGEN DISCRIMINATION BY THE TCR. This chapter systematically quantifies the antigen discriminatory strength by performing a meta-analysis of published data for a large number of mouse and human TCR systems. We will see that the discrimination strength of TCR is weaker than originally believed but is still uniquely enhanced

compared to other ligand receptors. This chapter also sheds light on the cellular mechanism that regulates antigen discrimination.

CHAPTER 4: REVISED 3D AFFINITIES FOR THE OT-I TCR. The OT-I TCR is one of the most commonly studied TCR systems. In this chapter, the OT-I interaction affinity to 20 variant peptides is measured at physiological temperatures. These measurements include the interaction of OT-I with naturally occurring self-peptides. Combined with functional data, this data validates the enhanced but imperfect discrimination strength identified in the previous chapter.

CHAPTER 5: QUANTIFYING THE BIVALENT BINDING OF ANTIBODIES. In Chapter 5 we will shift our focus to antibodies. A particle-based model is presented that can accurately quantify the bivalent binding parameters of antibody-antigen interaction from SPR data. This model allows us to explain and predict the functional effectiveness of antibodies.

CHAPTER 6: BIVALENT BINDING TO STUDY TCR-ANTIGEN INTERACTIONS. In this chapter a new method is introduced to measure ultrafast kinetic interactions with SPR. This method relies on creating a synthetic bivalent TCR to increase binding affinity, taking inspiration from antibody bivalent binding. The particle model developed in Chapter 5 is employed to obtain accurate parameters of low-affinity interactions.

CHAPTER 7: CONCLUSION In the last chapter, the main findings of this thesis are summarised and their future implications for both research and therapeutic applications are discussed.

1.2 *Contributions*

Throughout my PhD, I collaborated with many people who contributed data to the projects presented in this thesis. This thesis is largely written in the first-person plural to stylistically reflect the support and influence of those involved in this research. However, all work presented within this thesis is my own except for the contributions by others clearly stated below.

Enas Abu Sha, Johannes Pettmann, Mikhail Kutuzov developed and tested the ultra-low affinity SPR methods used in Chapter 4. Mikhail Kutuzov also helped me produce the soluble TCR and pMHC proteins for the SPR experiments in Chapter 4 and Chapter 6. I would like to thank Andrew Sewell for providing me with the expression plasmid for the OT-I TCR. Audrey Gerade and her lab performed the functional T cell experiments in Chapter 4. Dan Wilson derived the equation for fitting a kinetic proofreading model used in Chapter 3 and Chapter 4.

Samuel Isaacson and Daniel Wilson developed and implemented the bivalent particle-based model introduced in Chapter 5. Tiong Kit Tan and Wanwisa Dejnirattisai provided the anti-RBD antibodies used in Chapter 5. Mikhail Kutuzov conducted all bivalent SPR experiments, while Robert Donat conducted the monovalent SPR experiments. The molecular dynamic simulations of antibody/antigen binding in Chapter 5 were performed by Daniel Nissley. Antibody neutralisation experiments were performed by William James and Wanwisa Dejnirattisai.

Claudia Driscoll produced the DoubleCatcher protein and monovalent streptavidin used in Chapter 6.

1.3 *Publications*

Parts of this thesis have been published in the following publications.

Pettmann J, Huhn A, Abu Shah E, Kutuzov MA, Wilson DB, Dustin ML, Davis SJ, van der Merwe PA, Dushek O. (2021) The discriminatory power of the T cell receptor. *Elife*.

Pettmann J, Awada L, Różycki B, Huhn A, Faour S, Kutuzov M, Limozin L, Weikl TR, van der Merwe PA, Robert P, Dushek O. (2023) Mechanical forces impair antigen discrimination by reducing differences in T-cell receptor/peptide–MHC off-rates. *The EMBO Journal*.

Huhn A, Nissley DA, Wilson DB, Kutuzov MA, Donat R, Tan TK, Zhang Y, Barton MI, Liu C, Dejnirattisai W, Supasa P *et al.* (2023) The molecular reach of antibodies determines their SARS-CoV-2 neutralisation potency. *bioRxiv*.

During the past few years, I wrote and edited several articles on Wikipedia, including articles on the T-cell receptor, kinetic segregation, non-catalytic tyrosine-phosphorylated receptors and neutralising antibodies.

2

BACKGROUND

2.1 The adaptive immune response

The human immune system defends our body against potentially dangerous invaders. It destroys foreign pathogens, such as viruses, bacteria, protozoa, helminths, and fungi, as well as toxins. It also protects us from degenerated and cancer cells, and it clears our body from dead cells and damaged tissue. These functions are performed by highly specialised cells that employ intricate signalling networks to detect and react to incoming threats.

We generally separate the immune response into an innate response and an adaptive response. Cells of the innate immune system produce germ-line encoded receptors that recognise conserved patterns present in many microbes and toxins, for example, lipopolysaccharides on the surface of bacteria, or single-stranded DNA carried by viruses[2]. This triggers an inflammatory response resulting in the killing of the pathogens. Because of the large number of cells that carry the same receptor, the innate immune system can rapidly recognise and respond to an invader.

The adaptive immune system, on the other hand, recognises highly specific structures of a particular pathogen strain, so-called antigens. The main cell types of the adaptive immune system are lymphocytes; specifically lymphocytes derived from the thymus (T cells) and lymphocytes derived from the bone marrow (B cells) that roam around the body and recognise antigens. They express antigen-specific receptors: the T-cell receptor (TCR) on T cells and immunoglobulin (Ig) expressed by B cells. Immunoglobulins occur either as B-cell receptors (BCRs) on the B cell surface or in secreted form known as antibodies. TCR and BCR genes have a common ancestor as evidenced by the similar domain structure, signalling pathway

and development[3–5]. During T and B cell development, random somatic recombination of the genes encoding these antigen receptors allows the generation of millions of different variants of the receptor proteins. Hence, each lymphocyte carries a different antigen receptor with a unique specificity to a pathogen. Collectively this highly diverse receptor repertoire can recognise a plethora of different antigenic structures. Upon antigen recognition, the antigen-specific cells start to proliferate to generate many cells with the same antigen-specificity, a process known as clonal expansion[6,7]. Random generation of antigen receptors could generate receptors that bind to healthy, endogenous cells, resulting in an attack of self-tissue. A crucial feature of antigen-specific lymphocytes is therefore their ability to discriminate between foreign and self-antigens, giving rise to immunological tolerance of self-tissue.

The adaptive immune system employs a range of effector functions to eliminate pathogens in the most effective way. Depending on the type of pathogen, whether it is an extracellular or intracellular bacterium, a virus infection, or a parasite, a different effector response is launched. Even though TCRs and BCRs arose from the same ancestor, they occupy distinct functions in the adaptive immune response and recognise different types of antigens. B cells recognise a wide variety of structures of extracellular pathogens and their toxins. After binding to an antigen, they start secreting antibodies with the same antigen specificity as their BCR. Antibodies bind to pathogens or toxins. In some cases, this can directly neutralise them, for example by blocking important structures on the surface of viruses such that they cannot infect their host cells anymore. In other cases, antibody binding allows the recruitment of the complement system, which can directly destroy pathogens. It also allows the recognition and elimination of pathogens by cells of the innate immune system. T cells, on the other hand, recognise foreign antigens in the form of short peptides presented by the major histocompatibility complex (MHC) on cell surfaces. These peptides are generated inside the cells through routine protein digestion, which allows T cells to detect intracellular pathogens and cancer cells. T cells differentiate into cytotoxic T cells or helper T cells. Upon antigen recognition, cytotoxic T cells can directly kill the infected cell, while helper T cells coordinate an immune response through activation of other cells of the immune system, including B cells. The immune system has the ability to remember specific antigens it has encountered by generating long-lived T and B cells. This immunological memory allows for a more rapid and effective response upon subsequent exposure.

The adaptive immune response must maintain a careful balance between activation and tolerance to ensure adequate lymphocyte responses to infections while preventing autoimmunity due to excessive activation. Therefore the immune system employs multiple mechanisms to precisely control lymphocyte activation. In the following sections, the structure of lymphocyte antigen receptors and their binding partners will be introduced as well with the processes that regulate lymphocyte activation and immunological tolerance.

2.2 *T cell receptors*

2.2.1 *TCR binds processed peptides presented by MHC*

MHC proteins bind short peptide fragments that are between 8 - 15 amino acids in length (peptide-MHC complex, pMHC for short), which allows the presentation of these peptides to T cells. There are two classes of MHCs, MHC Class I and MHC Class II. The two classes obtain their peptides from different sources and importantly differ in the immune response they trigger[8]. The general structure of both MHC class I and II is quite similar. Both consist of two protein chains that form a dimer (Fig. 2.1A and B). Proximal to the membrane, they have two Ig-like domains, and further away from the membrane, two domains create a peptide binding groove, which facilitates the binding and presentation of peptide fragments . In both MHC classes, peptides are held in place between two anti-parallel alpha helixes with a base composed of eight anti-parallel beta-pleated sheets (Fig. 2.1C). Peptide fragments bind stable to the peptide binding groove via a series of ionic and hydrogen bonds. The amino acids of the peptide that interact with MHCs are called anchor residues.

To ensure that a broad range of peptides can be bound and presented, MHC genes are highly polymorphic, with a total of 38000 different MHC alleles currently identified in the human population[10,11]. An individual can carry up to 6 different MHC Class I alleles and 6-8 different MHC Class II alleles. The polymorphism is located at the base of the peptide binding resulting in amino acid differences at key peptide binding sites[12]. Thus every MHC allele has a slightly different substrate preference.

The MHC class I molecule is made of a polymorphic heavy α chain, composed of three extracellular domains (α1, α2, and α3) and a transmembrane domain. Domains α1 and α2

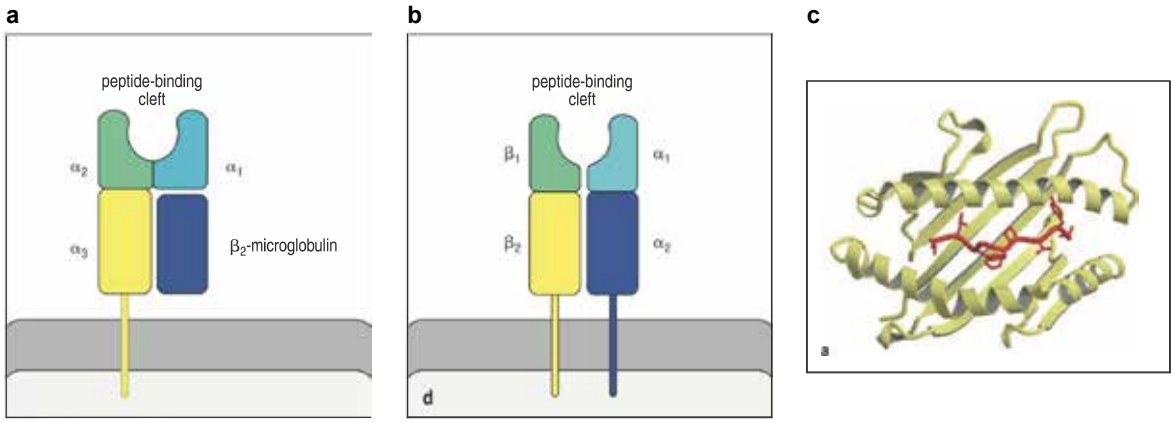

Figure 2.1: MHC structure. (A) MHC Class I schematic (image taken from[9]). **(B)** MHC Class II schematic (image taken from[9]) **(C)** Structure of peptide binding groove of MHC Class I (image taken from[9])

form the peptide binding groove, whereas α3 is an Ig-like domain. The heavy α chain is noncovalently associated with the non-polymorphic β2-microglobulin (β_2m) domain, which forms the second Ig-like domain (Fig. 2.1A). MHC Class I molecules bind peptides that are between 8 and 10 amino acids long. MHC class II is composed of two polypeptide chains, α and β, each consisting of two domains and a transmembrane domain (Fig. 2.1B). The N-terminal domains of the α and β chains combine to form the peptide binding groove. Compared to class I, class II can bind significantly longer peptides, with a length ranging from 13 to 17 amino acids.

2.2.2 *Generation of pMHC*

Class I and Class II MHCs are expressed on distinct cell types and present peptides from different sources, reflecting the different immune responses they trigger. MHC Class I molecules are expressed by every cell type in the body. They present peptides that are derived from proteins in the cytosol of the cells[13]. This enables the detection of antigens associated with intracellular infections and cancer cells. Peptides presented by MHC Class I are identified by cytotoxic T cells, which can promptly eliminate the recognised cell. Cytotoxic T cells express the CD8 surface receptor ($CD8^+$ cells) that binds to MHC Class I.

On the other hand, MHC class II molecules are exclusively found on "professional" antigen presenting cells (APCs). These mainly include dendritic cells, B cells, and macrophages. Peptides originate from materials taken up from the extracellular environment, such as extra-

cellular pathogens, and cellular debris[13]. Recognition of MHC Class II occurs by helper T cells, which subsequently stimulate other effector cells to efficiently eliminate the infection. T helper cells express the CD4 coreceptor ($CD4^+$ T cells) that can bind MHC Class II molecules. The mechanism of peptide generation and presentation on MHCs is described in detail in the following section.

FOR MHC CLASS I peptide presentation, proteins in the cytosol are degraded by the ubiquitin-proteasome complex[14]. Cytosolic proteins tagged for degradation with ubiquitin are delivered to the proteasome, a multicomponent protease complex[15]. The central core of the proteasome contains catalytically active β-subunits that cleave proteins into peptides, typically 8-10 amino acids in length. These peptides are then transported into the endoplasmic reticulum (ER) by the transporter associated with antigen processing (TAP), an ABC transporter composed of a TAP1–TAP2 heterodimer[16]. Inside the ER, peptides are loaded onto MHC Class I molecules by a large multimeric complex called the peptide-loading complex (PLC). The PLC includes TAP, tapasin, ERp57, calreticulin, and calnexin[17]. Calnexin stabilises the MHC Class I alpha chain until beta2m is bound. In the absence of a peptide, the MHC molecule is very unstable and requires the chaperones calreticulin and ERp57 for stabilisation. Tapasin binds both to ERp57 and the TAP complex, positioning the empty MHC Class I molecules close to the source of peptides. Furthermore, tapasin stabilises the peptide-binding groove in an open position for optimal peptide loading[18]. Once loaded with a peptide, the MHC Class I molecule dissociates from the PLC and is transported to the cell surface.

FOR MHC CLASS II peptide presentation, extracellular antigens are captured via phagocytosis or endocytosis, mediated by various receptors such as the BCR, mannose receptor, complement receptors, and Fc receptors[13]. Alternatively, antigens can be taken up nonspecifically through macropinocytosis and autophagy. Internalised antigens are delivered to endolysosomal vesicles where antigen processing and MHC loading take place. Here, the proteins are exposed to acidic and reducing conditions that help unfold the proteins[19]. Proteolysis is catalysed by cathepsin proteases[20]. During the synthesis of class II MHC molecules in the endoplasmic reticulum, they associate with the invariant chain (Ii). The Ii blocks the MHC binding cleft to prevent peptide loading with cytosolic peptides and contains a sorting signal in its N-terminal tail that directs the transport of MHC Class II to endolysosomal vesicles. Once in these vesicles, cathepsins cleave the invariant chain, leaving a small fragment bound to the binding groove,

called the CLIP peptide. HLA-DM, a protein similar to MHC Class II, facilitates the exchange of CLIP for antigenic peptides. Through interactions with HLA-DM, bound peptides are removed from the MHC Class II binding groove and replaced with other peptides[21]. This cycle of peptide replacement continues until a high-affinity peptide is found that can no longer be displaced by HLA-DM. This process generates highly stable MHC Class II-peptide complexes. The pMHC complex is then transported to the cell surface for presentation to T cells.

Importantly, during pMHC generation, antigen-presenting cells do not differentiate between antigens from foreign pathogens and antigens that originate from healthy endogenous cells (self-antigens) and thus process and present a large number of self-protein derived pMHCs whether an infection is present or not. In an infected cell, the numbers of foreign pMHC can be very low. For example in HIV-infected CD4+ T-cells, only 8-46 pMHCs out of approximately 100 000 total pMHCs per cell present HIV-specific peptides[22].

2.2.3 *Structure of the TCR*

Peptide-MHC complexes interact with the αβTCR that is expressed by most T cells. The αβTCR is a heterodimeric protein consisting of an α chain (TCRα) and a β chain (TCRβ) linked by a disulfide bond. Every T cell expresses about 30,000 - 40,000 T-cell receptors on its membrane[23]. A minority of T cells express the unconventional $\gamma\delta$ TCR. Here we will only be discussing the αβTCR.

The TCRα and TCRβ chains both consist of two extracellular domains - a variable domain and a constant domain. These are followed by a connecting peptide (Cp), a transmembrane domain, and a short cytoplasmic tail (Fig. 2.2A). The variable domain is responsible for binding to pMHC. This region is assembled by random recombination during T cell development in the thymus and therefore differs between TCRs. The structure of the constant region, on the other hand, is germ-line encoded and shared by all TCRs.

Structural diversity of the variable domain is achieved by somatic recombination from a large number of potential gene fragments in the TCR loci[9]. The TCRα locus is formed from the variable (V) and joining (J) gene segments, while the TCRβ locus includes an additional diversity (D) segment along with the V and J gene segments. VDJ recombination is

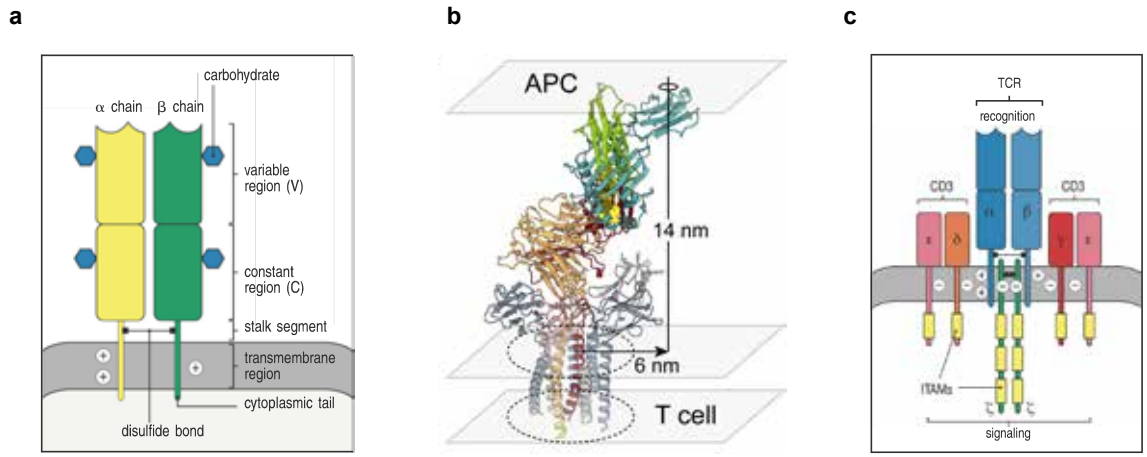

Figure 2.2: TCR structure. (A) Schematic of αβTCR (image taken from[9]). **(B)** CryoEM structure of full αβTCR-CD3 complex (image taken from Sušac et al.[24]) **(C)** Schematic of full TCR-CD3 complex (image taken from[9]

carried out by the recombination activating gene (RAG)1 and RAG2, which randomly bind to recombination signal sequences (RSS) flanking the V, D, or J gene segments. This binding brings the segments into close proximity, allowing the intermediate DNA sequence to be excised. Non-template encoded and palindromic nucleotides are randomly added at VDJ joints by terminal deoxynucleotidyl transferase (TdT), a template-independent DNA polymerase, and the Artemis nuclease, respectively, along with the removal of nucleotides. Random nucleotide addition by TdT contributes to approximately 90% of T cell repertoire diversity[25].

The TCR variable region contains six complementarity-determining regions (CDRs), three per chain called CDR1, 2 and 3. CDRs are hypervariable loops that form the binding site for pMHC. Importantly, they bind to both the antigenic peptide and the MHC itself[12,24]. Structural analyses of TCR of TCR/pMHC complexes have revealed that the peptide is primarily bound by the CDR3α and CDR3β loops. CDR3 lies at the junction between the rearranged V, D, and J segments and thus includes randomly added nucleotides, resulting in a high degree of genetic variability. CDR3 loops therefore significantly contribute to the specificity of the TCR. The interaction between MHC and TCR is primarily mediated by CDR1 and CDR2 however they frequently also contribute to peptide binding. In contrast to the CDR3, CDR1 and CDR2 are entirely encoded by V genes[12,26]. The αβTCRs bind pMHC with relatively weak affinity (1 µM-100 µM) compared to other surface ligand receptors[27,28].

Crystal structures reveal that both TCR and pMHC extracellular domains measure about 7 nm in length[29,30]. Together, a TCR-CD3 complex bound to pMHC spans an intermembrane

distance of approximately 14 nm[24,31] (Fig. 2.2B). In contrast to the crystal structures, recent CryoEM structures of human TCR-CD3 complexes obtained in a native-like lipid environment suggest that the TCR's extracellular domain has a more compact structure, measuring approximately 3-4 nm[32].

In the plasma membrane, the αβTCR forms a complex with the CD3εγ, CD3εδ, and CD3ζζ dimers through interactions in their transmembrane and Cp domains[33] (Fig. 2.2C). The CD3 proteins have long, unstructured cytosolic tails containing tyrosine residues that can bind signalling proteins during TCR activation. Specifically, they contain immunoreceptor tyrosine-based activation motifs (ITAMs), which are short amino acid sequences consisting of two conserved tyrosines and two leucines or isoleucines spaced at specific intervals (YxxL/I-X(6-8)-YxxL/I, where Y is tyrosine, L is leucine, I is isoleucine, and X is any amino acid)[34,35]. When the tyrosine residues within ITAMs become phosphorylated they serve as binding sites for SH2 domain-containing proteins. The TCR alpha and beta chains themselves do not carry any signalling domains; thus the CD3 domains act as adapter proteins that propagate the pMHC/TCR binding event to the downstream signalling pathway. Each of the CD3γ/δ/ε subunits is composed of a single extracellular Ig domain and a cytosolic domain containing a single ITAM motif. On the other hand, CD3ζ only has a short extracellular domain but a long cytoplasmic domain containing three ITAM motifs. In addition to ITAMs, the CD3 cytoplasmic tails contain a proline-rich region (PRR) and "basic rich stretch" (BRS) motifs that are abundant in positively charged amino acid residues. Only recently the structure of the full TCR-CD3 complex has been solved, providing insight into the arrangement of TCR and CD3 dimers[24,32,36,37]. The structure shows that the αβTCR is positioned at the centre of the complex while CD3 dimers assemble around it. The structure of the cytoplasmic tails has not yet been resolved due to low electron density in cryoEM images, likely because they are unstructured and highly mobile. However, Nuclear Magnetic Resonance (NMR) and fluorescence resonance energy transfer (FRET) experiments have shown that the CD3 cytoplasmic domains bind to the plasma membrane via their BRS domain interacting with anionic phospholipids[38,39]. Upon binding of TCR/pMHC, these domains dissociate from the membrane[40].

2.2.4 *T cell signalling and activation*

T cells travel through the body via the blood and lymphatic system, continuously searching for foreign antigens. They move in response to chemical signals, known as chemokines, which guide them towards areas of infection or inflammation. When T cells encounter antigen-presenting cells or other target cells, they scan the pMHC molecules on the surface of these cells for their cognate pMHC, which their TCR can bind with high specificity.

Upon binding to pMHC, the TCR initiates a signalling cascade that leads to the activation of the T cell. The signalling pathway involves protein phosphorylation, transcription factor activation and cytoskeletal remodelling. During this process, T cells form an immunological synapse that allows them to stay in contact with the target cell for several hours. Once activated, T cells undergo rapid proliferation, and antigen-inexperienced naïve T cells differentiate into effector and memory cells. Effector T cells then carry out various functions, such as releasing cytokines to recruit other immune cells, providing help to B cells to produce antibodies, or directly killing infected or abnormal cells. TCR activation is modulated by additional signals from co-signalling receptors and cytokines. In the following section, the antigen recognition and signalling events leading to T cell activation are discussed.

2.2.4.1 *Target cell scanning by microvilli*

The extracellular surface of APCs and other target cells are covered by the glycocalyx, a dense matrix of glycoproteins, glycolipids, and carbohydrates that extends 50 nm-500 nm from the membrane. It acts as a physical barrier, protecting the cell from close membrane contact with other cells[41,42]. The glycocalyx also hinders TCR/pMHC recognition[43]. To penetrate the glycocalyx, T cells have numerous finger-like protrusions on their membrane surface termed microvilli, first observed by scanning electron microscopy[44]. Microvilli measure between 100 nm and 4 µm in length and between 70 and 350 nm in diameter[45,46]. They contain actin filaments, which allow them to be highly mobile and exert force on the glycocalyx of the target cell. This process physically excludes the glycocalyx on the target cells[47]. Glycocalyx puncture by microvilli and the formation of small contacts of less than 0.5 µm in diameter on supported lipid bilayers were observed using total internal reflection fluorescence microscopy[43]. T cells express CD2, a cell adhesion protein interacting with CD58 on the target cell[48]. This interaction is required to stabilise the contact between the T cell and the target cell for efficient pMHC

scanning[43]. Thus, microvilli allow the penetration of the glycocalyx and drive membrane apposition for CD2 binding, allowing the T cell to establish close membrane contacts and scan the surface for their cognate antigen[47].

2.2.4.2 *TCR triggering*

The first observable step in the TCR signalling pathway is the tyrosine phosphorylation of the CD3 ITAM motifs by the protein tyrosine kinase Lck[49,50]. The phosphorylated ITAM residues serve as docking sites for downstream signalling molecules, which can propagate the signal[51,52]. Receptor triggering describes the process by which a ligand-receptor interaction induces biochemical changes in the intracellular signalling domain of the receptor. For the TCR this involves inducing changes in the CD3 proteins that result in ITAM phosphorylation. The TCR-CD3 complex has no intrinsic kinase activity, the ITAMs of the CD3 proteins are instead phosphorylated by the Lck kinase. Dephosphorylated Lck in its open and active conformation was found to be present in T cells before TCR/pMHC binding, indicating that a significant proportion of Lck is active and capable of phosphorylating CD3 ITAMs before TCR engagement[53,54]. To prevent tonic signalling, TCR triggering needs to make ITAMs receptive to phosphorylation upon pMHC binding, while an unphosphorylated state is maintained in the absence of TCR engagement. How pMHC binding to TCR accomplishes this perturbation is not fully understood. Various mechanisms have been proposed, including kinetic segregation of kinases and phosphatases, TCR clustering and conformational changes of the TCR-CD3 complex[55]. These competing mechanisms are discussed below.

KINETIC SEGREGATION The kinetic segregation model proposes that even before pMHC binds the TCR, CD3 ITAMs are accessible for phosphorylation and are thus constantly phosphorylated by Lck[56]. However, TCR triggering is avoided in the unbound state due to the presence of the CD45 phosphatase which readily removes phosphorylations from tyrosine residues and inhibits signal initiation. According to the model, CD45 is physically excluded from the bound TCR complex, perturbing the balance of kinase activity to phosphatase activity in favour of phosphorylation. This results in the accumulation of ITAM phosphorylation and initiation of the signal. The concept of physical exclusion of CD45 stems from the observation that the ectodomain of CD45 is much larger than the TCR pMHC complex[48]. The interaction between ligand and receptor brings the membranes into close contact, and the gap between membranes

of approximately 14 nm is too narrow for membrane proteins with large ectodomains to diffuse into the region, while it is still accessible for the small Lck kinase.

Support for this model comes from the observation that the chemical inhibition of tyrosine phosphatases induces ITAM phosphorylation and signalling even in the absence of ligand binding[57]. Furthermore, the segregation of CD45 from ligand-binding regions has been confirmed experimentally using super-resolution microscopy[31]. It was also shown that when the extracellular domain of CD45 was artificially truncated such that it was able to enter the close contact zone, TCR triggering was inhibited[58,59]. The same behaviour was observed when MHC was elongated such that it could not form close contact zones[58,59].

CLUSTERING The discovery that the TCR is not activated by a single soluble pMHC, but by pMHC dimers or other multimeric pMHC complexes led to the idea that TCR multimerisation or clustering is necessary for TCR activation[60–63]. It was also observed that TCR microclusters form around the initial pMHC binding site[64–66]. Further support came from experiments showing that receptor crosslinking or artificial CD3ζ clustering is sufficient to initiate a signal[67,68]. Although it has been clearly shown that artificial clustering can induce T cell activation, we lack evidence that clustering is happening *in vivo*. Analysis of the stoichiometry of TCRs upon ligand binding identified exclusively monomeric TCR–CD3 complexes, contradicting T cell activation via clustering[69].

CONFORMATIONAL CHANGE Another model proposes a conformational change of the TCR-CD3 complex as a mechanism for TCR triggering. Structure analysis using NMR and cryoEM have revealed that the TCR-CD3 complex can adopt different conformations[32,70]. It has been proposed that when the CD3 cytoplasmic tails are membrane-bound in the untriggered state of the TCR, the ITAMs are inaccessible for Lck phosphorylation[38,39]. According to this model, the binding of pMHC induces a conformational change in the receptor. Through allosteric effects, the structural change at the pMHC/TCR interface is propagated to the cytoplasmic CD3 regions. As a result, the CD3 cytoplasmic domains dissociate from the membrane and become accessible for phosphorylation.

Conformational changes in the TCR ectodomains upon pMHC binding have been observed[71], and modelled using molecular dynamic (MD) simulations[72]. Furthermore, in a cell-free assay using a purified TCR-CD3 complex, it was shown that the Nck tyrosin kinase

only interacted with CD3 when pMHC was bound by the TCR, indicating that a conformational change takes place upon pMHC binding, even in the absence of ITAM phosphorylation[73]. However, we currently still lack evidence that conformational change is required for ITAM phosphorylation. It was later shown that the Nck/CD3 interaction is not essential for TCR triggering[74,75]. Furthermore, in experiments where the BRS regions that allow CD3 membrane interaction were mutated to prevent membrane binding, no increased signalling was observed.[40,76]. Experiments using mutated ITAMs suggest that TCRζ membrane dissociation requires phosphorylation of TCRζ ITAMs[40]. So far no crystal or cryoEM structures of the TCR-CD3 complex have shown direct evidence for a conformation change in the CD3 cytoplasmic tails upon pMHC engagement, as resolving the unstructured CD3 tails with these methods has proven challenging. Experimental systems that use artificial TCR systems, for example when the extracellular domain was exchanged against photoreceptor phytochrome B[77], DNA[78], SpyCatcher system[79] or antibodies as in the case of chimeric antigen receptor (CAR), also allow TCR triggering, which questions the importance of a conformational change of the TCR for triggering.

In augmentation to the conformational change model, recent studies have proposed that the TCR acts as a mechanosensor; conformational change of the αβTCR is induced due to the presence of tangential force on the TCR/pMHC complex generated by cell movement[80,81]. Force is generated by membranes deforming to allow for TCR-pMHC binding, by additional adhesion bonds between T cells and target cells, as well as cell movement[82]. The induction of conformational change by force on the cell-cell interface would explain why conformational change is not observed in crystal and cryoEM structures of the TCR/pMHC complex, as these structures are generated in the absence of force. Furthermore, it explains why single soluble pMHC do not trigger a TCR response. However, precise measurements of the force acting on the TCR/pMHC complex via a FRET-based sensor revealed a force of less than 5 pN, indicating a minimal force that may not be strong enough to induce significant conformational changes[83].

2.2.4.3 *Proximal pathway*

Once a pMHC molecule binds to TCR, the coreceptors CD8 and CD4 can bind MHC Class I and Class II, respectively. Lck is associated with the cytoplasmic tails of CD4 and CD8[84]. The role of the coreceptor interaction for TCR signalling in mature T cells is not fully understood. Ex-

periments have shown that the coreceptor binding can stabilize the TCR/pMHC complex[85,86] and increase T cell sensitivity by facilitating the recruitment of Lck to the TCR[87–89]. The augmentative effect of coreceptors may depend on the strength of the TCR/pMHC interaction[90].

After CD3 ITAMs are phosphorylated by Lck, the protein tyrosine kinase ZAP-70 is recruited to the TCR-CD3 complex[51]. ZAP-70 has a tandem SH2 domain that can bind to the phosphorylated ITAM motifs. This brings ZAP-70 into close proximity to Lck which in turn phosphorylates and thereby activates ZAP-70. ZAP-70 can phosphorylate multiple tyrosine residues of the transmembrane protein LAT. LAT is a scaffolding protein that is attached to the cell membrane. Although it lacks any catalytic activity, it plays a crucial role in the activation of many downstream signalling proteins. These proteins, along with other scaffolding proteins, bind to the phosphorylated tyrosine residues on LAT via their SH2 domains. This brings them in close proximity to ZAP-70 and Lck which facilitates the activation of downstream signaling proteins and promotes the further phosphorylation of scaffold proteins. This results in the formation of large clusters of LAT that act as highly cooperative signalosomes[91,92].

2.2.4.4 *Downstream pathway*

Molecules that bind the LAT complex include the guanine nucleotide exchange factor VAV1 and Phospholipase Cγ1 (PLCγ1). VAV1 stimulates cytoskeletal reorganization through activation of Rho family GTPases, while PLCγ1 generates second messenger molecules diacylglycerol and inositol-trisphosphate. These molecules disperse throughout the cell to trigger a calcium release and to activate downstream signalling effectors such as mitogen-activated protein kinases and protein kinase C.

The result of these signalling events is the activation and nuclear translocation of transcription factors. This includes the activator protein 1 (AP1), the nuclear factor-κB (NFκB), and the nuclear factor of activated T cells (NFAT). These factors, along with signals from co-signalling receptors and cytokine receptors, coordinate diverse T-cell responses, including proliferation, differentiation, migration, cytokine generation, and cytotoxic activity.

2.2.4.5 *Signal intergration*

When TCRs are stimulated, the quality or quantity of the resulting signalling is affected by various factors, such as the strength and length of stimulation. For full T cell activation, it is proposed that multiple TCRs must be engaged, either by multiple pMHC molecules interacting

simultaneously or through serial triggering[93]. Serial triggering refers to the sequential engagement and activation of numerous TCR molecules by a single pMHC ligand[94]. Studies have shown that a single pMHC ligand can engage and trigger up to 200 TCRs in less than an hour[95].

At the single-cell level, T-cell activation follows a digital, switch-like response, where T cells only activate if the stimulus exceeds a specific threshold[96,97]. Below the threshold, the T cell remains in a non-activated state, without any intermediate states. This switch-like response may help to reduce noise and may allow complex dynamics on a population level[98]. The precise biochemical steps encoding this response are not yet fully understood.

On a population level, the T cell response gradually increases as the concentration of ligands increases, representing an analogue response[96]. The difference between single-cell and population response can be attributed to the biological noise the system experiences, such as the non-uniform distribution of pMHCs on APCs and variations in sensitivity within the T-cell population. The population response can be characterized by a dose-response plot, which tracks the T-cell response over a range of pMHC concentrations. The response of T cells to a specific ligand can be assessed in terms of its *efficacy* and *potency*. Efficacy denotes the maximum amplitude of the signalling response triggered by the ligand. Potency refers to the concentration of the ligand required to induce a physiological response, with lower concentrations indicating higher potency. Potency is commonly quantified using the EC_{50} value, which represents the concentration of the ligand necessary to elicit a half-maximal response. Both efficacy and potency can be influenced by various factors, including the affinity of the pMHC for the TCR, the abundance of TCRs on the cell surface, the efficiency of downstream signalling pathways, and the presence of co-stimulatory or inhibitory signals.

2.2.5 *T cell maturation*

T cells originate as precursor cells from the bone marrow and mature in the thymus. The thymus is made up of numerous lobules, each separating into a peripheral thymic cortex, and a central medulla. It contains a network of epithelial cells known as thymic stroma with which the developing T cells (called thymocytes) interact. Intrathymic dendritic cells can also be found in the medulla, along with macrophages. Early experiments revealed the crucial role of

the thymus in T cell development. When the thymus was removed from mice directly after birth, it was observed that they did not produce functional T cells[99].

After commitment to the T cell lineage, T cell progenitor cells initiate rearrangement of their TCR genes beginning with the TCR beta chain and subsequently proceeding to the TCR alpha chain. T cells that fail to express a functional TCR after recombinations are deleted. To make sure the newly assembled TCR can recognise peptides in an MHC Class I or Class II context, only T cells that interact with peptide-MHC complexes receive a survival signal, a process known as positive selection. To prevent T cells from reacting against self-peptides, developing T cells whose receptors interact strongly with self-antigens get eliminated in a process called negative selection.[100]. Positive and negative selection occurs in discrete thymic microenvironments. The resulting T cell population express a TCR repertoire that possesses a high specificity towards foreign antigens. Below, the process of positive and negative selection is discussed in detail.

POSITIVE SELECTION Positive selection occurs in the thymic cortex and requires thymocytes to interact with cortical thymic epithelial cells (cTECs) presenting self-peptides on MHC molecules. Only thymocytes that can recognise pMHC receive survival signals and mature further. Positive selection ensures that the mature T cells are "MHC-restricted," meaning they can only recognise antigens when they are presented on the host's own MHC molecules[101]. The peptides presented by cTECs originate from their cytosol. The cTECs express a unique catalytic subunit of the proteasome called β5t, which assembles with 3 other subunits to form the catalytic domain of the proteasome complex[102]. The β5t subunit has an altered substrate specificity compared to proteasomes incorporating the β5 subunit expressed under normal conditions and the β5i subunit expressed by infected cells. This results in the production of different peptide fragments for MHC Class I presentation[103]. Similarly, for antigen presentation by MHC Class II molecules, cTECs express the unique lysosomal proteases cathepsin L and thymus-specific serine protease[101]. While studies have demonstrated that mice lacking a specialized peptidome in the thymus cortex exhibit significant defects in T cell positive selection[102,104], the exact function of this altered peptidome remains unknown.

Positive selection does not just depend on TCR recognising the MHC, but it has been shown that the structure of the peptide bound to the MHC molecule significantly influences the outcome of positive selection. It has been shown that only certain self-peptides can induce

positive selection of TCR transgenic thymocytes[105] and that self-peptides that induce positive selection for one T cell clone are not capable of inducing positive selection of another clone[106].

During positive selection, the linage fate of T cells is determined. Double-positive thymocytes, which initially express both CD4 and CD8 co-receptors, cease to express one co-receptor to become single-positive cells based on whether their TCR recognises MHC class I or II[107]. CD8 is initially downregulated regardless of whether the TCR recognises MHC class I or II[108,109]. This observation led to the proposal of the kinetic signalling model as a mechanism for T cell lineage fate commitment. The model argues that the lineage is decided by TCR signalling duration[108]. For MHC class I-restricted TCRs that depend on CD8 for signalling, CD8 downregulation leads to shorter, interrupted signals, directing differentiation into CD8+ cytotoxic T cells. Conversely, TCR signalling in MHC class II-restricted cells remains persistent, promoting differentiation into CD4+ helper T cells. Recent findings support this model, showing that the T cell functions are reversed if the co-receptor proteins encoded by the Cd4 and Cd8 genes are switched[110]. CD4+ T cells become cytotoxic, and CD8+ T cells take on helper functions.

NEGATIVE SELECTION After successive positive selection, thymocytes migrate to the medulla. Here, medullary thymic epithelial cells (mTECs) and dendritic cells present a wide array of self-antigens to developing thymocytes. This repertoire of self-antigens includes tissue-specific antigens due to the expression of the autoimmune regulator (AIRE) gene in mTECs, which allows for the presentation of antigens that are otherwise restricted to specific peripheral tissues. Thymocytes that are strongly activated by binding to self-antigens are eliminated via induced apoptosis. This process ensures that the mature T cell repertoire does not contain any potentially autoreactive T cells. This is known as the central tolerance.

The percentage of thymocytes that complete maturation is estimated to be around 5% or lower[111]. Only roughly 20-25% of thymocytes successfully survive positive selection, indicating that the majority of generated TCRs are incapable of binding to peptides presented by MHC. Following positive selection, between 10 and 50% of thymocytes proceed to survive negative selection.

After positive and negative selection, the resulting T cell population express a TCR repertoire that possesses a high specificity towards foreign antigens. Studies have shown that pMHC

complexes with low affinity for TCRs (T-cell receptors) induce positive selection, while high-affinity pMHC complexes lead to negative selection[112–114]. Experiments conducted on fetal thymic organs have demonstrated the existence of a distinct affinity threshold that separates positive and negative selection[114]. Positive and negative selection occurs in different temporal and spatial locations, which could explain the observed affinity distribution. Initially, during positive selection, all TCRs with any level of affinity to pMHC (low and high) are selected. Then, during negative selection, only high-affinity TCRs are eliminated. The difference in response could be regulated by the TCR's sensitivity. In line with this, it has been demonstrated that certain proteins expressed in thymocytes can modulate sensitivity[115].

It has been observed that ligands that positively select a TCR in the thymus can induce proliferation in mature T cells, but the T cells did not differentiate into effector cells[116–119]. This led to the hypothesis that low-affinity self-peptide interactions contribute to the maintenance and homeostasis of peripheral T cells.

In summary, after positive and negative selection in the thymus, the TCR repertoire is biased towards recognising foreign antigens with higher affinity compared to self-antigens, while maintaining a low but not neglectable affinity toward self-antigens.

2.2.6 *Requirements for antigen recognition*

Antigen recognition by the TCR faces unique requirements which involve balancing sensitivity, specificity, cross-reactivity, and speed to ensure effective immune responses against pathogens while avoiding harmful reactions against self-antigens. Their importance for antigen recognition is discussed below.

AFFINITY The affinity of a TCR/pMHC interaction is determined by the stability of the complex. Higher affinity indicates greater stability, typically characterized by long binding times and slow unbinding rates. Affinity is quantified in units of Molar, with lower values indicating higher affinity. The affinity between TCR and its cognate pMHC, which induces a strong activation, is in the range of 1 µM-100 µM. This is a weaker binding affinity in comparison to other surface ligand receptors such as cytokine receptors (1 pM-100 pM)[120] or antibodies.

Various affinity measurements have been conducted to determine what is the affinity of interactions between positive selecting peptide-MHCs and TCRs. One study by Alam et al.[112] found that the affinity of a positive selecting peptide was only 4-fold lower than that of the cognate peptide (20 µM compared to 6 µM for the cognate ligand). The affinity of naturally occurring peptides for the same TCR was found to be approximately 140 µM measured at 10°C. Other studies have estimated affinities for positive selecting peptides to be over 10-fold lower than that of the cognate pMHC, with affinities of over 500 µM. So far, we do not have a conclusive affinity measurement of positive selecting self-peptides at 37°C. The weak affinity may allow TCR to screen a large number of pMHC on a target cell within a short time and engage in serial triggering.

SENSITIVITY TCRs must be sensitive enough to respond to foreign pMHC even if present at low concentrations on antigen-presenting cells. For example in HIV-infected CD4+ T-cells, only 8-46 pMHCs out of approximately 100 000 total pMHCs per cell present HIV-specific peptides[22]. Other studies showed that only 0.1% of all MHC molecules on a cell present a specific peptide[121]. Some viruses, like Cytomegalovirus, are able to downregulate pMHCs presentation.

In vitro T cell activation assays have shown that the TCR can be activated by as little as one high-affinity pMHC, demonstrated with using APCs presenting a single pMHC[122,123], with an isolated pMHC coupled to a DNA origami surface[93].

The sensitivity of T cells towards antigens is not a constant value. It can be adjusted by altering the expression levels of TCR, coreceptors, and co-signalling receptors, or by expressing intracellular proteins that influence the TCR signalling pathway[124].

DISCRIMINATION TCRs exhibit high specificity for foreign antigens, preventing the immune system from targeting the body's own cells. While thymic selection biases the TCR repertoire towards foreign peptides, TCRs maintain a low, but non-neglectable affinity for self-peptide-MHC complexes as a consequence of positive selection[119]. Consequently, additional tolerance mechanisms in the periphery are necessary to prevent T cells from being activated by low-affinity self-pMHC interactions, even when present at high concentrations. This ability of T cells to discriminate between foreign and self-pMHCs is termed antigen discrimination.

The challenge is that foreign and self-antigens can be quite similar. For instance, cancerous tissue may differ from healthy tissue by only a few mutations while viruses like the Epstein-Barr virus mimic human proteins to evade immune detection[125,126]. Early experiments investigating the effects of peptide variants on TCR affinity and T cell function have revealed that positive-selecting, self-peptides can differ from the activating, cognate peptide by just a single amino acid and only have a marginally, 3-5-fold lower affinity. However, they completely failed to elicit a T cell response, even when the pMHC concentration was increased by 10^5-10^6-fold[112,127–131]. These studies suggested that TCRs are capable of detecting minute biophysical differences in pMHCs and amplifying them to large differences in potency. Decreased binding strength cannot be compensated by an increase in pMHC concentration.

Failure in precise antigen discrimination can have detrimental consequences, such as T cells wrongly recognising and attacking self-tissue and thus causing autoimmune diseases, or T cells not reacting to pathogens and cancerous cells.

CROSS-REACTIVITY While antigen specificity is essential, some level of cross-reactivity is also an inherent and necessary feature of TCR recognition to provide broad protection against diverse pathogens. TCR cross-reactivity refers to the ability of a single TCR to recognise multiple distinct pMHC complexes. This concept was initially proposed by Mason[132], who showed that the necessity for cross-reactivity arises from the vast number of potential peptide fragments - estimated at over 10^{15} - that can be presented by MHCs, while the number of T cells in the body is limited to about 5×10^{11} cells[133]. Thus, for the limited pool of TCRs to effectively recognise the multitude of theoretical foreign peptides, each TCR must be able to respond to multiple antigens. In consequence, each peptide can be recognised by several different receptors, which leads to polyclonal T-cell responses. There are further advantages of cross-reactivity for the immune response. Firstly, it enables a quicker adaptive immune response, as a cell presenting a foreign peptide needs to encounter fewer T cells before a T cell is found that responds to it. Additionally, cross-reactivity provides a robust response to pathogens that mutate their antigens, as memory T cells can still recognise and respond to similar epitopes. Mason's theoretical calculations estimated that each TCR needs to respond to 10^6-10^7 different antigens, a figure that has been corroborated experimentally[134–136].

The mechanism underlying cross-reactivity involves flexibility in the CDR loops of the TCR or altered binding orientation, allowing for slight alterations in peptide shape[137]. Interestingly,

studies have shown that not all recognised peptides exhibit the same potency[134]. While a fraction of peptides elicit a strong response at low antigen concentrations, comparable to the cognate peptide, a larger proportion of peptides require higher concentrations to activate the T cells. Moreover, TCR cross-reactivity is not solely achieved by the recognition of numerous unrelated peptides. Instead, peptide residues that are in direct contact with the CDR loops tend to be conserved, while there is more tolerance for substitutions in peptide residues that are located outside the TCR interface[136].

While cross-reactivity enables T cells to identify a diverse range of pathogens, excessive cross-reactivity may prompt immune reactions against endogenous tissues, resulting in autoimmune disorders. Thus, T cells need to uphold non-responsiveness to self-peptides despite the substantial level of TCR crossreactivity.

SPEED TCR recognition needs to be rapid to mount an effective immune response against invading pathogens. T cells must quickly identify foreign antigens to initiate the appropriate immune reaction, whether it involves activating other immune cells, killing infected cells, or producing antibodies. Experiments have shown that T cells spend only 1-5 minutes with an APC if they fail to recognise an antigen[138] and T cell activation occurs within seconds of binding to a specific antigen[91,96].

2.2.7 *Models for antigen discrimination*

It is remarkable how TCRs achieve high antigen discrimination, while also maintaining high sensitivity and cross-reactivity and making the decision to activate at an incredible speed[139]. TCRs must discriminate between structurally similar foreign and self-peptides while being sensitive to low antigen quantities. Typically, specificity and sensitivity are inversely related, yet TCRs optimize both simultaneously. They need to maintain non-reactivity to self-antigens despite high TCR cross-reactivity. Finally, the decision whether to activate or not must happen within seconds. No other surface receptor has been found to exhibit such a level of ligand discrimination, emphasizing the exceptional nature of TCRs in this regard.

The degree of antigen discrimination and its underlying mechanisms are still debated. While it is widely acknowledged that the potency of a pMHC is influenced by its binding strength to the

TCR[140], there is controversy regarding the specific chemical parameters of pMHC molecules that determine TCR triggering. While some studies argue for the affinity of pMHC/TCR interaction as the primary factor, others propose the influence of the mechanical properties of pMHC under force. It is further debated whether antigen discrimination is an intrinsic property of the TCR-CD3 complex or if it is encoded within the TCR signalling pathway. Multiple mechanisms for antigen discrimination have been proposed[55,139,141,142], which are discussed below.

OCCUPANCY MODEL One of the simplest models that describes the relationship between ligand binding and receptor response is the occupancy model, introduced by Clark[143] in 1926. This theory is based on the law of mass action, and it states that the response is directly proportional to the number of receptors occupied, ie. bound, by the ligand at equilibrium binding[144]. Receptor occupancy is determined by ligand affinity and concentration. Importantly, with the occupancy model, a reduction in ligand affinity can be compensated by a linear increase in ligand concentration. While this model is routinely used to model drug interactions for many surface receptors[145], it fails to explain the high discrimination strength of the TCR[112,141]. This required the development of more advanced models for antigen discrimination beyond mass action.

KINETIC PROOFREADING MODEL The kinetic proofreading (KP) model was originally introduced by Hopfield[146] as a mechanism for error correction during the loading of tRNAs with the correct amino acids. McKeithan[147] applied the model to TCR activation to explain antigen discrimination. Essentially, the model introduces a time delay between ligand binding and receptor activation. This delay is achieved by several biochemical steps, called proofreading steps, that take place between ligand binding and receptor activation. Only once all proofreading steps are completed, the receptor is activated. Dissociation of the ligand from the receptor before all proofreading steps have occurred leads to a reversal of the modification. From a thermodynamic perspective, the energy required to perform the proofreading steps allows the discrimination strength to be increased beyond what is possible with mass-action kinetics. In this model, the T cell activation is determined by the lifetime of the TCR/pMHC complex. Only pMHCs that bind long enough to the TCR can trigger the downstream TCR pathway. According to the KP model, a decrease in lifetime can still be compensated by an

increase in concentration. However, increasing the time delay, either by increasing the number of proofreading steps or by decreasing the rate at which each step takes place, amplifies the difference in lifetime between two pMHCs in a non-linear manner. This means, that the longer the delay, the higher the concentration needed to compensate for the difference in lifetime.

Biologically, it is assumed that the delay comes from multiple phosphorylation events on the TCR adaptor protein CD3 and other signalling components of the TCR signalling pathway such as ZAP-70[148]. If the pMHC dissociates before the receptor is triggered, the TCR is rapidly dephosphorylated. Support for the model comes from experiments using an artificial TCR system where the pMHC binding time is under optogenetic control, while all other binding parameters stay constant[77,148]. In this experimental system, the complex lifetime is a good predictor of T cell response. Comparing kinetic proofreading simulations to experimental data shows that the model can account for specificity, however may not be able to account for the sensitivity of the TCR[148]. Altan-Bonnet and Germain[96] simulated the kinetic proofreading model for two pMHC with a 5-fold difference in complex lifetime, to test whether the T cell can be differentially activated by only the peptide with longer binding while maintaining the experimentally determined sensitivity and speed of the activation. The simulation revealed that the kinetic proofreading model is not sufficient to explain antigen discrimination without the loss of ligand sensitivity.

EXTENDED KINETIC PROOFREADING MODELS Doubts about whether the KP model can sufficiently explain the high specificity and sensitivity of the TCR led to proposals of additional mechanisms that augment kinetic proofreading. Aleksic et al.[149] proposes that not just the binding time but instead the confinement time determines TCR activation, which not only depends on the complex lifetime but also the time it takes for pMHC/TCR to form. Specificity can be further improved by introducing positive or negative feedback to the kinetic proofreading (KP) model, for example by adding negative feedback in the proximal TCR signalling pathway that reduces the impact of high pMHC concentrations[150]. Phosphatase SHP-1 was suggested to be the main regulator of the negative feedback. The model can explain the discrimination of pMHC with five-fold different affinity. However, the model predictions for SHP-1 have not been verified so far. Another model suggests induced TCR rebinding upon ligand binding[151]. According to this model, TCR clusters grow when TCR is triggered, such that a pMHC that dissociates from one TCR is likely to rebind another TCR immediately,

creating positive feedback. However, interactions between TCRs upon pMHC binding have not been experimentally observed[152].

TCR AS MECHANOSENSOR Huang et al.[153] measured the lifetimes of the TCR/pMHC complex at the cell-to-cell interface. These interactions are considered two-dimensional (2D) due to the proteins being restricted to lateral movement on the membrane. Unexpectedly, the 2D lifetimes were significantly different than the three-dimensional (3D) lifetimes measured between soluble TCRs and pMHCs in solution. Furthermore, the 2D affinities correlated better with T cell response than the 3D counterparts. This observation suggested that pMHC-TCR bond lifetimes are modulated by the cellular environment.

The observation that TCR triggering is sensitive to mechanical force has led to experiments testing the impact of force on antigen discrimination[81]. Liu et al.[154] showed that TCR interaction with activating pMHC has an increased lifetime at higher forces. This phenomenon, so-called catch bond formation, was not observed for non-activating peptides. A dynamic structural model of TCR activation was proposed. According to this model, non-activating peptides form slip bonds, where the lifetime of the receptor interaction decreases with increasing tensile force, while catch bonds are produced by activating peptides, where the lifetime increases with increasing force. Hence, antigen discrimination with a strong affinity threshold is explained by the increased difference in bond lifetime under force at the cell-cell interface. Structural analyses further suggested that the binding of activating pMHC under force induces a conformational change in the TCR[155]. This insight has prompted the integration of the catch bond model of antigen discrimination with the conformational change model of TCR triggering, proposing that antigen discrimination is an intrinsic property of the TCR. This model can explain the high discrimination; only the cognate peptide can induce the specific conformational change. If a peptide with a small variation in sequence fails to induce the conformational change, it cannot activate the receptor[139]. This lack of activation cannot be compensated by an increase in ligand concentration. Therefore discrimination is completely defined at the level of the TCR/pMHC interaction.

However, the experiments that observed catch bonds upon pMHC binding have been performed with living T cells, capable of signalling. In the experiments, TCR and pMHC were brought into contact for approximately 100 ms. This may be enough time to initiate an intracellular response by the TCR. Thus we cannot conclusively say whether the catch bond

phenomenon is the cause of antigen discrimination or just a consequence of it because T cells had time to build up additional adhesion bonds after activation. Cell-free measurements of TCR-pMHC bond kinetics under force did not show catch bond behaviour, arguing for catch bond being a consequence of antigen discrimination[156,157].

In conclusion, we must obtain more precise data on both 3D and 2D affinities and kinetics across various TCR systems to effectively compare different models and elucidate the mechanisms underlying antigen discrimination.

2.3 *Antibodies*

Antibodies are produced by B cells during an immune response and form the humoral component of the adaptive immune system. Unlike TCRs, which are restricted to binding short peptides presented by MHC on cells, antibodies can bind a much wider range of antigens. In general, they can recognise any structure whose surface complements that of the antibody[158]. This includes fully folded proteins such as viral glycoproteins[159], polysaccharides,[160,161], microbial toxins[162], and lipids like phospholipids on apoptotic cells[163,164]. This versatility enables antibodies to target a wide range of potential pathogens and foreign substances. By binding to their targets, antibodies can neutralise pathogens or toxins and mark them for destruction by other immune cells.

B cells mature within the bone marrow, where they undergo somatic recombination of the BCR encoding genes, akin to TCR gene recombination, to generate a diverse repertoire of BCR structures. Like T cells, self-reactive B cell clones are eliminated during maturation to prevent autoimmune reactions. After maturation, B cells migrate to lymph nodes and the spleen, as well as other SLO[165]. In SLOs, antigens from lymphatic fluid or blood accumulate and are presented to B cells, increasing the chances for B cells to encounter their cognate antigens and providing the optimal environment for B cell activation. Upon recognition of a foreign antigen binding to the BCR, B cells proliferate and differentiate into plasma cells, which start to produce and secrete large quantities of antibodies. Antibodies undergo a second diversification step after antigen recognition, called affinity maturation, where B cells increase the binding strength of antibodies to their specific antigens through mutations and selection.

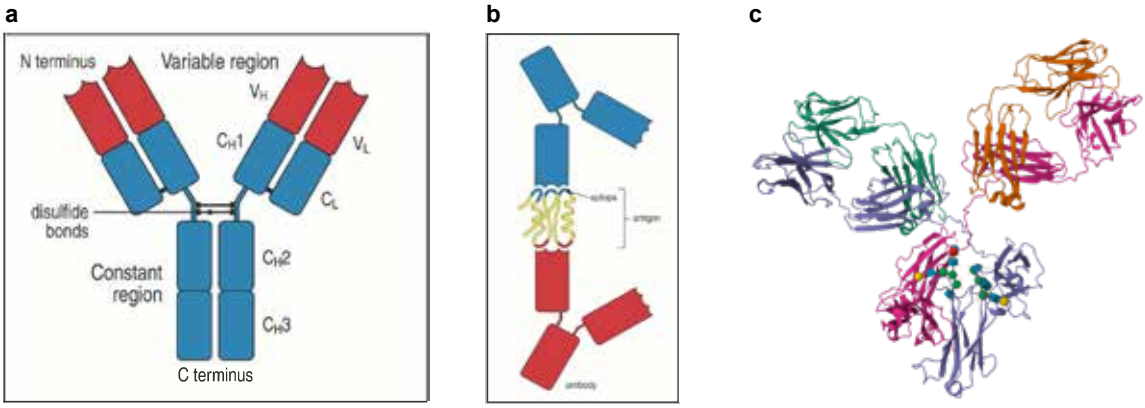

Figure 2.3: Antibody structure. (A) Antibody schematic (image taken from Murphey[9]). **(B)** Two antibodies interacting with two separate epitopes on the same antigen (image taken from Murphey[9]) **(C)** Crystal structure of IgG1 antibody (PDB structure 1IGY)

2.3.1 *Antibody structure*

The first crystal structures of antibodies were published in 1971 by Sarma et al.[166] and Poljak et al.[167]. Antibodies consist of four polypeptide chains, two identical heavy chains and two identical light chains. The chains assemble into a Y-shaped structure (Fig. 2.3A). Each "arm" of the Y-shaped structure is formed by one light chain and the N-terminal half of one heavy chain. This part of the antibody is called Fab fragment, for fragment antigen binding. It resembles the structure of the TCR, separating into a variable domain that forms the antigen binding site and varies between antibodies, and a constant domain. The two Fab fragments are connected to the "trunk" of the Y-shaped structure via a flexible polypeptide chain called the hinge region. The flexibility of the hinge allows the independent movement of the Fab fragments, as demonstrated by electron microscopy[168–172]. The trunk is also called Fc fragment (fragment crystallizable) and is formed by the C-terminus halves of the heavy chains. The Fc fragment is part of the constant region of the antibody.

Antibody diversity is achieved by somatic recombination of variable (V), diversity (D), and joining (J) gene segments in the BCR loci similar to the TCR rearrangement. The heavy chain of the BCR is assembled from V, D, and J segments, while the light chain is formed from V and J segments only. As for the TCR, this recombination is mediated by RAG1 and RAG2. Additional diversity is generated at the V(D)J junctions by the random addition of non-template encoded nucleotides by TdT.

As for the TCR, antibodies have 6 hypervariable CDR loops at the tip of each arm that create an antigen-binding site. Antigens for antibodies can be complex macromolecules, mainly proteins, but also sugar molecules and lipids[158]. Antigens can be soluble or bound to the surface of a pathogen. The specific site of an antigen to which an antibody binds is called an epitope. A single antigen can have multiple epitopes (Fig. 2.3B). The binding modes of antigens to antibodies can vary widely. Antibodies can bind conformational epitopes, made up of separate segments of the antigen, or linear epitopes, made up of a single segment. The interface between the antibody and epitope can be concave, flat, or convex, with the antigen-binding site forming pockets, grooves, or even extended loops protruding into recesses on the surface of the antigen. Binding involves noncovalent interactions such as electrostatic interactions, hydrogen bonds, and van der Waals forces[9].

Because antibodies have two antigen binding sites they are able to simultaneously bind to two antigens, such as two glycoproteins on a virus surface or repeating sites on bacterial lipopolysaccharides. This bivalent binding increases the overall binding strength of antibodies to surface antigens and allows cross-linking of soluble antigens[173]. The flexibility of the hinge region and the V-C junction provide spatial tolerance, enabling them to bind to two antigens that are spaced apart by varying distances.

The constant region can take one of five biochemically distinguishable structures, that differ in their hinge and Fc fragment structure. Based on the structure of the constant domain we differentiate five antibody isotypes. The five isotypes are immunoglobulin M (IgM), immunoglobulin A (IgA), immunoglobulin D (IgD), immunoglobulin G (IgG) and immunoglobulin E (IgE) and they have different functions in the immune response. The most abundant isotype is IgG which itself has several subclasses (IgG1, 2, 3 and 4 in humans).

The B-cell receptor is a membrane-bound antibody. Similar to the TCR, the BCR associates with two adaptor proteins Igα and Igβ, which have long intracellular domains containing ITAM motifs that are critical for signalling[174]. The whole complex spans approximately 18 nm[175].

2.3.2 *Effector functions of antibodies*

Antibodies make up the humoral responses of the adaptive immune system. They have several different functions:

NEUTRALISATION Binding to a pathogen or its toxic product, antibodies can directly inhibit infection or killing of host cells. Neutralisation can happen through various mechanisms, including aggregation of pathogens or sterically blocking receptors of pathogens needed for attachment and entry of host cells.[176]

COMPLEMENT ACTIVATION The complement system is a set of proteins in the blood and other fluids that assemble on the surface of pathogens, leading to the destruction of pathogens, the recruitment of immune cells and the phagocytosis of the pathogen. Antibodies bound to pathogens can recruit the first component of the complement system, initiating its assembly and activation[9].

OPSONISATION Antibodies can bind to pathogens and tag them for destruction by immune cells. Immune cells, such as granulocytes (neutrophils, eosinophils, basophils and mast cells), macrophages, natural killer (NK) cells, and dendritic cells, express Fc receptors that bind to the Fc fragment of antibodies[177]. This interaction triggers various downstream effects depending on the type of immune cell involved. Granulocytes and macrophages are capable of phagocytising and breaking down antibody-coated pathogens[176]. NK cells among other immune cells initiate antibody-dependent cellular cytotoxicity (ADCC), which kills pathogens through the release of proteins such as perforin and granzymes[178]. Furthermore, dendritic cells capture pathogens to present antigens to T cells, thereby facilitating adaptive immune responses[179].

2.3.3 *B cell activation*

In the lymph node, B cells encounter a variety of antigens[180]. These include soluble antigens, such as low molecular mass toxins, which can freely diffuse into secondary lymphoid organs (SLOs). Larger antigens are membrane-bound and presented on the surfaces of macrophages, dendritic cells, or follicular dendritic cells (FDCs). These larger antigens consist of intact pathogens like viruses and bacteria, as well as antigenic material secreted by pathogens or cleaved off by proteases and other enzymes. Antigens can be directly bound by pattern recognition receptors and scavenger receptors, or in opsonised form as immune complexes via complement or Fc receptors.

The signalling pathway of the BCR is similar to that of the TCR. Antigen binding to the BCR triggers the phosphorylation of ITAMs in its Igα and Igβ adaptor proteins, leading to a phosphorylation cascade that results in calcium influx and NF-κB activation[181]. The exact mechanism of BCR triggering is still debated. It has been shown that only multivalent, large monovalent, or membrane-bound antigens can activate BCRs, whereas small monovalent antigens do not[182,183]. In the resting state, BCRs occur as monomers, dimers, or loosely associated clusters on the B cell membrane[182]. Upon antigen binding, large BCR clusters form[184,185]. This clustering may change the accessibility of ITAMs for kinases and exclude phosphatases, thereby allowing ITAM phosphorylation. Consistently, CD45 segregation from these BCR clusters has been observed[186]. Further experiments have shown that antigen binding causes a conformational change, unmasking a clustering interface within the membrane-proximal domains of BCRs that facilitates oligomer formation[187]. Mechanical forces acting on the BCR-antigen bond may contribute to this conformational change (Wan 2015, Shen 2019). Moreover, kinetic segregation of CD45 by bulky or multivalent antigens has been suggested as a mechanism for BCR triggering, similar to the model proposed for TCR triggering[182]. It could be that in order to accommodate and respond to a broad range of antigen structures, the BCR triggering mechanism varies depending on the size, structure, and presentation of antigens on antigen-presenting cells.

Full B cell activation requires a second signal from activated T helper cells that are specific for the same antigen. To achieve this B cells take up the recognised antigen and present it to T cells. The uptake of the antigen occurs in an immune synapse that forms between the B cell and the APC upon BCR engagement,[188]. BCRs cluster in the centre of the synapse surrounded by a ring of adhesion molecules. The B cell exerts a pulling force, generated by the cytoskeleton, on the bound BCR-antigen complex to extract the antigen from the presented surface and internalise it[189]. The applied force weakens the bond between antibody and antigen, resulting in low-affinity interactions to rupture within physiologically relevant timescales (1 - 3min), while allowing the preferred internalisation of high-affinity antigens. This allows B cells to efficiently scan antigens in a short time frame[190,191]. This "mechanical testing" of the strength of the BCR-antigen interactions has been suggested as a mechanism for antigen discrimination[189,192–194].In addition to force exertion, lysosomal proteases are secreted at the immune synapse to enhance the extraction of immobilised antigen[195].

Internalised antigens are degraded and loaded onto MHC Class II for the presentation of antigens to helper T cells. T cells specific for the presented antigen then provide signals required for B cell survival and proliferation through engagement of the CD40 surface receptor and release of cytokines. Afterwards, B cells either differentiate into extrafollicular plasmablasts, which rapidly produce antibodies, or they remain in the follicle and undergo affinity maturation. After this process, they can further specialise into either plasma cells, which secrete high-affinity antibodies, or memory B cells.

Some antigens, such as non-protein microbial antigens, can activate B cells without T cell help. In this case, a second signal comes from the recognition of pathogen-associated molecular patterns via pattern recognition receptors (e.g., lipopolysaccharides or bacterial DNA) or from binding repetitive, polymeric structures found on the surface of bacteria.

2.3.4 *Diversification of the antibody response*

After the initial antigen recognition by B cells, the antibody repertoire is further diversified in order to enhance antigen binding and improve the effector functions[196]. Diversification happens through two processes: somatic hypermutation in the variable region and isotype switching. Unlike the generation of the initial antibody repertoire during B cell maturation, which happens in the absence of antigen, this secondary diversification is driven by BCR/antigen interactions. This secondary modification of the immunoglobulins genes is in stark contrast to the TCR genes that cannot further adapt to the antigens. Somatic hypermutations are introduced in the variable region of immunoglobulins. B cells express activation-induced cytidine deaminase (AID), which selectively deaminates cytidine residues (converting cytosine to uracil) in the variable region. The subsequent DNA repair process introduces random mutations around the deaminated site. Because mutations are random, they can both improve or decrease the binding affinity to the antigen. Through interaction with antigens and T cells in the lymph nodes, only B cells that have generated immunoglobulins with a high affinity are selected for survival. B cells with detrimental mutations are eliminated by apoptosis because they either fail to produce functional BCRs or are outcompeted by B cells with higher antigen affinity and therefore do not receive T cell survival signals. Through multiple rounds of mutations, the antigen affinity of the immunoglobulin repertoire is increased. . Through the process of affinity maturation, the affinity of the antigen binding site to the epitope can be increased by 300-fold

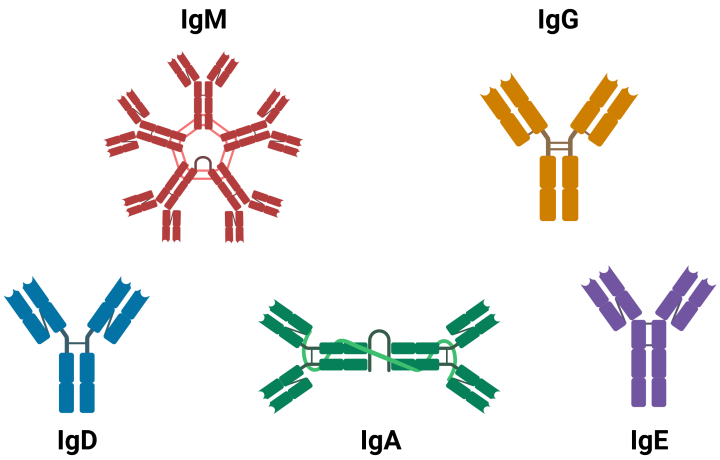

Figure 2.4: Antibody isotypes. Schematic of antibody isotypes IgM, IgG, IgD, IgA and IgE found in humans (image taken from Wikipedia[200]).

(measured for influenza-specific antibodies[197]) up to a 10 000-fold increase (measured for antibodies binding small haptens[198]). Affinity-matured antibodies have a mean affinity of 1 nM[196].

For isotype switching the constant domain of the immunoglobulin is changed via DNA recombination[199]. AID introduces double-strand breaks in specific switch regions upstream of the constant region. The breaks are then repaired by joining different switch regions, resulting in the expression of a new antibody isotype. Naive B cells express IgM and IgD. After antigen recognition, the same variable domain can be expressed as IgG, IgA or IgE isotype. Which isotype is expressed depends on which effector capacities are required. The different functions of the isotypes are discussed in the next section.

The different antibody subtypes can be found in different regions of the body and have different functions[181,199] (Fig. 2.4):

IGM IgM is expressed on the surface of naive B cells and acts as the BCR that initially binds to a complementary antigen. Upon antigen stimulation, it can be secreted as a pentameric version, with five units held together by a protein called the J chain. IgM is especially important during the initial immune response and is efficient at cross-linking pathogens and activating the

complement system. IgM is produced early in the immune response when affinity maturation has not yet occurred. The affinity between IgM and epitope can therefore be relatively low, however, the high multivalency of pentameric IgM can make up for this by increasing binding strength through binding up to 10 antigens at once.

IGD IgD is coexpressed with IgM on the surface of all mature B cells and secreted to a very small amount. Its exact function is not fully understood, but it may play a role in the activation of B cells and the regulation of immune responses. After activation, B cells can undergo isotype switching to produce the IgG, IgA or IgE subtypes.

IGG IgG is the most abundant antibody in the bloodstream, comprising about 75-80% of total circulating antibodies. It is found in all body fluids and is involved in opsonization, neutralization, and complement activation. IgGs have a long half-life (24 days) and therefore play a key role in long-term immunity.

IGA IgA is predominantly found in mucosal membranes. It can be secreted as a dimeric version with the J chain linking two IgA units together. IgA protects against infections at mucosal sites, for example by preventing pathogen attachment to mucosal surfaces.

IGE IgE is primarily associated with allergic reactions and defence against parasitic infections. IgE binds to Fc receptors on mast cells and basophils, triggering the release of inflammatory mediators such as histamine in response to allergens.

2.4 *Protein-protein interactions*

Protein-protein interactions give rise to protein complexes with high specificity and affinity, which play a central role in coordinating various biological functions within the dynamic environment of the cell. These interactions include receptor-ligand interactions which enable cells to sense and respond to their surroundings, as we have seen for the TCR and antibodies in the previous sections. The atomic details of protein binding interfaces encode the information about how proteins interact. Techniques such as X-ray crystallography and surface plasmon

resonance facilitate the study of both static structures and dynamic parameters of these interactions, providing insights into the thermodynamic principles that govern protein interactions. The following section discusses the fundamental principles governing protein interactions and introduces methodologies employed to characterize these mechanisms.

2.4.1 *Molecular mechanisms of protein interactions*

Protein-ligand interactions are governed by thermodynamic principles. Favourable intermolecular forces and bond formation drive the formation of non-covalent protein complexes. The thermodynamic system of protein interactions consists of the solute (protein and ligand) and the solvent (water and buffer ions). Electrostatic forces, hydrogen bonds, van der Waals interactions, and steric complementarity at the protein-protein interface influence the formation and stability of the protein complexes. These factors are determined by the protein structure.

When a protein-ligand complex forms at constant pressure, changes in the system's enthalpy (ΔH), entropy (ΔS), and Gibbs free energy (ΔG) occur. The Gibbs energy change is the key parameter indicating the spontaneity of the binding process:

$$\Delta G = \Delta H - T \cdot \Delta S \tag{2.1}$$

For the protein-ligand binding to occur spontaneously, the change ΔG must be negative. This negative ΔG results from the favourable interactions between the protein and ligand, which contribute to a negative binding enthalpy (ΔH). However, this must overcome the entropic penalties, represented by the negative change in entropy (ΔS), that occur upon binding. The stability of the protein-ligand complex is determined by the magnitude of the negative free energy change upon binding. A larger negative free energy change indicates a more stable complex, reflecting stronger favourable interactions between the protein and ligand relative to the entropic penalties.

2.4.2 *Parametric description of protein interactions*

An interaction can be defined by its binding parameters, which allow the quantification of the binding rate and strengths of an interaction. For instance, in a reversible bimolecular

interaction involving ligand L and receptor R mixed in solution, their time-dependent reaction can be expressed as

$$R + L \underset{k_{off}}{\overset{k_{on}}{\rightleftharpoons}} RL\,,$$

where RL is the receptor-ligand complex. The kinetic rates k_{on} and k_{off} describe the time it takes for the receptor to bind to the ligand (association) and unbind in reverse reaction (dissociation).

ASSOCIATION RATE (k_{ON}) The association rate k_{on} (in units $M^{-1}s^{-1}$) is the rate at which a receptor and ligand bind to form a complex at a given concentration. Association happens upon random collisions of the proteins, and k_{on} is therefore dependent on the concentration of R and L; the higher the concentration, the higher the likelihood of a collision. Diffusion is often the key rate-limiting factor for protein association. Furthermore, precise orientation of the protein interfaces is required for binding, which decreases the association rate. Long-range electrostatic forces can increase association rates by facilitating attraction between the proteins. Structural flexibility of the complex also affects k_{on}; if structural rearrangements of proteins are needed for binding, k_{on} is reduced. Typical k_{on} rates range from 10^5 to $10^7\,M^{-1}s^{-1}$ [201].

DISSOCIATION RATE (k_{OFF}) Dissociation rate k_{off} characterizes the rate at which the protein-protein complex unbinds. Unlike k_{on}, k_{off} is not concentration dependent. k_{off} is determined by the strength of short-range interactions between the proteins, such as van der Waals forces, hydrogen bonds, hydrophobic interactions, and ionic bonds. Normal ranges for k_{off} can vary widely, ranging from $1\,s^{-1}$ to $10^{-7}\,s^{-1}$. k_{off} allows the calculation of the average bond lifetime ($1/k_{off}$) and half-life of the complex ($\tau_{1/2} = \ln(2)/k_{off}$), which represents the time required for half of the complexes to dissociate on average.

At thermodynamic equilibrium, the forward binding reaction is equal to the reverse unbinding reaction, the overall change complex concentration is zero. We can therefore write:

$$k_{on}[R][L] = k_{off}[RL]\,, \tag{2.2}$$

where $[R]$, $[L]$ and $[RL]$ are the equilibrium concentrations of the free receptor, free ligand, and receptor-ligand complex, respectively. Following the law of mass action, we can define the dissociation constant K_D:

$$K_D = \frac{k_{off}}{k_{on}} = \frac{[R][L]}{[RL]} \tag{2.3}$$

The dissociation constant K_D, first introduced by Schild[202] is a quantitative measure of the strength of an interaction between two molecules, such as a protein and a ligand. It is defined as the concentration of the ligand at which half of the binding sites on the protein are occupied by the ligand. The dissociation constant is often used to quantify the affinity of an interaction. A lower K_D value indicates higher affinity, meaning that the molecules bind more tightly to each other. Conversely, a higher K_D value indicates lower affinity, meaning that the binding interaction is weaker.As K_D is determined by the ratio of k_{off} to k_{on}, interactions with the same affinity can have very different kinetics.

The relationship between the affinity of an interaction (as determined by K_D) and the thermodynamic energy (Gibbs free energy (ΔG)) associated with the formation of the interaction can be described by the following equation:

$$\Delta G = RT \ln \left(\frac{K_D}{c_0} \right) \tag{2.4}$$

where R is the gas constant, T is the temperature of the system and c_0 represents the concentration chosen to define the standard state. In the context of the equation, c_0 typically refers to the concentration of the interaction partners in the absence of the interaction.

The simple reaction used above describes the interaction between two monovalent proteins, i.e. each binding partner has only a single binding site and therefore they form a 1:1 complex. This is the case for the interaction between the TCR and its pMHC ligand. However many protein interactions are multivalent, i.e. proteins with multiple binding sites participate in the interaction. Antibodies can engage in bivalent interactions, interacting with two binding sites as presented by IgG and IgE, in tetravalent interactions, such as IgA with four sites and decavalent interactions, such as IgM with 10 binding sites. Multivalent interactions increase the overall binding strength of the binding partners and can lead to the formation of higher-order complexes, such as protein aggregates or multimeric protein assemblies[173].

The 3D affinity of a soluble receptor-ligand interaction may not directly correspond to the 2D affinity they experience on the cell surface[203,204]. Unlike soluble proteins with three-dimensional translational and rotational freedom, translational and rotational freedom for membrane proteins is limited to two dimensions. 2D association rates can be reduced due to the slower diffusion proteins experience in the cell membrane or enhanced due to proteins being anchored in the membrane in the preferred orientation of the interaction partners[205,206], while decreases in dissociation rates have been observed in 2D systems[207–209]. While 2D and 3D parameters generally correlate when measured for the same protein pairs, differences arise across different protein pairs[205].

2.5 *Surface Plasmon Resonance*

Surface Plasmon Resonance (SPR) is a label-free, highly sensitive technique used for the study of biomolecular interactions, including protein binding. SPR measures the binding over time, which allows the determination of the specificity, kinetics and affinity of an interaction. Some of the earliest protein interactions studied with SPR were antibody-antigen interactions which were conducted in 1983[210–212]. The first SPR measurements of TCR interacting with pMHC were performed by[213] in 1994. Since then SPR has been widely used in drug discovery, protein engineering, and basic research in biochemistry and biophysics.

In an overly simplified way, when polarised light with a particular angle hits a thin metallic film, the energy of the light is absorbed and causes the oscillation of free electrons (Fig. 2.5A). The phenomenon is called surface plasmon resonance. The angle at which the incident light excites the surface plasmon resonance depends on the refractive index of the metallic film and is highly sensitive to any change such as the adsorption of molecules to the surface. This makes it ideal for detecting molecular interactions[216] without the need to label the molecule with fluorescent, radioactive, or other detectable markers. When molecules bind to the surface of the metallic film, the shift in resonance angle is detected. The magnitude of this shift is directly proportional to the amount of molecule bound to the surface.

To measure protein binding between a ligand and its receptor, the ligand is immobilized on the metallic surface of a sensor chip. The receptor is then injected over the sensor surface (Fig. 2.5B). The shift in resonance angle that happens when the receptor binds the ligand is

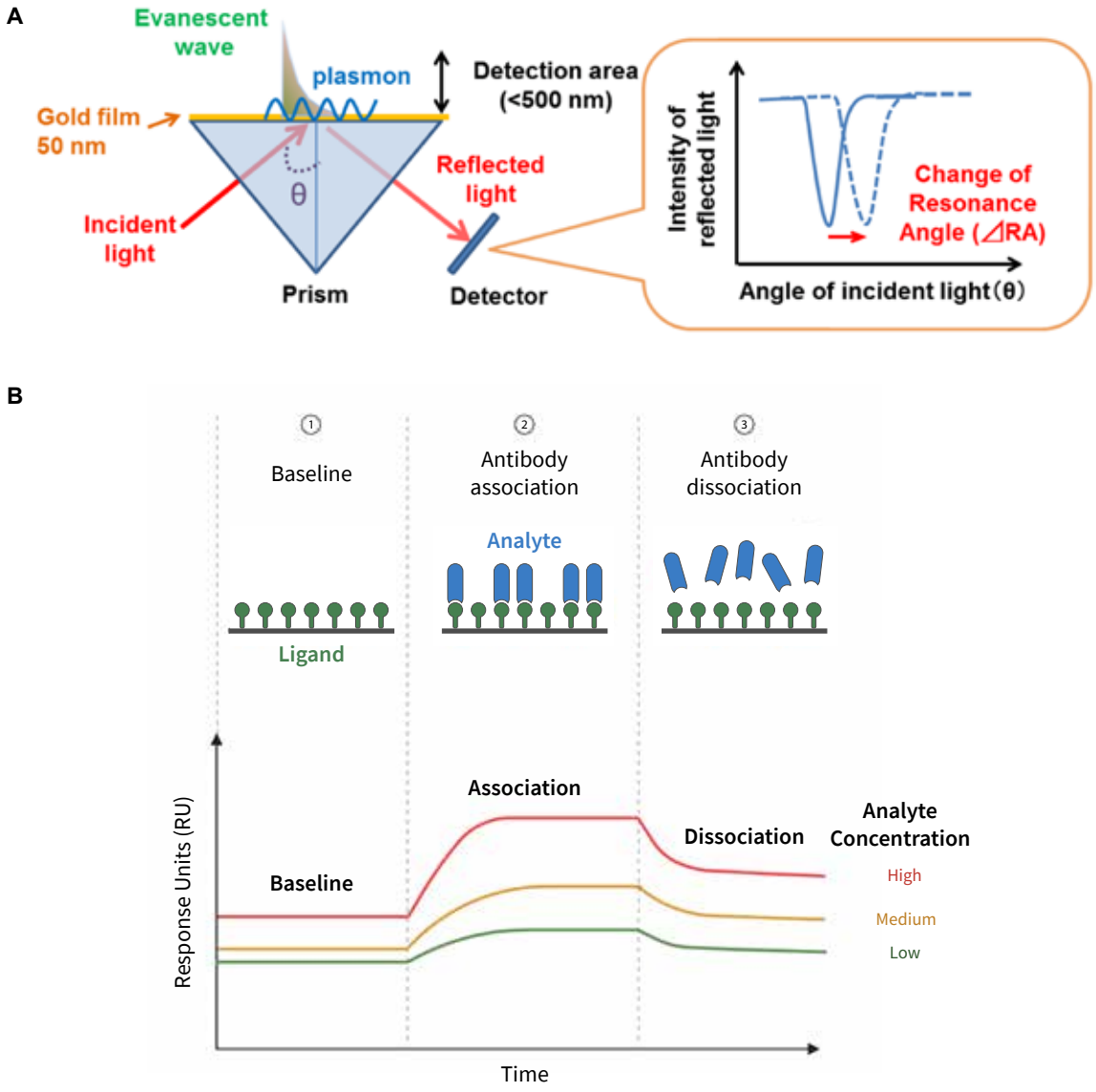

Figure 2.5: Surface Plasmon Resonance (SPR) for measuring protein binding. **(A)** SPR detects changes in the refractive index within a limited detection region, typically spanning less than 500 nanometers, resulting in shifts in the resonance angle. Image taken from Yanase et al.[214]. **(B)** These changes in resonance angle are then translated into measurable signals (resonance units), providing real-time analysis of biomolecular interactions occurring at the sensor surface. During the association phase, the analyte is injected over the ligand immobilised on the sensor chip. The analyte binds to the ligand and an increase in response is observed until it reaches a steady state. Subsequently, during the dissociation phase, buffer solution replaces the analyte, the analyte unbinds and a decrease in signal is observed. Figure modified from Nguyen et al.[215].

measured over time and converted into arbitrary response units (RUs). This produces binding curves that can be analysed using various models to extract kinetic parameters of the binding interaction, including association and dissociation rates and affinity.

For the simple 1:1 interaction introduced above, the association phase can be fitted with the following equation to estimate the kinetic parameters of the interaction:

$$[RL] = [RL]_{\text{eq}} \left(1 - \exp(-(k_{\text{on}}[R] + k_{\text{off}})t)\right) , \tag{2.5}$$

where $[RL]_{\text{eq}}$ is the amount of receptor-ligand complexes in steady state, and $[R]$ is the concentration of free receptor.

Receptor dissociation follows a simple one-phase exponential decay model:

$$[RL] = [RL]_0 \exp\left(-k_{\text{off}}t\right) . \tag{2.6}$$

K_D can be either calculated from the kinetic parameters or using the steady state binding response and concentration using the relation:

$$[RL]_{\text{eq}} = \frac{[R][L_{\text{max}}]}{K_D + [R]} \tag{2.7}$$

where $[L_{\text{max}}]$ is the total amount of ligand on the surface of the sensor chip.

Here, binding parameter estimation from SPR data was exemplified using a simple 1:1 interaction model. Multivalent protein interactions require more complex interaction models.

3

META-ANALYSIS OF TCR DISCRIMINATION

3.1 Introduction

In contrast to other ligand receptors, such as Cytokine receptors or receptors binding to neurotransmitters, the TCR has not co-evolved with its ligand. Instead, each T cell expresses a clonotypically unique TCR generated by gene rearrangements, insertions, deletions, and point mutations during T cell development in the thymus. As a result, an individual human has a large repertoire of more than 10^8 TCRs[217–219] that allows T cells to recognise a large number of peptide sequences presented by the host MHC molecules.

APCs present both antigens derived from foreign pathogens and antigens that originate from endogenous cells (self-antigens) on their surface. Even during an infection, the number of foreign antigens that are presented can be quite low compared to the large number of only self-protein derived peptide-MHCs (pMHC)[22]. The difficult task to discriminate between foreign antigens and self-antigens therefore falls to the TCR. After thymic selection, the TCR repetoire can bind foreign antigens with a high affinity and self-peptides with a low, but non-neglectable affinity[114]. To prevent T cells from being activated by self-peptides, the TCR therefore must be able to discriminate between high-affinity foreign pMHCs, present at low frequencies and low-affinity self-pMHCs, present at high frequency.

The degree of this discrimination between antigen affinities and the underlying mechanisms are still debated[55,139,142]. Early experiments using T cells from the OT-I, 3L.2, and 2B4 transgenic TCR mice, have shown that MHCs presenting mutated peptides with a very small 3-5 fold reduction in affinity abolished the T cell response[112,127–131]. This suggests that the TCR is capable of near-perfect antigen discrimination, where only higher affinity pMHCs can

elicit a T cell response, but not slightly lower-affinity pMHCs and increasing the concentrations of the ligand does not compensate for the low affinity.

A simple receptor occupancy model, where the T cell response is directly proportional to the number of ligands bound to the TCR, cannot explain near-perfect discrimination[139,220]. Hence there is considerable effort in the community to identify the underlying mechanism of TCR discrimination. One of the most widely accepted model is the KP model, which suggests that the TCR undergoes several time-delaying steps before the TCR is fully activated[147,221]. Only ligands that remain bound for a long enough time to complete all proofreading steps can activate the receptor. However, the model is unable to explain near-perfect discrimination without losing the high ligand sensitivity of the TCR[96]. This has led to the proposal of additional mechanisms that augment the kinetic proofreading model such as feedbacks, conformation changes and catch bonds induced by molecular forces[71,96,150,151,153,222–231].

However, recent studies have found T cells to respond to lower-affinity antigens if expressed at higher concentrations. For example, the recognition of low-affinity self-pMHCs has been implicated in off-target toxicity in T cell therapies[232] and T cell-mediated autoimmune diseases have been associated with an increased expression of self-antigens[233,234]. It has also been shown that interactions with low-affinity self-peptides induce the proliferation of T cells in the periphery[235,236]. Moreover, as the number of potential antigens is larger than the size of the TCR repertoire, cross-reactivity must be inherent to the TCR to prevent pathogen evasion[132,237].

To resolve the apparent discrepancy between the original mouse TCR data suggesting near-perfect discrimination and data emerging from the other T-cell studies, we systematically quantified the antigen discrimination strength of the TCR. A large number of different mouse and human TCRs have been isolated and the affinity and potency of their TCR/pMHC interaction have been characterised. This motivated us to perform a meta-analysis of existing data to quantitatively determine the discrimination strength. In this chapter, we will introduce a quantitative measure of discrimination, the discrimination power α, that allows us to compare the discrimination strength across different studies, TCRs, and experiment setups. In contrast to the original murine studies, we find that the ability of T cells to discriminate antigens is enhanced, but imperfect and trace discrepancies to issues with the TCR/pMHC affinity measurements for the original murine TCRs. We then combine the experimentally observed

discriminatory power with mathematical modelling to test mechanistic models of antigen discrimination. We show that the standard kinetic proofreading model is capable of explaining the imperfect discrimination strength. We also identify signalling proteins that can influence the strength of antigen discrimination.

3.2 *Results*

3.2.1 *Quantifying ligand discrimination with a discrimination power*

The TCR/pMHC interaction is characterised by the association rate (k_{on}, $M^{-1}s^{-1}$), the dissociation rate (k_{off}, s^{-1}) and the dissociation constant $K_D = k_{off}/k_{on}$, a measure of affinity between pMHC and TCR (Fig. 3.1A). We define the strength of ligand discrimination as the ability of the TCR to amplify differences in ligand affinity (or off-rate) into larger changes in ligand potency, which is the ligand concentration required to produce a given level of T cell response. This is seen as a shift in the dose-response curve (Fig. 3.1B).

Ligand potency (P) often correlates linearly with K_D on logarithmic axes (Fig. 3.1B). This suggests a power-law relationship (i.e. $P = 10^C(K_D)^\alpha$). The power (α) is the slope on logarithmic axes (i.e. $\log(P) = C + \alpha log(K_D)$) and relates the fold change in K_D to the fold change in potency. Power α is a measure of discrimination strength. It is a dimensionless parameter, independent of different affinity and potency measurements, and hence can be used to compare discrimination between studies. The y-intercept, C, is a measure of ligand sensitivity, however, it is not dimensionless, and hence cannot be used to compare sensitivity between studies. To illustrate how α can be obtained from T-cell experiments, we simulated the T-cell response (R) over ligand concentration (L) using a saturated Hill function ($R = L/(K_D)^\alpha + L$) for ligands of different affinities and different α values (Fig. 3.1C). Ligand potency can be obtained from these dose-response curves by calculating ligand concentration at 50% of the maximal T-cell response. When plotting ligand potencies over K_D, we obtained a straight line on a logarithmic scale with the slope being equal to discrimination power α (Fig. 3.1C). Depending on the value of α, we observe a different level of discrimination. When $\alpha = 9$, a small, 4-fold increase in K_D nearly abolishes the response, consistent with near-perfect discrimination observed for the TCR. On the other extreme, when $\alpha = 1$, a 4-fold change in affinity can be compensated by

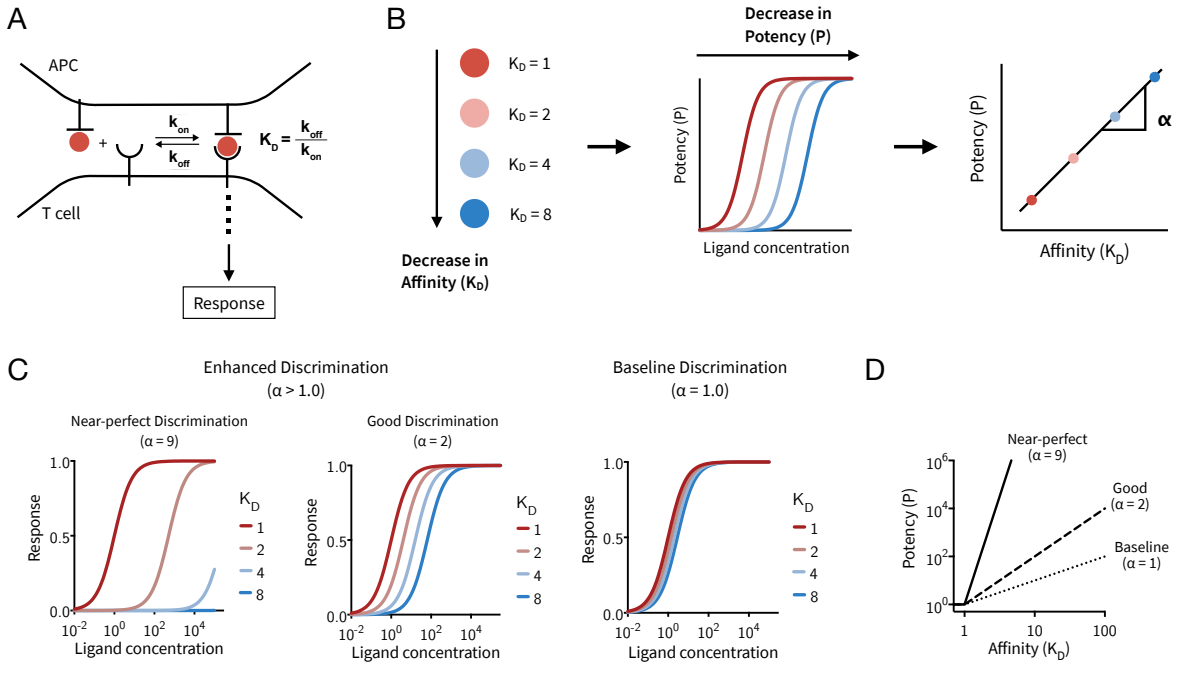

Figure 3.1: Quantifying ligand discrimination with a discrimination power (α). **(A)** Schematic showing TCR binding to peptide-MHC on the surface of an antigen-presenting cell. **(B)** TCR discrimination can be quantified by measuring how much a change in ligand affinity affects ligand potency. Lower affinity peptides (left) have a dose-response curve that is shifted to the right (middle). The concentration of ligand producing a response of 50% (potency) is plotted over affinity (K_D), producing a linear correlation on a log-log plot (right). The discrimination power (α) is the slope of this correlation. **(C)** Simulated T-cell response over the ligand concentration for four representative ligands with K_D 1, 2, 4 and 8 µM. Examples of T-cell response profiles are shown for near-perfect discrimination ($\alpha \geq 5$, left), good discrimination ($1 < \alpha < 5$, middle), and baseline discrimination ($\alpha = 1$, right). **(D)** Potency/affinity plot from data in (C), showing the difference in slope for different discrimination strengths.

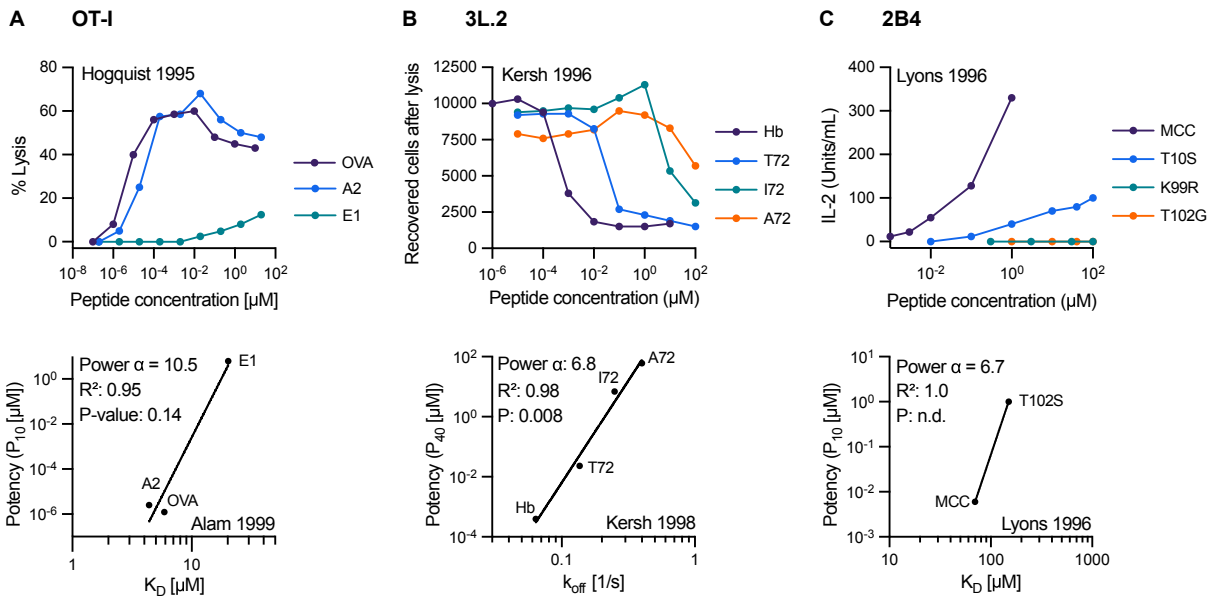

Figure 3.2: Original mouse TCR data suggests near-perfect discrimination. T cell dose-responses over the peptide concentration (top row) and potency/affinity plots (bottom row) for the **(A)** OT-I, **(B)** 3L.2, and **(C)** 2B4 mouse TCRs. The log-transformed Affinity/potency data was fitted with a linear regression. The discrimination power (α) equals the slope on the log-transformed data. Additional information on each data is provided in Table A.1 (ID: 2 (OT-I), 11 (3L.2), and 14 (2B4)).

the same 4-fold change in ligand concentration. We define discrimination powers between $\alpha = 2 - 5$ as enhanced but imperfect discrimination, whereas discrimination power of 1 and >5 as baseline and near-perfect discrimination, respectively.

3.2.2 *Early mouse TCR data suggests near-perfect discrimination*

First, we sought to determine the value of α for the original mouse TCR data, which has shaped our current view of TCR being capable of near-perfect discrimination.

The OT-I TCR recognises the chicken ovalbumin peptide with the amino acid sequence SIINFEKL when presented on MHC class I H2-K^b molecules. The affinity of OT-I to a set of variant peptides was originally measured by SPR by Alam et al.[128]. In this study, binding kinetics at 37°C showed an unusual biphasic binding behaviour. We therefore used the affinity data at 25°C to determine the discrimination power. Functional T cell response, measured by the percentage of target cells killed (Fig. 3.2A), was published in an earlier study[127]. We defined ligand potency as ligand concentration that produces 10% T-cell activation to include peptide variant E1 in the dataset. When we plotted potency over K_D, we found a near-perfect discrimination power α of 10.5 (Fig. 3.2A). This is a result of the E1 peptide variant having

a 5×10^6-fold lower potency despite apparently binding with only a 3.5-fold lower affinity compared to the wild-type OVA peptide. We found similar values of α (12, 18, and > 5.1) when using affinity and functional data from other studies[96,112,238] (Table A.1 ID 1-4).

Similar levels of antigen discrimination were observed for the 3.L2 TCR, a TCR that recognises a murine haemoglobin peptide presented on MHC class II I-Ek. T cell response to a range of peptide variants was measured by target cell lysis[129] (Fig. 3.2B). In a following study, affinity and binding kinetics were measured[130]. In this case, dissociation rate k_{off} correlated better with peptide potency than K_D values, and were therefore used to calculate discrimination power α (Fig. 3.2B and Table A.1 ID 11). As k_{off} rates and K_D values correlate well[149,239], we assume that using k_{off} instead of K_D values will not affect the final result. The data produced a discrimination power α of 6.9.

Affinity and potency data measured for the 2B4 TCR further supported the idea of perfect discrimination[131]. The 2B4 TCR recognises a Moth Cytochrome C peptide (MCC) presented on MHC class II I-EK. T cell response measured by IL-2 production showed that a 7-fold decrease in affinity between the cognate MCC peptide and the variant peptide K99R completely abolished T cell response (Fig. 3.2C). The resulting discrimination power is $\alpha = 6.7$ (Fig. 3.2C and Table A.1 ID 14)

Due to a limited amount of data points in these experiments, the correlation was only significant for 3.L2 TCR. Nevertheless, a mean power α of 9.0 calculated from the original mouse studies suggests near-perfect discrimination.

3.2.3 *Revised data produce lower discrimination powers than original data*

Since the original mouse studies have been published, these TCRs have been used for a variety of other studies. As a consequence, new affinity measurements were generated, which allowed us to revisit the original data.

Recent affinity measurements by Stepanek et al.[240] for the OT-I TCR at 25°C found an 8-fold lower affinity between OT-I and its cognate peptide N4 than the original measurements. Peptides with an affinity of 1000 µM still induced a T cell response, indicating that a wider range of affinities can be recognised by the OT-I TCR clone. Although E1 which apparently bound with K_D = 20 µM in the original studies could not activate T cells, this study reports other peptides with K_D = 288 µM that could induce T cell responses. This suggests that the

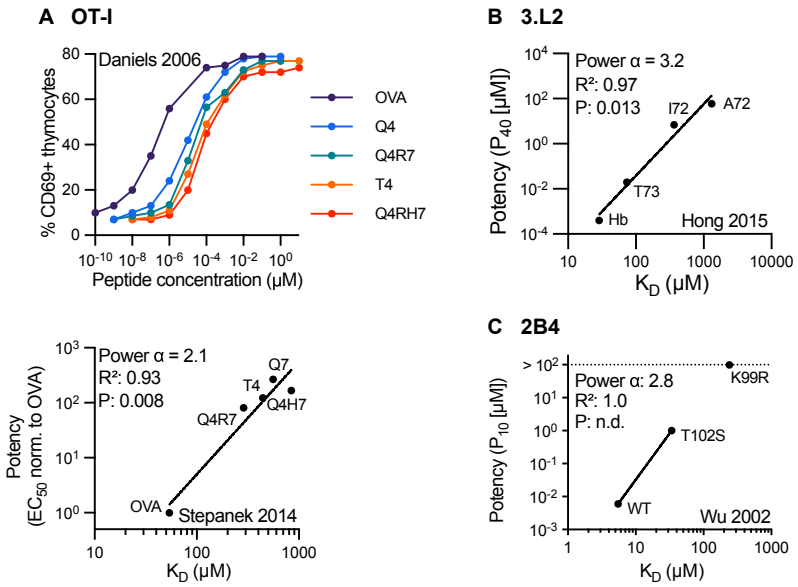

Figure 3.3: Revised analyses of the original mouse TCRs reveal lower discrimination powers. Revised analysis of the original murine TCRs by using **(A)** new functional and SPR binding data for OT-I, **(B)** new SPR binding data for 3.L2, and **(C)** new SPR binding data for 2B4. Additional information on each panel is provided in Table A.1 (ID: 5 (OT-I), 13 (3L.2), 17 (2B4).

original studies overestimated the affinity of OT-I/pMHC interactions. Unfortunately, affinity measurements for peptide variants in original OT-I studies have not been repeated, preventing us from directly comparing discrimination strength between revised and original data. Instead, we determined the discrimination power for OT-I from a set of four other peptide variants for which T-cell activation and OT-I-TCR binding properties were characterised by Daniels et al.[114] and Stepanek et al.[240] (Fig. 3.3A). This dataset showed a significant correlation between K_D and potency with an appreciably lower discrimination power of 2.1 (Table A.1 ID 5). This means to fully abolish T cell response (change in potency > 10^6), peptides have to have a 1000-fold lower affinity compared to the cognate peptide. This is in stark contrast to the original peptides, where a fold change of 5 was enough to abolish T cell response.

For the 3.L2-TCR, revised affinity measurements for original peptide variants are available[241]. The revised measurements show a wider variation in k_{off} and K_D than originally reported, especially weakly-stimulating peptides have a K_D around 1000 µM (Fig. 3.3B). Calculating power α using the original potency data and the revised K_D values produced $\alpha = 3.2$ (Table A.1 ID 13). Here, K_D instead of k_{off} was used, as for 2 of 4 peptides, the k_{off} could not be accurately determined.

Similarly, revised SPR measurements for the 2B4 TCR by Wu et al.[242] report a 50-fold difference in affinity between the cognate and non-stimulatory peptides (Fig. 3.3C). When

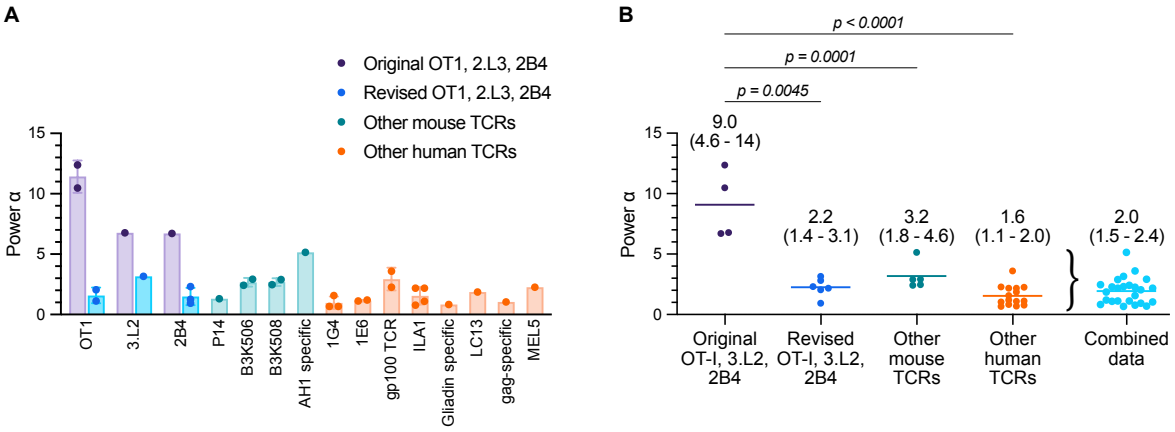

Figure 3.4: Statistical analyses across multiple TCR/pMHC systems confirm lower discrimination powers. **(A)** The discrimination powers of individual TCR/pMHC systems. **(B)** Comparison of discrimination powers from the original mouse TCR data (n=4), revised mouse TCR data (with revised SPR data, n=6), and other mouse (n=5) and human (n=15) TCRs. Statistical significance was determined using one-way ANOVA.

re-plotting revised K_D values with original potency data we found a lower discrimination power of $\alpha = 2.2$ and $\alpha = 2.3$ (Table A.1 15 and 17). Data from two additional 2B4 studies produced similar α values of 2.3 and 0.95 (Table A.1 ID 18 and 19).

The revised SPR data gives a mean value of $\alpha = 2.2$ (Fig. 3.4A, Table A.1 ID 1-19), suggesting that the discrimination power of these TCRs may be lower than previously thought.

3.2.4 *Other mouse and human TCRs confirm lower discrimination*

Over the last 20 years, numerous other mouse and human TCRs have been characterised. In a literature search, we identified 12 TCR systems which had been characterised based on their affinity and potency, allowing us to determine the discrimination power α.

For this systematic analysis, we only included studies that provided monomeric TCR/pMHC binding data measured by SPR. In addition, dose-response data was required in order to estimate the potency of each ligand interaction. We used studies where different peptides bound to a single TCR, multiple TCRs bound to the same peptide, or studies that relied on a combination of both. For additional inclusion criteria see methods.

In total, we identified 12 TCR systems, separated into 4 mouse TCRs (P14, B3K508, AH1 specific) and 8 human TCRs (1E6, gp100 specific, ILA1, gliadin specific, LC13, gag-specific, and MEL5). We generated 51 potency plots (Fig. A.2, A.3, A.4) and calculated the discrimination

power (Fig. 3.4A) (Table A.1 ID 20-70). Other mouse TCRs produced a mean power α of 3.2, and for human TCRs α was 1.6. These discrimination powers are significantly lower than those of the original mouse studies and similar to the revised studies (Fig. 3.4B). Collating all significant discrimination powers from revised, other mouse and human systems, we found the mean α value to be 2.0. We can conclude that the discrimination strength of the TCR is significantly lower than previously believed. Rather than near-perfect discrimination, the TCR displays enhanced, but imperfect discrimination, allowing low-affinity peptides to activate T cells if their concentration is high enough.

3.2.5 *The discrimination power is similar for different T-cell responses but depends on co-receptors and the antigen presentation surface*

Measurement of T-cell activation differed substantially between studies. We included potency data obtained from both $CD4^+$ and $CD8^+$ cells and multiple activation readouts. Additionally, we calculated the discriminatory power for experimental systems with differences in co-receptor binding and peptide presentation. We next investigated whether these differences biased the estimated discriminatory powers.

Grouping discrimination powers based on whether $CD4^+$ or $CD8^+$ T cells were used in the study showed no significant difference (Fig. 3.5A). Different T-cell responses, such as lysis of target cells, proliferation, cytokine production or surface marker expression also showed no significant differences in discrimination (Fig. 3.5B).

Next, we examined the role of CD4/CD8 co-receptor binding on discrimination. We identified four studies where potency was measured when co-receptor binding was absent[114,243–245](Table A.1 ID 5, 10, 55, 57, 65). We found a significant increase in power α if co-receptors could not bind to pMHC using all data (Fig. 3.5C) as well as when we limited the analysis to paired data where both data points were measured with the same TCR (Fig. 3.5D). The importance of co-receptor binding for T cell sensitivity has been reported before[85,87]. Our data suggests that the increase in sensitivity due to co-receptor binding comes at the cost of lower discrimination strength.

All studies included in the analysis so far used functional assays where pMHC was presented on the surface of APCs. Several studies have also examined T-cell responses to recombinant pMHCs coated on plates. In these more artificial plate assays, no co-signalling receptors are

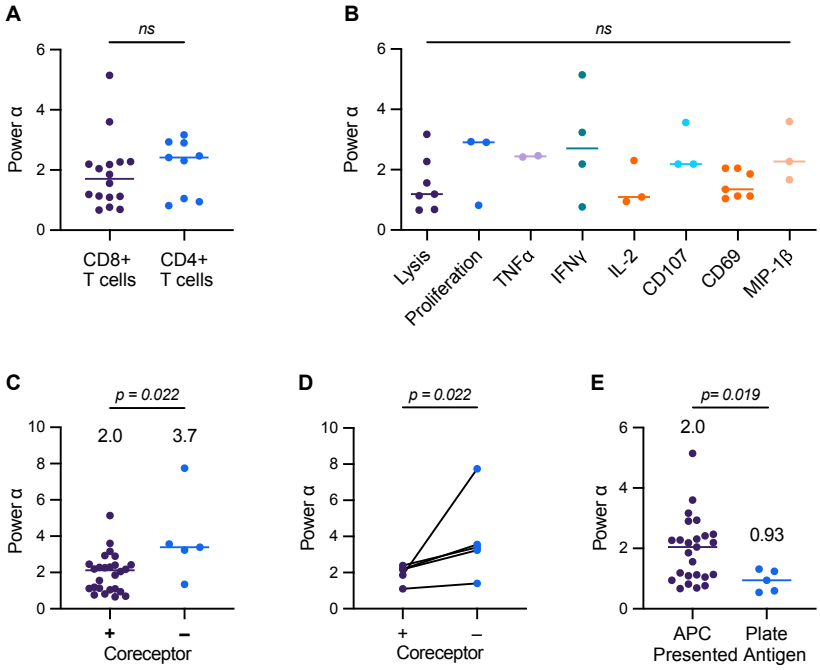

Figure 3.5: Discrimination powers that can be modulated by coreceptors and the antigen presentation surface. **(A)** Comparison of discrimination power α between $CD4^+$ and $CD8^+$ T cells. **(B)** Comparison between different measured T cell responses, including lysis of target cells, T cell proliferation, production of various cytokines and surface receptors. **(C)** Comparison between conditions with and without the CD4/CD8 co-receptors. Coreceptors are removed via knockout or antibody blocking. **(D)** Comparison as in C but for paired data (i.e. where both conditions were present in the same study). **(E)** Comparison between the use of antigen-presenting cells pulsed with peptides or artificial plate surfaces to present antigens. Data with antigen presented on plates or without coreceptors were not included in any other analyses shown in panels A and D and analyses is based on combining the revised OT-1, 3.L2, and 2B4 data, other mouse TCRs, and other human TCRs that together produce a mean value of $\alpha = 2.0$ (95% CI of 1.5 to 2.4). Complete list of all 70 calculated powers can be found in Table A.1.

present that could influence T-cell activation. Comparing α values from APC assays and plate assays, we found a significant reduction of α from 2.0 on APCs to 0.93 in the plate assays (Fig. 3.5E). This was confirmed by experiments directly comparing discrimination power for the 1G4 TCR on plates and APCs[246], indicating that additional interactions with the APC membrane improve discrimination. Consistent with this, our lab found that the addition of ligands to the adhesion receptor CD2 and LFA-1 to a plate assay can increase discrimination[246]. Taken together, this suggests that discrimination may not be entirely intrinsic to the TCR and co-receptors and other surface receptors can influence the T-cell discrimination strength.

3.2.6 *Proteins in proximal signalling pathway influence discrimination*

In some studies, we found functional data from T cells with a mutation in their signalling pathway. This gives us the opportunity to test if mutations in downstream proteins in the TCR signalling cascade impact antigen discrimination.

Stepanek et al.[240] expressed a CD8 fusion protein that contains the intracellular tail of CD4, which resulted in a higher number of active Lck bound to the co-receptor. When plotting the potency over affinity we observe a decrease in power α for mutant CD8 compared to wild-type CD8 (Fig. 3.6A). Shen et al.[247] investigated the effect of a ZAP70 mutation that weakened the auto-inhibitory conformation of ZAP70. We observe a small decrease in power α for this ZAP70 mutation (Fig. 3.6B). In two studies by Lo *et al.*, the amino acid adjacent to the tyrosine residue Y132 (human) or Y136 (mouse) of a LAT phophorylation site was mutated, resulting in accelerated phosphorylation by ZAP70[243,248]. When the effect of the mutation was tested on Jurkat cells expressing wild-type or mutated LAT, no change in discriminatory power α is observed, however, Jurakt cells with mutated LAT have higher sensitivity (Fig. 3.6C). In a subsequent study, the effect was tested in naive OT-I T cells isolated from transgenic mice. In contrast to the previous study, we observe a difference in discrimination power α (Fig. 3.6D). The discrepancy between naive murine OT-I T cells and Jurkat OT-I T cells may be a result of the Jurkat T cell being a poor model for discrimination because it exhibits baseline discrimination, which is lower than that observed with primary human T cells.

In summary, potency data from mutated T cells suggests that the signalling proteins Lck, ZAP-70 and LAT play a role in antigen discrimination (Fig. 3.6E). Impairing protein function in the proximal TCR signalling pathway reduces the discrimination strength of the TCR.

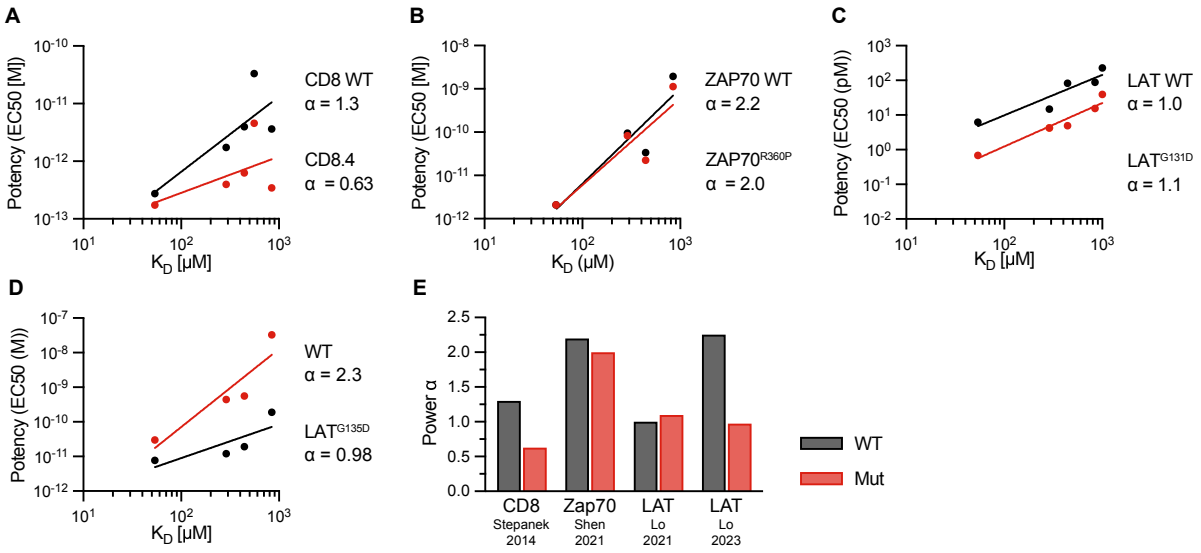

Figure 3.6: Mutations in signalling proteins affect discrimination strength. Potency/affinity plots wild-type (WT) vs mutation (Mut) for **(A)** CD8.4, fusion protein with extracellular part of CD8a and a cytoplasmic CD4 tail, which increases Lck bound to the co-receptor. Potency measured via CD69 upregulation in thymocytes from OT-I transgenic mice[240]. **(B)** ZAP70 R360P mutation weakening auto-inhibition of ZAP70, potency measured by CD69 upregulation in naive CD8+ OT-I T cells isolated from TCR transgenic mice[247] **(C)** LAT G131D mutation increases the phosphorylation rate of LAT residue Y132. Potency measured from Erk phosphorylation in OT-I+hCD8+ Jurkat cells[243]. **(D)** Impact of LAT G135D mutation, the mouse ortholog to LAT G131D in (C). Potency measured via CD69 upregulation in naive OT-I CD8 T cells isolated from TCR transgenic mice[248]. **(E)** Comparison of discrimination power α from (A) - (D) between wild-type and mutated proteins in TCR signalling pathway.

3.2.7 *The kinetic proofreading model can explain TCR discrimination*

We can use the quantitative value of TCR discrimination to further explore the mechanism of antigen discrimination. The kinetic proofreading (KP) model proposes that the TCR undergoes a series of N biochemical steps, each with rate k_p, between ligand binding and a productive TCR signal[147,221] (Fig. 3.7A). Only high-affinity ligands remain bound long enough to complete all steps and activate the receptor. This model was rejected because it was unable to explain the near-perfect discrimination suggested by the early mouse data without simultaneously losing the high sensitivity[96]. In light of the lower discrimination shown by the revised data, we can revisit the KP model. The relationship between affinity and potency predicted by the KP model can be expressed mathematically (Fig. 3.7B). This allows us to vary the model parameters and determine whether both discrimination and sensitivity can be achieved for different levels of discrimination (Fig. 3.7C). We confirmed previous reports that the KP model cannot explain near-perfect discrimination (Fig. 3.7C left). However, it simultaneously achieved sensitivity and the revised lower discrimination (Fig. 3.7C right), suggesting that the KP model is a suitable model to explain TCR discrimination.

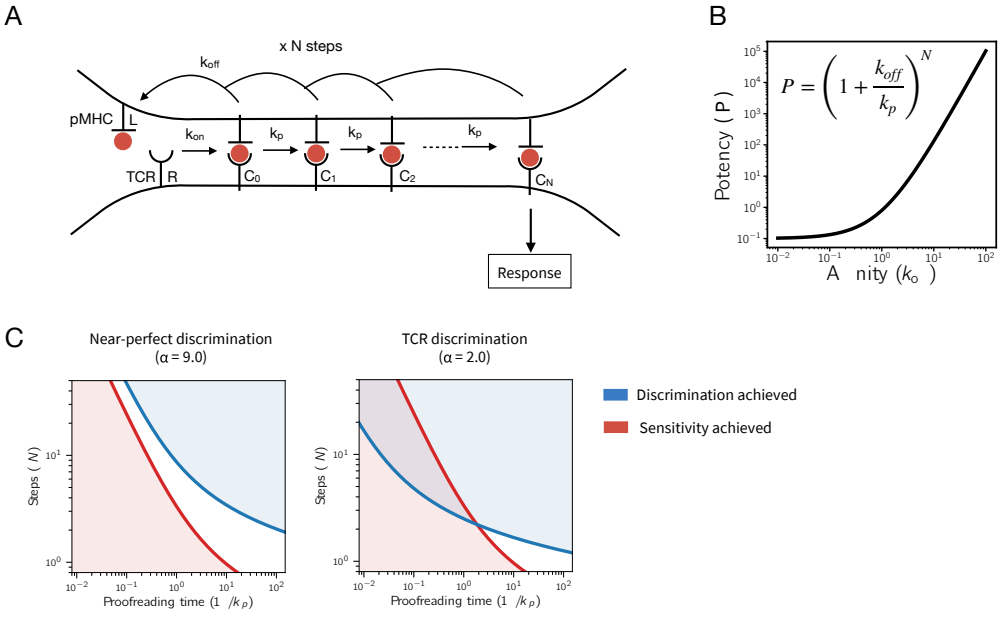

Figure 3.7: Kinetic proofreading can explain the TCR discrimination power and sensitivity. (A) Schematic of the kinetic proofreading (KP) model with N steps and a rate k_p **(B)** Potency over dissociation rate k_{off} predicted by the KP model. **(C)** Variations of the number of steps (N) and the proofreading time ($1/k_p$) indicate whether the constraints of sensitivity (red) and discrimination (blue) are met for different levels of discrimination (near-perfect and good). Both sensitivity and discrimination is achieved for the parameter regime where the curves overlap.

3.2.8 *The ligand discrimination power of the TCR is higher than conventional surface receptors*

The observation that discrimination is substantially lower than previously thought raises the question of whether the TCR discrimination strength is still unique among other ligand receptors.

Ligands have been engineered that bind receptors with various affinities in an effort to study their basic function and to exploit them therapeutically. This allows us to compare discrimination strength between different receptor families. We included Cytokine receptors type I and II, Receptor tyrosine kinases (RTK), G-protein coupled receptors (GPCRs), Chimeric antigen receptors (CARs) and B-cell receptors (BCRs) in our analysis. We included studies where affinity was measured by methods other than SPR, such as radioligand binding assay. While such methods have a lower sensitivity, unable to accurately measure very low affinities, they are accurate in the nanomole affinity range these ligand-receptors interactions exhibit.

Cytokine receptors consist of two subunits. When bound to their soluble ligand, the subunits dimerize, which brings the Janus kinases (JAKs) bound to the cytosolic domain of each subunit in close proximity. This allows for trans-auto-phosphorylation inducing JAK activation leading to further signalling events that culminate in transcriptional activity mediated by STAT molecules. We identified 5 studies that provided affinity and potency data of a panel of mutated cytokines binding to the receptor subunits[249–253]. Shown in Fig. 3.8 as a representative example, Moraga et al.[250] generated a panel of IL-13 mutants, that exhibited a broad range of affinities towards the IL-13Ra1 subunit while maintaining wild-type affinity to the IL-4Ra. Cell response induced by these mutated ligands was measured by CD86 upregulation in a dose-response experiment, from which we obtained potency values (Fig. 3.8A left). A significant correlation between potency and K_D was observed (Fig. 3.8A right), with a discrimination power of α = 0.44. Other studies on IL-2[249], IL-6[253] and IFN1[251,252] receptors showed a similar discrimination power, resulting in a mean discrimination power of $\alpha = 0.66$ (Table A.2 ID 1-13).

Receptor tyrosine kinases consist of two subunits with intrinsic tyrosine kinase activity in their cytoplasmic domains. Similar to cytokine receptors, ligand binding induces dimerisation of two subunits leading to receptor activation. We identified two studies to include in the analysis[254,255]. For example, Ho et al.[254] measured the activation of the c-Kit receptor when

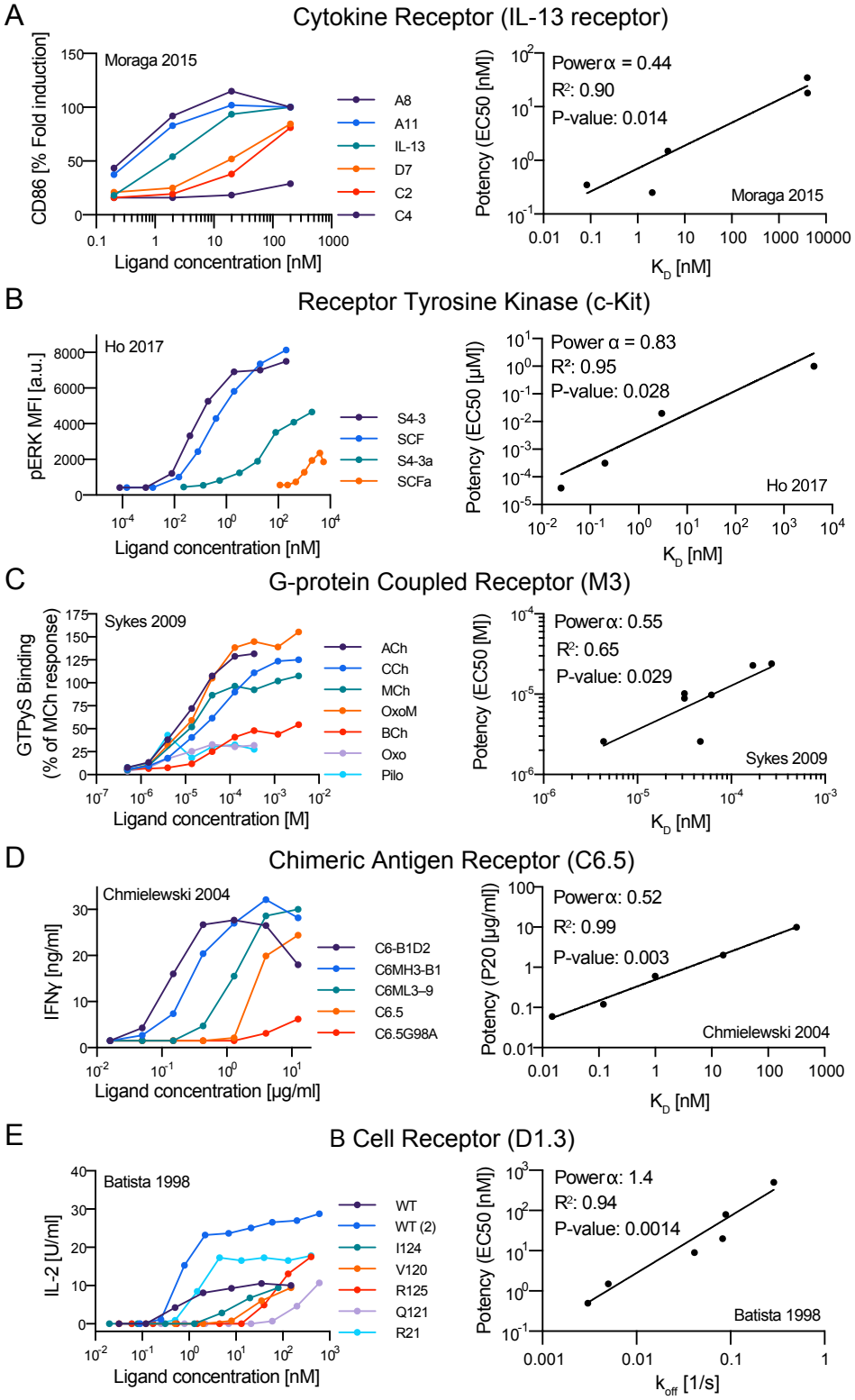

Figure 3.8: The discrimination power can be determined for other surface receptors. Representative dose-response (left column) and potency over K_D or k_{off} (right column) for **(A)** the IL-13 cytokine receptor, **(B)** the c-Kit receptor tyrosine kinase, **(C)** the muscarinic M_3 G-protein coupled receptor, **(D)** ErbB2-specific chimeric antigen receptors, and **(E)** a lysozyme-specific B cell antigen receptor (D1.3).

stimulated with Stem Cell Factor (SCF) mutants of different affinities. Potency measured from ERK phosphorylation correlated well with K_D, resulting in a power α of 0.83 (Fig. 3.8B). On average we find a discrimination power of $\alpha = 0.86$ across all studies (Table A.2 ID 15 and 16)

G-Protein coupled receptors undergo a conformational change upon ligand binding leading to signal transduction. Ligands can bind to different sites on a given GPCR, inducing distinct downstream signals. To ensure the cellular response is consistent for our analysis, we focused only on ligands that bind the same binding site with different affinities. Sykes et al.[256] measured the activation of the M3 muscarinic receptor by 7 agonists of different affinities. Functional response was measured via GTPγS binding to activated G-protein and intracellular calcium levels (Fig. 3.8C left). We identified a power alpha of 0.55 and 0.77 for GTPγS binding and calcium response respectively (Fig. 3.8C right). We found 3 additional studies involving A2A receptor[257], and the chemokine receptors CXCR4[258] and CXCR3[259]. The mean discrimination power is $\alpha = 0.76$ (Table A.2 ID 17-24).

Chimeric antigen receptors, used for T cell therapy, are designed to recognise a specific antigen on cancer cells and initialise target cell killing when expressed on a T cell. They consist of an antibody-like extracellular domain fused to the intracellular signalling domain of the TCR. To optimise CAR T-cell therapies, CAR/antigen affinities have been modified and tested. In the study by Chmielewski et al.[260], an anti-ErbB2 CAR was mutated to generate a panel of receptors with a range of affinities. For functional T-cell experiments, ErbB2 was immobilised on a plate at various concentrations. T cell activation was measured by IFNγ production (Fig. 3.8D left). Potency showed a significant correlation with K_D with a discrimination power of $\alpha = 0.52$ (Fig. 3.8D, right, ID 25). We identified 2 additional studies including another ErbB2 CAR[261] and a DNA-based CAR[78] (Table A.2 ID 25-28). All functional experiments in these studies were conducted with a plate assay. The resulting mean discrimination power is α= 0.94.

The B cell receptor, similar to the TCR, has evolved to bind to a large number of unknown foreign antigens. It consists of a membrane-bound antibody, and an adapter molecule containing ITAM motifs similar to the CD3 chains of the TCR. Importantly, each BCR contains two identical binding sites for its ligand. Although several studies measured BCR affinity to antigens, especially in the context of affinity maturation, we only found a single study that provides sufficient dose-response data for us to obtain potency values[262]. The study included two lysozyme-specific BCRs exposed to a series of mutated lysozyme antigens. The average discrimination power of these two BCR systems was $\alpha = 1.3$ (Fig. 3.8E and Table A.2 ID 29

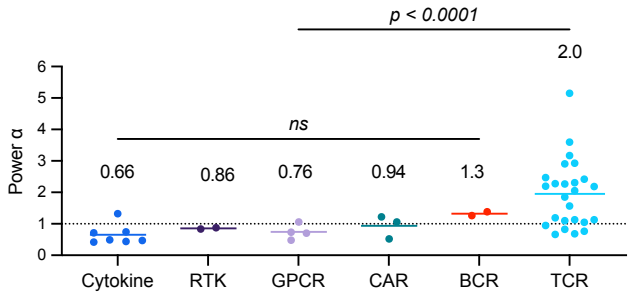

Figure 3.9: The discrimination power of the TCR is higher than other surface receptors. Discrimination powers from all studies included in our analysis (Table A.1 for TCRs and Table A.2 for other receptors). Comparisons within other receptors (cytokine receptors, RTKs, GPCRs, CARs and BCRs) and between other receptors and the TCR were performed using a one-way ANOVA and a non-paired t-test, respectively. Additional information on each panel is provided in Table A.2 (ID: 5 for panel A, 15 for B, 20 for C, 25 for D, and 29 for E).

and 30). This was the only other receptor next to the TCR that showed a discrimination power greater than 1.

In summary, discrimination power α is near 1 for Cytokine receptors, RTKs, GPCRs, CARs and BCRs (Fig. 3.9). We do not see any significant difference in power α between them. As a group, the discrimination power is significantly lower compared to the TCR, confirming that the TCR has a uniquely high discrimination among other ligand receptors.

3.3 *Discussion*

Systematic analysis of the discrimination power α

Understanding antigen discrimination is critical for understanding autoimmune responses and off-target toxicity in T-cell therapies. Previous studies on pMHC-TCR affinity have demonstrated a general role of pMHC-TCR affinity for T cell activation. However, they have concluded that the TCR exhibits near-perfect discrimination between high and low-affinity peptides while maintaining high sensitivity.

By introducing the discrimination power α as a measure of discrimination strength, we calculated the discrimination for multiple TCRs using an extensive literature search. This made it possible to perform a quantitative comparison across 12 TCR systems producing 51 potency over affinity plots. We found that the TCR exhibits an enhanced discrimination power of $\alpha = 2.0$. This is a significantly lower discrimination strength than suggested by original

mouse data which revealed near-perfect discrimination of $\alpha \sim 9$. This imperfect discriminatory power is consistent with recent work using human T cells expressing 1G4 and A6 TCR[246].

The discrepancies between the original and subsequent data on antigen discrimination are likely a result of over-estimated affinity values in the original studies. These affinity measurements were performed using SPR, which in the 1990s was an emerging technology and its limitations and pitfalls were yet to be identified. Although the high sensitivity of the instrument enabled the detection of low-affinity TCR/pMHC interactions, direct affinity measurements required high TCR concentrations which were often achieved by concentrating the TCR. This can result in protein aggregation, and indeed, the bi-phasic nature of TCR/pMHC binding in the original studies is now understood to be a hallmark of protein aggregation in SPR. Together with higher sensitivity SPR instruments and the pioneering work in the original SPR data, scientists can now regularly obtain reliable monomeric affinity estimates using SPR.

Limitations of systematic analysis

It is worth noting that while potency typically correlates with the solution or three-dimensional (3D) affinity measured by SPR, a lack of correlation was reported in a subset of the studies we analysed. We found that in studies that varied the TCR clone rather than the peptide sequence, there was a higher likelihood of no correlation (see Gp100-specific TCR Table A.1 ID 45 vs ID 47, and MEL5 TCR Table A.1 ID 70 vs ID 69). Serval factors could contribute to this; such as different TCR expression levels between clones, as it has been shown that lower expression of TCR reduces T cell response[23]. Furthermore, cell lines expressing one TCR clone that have been in culture for a long time can diverge and may accumulate mutations that influence T cell response. It has also been suggested that the strength of the T cell response is tuned to the affinity of their TCR to self-peptides[263], and can therefore vary between TCR clones. Additionally, certain methods for measuring T cell activation, such as protein phosphorylation, calcium signalling, or degranulation, produced lower correlation as surface marker expression, cytokine production, or target cell lysis (see ILA1 TCR Table A.1 ID 52 vs ID 53-57). This is likely due to the lower sensitivity of these detection methods, which cannot measure T-cell responses at low antigen densities.

Some exceptions can be attributed to structural factors. For example, a pMHC was found to be able to bind the TCR but not activate T cells due to an unusual docking geometry that

prevented co-receptor binding[264]. In another case, mechanical forces were suggested to affect some TCR-ligand interactions differently than others[154,155]. In a third example, surface or two-dimensional (2D) TCR/pMHC binding parameters measured within the T cell contact interface were found to predict the T cell response more accurately than 3D binding parameters measured in SPR[153]. However, this result was based on the original SPR data for the OT-I system, which was the only data available at the time. A subsequent study found that the 2D and 3D binding parameters for the 1E6 TCR were equally accurate at predicting the T cell response[265]. Overall, these studies suggest that there may be exceptions where 3D binding properties do not correlate with potency.

Mechanism of enhanced discrimination

Using power α as a quantitative value of TCR discrimination allows us to further explore the mechanism of discrimination. The kinetic proofreading model can explain both the enhanced discriminatory power and the high sensitivity of the TCR. In a recent publication, the KP model was fitted to the affinity and potency data of the 1G4 and A6 TCR, which allowed the determination of the number of proofreading steps N and the proofreading time. The study estimated the number of proofreading steps to be 2.7 steps and a short proofreading time delay of 2.8 s[246]. Consistent with these findings, studies utilizing a microscopy approach with light-controlled pMHC binding observed similar time delays between TCR/pMHC binding and downstream phosphorylation events[77,91]. Another study using light-controlled TCR activation found a similar degree of discrimination that was consistent with a kinetic proofreading model[148].

The proximal phosphorylation steps in the TCR signalling cascade may represent the biochemical delay steps described by the KP model. Evidence for this comes from our observation that mutations in the proximal signalling proteins Lck, ZAP70 and LAT change the discrimination power. However, our analysis shows discrepancies between Jurkats and naive T cells isolated from mice. Using systematic modification of proteins in the downstream signalling pathway and measuring their impact on the discrimination power may allow us to identify other proteins involved in kinetic proofreading[266].

Our analysis showed no difference in discrimination between different T-cell responses, which is in line with recent data showing that $CD8^+$ T-cells have a shared antigen threshold for

different T-cell responses[267]. This is further evidence that antigen discrimination is happening in the proximal TCR signalling pathway. Furthermore, we have shown that discrimination can be affected by the presence of CD4 and CD8 coreceptors. The increase in discrimination in the absence of coreceptor binding could be due to impaired Lck recruitment to the TCR and/or a lack of stabilisation of low-affinity TCR/pMHC complexes. Other co-signalling receptors found to impact discrimination power such as CD2 and LFA-1[246] might also interfere with the proximal signalling pathway. Also the size of microvilli-contacts has been implicated in modulating antigen discrimination[43].

Discrimination power of other ligand receptors

TCR shows enhanced discrimination compared to other ligand receptors, which exhibit baseline discrimination with α approximately 1. One reason for this low discrimination strength may be that these receptors do not employ kinetic proofreading, but rather are triggered immediately after ligand binding. However, there are important differences in the experiments used for determining power α for TCR and other receptors that may contribute to the apparent lower discrimination of other receptors. Firstly, the ligands used for other receptors bind with higher affinities (in the range of 1nM- 1µM) than pMHC to TCR (1µM - 1mM). The potency for the TCR also shows a plateau for ligands with K_D <1 μM. Therefore, conventional receptors may also display enhanced discrimination if tested with lower-affinity ligands. Secondly, there may be less contribution from co-signalling receptors that influence the discriminatory power, because Cytokine receptors, RTKS, and GPCRs bind to soluble ligands, without any additional signal. Similarly, the discriminatory power of the CAR and BCR systems included in this study was measured with a plate assay without the presence of accessory receptors. For the TCR we saw that functional data generated on plate experiments resulted in a power α around 1 indicating that the TCR on its own does not show any enhanced discrimination.

Only the BCR showed a power alpha above 1. However, this conclusion is made on a limited dataset, and more data on the BCR would be necessary. For the BCR its ability to bivalently bind to a target has to be taken into account when measuring affinities.

TCRs, CARs and BCRs belong to the family of non-catalytic tyrosine-phosphorylated receptor (NTR)s, characterised by the presence of ITAM motifs in their cytosolic domains[268]. The CAR contains cytosolic domains of the TCR and is therefore assumed to activate the same

downstream signalling pathway. We therefore expected the CAR to have enhanced discrimination similar to the TCR. To test whether there is indeed a role for ITAM-based signalling in enhanced discrimination, a more controlled stimulation assay needs to be developed. For optimal comparison, we would need a system where the extracellular domain stays constant, so it can be activated by the same ligands and in the same cellular system, while the intracellular domains can be changed. Inspiration can be taken from other reductive platform systems such as those developed by Denham et al.[79], Barton et al.[269], Patel et al.[270]. TCRs and BCRs may use different mechanisms to discriminate antigens. While the signalling pathway of the BCR is similar to the TCR, The conditions for antigen recognition by BCR differ significantly from those of the TCR. BCR binds to its cognate antigen with higher affinity and can engage in multivalent binding, increasing the binding strength even further. Furthermore, the B cell exerts a pulling force on the BCR-antigen interaction[189], which has been suggested as a BCR intrinsic mechanism for antigen discrimination[192,194].

Implications

The imperfect discrimination power that we report for the TCR highlights the important role of T-cell extrinsic mechanisms of tolerance, such as dependence on the APC (e.g. costimulatory and inhibitory receptor ligands) and other cells (e.g. T_{reg} cells). Moreover, it highlights that the concentration of lower-affinity antigens can have important roles in regulating T cell responses in pathology and normal immune surveillance[233,234]. It may also allow a new perspective on autoimmune diseases: An enhanced but imperfect discrimination allows T cells to respond to low-affinity self-antigens if present at a high concentration, suggesting that abnormally high levels of self-antigens may trigger autoimmune responses. Future research could explore strategies to modulate or regulate these antigen levels, offering new avenues for autoimmune disease treatment. Targeted interventions might focus on preventing the overproduction of self-antigens, thereby reducing the likelihood of T cells mistakenly attacking healthy cells. Further consequences of this work exist for cancer immunotherapy. Researchers might explore ways to enhance the discrimination abilities of T cells by modifying proteins involved in kinetic proofreading, allowing them to selectively target cancer cells without inducing off-target killing. This may lead to more effective and precise cancer treatments with reduced side effects. Lastly,

this work is a testimonial for the need to revisit scientific data and conclusions drawn thereof when discrepancies arise even when they are widely accepted in the scientific community.

4

REVISED 3D AFFINITIES FOR THE OT-I TCR

4.1 *Introduction*

The OT-I-TCR is one of the most commonly used TCR transgenic mouse models in immunology. Our understanding of antigen recognition and discrimination, including central and peripheral self vs non-self discrimination, has been heavily influenced by experiments using OT-I thymocytes and peripheral T cells[96,112,271,272].

The OT-1 TCR recognises a peptide from the ovalbumin protein (amino acids 257-264: SIINFEKL) (abbreviated to N4) bound to murine H-2K^b MHC Class I. This TCR was initially identified in mice primed with the ovalbumin peptide (then also known as clone 149.42 and 42.12)[273]. Using structural analysis, it has been discovered that the cognate SIINFEKL peptide binds to H2K^b via its amino acids in position Ile-P2, Phe-P5, and Leu-P8, while the amino acids Asn-P4, Glu-P6 and Lys-P7 are accessible for TCR binding[272,274].

Since the first experiments with OT-I, variants of the cognate N4 peptide have been created, with amino acids in positions 1, 2, 4 and 7 mutated. In initial experiments, it was shown that cognate N4 peptide has a high affinity to OT-I and induces negative thymic selection, whereas variant peptides with lower affinity induce positive selection[114,127]. As discussed in Chapter 3, the initial affinity measurements for these variant peptides gave rise to the idea of perfect discrimination[96,112,128]; a modest 5-fold reduction in antigen affinity can abolish the T cell response unless the antigen concentration is increased by more than 1 000 000-fold.

However, many other human and mouse TCRs show imperfect discrimination, where an antigen with a 5-fold lower affinity can activate T cells if its concentration is increased by just 25-fold. Recently the affinity of OT-I to different peptide variants has been measured at 25°C[240]. Contradictory to the original experiments, T cells could still be activated with

peptides that had an affinity of K_D = 1000 µM, 20-fold lower than the affinity of OT-I to its cognate N4 peptide, showing enhanced but not perfect discrimination. However, the affinity measurements from original mouse studies have not yet been repeated and most published affinity measurements were done at 25 °C. When the affinity of OT-I binding its cognate peptide N4 was initially measured, the binding interaction displayed a biphasic binding at 37°C. This behaviour was not observed at 25°C nor for non-stimulating peptides. Furthermore, no kinetic binding parameters for the OT-I interactions are known. Because of this lack of data, the original OT-I data is still routinely used in recent studies to validate models or reject ligand affinity as a predictor of T cell response[150,153,241].

The OT-I TCR is unique in that bona fide positively selecting peptides have been identified. Measuring the affinity of these self-peptides will give us insight into the discrimination strength that is required for positive selection. These self-peptides were identified using experimental methods and bioinformatics analyses[105]. Through experimental efforts, H–2K^b–associated peptides were identified from thymus tissues, including C57BL/6 mouse thymi and thymus cell line EL4 and LB27.4. The extracted peptides were screened for positive selection of OT-I-expressing T cells using a coreceptor dulling assay. In parallel, a bioinformatics-based strategy involved searching databases for mouse protein fragments with H–2K^b MHC anchor binding motifs. These fragments were searched for analogues of the N4 peptide. Both approaches identified peptides derived from F-actin capping protein (Cappa1$_{92-99}$) and from β-catenin (Catnb$_{329-336}$) as positive selecting self-peptides. Additionally, peptides Mapk1 (Mapk1$_{19-26}$) from the ERK-2 protein and Stat3 (Stat3$_{53-60}$) were identified as peptides that neither induce positive nor negative selection. The natural presentation of these four self-peptides on MHC complexes in cortical thymic epithelial cells was confirmed[103].

We are lacking a complete dataset for the affinities of the OT-I at biological conditions that also includes self-peptides. In this chapter, using an SPR protocol developed to measure ultra-low affinity TCR/pMHC interactions, we systematically measure the interaction of the OT-I TCR with 20 different pMHCs, including 4 self-peptides. We first determine the kinetics of OT-I/pMHC-N4 interaction at 25°C and 37°C to understand the temperature dependence of OT-I before turning our attention to systematically measuring affinities for all interactions. With these revised 3D affinities at hand, we explore their implications for T-cell antigen discrimination and the mechanism thereof. Our major conclusion is that the revised 3D

affinities reconcile apparent differences between the OT-I TCR and other mouse and human TCRs. This underlines the importance of accurate SPR measurements to study T-cell responses.

4.2 Results

4.2.1 OT-I affinity and binding kinetics to cognate N4 peptide

We studied OT-I interactions using a soluble OT-I TCR construct with a human constant domain and an engineered disulfide bond between the α/β constant domains, as previously described[240]. For SPR affinity measurments, pMHC was immobilised on a CM5 chip and TCR was injected at increasing concentrations (Fig. 4.1A-B). All SPR binding data were referenced against a control flow cell containing matched immobilisation levels of CD86 and against buffer injection to prevent volume exclusion effects (double referencing). The K_D of the pMHC/TCR interaction is determined by plotting the steady-state binding response over TCR concentration and fitting it with a 1:1 binding model (Fig. 4.1C).

Measurement of OT-I TCR binding to its cognate peptide SIINFEKL (N4) across a range of immobilisation levels produced an average K_D of 34 μM at 37°C, and 100 μM at 25°C (Fig. 4.1D). In contrast to the original measurements, we found no evidence for a 2-step binding process at 37°C (Fig. 4.1A).

More recent attempts to study the OT-I/pMHC-N4 interaction suggest a very fast dynamic interaction (k_{off} = $>1\,s^{-1}$)[240], which makes it challenging to obtain accurate binding rate measurements using the BiaCore T200 instrument with a sample rate of 10 Hertz. Additionally, the flow cells in a Biacore T200 instrument are connected in series, which means the ligand flows through flow cell 1, which acts as the control flow cell, before passing through flow cell 2, used for the sample. This can lead to misaligned injection start and end times, which introduces artificial spikes at the start and end of the injection phase after double referencing. These spikes can conceal important kinetic information for very dynamic interactions such as those expected for the OT-I TCR. To overcome these limitations, we used the WAVEsystem by Creoptix, which uses grating-coupled interferometry (GCI) to measure protein binding[275]. GCI has a higher sensitivity than SPR. The WAVEsystem has flow cells connected in parallel,

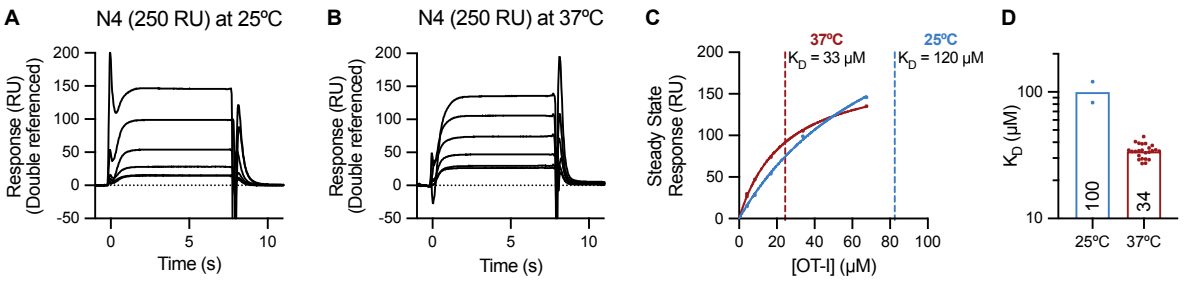

Figure 4.1: OT-I affinity to cognate peptide at 25°C and 37°C. (A-B) Representative SPR sensograms showing injections of 8 different OT-I-TCR concentrations over immobilised murine H-2K^b MHC Class I loaded with ovalbumin$_{257-264}$ SIINFEKL (N4) peptide at A) 25 °C and B) 37°C. **(C)** Steady-state binding response (RU) from (A) and (B) plotted over the TCR concentration (filled circles). Data was fitted with a one-site specific binding model to determine K_D (solid line). **(D)** Fitted K_D of OT-I/pMHC-N4 interaction from multiple SPR experiments (n=2 and n=23 for 25°C and 37°C respectively).

which ensures that each flow cell receives the analyte at the same time (Fig. 4.2A). Additionally, the instrument has a sample rate of 40 Hertz.

The WAVEsystem employs two methods to obtain kinetic binding rates. The first method uses multicycle injections. As for Biacore, increasing TCR concentrations are injected, and the dissociation of each injection is fitted with a one-phase exponential decay model returning k_{off} (Fig. 4.2B). The second method is the waveRAPID method, in which the analyte is injected for different lengths of time (Fig. 4.2C). Each dissociation phase is then fitted with a simple dissociation model to obtain k_{off}. As with SPR, we reduce potential rebinding artefacts by ensuring that rate constants are similar across different pMHC immobilisation levels (150 RU-350 RU). We performed both methods at 25°C and 37°C and measured a k_{off} rate of 2.8 s^{-1} at 25°C and 4.3 s^{-1} at 37°C (Fig. 4.2D). To obtain association rate k_{on}, the association phase in the multicycle data was fitted with a one-phase exponential model, returning the observed rate k_{obs} (Fig. 4.2E). We can determine k_{on} from k_{obs} values over OT-I concentration using the relation $k_{obs} = k_{on} \times [TCR] + k_{off}$. This produces a k_{on} of 1.25 $\mu M^{-1}s^{-1}$ which aligns well with the association rate estimated from K_D and k_{off} using the formula $k_{on} = k_{off}/K_D$ (Fig. 4.2F).

Taken together, SPR and GCI confirm that OT-I interacts with the N4 pMHC using a standard 1:1 binding model. The reported affinity for this interaction is on the weaker end for a foreign antigen compared to other murine and human TCRs[276] and moreover, it displays the fastest kinetics yet observed for a TCR including an on-rate of 1.25 $\mu M^{-1}s^{-1}$. and off-rate of 4.3 s^{-1}.

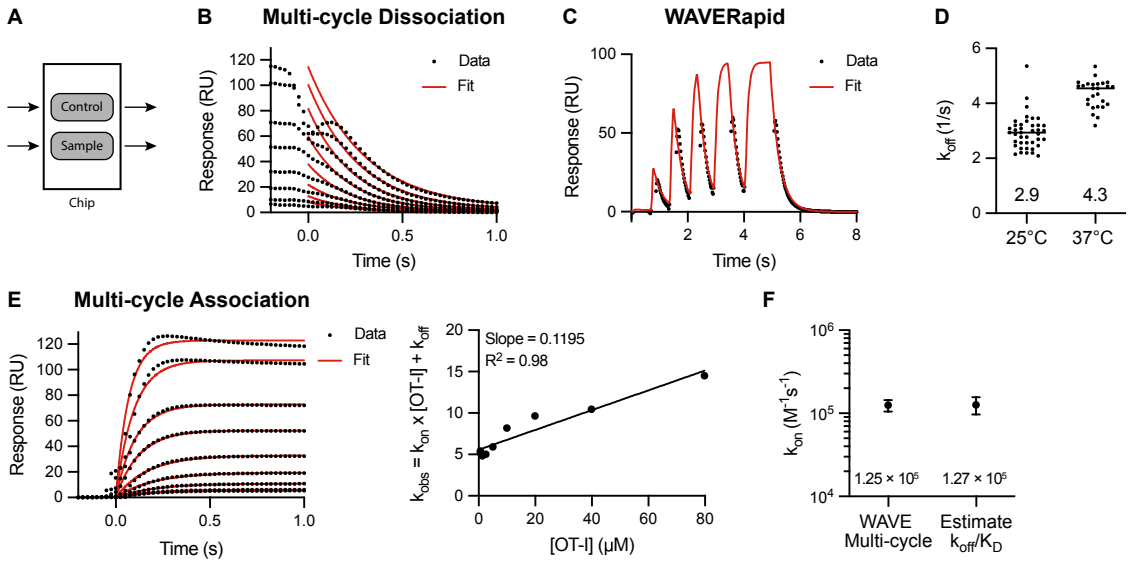

Figure 4.2: OT-I kinetics measured by WAVEsystem. **(A)** Schematics of flow path in WAVEsystem **(B)** Dissociation phase from grating-coupled interferometry (GCI) multicycle sensorgram fitted with a one-phase exponential decay model to determine k_{off} (red lines). **(C)** Representative waveRAPID sensogram of OT-I TCR binding immobilized pMHC-N4 at one concentration of TCR injected for increasing durations. Dissociation phases fitted with a one-phase exponential decay model to determine k_{off} (red lines). **(D)** Fitted k_{off} values from two and four independent experiments with different TCR and/or pMHC concentrations at 25°C (N=42) or 37°C (N=26), respectively. **(E)** Association phase from GCI multicycle sensogram fitted with a one-phase exponential model to determine k_{obs} (red lines). **(F)** k_{obs} values plotted of OT-I TCR concentration and fitted with a straight line to determine k_{on}. **(G)** Measured k_{on} rate from WAVE multicycle experiment and calculated k_{on} using the fitted values of k_{off} (4.3 s^{-1}) and K_D (34 μM).

4.2.2 *OT-I affinity measurement to variant peptides display large variation*

After characterising the binding interaction between OT-I and its cognate peptide N4, we set out to measure its affinity to a range of variant peptides. We selected a panel of 20 peptides commonly used in literature. The panel contained peptides with a single amino acid mutation, as well as the self-peptides Catnb, Cappa1, Mapk1 and Stat3. The stability of each peptide to the H-2K^b MHC was previously determined to be similar for these peptides[114,272].

As we expect many of these peptides to have a very low affinity to OT-I, we used a previously published SPR protocol optimised for ultra-low TCR/pMHC affinities[246]. Interactions with very low affinities (K_D >200 µM) cannot be measured accurately with a standard SPR equilibrium binding experiment. This is because when we plot the steady state binding response against TCR concentration to calculate K_D, the curve does not saturate at the highest TCR concentration. Since K_D is defined as the concentration of TCR producing half-maximal binding ($B_{max}/2$), the inability to saturate binding to determine B_{max} means that it is not possible to

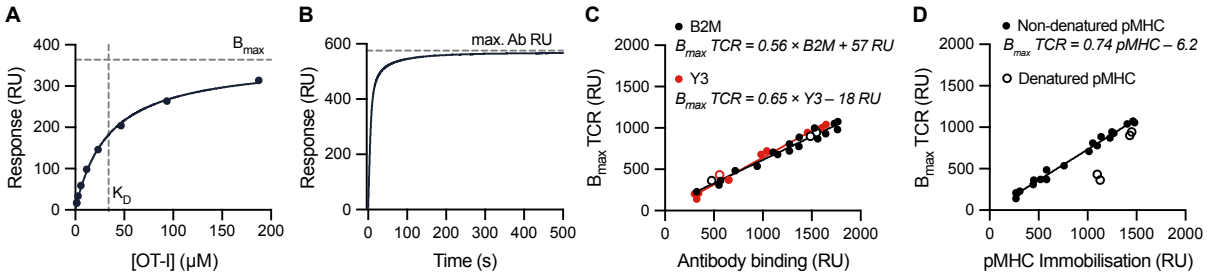

Figure 4.3: Establishing an antibody standard curve for ultra-low affinity measurements. (A) Steady-state binding over TCR concentration fitted with one-site specific binding model to obtain TCR B_{max} and K_D **(B)** Representative SPR sensogram of B2M antibody binding human β2m domain of pMHC following the injection of TCR in (A). **(C)** Empirical standard curve relating B2M and Y3 antibody binding to fitted TCR B_{max} obtained using high affinity peptides N4 and A2 (N = 17 for B2M, n = 9 for Y3). This standard curve will be used to determine the TCR B_{max} for low-affinity peptides as described in[246]. The correlation holds true for both non-denatured pMHC (filled circles) and pMHCs partly denatured by a short injection of glycine solution with low pH (empty circles). **(D)** Correlation between pMHC-N4 immobilisation level and TCR B_{max}. pMHC-N4 used came from the same protein preparation. For non-denatured pMHC (filled circles), pMHC immobilisation level correlates well with TCR B_{max}. Partly denatured pMHCs (empty circles) do not follow this correlation.

accurately estimate K_D. In the past, attempts to overcome this limitation involved lowering temperatures where K_D is expected to be higher or to increase the TCR concentration. However, the former produces estimates at non-physiological temperatures and the latter can produce protein aggregates artificially inflating affinity values.

Our lab recently developed a new SPR method that allows the measurement of ultra-low affinities[246]. In this method, after the TCR injection over immobilised pMHC, an pMHC conformation-specific antibody that only binds correctly folded pMHC is injected at the end of each SPR experiment. Because the antibody recognises the same population of pMHCs that the TCR can bind to, the maximum binding response of the antibody correlates linearly with the TCR B_{max} identified from equilibrium binding curves of high-affinity peptides over a range of immobilisation levels. This correlation acts as a standard curve to calculate the TCR B_{max} given the antibody B_{max} for low-affinity peptides where the TCR B_{max} cannot be accurately fitted from the binding curve. By constraining the B_{max} to the B_{max} value obtained from the standard curve, an accurate K_D can be obtained.

The standard curve relating maximum antibody binding to TCR B_{max} was generated with the cognate N4 peptide. The N4 peptide allowed an accurate measurement of TCR B_{max} (Fig. 4.3A). Antibodies used for the standard curve were conformation-specific, including the Y3 antibody and an anti-β2m antibody (Clone B2M), both binding only correctly folded pMHC complexes. The antibodies were injected for 800 s and the maximum binding response was

recorded (Fig. 4.3B). The TCR B_{max} plotted against maximum antibody response produces a linear correlation with a slope of 0.56 and 0.65 for antibodies B2M and Y3, respectively (Fig. 4.3C). No significant difference between the standard curves of B2M and Y3 was observed.

To test if antibody binding accurately predicts the amount of TCR binding, pMHC was partly denatured after immobilisation to remove the bound peptide. Even after denaturing, the data points of the antibody and TCR B_{max} for both the B2M and Y3 antibody fall on the standard curve (empty circles in Fig. 4.3C). When plotting immobilisation levels against TCR B_{max}, again a strong correlation is observed, however, pMHC that were partly denatured no longer correlate with TCR B_{max} (Fig. 4.3D). This confirms that the antibodies and the TCR recognise the same correctly-folded pMHC population immobilised on the chip and underlines the importance of predicting TCR B_{max} with a conformation-sensitive antibody.

For all subsequent experiments, we used the B2M antibody, which has the advantage of being universally applicable to all measurements with pMHC proteins containing human β2m. To avoid extrapolation from the standard curve, we only used pMHC immobilisation levels less than 2000 RU.

Next, we performed SPR experiments for 20 variant peptides, including 4 self-peptides (Fig. 4.4A-S, left). Steady-state binding response over OT-I concentration was fitted with a 1:1 binding model to estimate K_D, with the B_{max} constrained to the value obtained from the antibody standard curve (Fig. 4.4A-S, right). Average K_D values for the peptide panel are summarised in Table 4.1. All peptide information and K_D values are provided in Table S4.1. The affinities ranged from 34 μM for the cognate N4 peptide, to 2280 μM for R4 peptide. Peptides that exhibited higher affinities had one or two mutations with amino acids that have similar properties (e.g. lysine replaced by arginine in position 7) or with small and neutral amino acids (e.g. glutamine, threonine, alanine) (Fig. 4.4A-I). On the other hand, peptides with lower affinity had asparagine in position 4 replaced by a charged amino acid such as lysine, arginine, or glutamic acid (Fig. 4.4J, M-O). Alternatively, multiple amino acids were replaced by alanine, as was the case with the null peptide (SIAAFASL), which was designed to minimize TCR contacts (Fig. 4.4K). Some low-affinity peptides also had a very different sequence, such as the vesicular stomatitis virus-derived peptide VSV (Fig. 4.4L). Self-peptides produced affinities around 1500 μM- 2000 μM (Fig. 4.4P-S). Unexpectedly, the B2M antibody did not bind to the

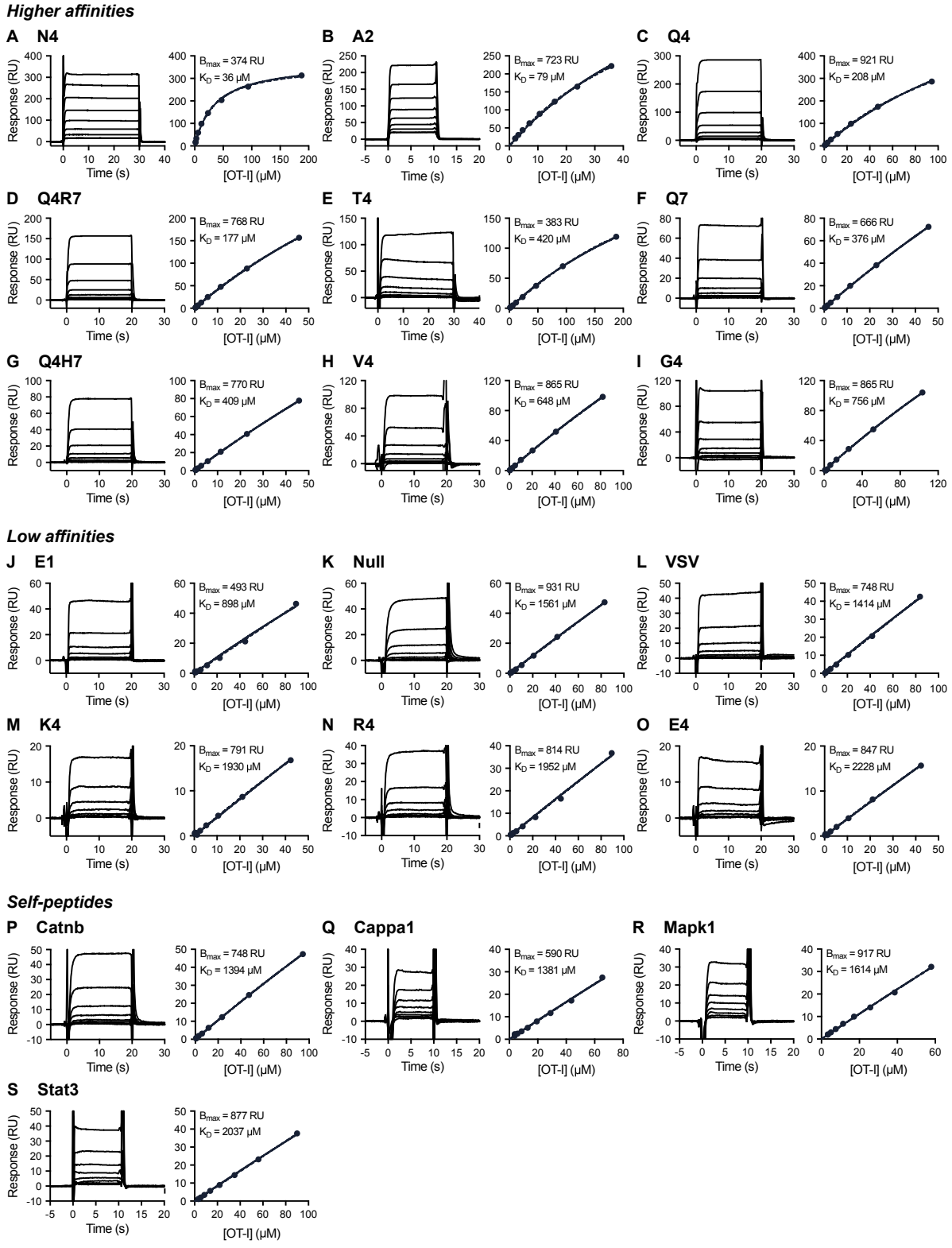

Figure 4.4: SPR curves for peptide variants. **(A-R)** Representative Surface Plasmon Resonance data. Left: Double-referenced sensograms. Right: Steady-state binding RU over TCR concentration. Data fitted with one-site specific binding model, where B_{max} was constrained to B_{max} determined from B2M antibody binding according to the standard curve in Fig. 4.3.

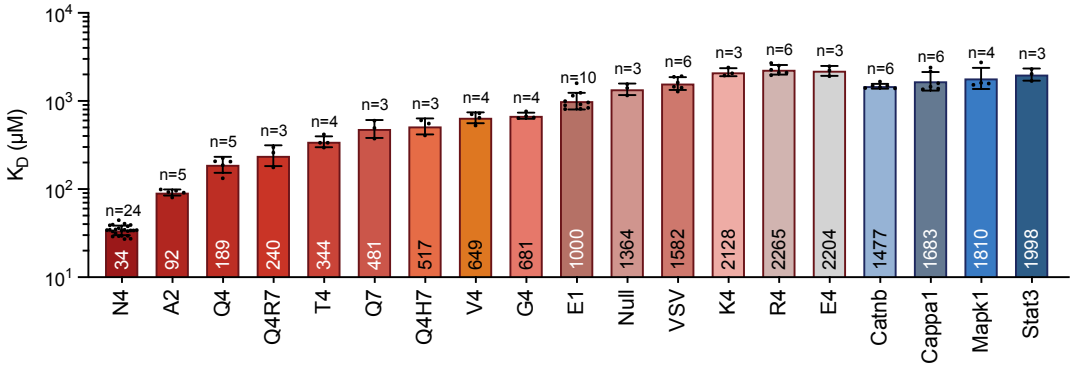

Figure 4.5: Affinities for peptide panel binding OT-I. K_D values measured for a panel of peptide variants binding OT-I TCR at 37°C. Name indicates the changed amino acid and position compared to the cognate N4 peptide. Mean values of K_D values are indicated in bars.

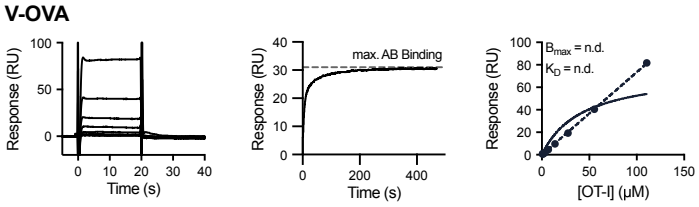

Figure 4.6: SPR of V-OVA. Representative Surface Plasmon Resonance data. Left: Double-referenced sensograms. Centre: Antibody B2M binding correctly folded pMHC in (A). Right: Steady-state binding RU over TCR concentration. Data fitted with one-site specific binding model, where B_{max} was constrained to B_{max} determined from B2M antibody binding according to the standard curve in Fig. 4.3.

V-OVA peptide even though it was immobilized on the SPR surface and detectable binding was observed to OT-I (Fig. 4.6). Therefore, we were unable to report an affinity for this interaction.

We compared our revised K_D values at 37°C to the original K_D values published previously[112,128,238] (Fig. 4.7A). Our revised measurements show lower affinity and while the affinity to the cognate N4 peptide is in a similar range (34 μM to 5 μM in the original data), the difference is amplified for non-stimulatory peptides E1 and R4 (Fig. 4.7A left). We now report that these peptides have a 30-65-fold lower affinity than the cognate peptide rather than the small difference of 5-10-fold difference originally reported (Fig. 4.7A right). The revised K_D values at 37°C correlate well with more recent affinity measurements at 25°C (Fig. 4.7B). However, we observe slightly higher affinities at 37°C. This is in line with our measurement of N4-OT-I interaction at 25°C (Fig. 4.1). Similarly, we find a large >40-fold lower affinity for self-peptides whereas more modest 15-25-fold differences were previously reported at 10°C[113] (Fig. 4.7C).

Table 4.1: K_D values for OT-I TCR at 37°C.

Peptide	Sequence	Mean K_D (μM)	STD	N
N4	SIINFEKL	34	4.4	24
A2	SAINFEKL	92	8.1	4
Q4	SIIQFEKL	190	36	5
Q4R7	SIIQFERL	250	63	3
T4	SIITFEKL	350	50	4
Q7	SIINFEQL	490	110	3
Q4H7	SIIQFEHL	520	100	3
V4	SIIVFEKL	650	89	4
G4	SIIGFEKL	680	56	4
E1	EIINFEKL	1000	250	10
VSV	RGYVYQGL	1600	260	6
Null peptide	SIAAFASL	1400	200	3
K4	SIIKFEKL	2100	230	3
R4	SIIRFEKL	2300	290	6
E4	SIIEFEKL	2200	290	3
Catnb	RTYTYEKL	1500	98	6
Cappa1	ISFKFDHL	1700	440	6
Mapk1	VGPRYTNL	1900	580	4
Stat3	ATLVFHNL	2000	310	3
V-OVA	RGYNYEKL	n.d.		

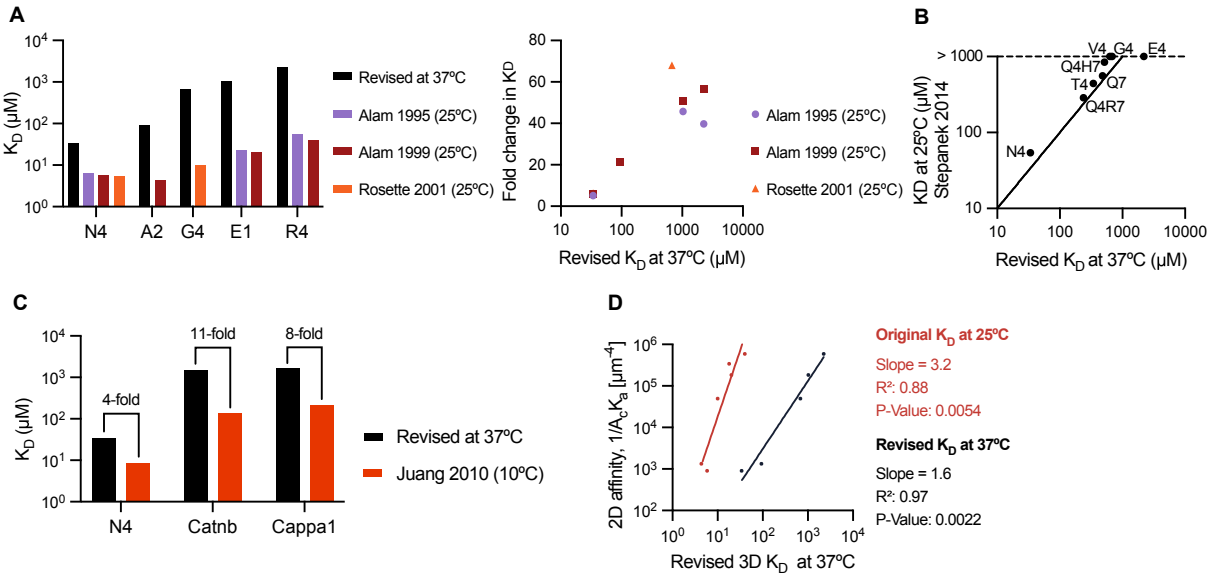

Figure 4.7: Comparison of K_D values to previously published data. **(A)** Comparison between original OT-I K_D values measured by SPR at 25°C[112,128,238] and our K_D values measured at 37°C. Our K_D values divert from the original values by a 5-fold difference for higher affinity peptides and an up to 70-fold difference for lower affinity peptides. **(B)** More recently published K_D values at 25°C for a smaller peptide panel[240] correlate well with our 37°C K_D values. **(C)** Comparison between self-pMHC K_D values measured at 10°C[113] and our revised K_D values measured at 37°C. **(D)** Correlation between OT-I 2D affinity values[153] and 3D affinity using original OT-I K_D values measured by SPR at 25°C[112,128,238] and our K_D values measured at 37°C.

4.2.3 *Revised 3D affinities display similar variation to 2D affinities*

In contrast to interactions between molecules in solution as measured by SPR, T cells recognise antigens on the surface of APCs, with TCR and pMHC restricted to the two-dimensional (2D) plane of the interacting cell surfaces. This has motivated the direct measure of 2D kinetics and affinities of the TCR/pMHC interaction[153]. Huang et al.[153] found that 2D affinities of the TCR for a panel of pMHC ligands possess broad dynamic ranges resulting in 2D affinity being a much better predictor of T cell activation than the 3D binding parameters. However, this comparison was made with the original K_D values. When we replot the 2D affinities with both the original K_D values and our revised data, we find that both datasets have a strong correlation with 2D affinity (Fig. 4.7D). However, the original 3D data displayed a very steep slope. On the other hand, the revised K_D values at 37°C display a more modest slope (Fig. 4.7D). While the original data suggests that the binding dynamics on the membrane are fundamentally different than soluble proteins in a 3D environment, the revised K_D values show that 3D affinity values faithfully reproduce the 2D affinities and hence T cell responses. Nevertheless, the slope

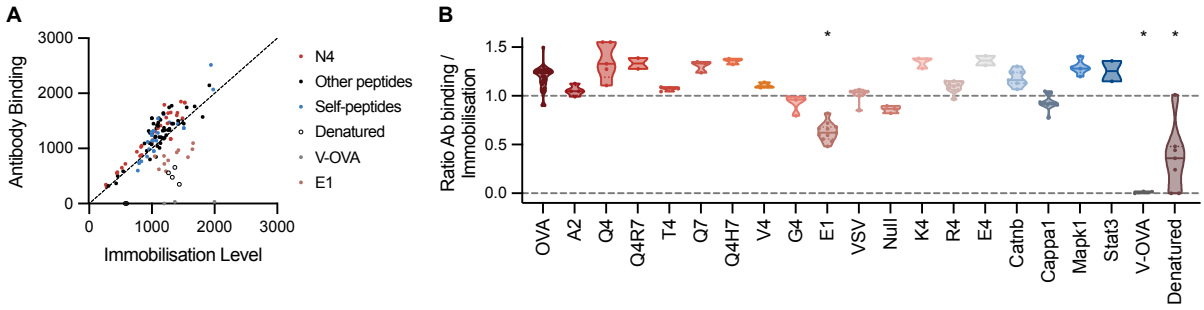

Figure 4.8: Immobilisation level compared to antibody binding, determining the fraction of correctly folded pMHC. (A) Correlation between pMHC Immobilisation level and B2M antibody binding RU for all peptide variants. Denatured pMHC-N4, as well as the peptide variants E1 and V-OVA divert from the general correlation, indicating partly or fully denatured pMHCs. **(B)** Ratio antibody binding to immobilisation level for all tested peptides. Peptides that have a ratio significantly less than 1 are marked with *.

between revised 3D data and 2D data is larger than 1, indicating that there is still a difference between 2D and 3D binding.

4.2.4 *SPR binding controls verify accurate affinity measurements*

Several control experiments were conducted to test the reliability of these affinity measurements. Firstly, the pMHC antibody binding might depend on the peptide, affecting the apparent levels of properly folded pMHC on the surface and thereby influencing affinity estimates. However, we observed a significant correlation between antibody binding and pMHC immobilisation, mostly unaffected by the peptide sequence (Fig. 4.8A), which is expected given that this antibody binds β_2M and not the peptide. The fraction of correctly refolded pMHC, calculated by dividing immobilisation level by antibody binding, was consistent for all peptides except V-OVA and E1 (Fig. 4.8B). In the case of V-OVA, we found that the antibody did not bind and therefore, we could not estimate affinity. In the case of E1, the antibody binding was consistently lower than expected. We observed a similar discrepancy between antibody binding and pMHC immobilisation when we intentionally denatured the pMHC on the surface. This may indicate that the pMHC stability of E1 and V-OVA in particular is much lower than the other pMHCs used in our study.

Surprisingly, even though fully denatured peptides and V-OVA do not show any antibody binding, we observed OT-I binding, indicating that the OT-I can bind the unfolded pMHC

(Fig. 4.9). As the antibody does not bind denatured pMHC, no B_{max} can be obtained using the standard curve. However, we can use the relation between pMHC-N4 immobilisation and OT-I TCR B_{max} in Figure 4.3 to estimate the B_{max} of the denatured pMHCs. Applying this analysis to both the denatured N4 and V-OVA peptides, we obtain a K_D of approximately 1500 µM for the denatured N4 and V-OVA pMHC.

Suppose the lower antibody binding to E1 is due to a part of the immobilised pMHC being unfolded. In that case, it raises the question of whether binding to the unfolded pMHC can influence the observed K_D measurement. We found that partly denatured pMHC-N4 resulted in the same K_D value as non-denatured pMHC. However, E1 is a low-affinity peptide, relying on an accurate determination of B_{max}. Furthermore, the affinity to unfolded pMHC is similar to E1 (1500 µM vs 1000 µM) and may therefore have a stronger effect on the measurement. To see whether partly denatured pMHC influences low-affinity measurements, we immobilised VSV to equal levels in three flow cells. VSV was chosen because it has an affinity similar to E1. In two flow cells we then partly denatured the pMHC to different extents by injecting low-pH glycine solution for different time lengths, resulting in the removal of 130 RU and 200 RU protein material. The B_{max} was estimated from the B2M binding, showing a decrease in correctly folded protein. However, the amount of TCR binding stayed the same. Fitting a one-site-specific binding model with constrained B_{max} resulted in a lower K_D for flow cells with a higher proportion of denatured peptide. This is likely due to the OT-I being able to bind to both denatured and correctly folded pMHC-VSV with a similar affinity, however the B2M antibody only binds correctly folded pMHC-VSV. Because of the lower B_{max} together with equal or higher binding response the estimated K_D progressively decreases as the degree of denaturing increases. This suggests that the estimated K_D for the pMHC-E1 is likely underestimated.

Even at high TCR concentrations, the low-affinity pMHCs that result from point mutations and self-pMHCs produce less than 50 RU. Small differences in binding response can occur due to a mismatch in immobilisation levels between the sample flow cell and control flow cell. This is known as volume exclusion effect; on an empty flow cell containing only streptavidin, analytes can come closer to the chip surface due to the lack of ligands and produce a signal without any specific binding. If this reference signal is subtracted from the sample flow with immobilized pMHC, it can result in an apparent negative binding. To prevent this, we immobilise CD86 in the control flow cell because it has a similar molecular weight as pMHC and will therefore

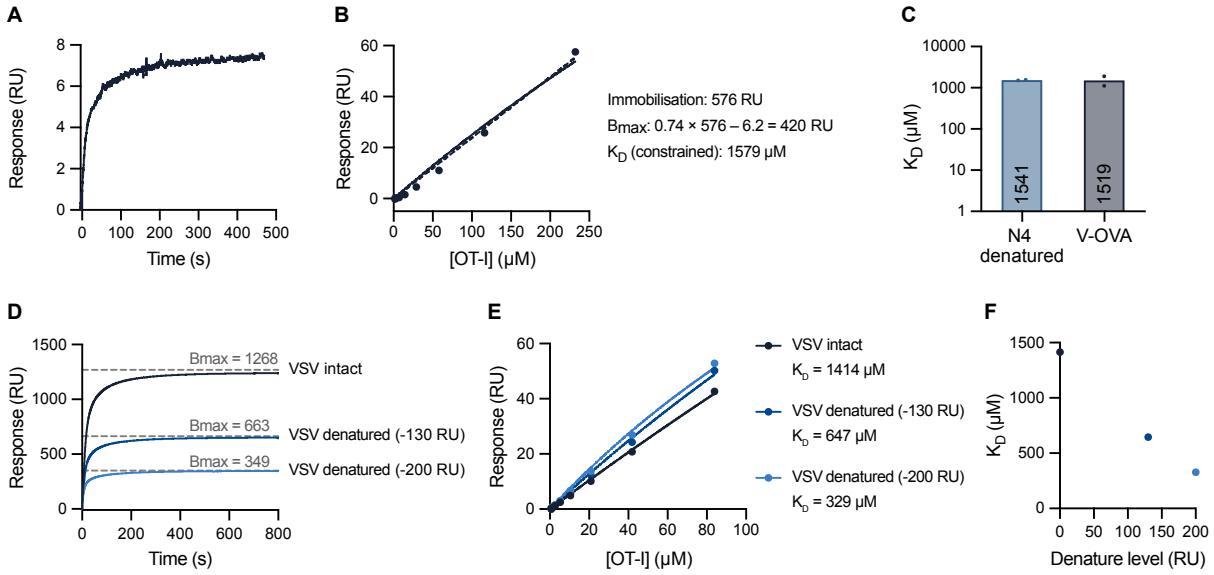

Figure 4.9: Effect of denaturation on K_D measurements of low-affinity pMHCs. **(A)** Representative SPR sensogram of B2M antibody binding pMHC-N4 that was fully denatured by injecting a glycine pH2 solution. The low antibody binding RUs indicated that most pMHC-N4 molecules are in an unfolded state. **(B)** Steady-State binding curve for denatured pMHC-N4. To estimate the affinity of OT-I to unfolded pMHC, the relation between TCR B_{max} and pMHC immobilisation in Fig. 4.3D was used to calculate a B_{max}. The data was fitted with a one-site specific binding model with constrained B_{max}. **(C)** Mean estimated K_D for TCR to denatured pMHC, calculated from denatured N4 and V-OVA. **(D)** Antibody binding curve to VSV denatured to different extents. **(E)** Effect of denatured pMHC on K_D measurement for VSV peptide. VSV was denatured to two different levels by injecting Glycine pH 1.7 solution for different lengths of time. The B_{max} was estimated from B2M antibody binding using the standard curve in Fig. 4.3D. Steady-state RUs were fitted with a one-site specific binding model with constrained B_{max}. **(F)** Estimated K_D for increasing level of pMHC denaturation. OT-I binding to pMHC-VSV with a high proportion of denatured pMHC returns a lower-than-accurate K_D value. Abbreviations: * = p-value≤0.05, ** = p-value≤0.01, *** = p-value≤0.001, **** = p-value≤0.0001.

exclude the analyte from the chip surface to the same extent as pMHC, preventing this artificial response[277] (Fig. 4.10A).

We aimed to match the immobilisation level of CD86 in the control flow cell as closely to the pMHC immobilisation levels as possible. We mostly achieve immobilization levels within 200 RUs (Fig. 4.10B). However, we also found a systematic difference in streptavidin immobilisation between the flow cells. We found that on CM5 chips, the first flow cell immobilises about 1000 RU more streptavidin than the other flow cells (Fig. 4.10C). As a result, we wanted to ensure that the binding response observed for OT-I binding to low-affinity peptides was not due to differences in immobilization, but instead due to specific binding. To achieve this, we injected ovalbumin as a control analyte protein over all four flow cells immobilised with only streptavidin. A perfect SPR surface should produce zero binding when each flow cell is subtracted. In this experiment, we used an ovalbumin concentration

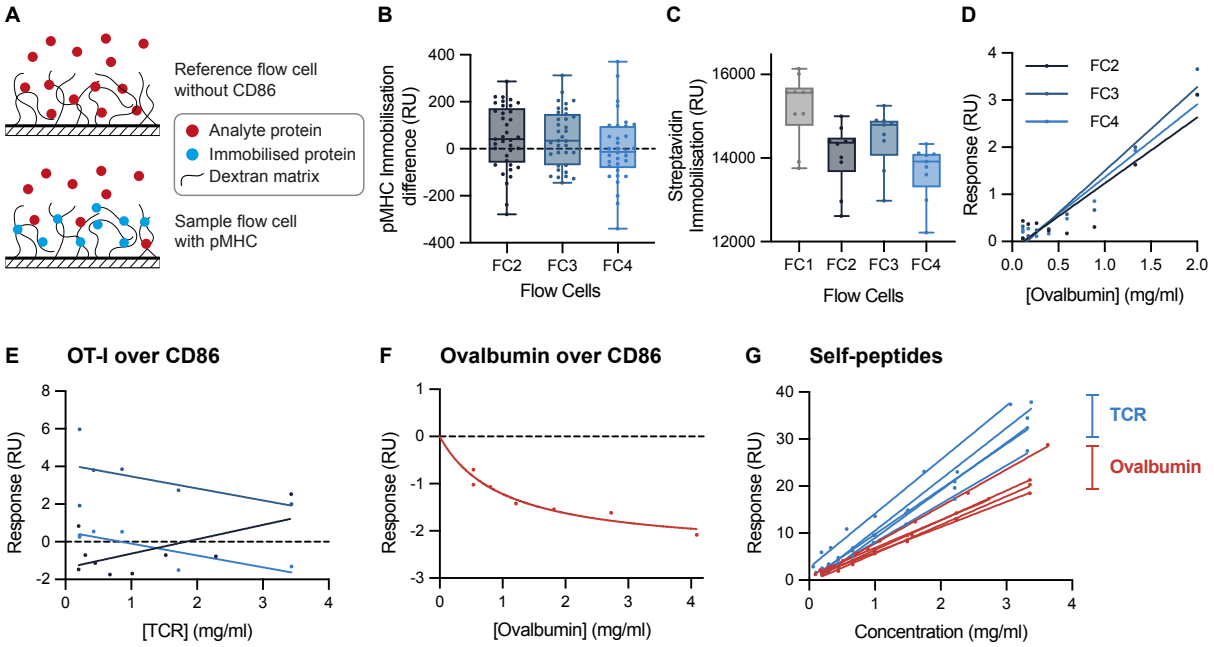

Figure 4.10: Binding between TCR and control proteins and between control proteins and pMHC is lower than between TCR and low-affinity pMHCs. **(A)** Schematic of volume-exclusion effect, adapted from [277]. **(B)** Difference in pMHC immobilisation level between sample and control flow cell (FC1). **(C)** Streptavidin immobilisation level between flow cells on CM5 chip. **(D)** Injection of ovalbumin over streptavin. Data is double-referenced to the control flow cell. **(E, F)** Surfaces coated with the control protein CD86 were injected with (E) TCR and (F) the control protein ovalbumin showing minimal binding responses. **(G)** The binding response of the TCR or the control protein ovalbumin over surfaces coated with self-pMHCs.

of 2.0 mg/ml, equivalent to an OT-I molar concentration of 40 µM. We observe a binding response of 3 RU at the highest ovalbumin concentration, linearly scaling with the ovalbumin concentration (Fig. 4.10D). This shows that a difference in streptavidin level can introduce a small difference in response. To test whether this artificial response is still present after immobilising ligands, we immobilised CD86 in both the control and sample flow cell and injected OT-I and ovalbumin (Fig. 4.10E and F). The binding response of OT-I to CD86 was less than 4 RU with no observable trend of increasing binding response at higher concentrations. Ovalbumin showed negative binding of less than 2 RU. This indicates that the artificial response created by mismatched immobilisation levels is minimal compared to the response we observe for low-affinity pMHC. Finally, we injected both OT-I and ovalbumin over self-pMHC. Comparing the response by TCR and ovalbumin at the same weight concentration, we see that the injection of ovalbumin produced significantly lower binding than the TCR confirming specific OT-I/pMHC binding (Fig. 4.10G).

Overall, we found that a small difference in response in the range of 5 RU could be introduced, but this artificial response is minimal compared to the response we observe for low-affinity peptides. We conclude that the observed binding response for self-peptides is due to specific OT-I interaction. The high binding response of ovalbumin to self-peptide pMHC could be attributed to a specific interaction between ovalbumin and pMHC, given that the binding response is higher than observed for the ovalbumin/CD86 interaction.

Lastly, we compared the affinity of pMHCs produced using bacterial (*E. coli*) and mammalian (HEK293) expression systems. The expression systems may produce pMHC with a different structure or glycosylation pattern that could influence TCR binding. When directly comparing K_D values for pMHCs produced by both methods, we found no difference for using *E.coli* or HEK-produced pMHC both for high and low-affinity peptides (Fig. 4.11).

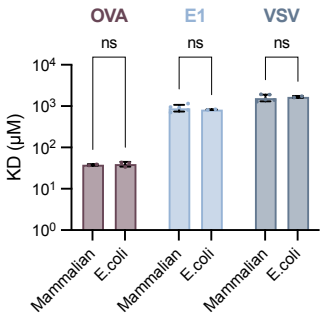

Figure 4.11: Comparison of pMHC produced in *E.coli* or HEK cells. E.coli produce pMHC where purified from inclusion bodies and refolded in the presence of human β2m and peptide. HEK pMHC were produced in Kb expressing in HEK-293T cells, followed by peptide exchange (ordered from NIH Tetramer facility)

4.2.5 *Revised discrimination power of OT-I TCR*

The apparently very small difference in affinity between stimulatory and non-stimulatory peptides observed in the original affinity data implied that the discriminatory power of the TCR is near-perfect[96]. Given the large differences between the original and revised OT-I affinities, we next sought to determine their relation to T-cell activation.

We first generated functional data using naive $CD8^+$ T cells from OT-I transgenic mice. For this, naive CD8+ T cells expressing the OT-I TCR were isolated from the spleens of OT-I transgenic mice (Fig. 4.12A). Splenocytes from mice were used as antigen-presenting cells and

pulsed with peptide before co-culturing them with the OT-I T cells. After 24 hours, T cell activation was measured by expression of the surface receptors CD69 and CD44. T cells showed a measurable response to peptides N4, A2, Q4, T4, Q7, Q4H7, and G4 for both CD69 and CD44 (Fig. 4.12B and C). A small fraction of T cells got activated with the low-affinity E1 pMHC at the highest concentration for CD69, but not enough to determine an EC_{50} value. E1 pMHC did not induce CD44 expression, likely due to a high background activation of 20%. The TCR was downregulated from the cell surface in a pMHC concentration and affinity-dependent manner (Fig. 4.12D). T cell activation for peptides with lower affinity than E1, including self-peptides, could not be detected with naive $CD8^+$ T cells.

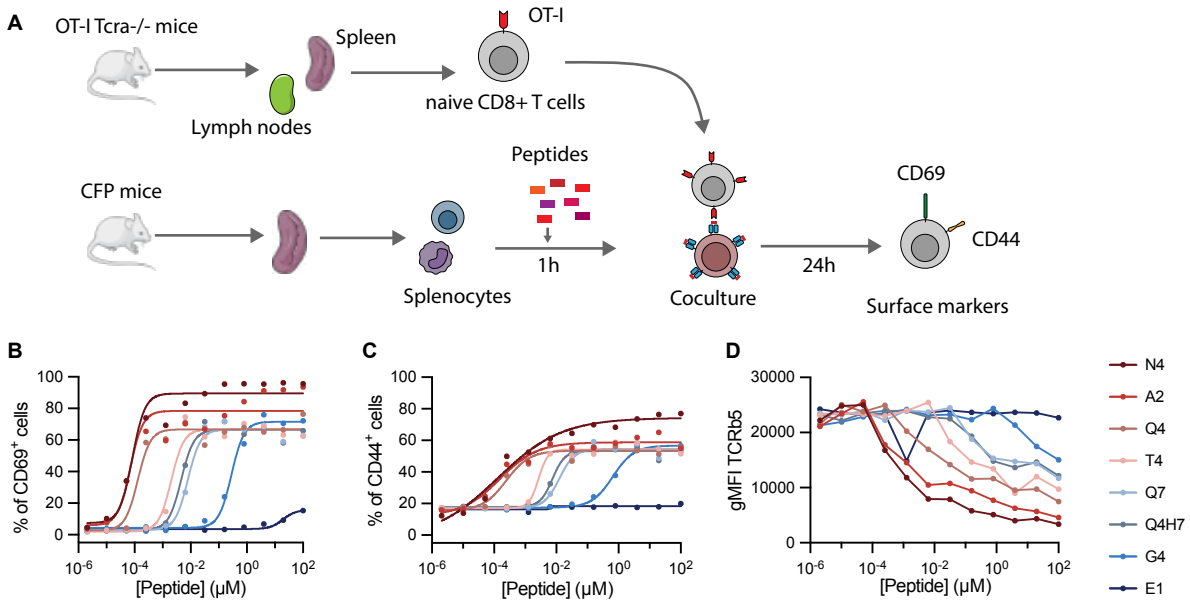

Figure 4.12: T cell activation by peptides. **(A)** Schematic showing T cell activation assay conducted with OT-I transgenic CD8+ T cells interacting with splenocytes pulsed with peptides. **(B, C)** Representative dose-response curves of OT-I T cells interacting with selected peptide panel after 24 hours. TCR activation is measured by the expression of (B) CD69 or (C) CD44 activation marker. The dose-response curve was fitted with a Hill curve to obtain the EC50 as a measure of potency. **(D)** Downregulation of OT-I TCR when stimulated with selected peptide panel for 24 hours. T cell activation assays were performed by Audrey Gérade, Lion F. J. Uhl and Jagdish M. Mahale.

As in Chapter 3, we can use potency and affinity to determine the discriminatory power. To directly compare the discriminatory power suggested by the original data and our revised values, we plotted the potency data with both the original affinities from Alam et al.[128], Rosette et al.[238] at 25°C and our revised K_D values (Fig. 4.13A). Both the original affinity data and the revised data correlate with potency, but there is a strong difference in slope. Fitting a power law to the data produces a discriminatory power of 10 for the original data. The revised data only produces $\alpha = 2.5$ for CD69 measurements and $\alpha = 2.9$ for CD44.

We next plotted potency over affinity plots for published functional data, again directly comparing original and revised K_D values (Fig. 4.13B-H). All datasets show a strong reduction in discrimination power between original and revised K_D values. Combining all datasets, we found that the revised K_D values return a much lower power of 2.8 compared to a mean power of 11.2 for the original K_D values (Fig. 4.13I).

This result confirms that the discrimination strength for the OT-I is enhanced, but not perfect, which is consistent with other mouse and human TCR systems analysed in Chapter 3.

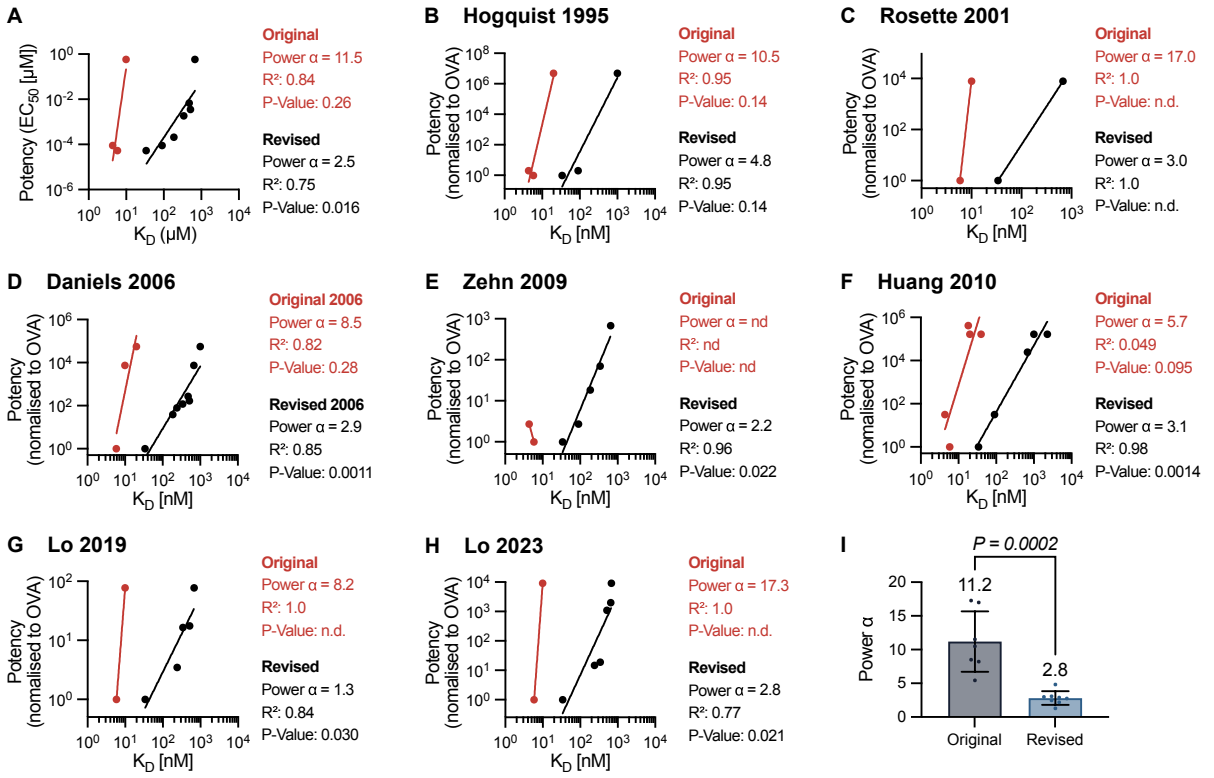

Figure 4.13: Revised Discriminatory Power. Potency data plotted against original K_D data at 25°C published by Alam et al.[128], Rosette et al.[238] and our revised K_D data at 37°C. Data was fitted with power law to obtain discrimination power α. **(A)** Potency-affinity plots with potency obtained as EC_{50} from functional experiments measuring CD69 expression in Fig. 4.12. **(B-H)** Potency-affinity plots with previously published potency data. **(B)** Potency data as P_{10} taken from[127]. **(C)** Potency data as P_{10} taken from[238]. **(D)** Potency data as EC_{50} taken from[114]. **(E)** Potency data as EC_{50} taken from[278]. **(F)** Potency data as EC_{50} taken from[153]. **(G)** Potency data as EC_{50} taken from[243]. **(H)** Potency data as EC_{50} taken from[248]. **(I)** Power α for original and revised K_D.

4.2.6 *Kinetic proofreading model fit*

In Chapter 3 we showed that the kinetic proofreading (KP) model can explain a discriminatory power of 2.0. Additionally, in a recent publication, we fitted the KP model to affinity and potency data obtained for the human 1G4 and A6 TCR to estimate the number of proofreading steps and the proofreading time[246]. The same analysis can be applied to the OT-I data. A simplified kinetic proofreading model was used to fit the affinity-potency data. In the KP model, potency is determined by the lifetime of the TCR-pMHC interaction, determined by k_{off}, rather than by K_D. As we only have K_D values, k_{off} for all peptides was estimated from K_D using $k_{off} = K_D \times k_{on}$, where we assume that k_{on} is identical for all peptides. We use $k_{on} = 1.3 \times 10^5\,M^{-1}s^{-1}$ as determined from kinetic measurements of the N4 pMHC/OT-I interaction (see Fig. 4.2). The simplified kinetic proofreading model contains three fitting parameters; the proofreading rate (k_p), the sensitivity (A), and the number of proofreading steps (N):

$$\text{Potency} = A \times \left(1 + \frac{k_{on} K_D}{k_p}\right)^N \tag{4.1}$$

Fitting the kinetic proofreading model to our functional T cell response produced an ambiguous fit where the values of individual parameters could not be accurately estimated. This often results because the data contains insufficient information to constrain the parameters. We therefore combined our functional data with all published potency data, normalised to cognate peptide N4, to create a larger dataset. Fitting the model to the combined dataset produced an unambiguous fit with N = 6.5 and $k_p = 38\,s^{-1}$. This gives a proofreading time of $\tau_{1/2} = k_p/N = 0.17\,s$.

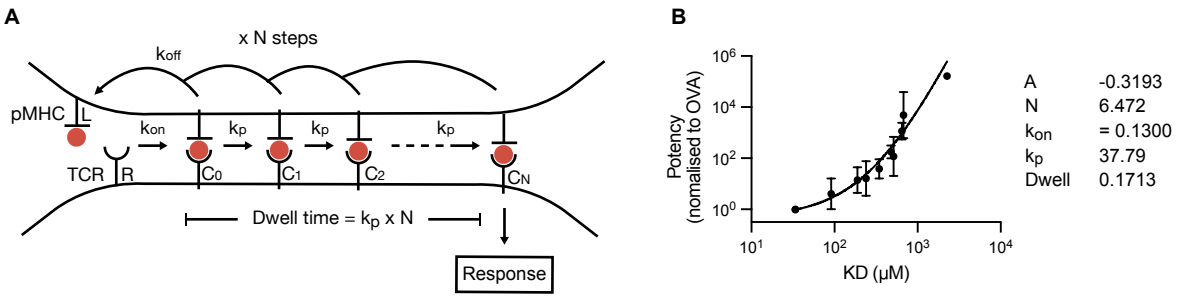

Figure 4.14: OT-I T cells operate kinetic proofreading with a short proofreading time. **(A)** Schematic of the kinetic proofreading model. **(B)** A fit of kinetic proofreading to ligand potency over revised 3D affinity data. The potency is displayed as a fold-change to the highest-affinity N4 pMHC and combines all the potency data from the 7 studies displayed in Fig. 4.13 and the data we generated. Data displayed as mean ± SD for each peptide variant. Best-fit parameters as indicated.

4.3 *Discussion*

The lack of accurate affinities of OT-I peptides at biologically relevant conditions has hindered the development and validation of models that aim to understand how the TCR/pMHC interaction controls T cell activation. Here we provide a comprehensive dataset containing the interaction affinities between the mouse OT-I TCR and a set of 19 peptide variants at 37°C. This dataset contains accurate measurements of self-peptide interactions that can induce positive selection in the thymus. We detect significantly lower affinity for non-activating peptides and self-peptides than previously reported ($K_D > 1000\,\mu M$). This data shows that antigen discrimination by the OT-I TCR is enhanced but imperfect.

OT-I affinity and kinetics

The affinity and kinetics of the OT-I/pMHC-N4 interaction showed an unusual temperature dependence. Whereas previous studies have reported similar or lower K_D values at lower temperatures[206] , the OT-I TCR affinity for N4 increases at higher temperatures. The reduction in K_D at 37°C comes for a strong increase in the k_{on} rate at 37°C compared to 25°C. This temperature dependence of K_D highlights the importance of measuring K_D values at 37°C. We did not observe a biphasic binding with a slow and fast association step at 37°C as described originally. This is in line with other TCR systems measured at 37°C[149,246]. Furthermore, while the affinity of OT-I interacting with its cognate peptide is similar to other TCRs[276],

the interaction shows much faster binding rates than other TCRs. For example, the 1G4 TCR interacting with its cognate pMHC has a 10-fold slower off-rate ($0.3\,s^{-1}$) and a 3-fold slower on-rate[149]. Similarly, off-rates for other TCRs range between $0.1\,s^{-1}$-$0.7\,s^{-1}$ [276]. The faster on-rates for OT-I are indicative of a lower degree of conformational flexibility. These very fast kinetics make it challenging to measure the kinetics of peptides with lower affinity than N4.

Peptide panel

Analysis of OT-I interaction with peptide variants returned a broad range of affinities. The affinities correlate well with functional data and 2D affinities. Our revised K_D values differ significantly from the original measurements, particularly for low-affinity peptides. We believe that this difference may be due to two reasons. Firstly, in the original data, B_{max} was fitted rather than constrained, and this has previously been shown to lead to under-estimates of K_D values[246]. Indeed, fitting K_D values is accurate for interactions with K_D values up to approximately 200 µM[246]. Secondly, the TCR in the original studies were likely aggregated, producing apparently higher binding and hence affinity values. The affinity of OT-I to self-peptides was approximately 50 times lower than to the cognate peptide N4. Out of the four self-peptides, Catnb induces the strongest dulling activity in T cells and also shows the highest affinity of all four measured self-peptides[105].

Regarding the accuracy of low-affinity K_D values, we have performed control experiments to ensure that the affinity is correct. Unrelated proteins, such as ovalbumin, that are not expected to bind to pMHC show minimal binding. We have also shown that the differences in the flow cells contribute a smaller than 5 RU response. However, because low-affinity peptides produce a very low binding response (<50 RU), such small non-specific binding events still can have a significant impact on the overall affinity. In addition, we showed that there is a significant binding of OT-I to denatured pMHC with an affinity of ∼1500 µM. For low-affinity pMHC that have affinity values in the same range, if a population of unfolded pMHC is present on the chip, this can result in lower-than-accurate K_D values. While we confirm that the fraction of correctly refolded peptides is consistent for all pMHCs except E1 and V-OVA, we cannot exclude the presence of a small fraction of unfolded pMHC, which may contribute to the observed binding response. Contribution from non-specific binding and binding to unfolded

pMHC may introduce a systematic error that scales with the K_D values. Overall, we have to assume that there is a larger uncertainty for the measured K_D values of low-affinity peptides.

The lowest measured affinity using our revised protocol was 2.2 mM, which is similar to the lowest affinity measured for the 1G4 and A6 TCR[246]. We speculated that this affinity represents the affinity floor, where the dominant energetic contribution to binding comes from contacts with the MHC, rather than the peptide. This is a direct consequence of positive selection, where TCRs must interact with a high density of ultra-low affinity pMHCs to avoid death by neglect and undergo positive selection.

Discriminatory power

The revised K_D values produce an enhanced discrimination of power (α = 2.9). This is similar to the discrimination power of other mice TCRs[246] and confirms that the OT-I TCR shows an imperfect but still enhanced discrimination.

Imperfect discrimination means low-affinity peptides can activate T cells if presented by MHCs at sufficiently high concentrations. This raises the question of whether self-peptide can activate T cells. Although T cell activation could not be observed when naïve T cells are presented with splenocytes pulsed with a high concentration of self-peptides, T cell activation for self-peptides has been previously reported[248,279] and mutations in the signalling pathway can even increase the response to self-peptides[248]. Furthermore, a T-cell response has been recorded for peptides E1 and R4 that have a similar affinity to self-peptides[127]. This shows that a high expression of self-peptides can activate peripheral T cells. As a result, T cell-mediated autoimmune diseases may be a result of the abnormal expression of high levels of self-pMHCs.

Kinetic proofreading fit

Fitting OT-I affinity-potency data with a KP model estimated 6.3 proofreading steps and a very fast proofreading rate of 37 s^{-1}, resulting in a proofreading time of only 0.17 s.

This is inconsistent with KP parameters published for the human 1G4 and A6 TCR[246] and other receptors[77,148]. For example, the human 1G4 TCR displayed a proofreading time of 2.8 s with under 3 proofreading steps. Several factors may explain the apparent discrepancy

between the OT-I and the 1G4/A6 data. Firstly, we use the assumption that k_{on} is identical for all pMHC when fitting the simplified KP model. If inaccurate, it would result in incorrect k_{off} values, which in turn would influence the value of k_p and hence the proofreading time. Secondly, it is important to consider that soluble OT-I may exhibit a slightly different structure and therefore affinity compared to OT-I expressed on the T cell surface. The soluble OT-I used in the SPR experiments was produced in *E.coli* and refolded *in vitro*. Although the same refolding strategy was used for the 1G4 and A6 TCR by Pettmann et al.[246], we found that the yield of the OT-I TCR refold was less than threefold compared to the 1G4 TCR refold, indicating that the OT-I is less stable than the 1G4 TCR. Additionally, in our OT-I construct, the murine constant domains of the wild-type OT-I were replaced with the human constant domains with an engineered cysteine for increased stability. It has also been shown that TCRs in lipid bilayers have distinctly different conformations to TCRs in detergent[32]. Therefore a soluble OT-I lacking a transmembrane domain may have a different conformation compared to a membrane-bound OT-I. Considering these modifications, it is uncertain if the conformation of the soluble OT-I used for affinity measurements mirrors that of the OT-I TCR expressed in functional T cell experiments. Another thing to note is that the SPR experiments do not measure the contribution of CD8 to affinity, which has been shown to stabilise low-affinity peptide-TCR interaction[86]. The reasons for the discrepancy could also be that discrimination is different in mouse and human cells or even between the OT-I and other TCRs For example, a catch bond has been reported for OT-I, both using a cellular assay[154] and protein-based assay[157]. This catch bond increases the affinity under force and therefore the affinity observed by the TCR on T cells is not the same as the affinity measured in SPR. This catch bond behaviour appears to be the exception instead of the norm, as other TCRs do not display any catch bonds[157,280]. We also observe that OT-I TCR is very sensitive compared to other TCRs. Even though the K_D value for its cognate peptide is about 5-fold lower than for the human 1G4 TCR, OT-I has similar if not lower potency values, which could be attributed to a catch bond.

Future implications

The findings of this study have important implications for advancing our knowledge of TCR interactions, T-cell activation and tolerance.

Firstly, the comprehensive characterisation of the OT-I system on affinity and function for various peptides at physiological conditions provides important data for future studies. Considering the frequent usage of the OT-I system in experiments, we are hoping that this dataset will be valuable to the research community. For example, the data can be used to evaluate models of T cell activation and signal transduction, improving our understanding of how T cells sense and respond to environmental signals. A significant aspect of the research lies in providing affinity values for the interaction of TCR with self-peptides. This data may shed light on the mechanisms behind positive selection in the thymus and peripheral proliferation of T cells. This information is crucial for unravelling the dynamics of T cell development and immune tolerance. This may inform strategies for modulating immune responses in various disease contexts, including autoimmune diseases and T cell based cancer therapies.

The provided affinity data could also be useful for identifying TCR targets. There is a considerable interest in using machine learning methods to predict TCR/pMHC specificity from TCR sequences. Being able to extract from the TCR repertoire which targets the T cells can bind, holds immense potential for diverse applications, including vaccine development, cancer therapy, and diagnostics. However one of the main challenges for an accurate prediction is the lack of high-quality negative data[281]. Most of the TCR/pMHC binding data used as input for the prediction algorithms has been obtained by using pMHC tetramers to identify specific TCRs. However, this method only captures true-positive TCR-pMHC pairs and not true-negative pairs. Therefore negative data is generated artificially, which introduces a bias to the data set and leads to inaccurate predictions. K_D values measured by SPR provide a quantitative measure of interaction strength, providing data on true low-affinity interactions, which could improve the predictive power of the algorithms.

However, the work also highlights the need for further characterisation of the OT-I TCR, for example, by solving its structure. It is concerning that the potency affinity relationship model described by the kinetic proofreading model does not align with the parameters measured for other TCR systems. Given the widespread use of OT-I as a standard mouse model, we should make sure that it functions like the standard and is not an exception to the norm. This emphasises the need for continued scrutiny and validation of commonly used models to maintain the reliability and consistency of experimental outcomes.

5

QUANTIFYING THE BIVALENT BINDING OF ANTIBODIES

5.1 *Introduction*

Antibodies are vital components of our adaptive immune system. They bind to antigens on the surface of pathogens, such as viral and bacterial glycoproteins or toxins. This binding leads to the direct neutralisation of the pathogens or the activation of immune responses. Additionally, due to their high specificity for their antigen, antibodies have been exploited for clinical diagnosis and treatment[282]. Their importance in fighting infections became particularly clear during the COVID-19 pandemic. High levels of neutralising antibodies strongly correlate with positive disease outcomes[283]. Convalescent plasma therapy, where patients receive plasma from recovered individuals containing antibodies, was one of the first treatments to show improved disease progression[284?]. Since then, several potent monoclonal antibody therapies have been developed and approved[285]. Furthermore, SARS-CoV-2 antibodies have been crucial for developing diagnostic tests, allowing the rapid detection of COVID-19 infections.

The majority of antibodies are bivalent molecules able to simultaneously bind two antigens. However, certain antibody isotypes can be associated with generating higher-valency structures, such as IgA or IgM that are tetravalent (4) and decavalent (10), respectively. Here we focus on the bivalent binding of IgG antibodies, which have two binding sites.

The function of antibodies is highly dependent on two factors: a strong affinity to their antigen and the ability to reach two antigens for bivalent binding. The importance of bivalent binding can be seen when comparing the neutralisation strength between IgG antibodies and their corresponding monovalent fragment antigen-bindings (Fabs). Even though IgGs and their corresponding Fabs have the same affinity to the antigen, IgGs exhibit up to 1000-fold

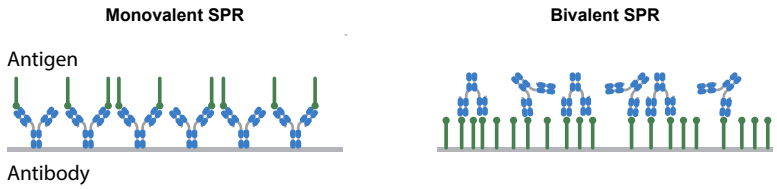

Figure 5.1: SPR configuration for measuring monovalent or bivalent antibody binding. For monovalent binding, antibody is immobilised on the SPR sensor chip and antigen is injected. For obtaining bivalent binding data, the configuration is revered; antigen is immobilised and antibody is injected

higher neutralisation potencies[286]. Indeed, the monovalent Fab/antigen affinity does not correlate well with neutralisation potency, indicating that other factors of the antigen-antibody interaction influence neutralisation[287]. A detailed understanding of bivalent binding may enable the identification of factors that influence antibody function. This is critical for the understanding of the initiation of immune responses and rational vaccine design.

Studying antigen-antibody interaction with SPR can help us to understand the dynamics of the interaction. Monovalent antibody-antigen binding affinities are typically obtained by immobilising the antibody on the surface of the SPR chip, while the soluble antigen is injected as an analyte (Fig. 5.1 left). In this configuration, the antigen binds to the antibody monovalently; an antigen can bind to a free binding site on an antibody with an association rate ('on rate', k_{on}), forming an antigen-antibody complex. Following binding, the antigen can unbind with a dissociation rate ('off rate', k_{off}). For monovalent interactions, these SPR binding curves can be fitted with a two-state well-mixed ordinary-differential-equation (ODE) binding model that provides estimates for k_{on} and k_{off} rates from which the dissociation constant (K_D) is calculated ($K_D = k_{off}/k_{on}$).

To study the bivalent interaction between antigen and antibody, the experiment setup can be reversed; the antigen is immobilised on the surface of the SPR chip, while antibodies are injected. Each antibody can bind to two antigens (Fig. 5.1 right). In the first binding step, an antibody in solution can bind with either arm to an immobilised antigen with an association rate k_{on} to form a one-antigen-antibody complex. The complex can revert back to free antigen and antibody with a dissociation rate k_{off}. The rates k_{on} and k_{off} are the same as the binding rates measured in the monovalent interaction. In a second binding step, the antibody in the complex can bind a second antigen with its free arm if the antigen is within the reach of the antibody. Bivalent binding models that are based on ordinary differential equations (ODEs)

have been previously reported for fitting bivalent antigen-antibody binding data. However, bivalent binding is a complex stochastic and spatial reaction, therefore ODEs that report the average behaviour of a large, well-mixed system, are ill-suited for quantifying bivalent binding.

In this chapter, I will describe a stochastic and spatial model, that can fit bivalent SPR antibody binding data and estimate both monovalent and bivalent binding parameters that fully describe a soluble bivalent antibody interacting with an antigen surface. Using this model we have developed a pipeline that quantifies antibody binding from high-throughput SPR experiments. Here, we test the pipeline using 80 antibodies that bind to the receptor binding domain (RBD) of the SARS-CoV-2 spike protein. The identified bivalent binding parameters allow us to understand what determines the ability of an antibody to bind bivalently. Finally, we use the model to predict the neutralisation potency of the antibodies.

5.2 *Results*

5.2.1 *Spatial and stochastic particle-based model*

To allow accurate fitting of bivalent SPR data, we developed a particle-based bivalent binding model that takes the spatial and stochastic aspects of the antibody-antigen interaction into account.

Firstly, the ODE-based bivalent model assumes that all interaction partners are well mixed, this means the antibody can bind any antigen with equal probability. However, this is not the case in the second binding step when the antibody is already bound to one antigen. The binding of the antibody to a second antigen in the second binding step can only happen if the second antigen is within the molecular reach of the antibody, defined by the maximal distance two antigens can be spaced apart for the antibody to still bind them simultaneously. We implement the spatial dependency of binding by using a spatial model. The algorithm generates a 3D space where a fixed number of antigens are randomly distributed. The molecular reach is defined by the radius of a sphere around the antibody, within which binding to two antigens is possible (Fig. 5.2 left, antibody reach depicted as a grey circle). All antigens within the sphere have the same probability of binding. In total, the particle-based model contains four parameters characterising the antibody-antigen binding interaction: the monovalent association

and dissociation rates k_{on} and k_{off}, which determine the affinity between the one antibody binding site and the antigen epitope; the bivalent association rate $k_{on,b}$ (in units s^{-1}) describing the rate at which the antibody bound to one antigen can bind a second antigen within reach; and molecular reach (in units nm). The model also included a constant of proportionality (C_p) to scale the antibody concentration to the response units.

Secondly, while the resulting SPR trace represents the average binding dynamics of a large number of interactions, the total number of interaction partners for each antibody is low, as the number of possible binding partners in the second binding step is limited to the antigens within an antibody's molecular reach, and will approach zero as more antibodies bind to the SPR surface. This low number of free antigens on a local scale leads to stochastic interactions that are not accounted for in the ODE model. In our model, the stochasticity of the interactions is implemented by using a Gillespie algorithm that simulates individual interactions of antibodies in the 3D space (Fig. 5.2 middle). The Gillespie algorithm is a widely used algorithm for stochastic simulation.

When using stochastic simulation, fitting a five-parameter model directly to the SPR traces is computationally expensive: We would need to search a high-dimensional space and try many thousands of different parameter vectors. The algorithm simulates the model for each parameter vector many times to obtain an averaged response and compares it with the experimental data. As a result, directly fitting stochastic models to experimental data is computationally challenging. To reduce fitting time, a surrogate model is used. A surrogate model contains pre-simulated SPR curves for any combination of parameters within a set range (Fig. 5.2 right). These previously produced curves can be used to interpolate what an SPR trace would look like for any new set of parameters that we have not simulated explicitly. This removes the need for simulating the curve for every parameter and reduces the fitting time to minutes.

Simulations of the model show the importance of molecular reach for bivalent binding. We perform forward simulations to predict SPR binding traces using the same biochemical parameters (k_{on}, k_{off}, and $k_{on,b}$) but with increasing reach (Fig. 5.3 bottom). We produced a 2D representation of our model reaction volume to visualise the impact of reach on antigen-antibody interactions (Fig. 5.3 top). Each antigen in the reaction volume is plotted as a circle, with the radius of the circle equal to the molecular reach. If the circles of two antigens overlap, they are close enough together for an antibody to be simultaneously bound by the same bivalent antibody. When we simulate the binding of antibodies with a small reach of 2.0 nm, none of

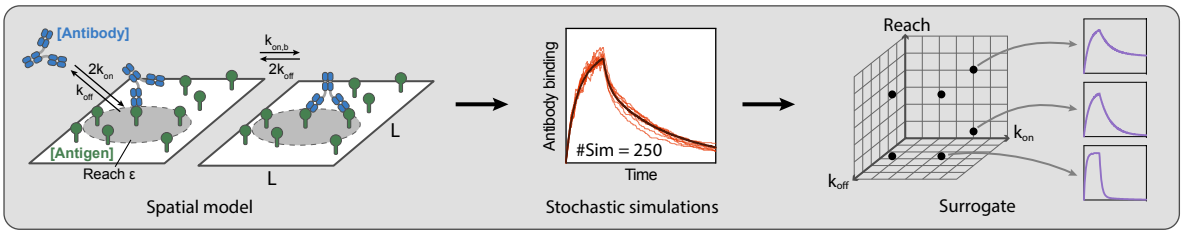

Figure 5.2: Workflow for fitting the particle model to bivalent SPR data. A schematic of the particle-model chemical reactions (left) used to perform simulations of the association and dissociation phase of antibody binding in bivalent SPR (middle, red traces), which are averaged to produce the predicted SPR trace for a given parameter set (middle, black traces). These averaged SPR traces are pre-tabulated for different parameter values (k_{on}, k_{off}, $k_{on,b}$, reach) using a computing cluster to produce a surrogate for the particle-based model that is used in data fitting (right). The particle-based model was developed by Samuel A. Isaacson and Daniel B. Wilson.

the circles overlap, and the antibody cannot bind bivalently to any antigen. The simulated SPR trace shows monovalent binding, with a quick dissociation time. A reach of 10 nm increases the fraction of antigens on the surface that can be simultaneously bound by the same bivalent antibody, which is reflected in an increase in dissociation time. When the antibody has a large reach of 30 nm, all antigens are available for bivalent binding, resulting in very slow dissociation. This shows that the molecular reach determines the average number of antigens that are available for the antibody to bind to bivalently at a given antigen concentration. Thus, increasing the molecular reach results in longer dissociation times because antibodies continue to rebind to antigens within reach on the surface.

5.2.2 *Validation of model produces correct monovalent binding parameters*

Next, we set out to validate that the particle-based model returns accurate binding parameters. We used the FD11A antibody, an IgG1 antibody which binds to the RBD of the SARS-CoV-2 spike protein. We first generated monovalent SPR data by injecting soluble RBD at multiple concentrations over a surface coated with the FD-11A antibody (Fig. 5.4A and B, left). All curves were simultaneously fitted with an ODE-based monovalent model, returning estimates for k_{on}, k_{off}, and K_D (Fig. 5.4C, red circles).

For bivalent SPR data, RBD is immobilised to the chip surface and FD-11A is injected with increasing concentrations. (Fig. 5.4A, centre and right). Fitting an ODE-based bivalent model which is included with the SPR fitting software to this data, returns inaccurate values for k_{on},

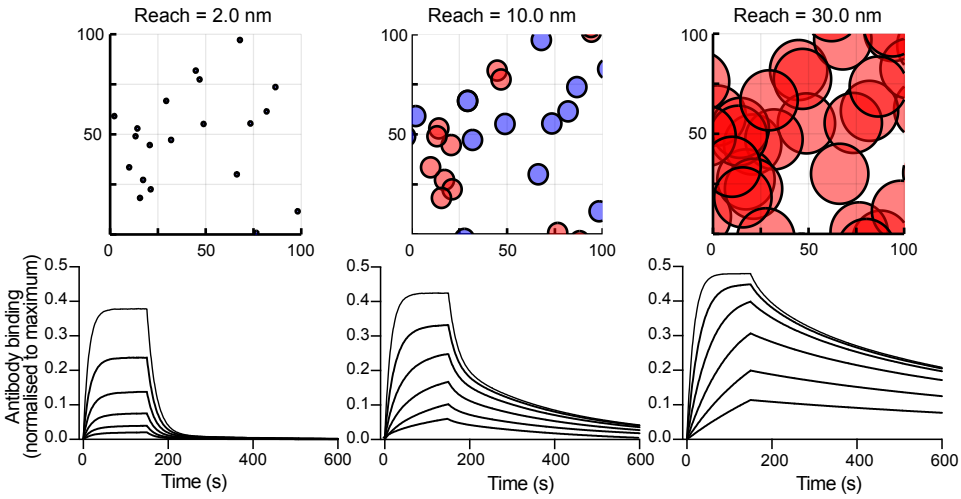

Figure 5.3: The molecular reach determines the amount of bivalent binding. Particle-model simulation of SPR binding curves (bottom) for antibodies with different values of molecular reach injected over randomised antigen distribution (top). Antigens are depicted as circles, the size of the circle scales with the reach. Two antigens within reach can be bound bivalently by the antibody (overlapping red circles), antigens outside of reach are bound monovalently (blue circles). The reach determines the number of antigens that can be bound bivalently. Parameter values: k_{on} = $0.05\mu M^{-1}s^{-1}$, k_{off} = $0.05s^{-1}$, $k_{on,b}$ = $1.0s^{-1}$, and [RBD] = 0.0025 nm^{-2}.

k_{off} and K_D (Fig. 5.4C, purple circles). These experiments show that the ODE-based bivalent model is insufficient to fit complex bivalent interactions.

Next, we fitted the particle-based model to the same dataset. The particle model produces an excellent fit (Fig. 5.4B right). We found that the particle model returns the same values for k_{on}, k_{off} and K_D as obtained from the monovalent SPR experiment (Fig. 5.4C, dark blue circles). Furthermore, the model also returns the bivalent interaction parameters $k_{on,b}$ and estimates a molecular reach of 35 nm (Fig. 5.4D).

To confirm that the parameters do not depend on antigen density, we plotted parameter values for FD-11A, obtained from multiple repeats against the RBD concentration (Fig. 5.5). There is no correlation for any of the parameters for the antigen concentration range we used (< 20 µM).

To further validate the particle model, we repeated the analysis above for four other IgG1 antibodies binding RBD. We confirmed that the particle model correctly returns parameter values for k_{on}, k_{off}, and K_D across a 100-fold variation (Fig. 5.6A). The bivalent parameters for the other antibodies are similar to FD-11A, with $k_{on,b}$ around $1s^{-1}$ and an average molecular reach of 38 nm (Fig. 5.6B). Our findings demonstrate that the particle-based model accurately quantifies the bivalent binding dynamics of antibodies.

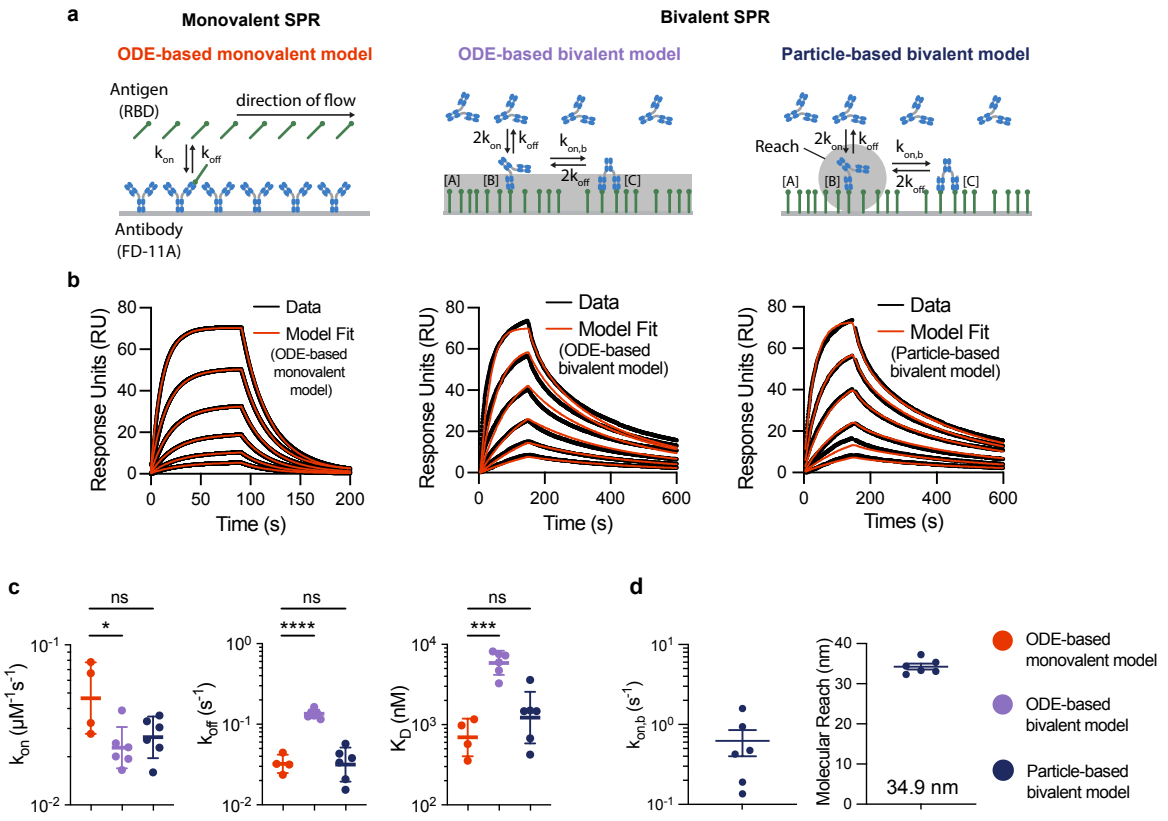

Figure 5.4: Particle-based model returns correct monovalent interaction parameters for FD-11A antibody. **(A)** Schematic of SPR experiment setup for monovalent (left) or bivalent (middle, right) SPR. For monovalent SPR, the antibody is immobilised on the chip surface and antigen is injected. The resulting SPR binding curves are fitted with an ODE-based monovalent model, returning parameters k_{on} and k_{off}. For bivalent SPR, the antigen is immobilised with the antibody being injected. ODE-based bivalent models assume all antigens are equally accessible in the second binding step (grey-shaded region), whereas, in the particle model, only antigens within reach (grey circle) can be bound. **(B)** Representative SPR traces for FD-11A antibody binding RBD of SARS-Cov-2 (black) with respective fit with the indicated model (red). SPR traces were generated by a 2-fold dilution of RBD starting at 2000 nM (left) or by a 2-fold dilution of FD-11A starting at 300 nM (middle, right - same data but different model fit). **(C)** Parameters k_{on}, k_{off} and K_D for FD-11A from monovalent SPR (N=4) or bivalent SPR (N=6), fitted with ODE-based bivalent model or the particle-based model. For statistical comparisons, a One-way ANOVA test was performed on the log-transformed values using Dunnett's test for multiple comparison correction. **(D)** Best fit parameters kon,b and molecular reach L returned by the particle model for FD11A antibody. Abbreviations: * = p-value$\leq$0.05, ** = p-value$\leq$0.01, *** = p-value$\leq$0.001, **** = p-value$\leq$0.0001. SPR data in this figure and all following figures was generated by Mikhail Kutuzov.

5.2.3 *Molecular Reach is determined by antibody and antigen size*

An average reach of 38 nm returned by the particle model for anti-RBD antibodies is surprisingly large in comparison to previous studies that attempted to measure the molecular reach of antibodies. Three studies, using DNA origami to separate antigens at defined distances and measuring the impact of increasing antigen separation on antibody binding, reported the

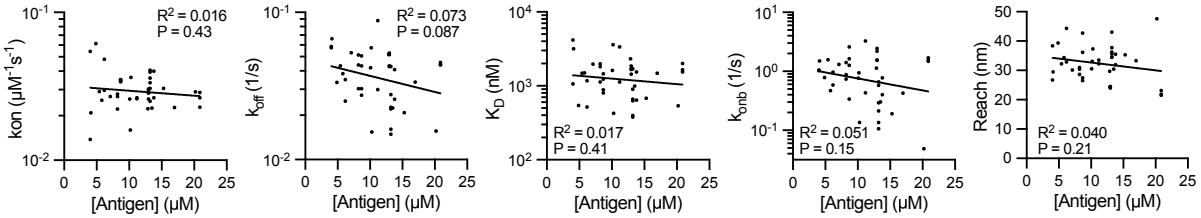

Figure 5.5: The fitted binding parameters are independent of the RBD antigen density. Parameters for the IgG FD-11A antibody binding RBD were determined by fitting the particle-based model to bivalent SPR data. The indicated parameter is plotted over the RBD antigen density ($N = 42$). The coefficient of determination (R^2) and the p-value for the null hypothesis that the fitted line and a horizontal line (i.e. no relationship between the binding parameter and RBD density) produce an equal fit to the data.

strongest IgG1 antibody binding when antigens were spaced between 10 and 16 nm apart, suggesting a maximum molecular reach of 17 nm for IgG1 antibodies[171,288,289]. Similarly, using crystal structures of IgG1 antibodies to measure the centre-to-centre distance between the antigen-binding sites of the two Fabs, suggests a molecular reach of 10-15 nm[287]. How can this discrepancy be explained? We noticed that one of the main differences in our experiments compared to these previous experiments is the size of the antigen used. Previous studies have used antigens smaller than 1 kDa (e.g. digoxin with a molecular weight of 780 Da[289], NIP-hapten with 320 Da[171], or 6x His-Tag with 1100 Da[288]). SARS-CoV-2 RBD in comparison has a molecular weight of 51.5 kDa, more than 50-fold larger than antigens used in previous studies.

We hypothesise that the size of the antigen contributes to the molecular reach. That means if we use an antigen of $\sim$ 1 kDa in size, the particle model should return a similar reach of 10 nm-16 nm as observed in previous studies. To test this hypothesis, we used an antigen that consists of a small peptide with phosphorylated tyrosine residues (p-Tyr) coupled to a Polyethylene glycol polymer of 3 molecules (PEG3) (Fig. 5.7A). The total molecular weight is 2230 Da. To show the direct influence of the antigen length on reach, we elongated the antigen by using a longer PEG polymer of 28 molecules (PEG28). The worm-like-chain (WLC) model can be used to estimate the length of the PEG linkers using the following formula: $2\sqrt{(N_{\mathrm{PEG}} l_c l_p)}$[290] where N_{PEG} is the number of PEG repeats, l_c is the contour length of each repeat (0.4 nm), and l_p is the persistence length of PEG (0.4 nm[291]). We get an average end-to-end linker length of 0.69 nm for PEG3 and 2.1 nm for PEG28.

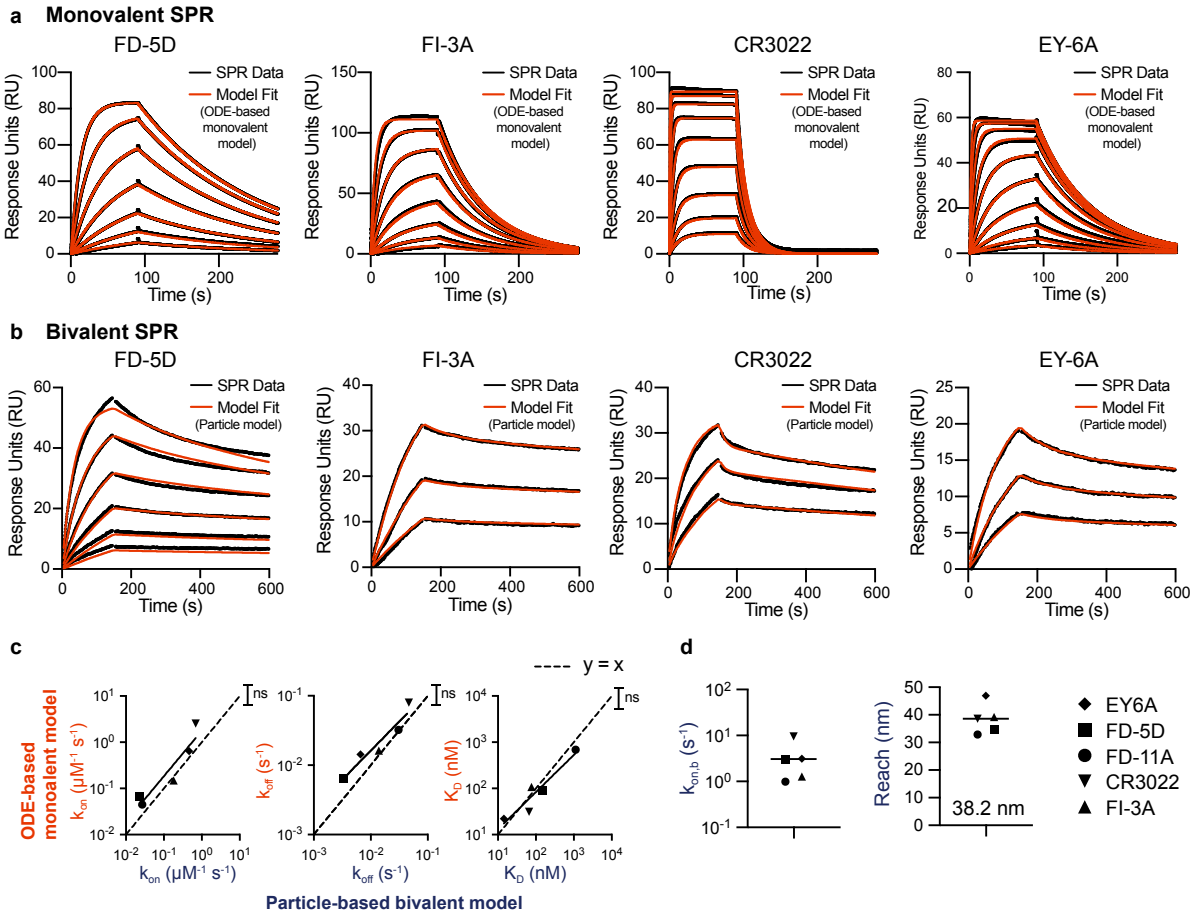

Figure 5.6: Validation confirmed with 5 other antibodies. **(A)** Representative monovalent SPR traces produced by injecting RBD (2000 nM with 2-fold dilutions) over surfaces immobilised with the indicated antibody. **(B)** Representative bivalent SPR traces produced by injecting the indicated antibodies over surfaces immobilised with RBD. Antibodies were injected using a 2-fold dilution series, with a top concentration of 300 nM, 5 nM, 5 nM, 5 nM, 5 nM for FD-5D, FI-3A, CR3022, EY-6A and REGN10987 respectively. RBD was immobilised at 7 - 15 μM. **(C)** Correlation of parameters k_{on}, k_{off}, K_D either obtained from monovalent SPR or bivalent SPR fitted with the Particle-based model for 5 antibodies binding RBD of SARS-CoV-2. Log transformed values were fitted with a linear line and tested on whether the slope differs from the line of identity (dashed line, y=x) using an F-test. **(D)** Best fit parameters $k_{on,b}$ and molecular reach for all 5 antibodies.

We used a commercial anti-p-Tyr antibody (PY20) to generate bivalent SPR binding curves for both PEG3-pTyr and PEG28-pTyr with varying antibody and antigen concentrations (Fig. 5.7B). For PEG3-pTyr, we measure a molecular reach of 10.2 nm (Fig. 5.7C, D), in line with previous reports that used small antigens, validating the reach calculation by our model. For PEG28-pTyr we measure an increased reach of 13.5 nm. We can calculate the theoretical difference in molecular reach using the estimated linker lengths. The predicted difference of 2.85 nm agrees well with the measured difference of 3.4 nm (Fig. 5.7E). We also observed an impact on k_{off}, K_D, and k_{on},b between PEG3 and PEG28, even though the binding epitope is the same for

both molecules. These differences may be associated with entropic changes which are often important in molecular binding to flexible polymers[292].

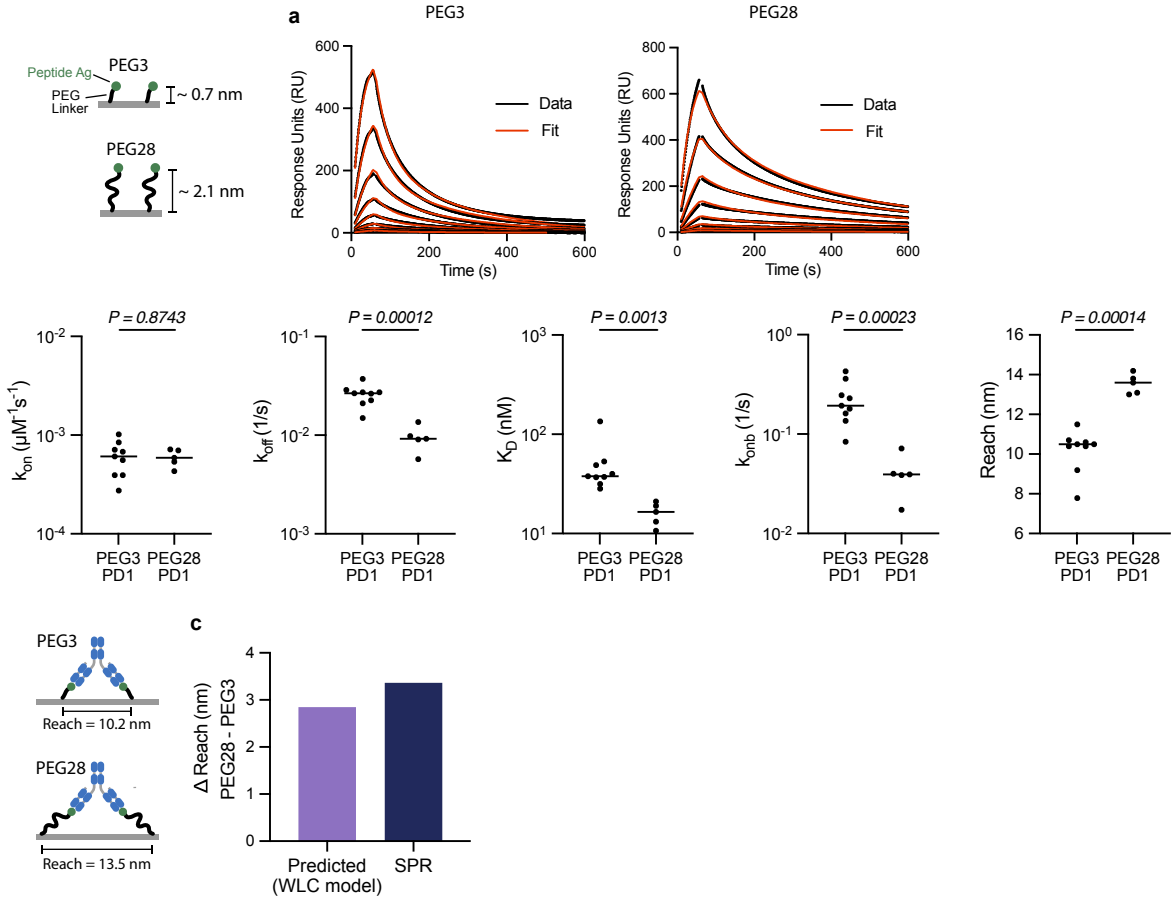

Figure 5.7: SPR of pegylated linker antigen shows dependence of reach with antigen size. **A)** Schematic of PEG antigens: phosphorylated tyrosine residues (green) linked to a PEG linker with either 3 amino acids (PEG3) or 28 amino acids (PEG28). Size of PEG linker is estimated with a worm-like-chain model. **(B)** Representative SPR traces of anti-phosphotyrosine antibody (PY20) injected of immobilised PEG3 or PEG28 antigen. The antibody was injected at 8 concentrations (25 nM with 2-fold dilutions). **C)** Best fit parameters ($N = 9$ for PEG3, $N = 5$ for PEG28). **D)** Comparison of theoretical difference in reach calculated using linker length and the measured difference.

5.2.4 *Molecular dynamic simulation confirms the impact of antibody and antigen size on molecular reach*

To determine if 38 nm is a reasonable molecular reach for RBD antibodies, we employed coarse-grained steered MD simulations. A model of antibody binding two RBD molecules was constructed. In the course of the simulations, RBD was moved away from the antibody at a constant velocity, leading first to a stretching of the antibody, before the proteins detached. We

defined the molecular reach as the distance between RBDs at the point of RBD detachment (Fig. 5.8A). MD simulations were run for 6 RBD antibodies for which a structure was published: FD-11A FD-5D, REGN10987, CR3022, EY6A, and FI3A. The MD simulations return a very similar reach as measured by SPR, with absolute differences in reach being smaller than 7 nm (Fig. 5.8B, C).

When excluding RBD from the measurement of molecular reach, by measuring the maximum distance between the two antigen binding sites of the antibody, we obtain a molecular reach of 18 nm. This is close to the reach that was previously reported and the reach obtained from the PEG experiments.

The MD simulations together with the PEG experiment show that both antibody and antigen size contribute to the total molecular reach. This has an important functional consequence. Larger antigens can be spaced further apart on a surface than smaller antigens but still allow the same amount of bivalent binding.

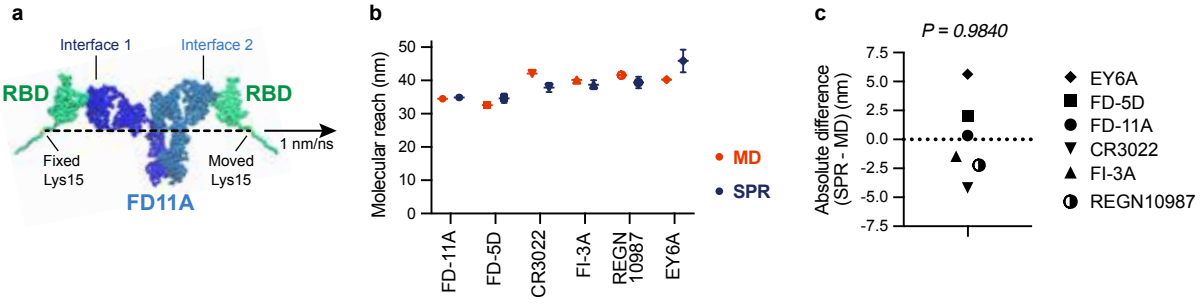

Figure 5.8: MD simulation confirms molecular reach. **(A)** Setup of molecular dynamic simulations. Structure of IgG1 FD-11A bound to two RBD antigens indicating the Lys15 biotinylation site (within an N-terminus AviTag), which anchors RBD to the SPR surface. The anchor point of RBD forming interface 1 was fixed while the one forming interface 2 was moved at a constant velocity. **(B)** Comparison of molecular reach estimated by MD simulation or SPR experiment. **C)** Difference between reach estimates in (B). A one-sample t-test is used to determine the p-value for the null hypothesis that the mean is 0.MD simulations were performed by Daniel Nissley.

5.2.5 *High throughput screen of 80 Covid antibodies*

We have demonstrated that the particle-based model accurately estimates the binding parameters obtained from bivalent SPR data. Subsequently, our objective was to employ the algorithm to measure binding parameters for numerous antibodies binding to the same antigen in a high-throughput screen. With monovalent SPR, conducting a high throughput screen to

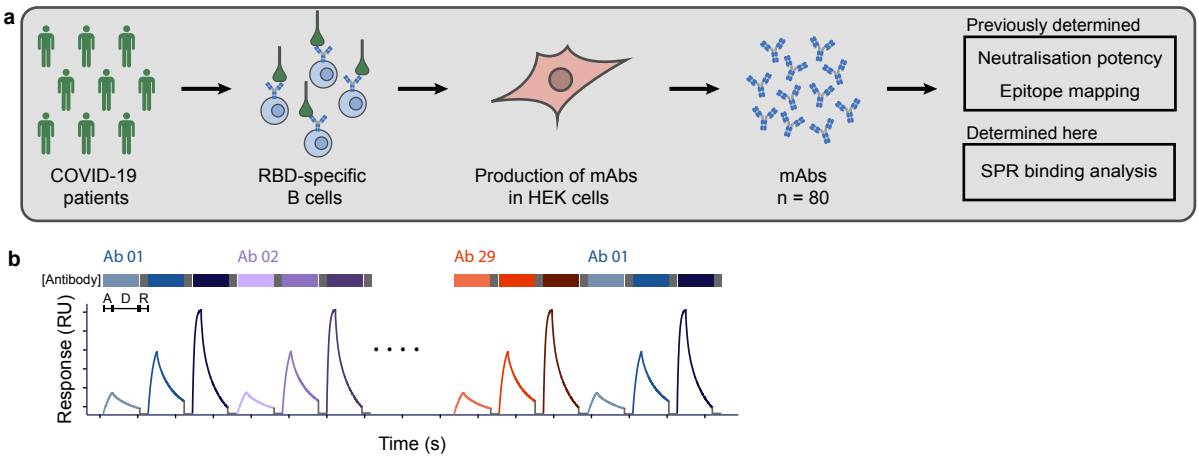

Figure 5.9: Setup of high throughput antibody screen. **(A)** Schematic for monoclonal antibody generation from COVID patients. **(B)** Workflow for high-throughput antibody screen. Antibodies are injected consecutively with three increasing concentrations. For quality control, the first antibody was injected again at the end of the experiment.

measure antibody affinities against the same antigen is not feasible, because each antibody has to be immobilised individually on a fresh chip surface, which prevents automated screening. Conversely, by generating bivalent SPR data, it becomes possible to immobilise the antigen once and subsequently inject multiple antibodies sequentially over the same antigen, eliminating the need for immobilising new antibodies.

To set up the antibody screen, we used IgG1 antibodies that bind to RBD of SARS-Cov-2, previously characterised by Dejnirattisai et al.[286]. The antibodies were obtained from convalescent COVID-19 patients. B cells from patients were selected for RBD-specific binding based on strong interaction with RBD. Antibody sequences of selected B cells were identified and subsequently expressed as monoclonal antibodies in HEK cells. The antibodies had been characterised based on their neutralisation potency and their binding epitope location on RBD (Fig. 5.9A). For the high throughput SPR, we immobilised RBD between 3 μM and 20 μM on the SPR chip surface. Antibodies at 3 different dilutions are injected sequentially. Each antibody injection is followed by a regeneration step to ensure the remaining antibodies unbind from the surface. Buffer is injected in between antibodies for double referencing (Fig. 5.9B). We generated data for up to 32 antibodies at a time, which required approximately 48 hours to run. In total, we screened 80 antibodies.

The long runtime of the SPR experiment (up to 48 hours), and the regeneration step after each injection may cause the antigen to denature throughout the experiment. We therefore needed to verify that RBD on the surface is stable throughout the SPR run and that its binding

capability is not lost. To analyse RBD stability we injected the FD-11A as both the first and last antibody of the SPR run and measured its maximum binding response in both runs (Fig. 5.10A). By calculating the ratio between the first and last maximum response, we then obtained the fraction of surface binding remaining at the end of the run (Fig. 5.10B). Most runs had over 90% of the surface remaining at the end of the run. We discarded any runs that had less than 90%.

During SPR data processing, we applied several selection criteria to the SPR data. SPR runs were excluded based on one of the following criteria (Fig. 5.10C-G):

NO SURFACE REGENERATION All antibodies were tested beforehand if the surface could be completely regenerated after the antibody bound. Any antibodies that remained on the surface after the regeneration step were not included in our screen (N=7) (Fig. 5.10E).

POOR PARTICLE MODEL FIT The particle model needed to show a good fit to the experimental SPR curves (N=12) (Fig. 5.10F).

EQUAL MONOVALENT FIT Each antibody injection was fitted both with the particle model and a monovalent interaction model. If the monovalent fit produced an equally good fit, there is not enough information in the dataset to conclusively determine bivalent binding parameters (N=16) (Fig. 5.10G). This may be the case if k_{off} is very strong and the antibody does not unbind.

Applying these exclusion criteria, we were left with 45 antibodies with reliable estimates of k_{on}, k_{off}, K_D, $k_{on,b}$ and reach (Fig. 5.11). Antibody affinities showed a 1000-fold variation ranging from 5 nM to 2 µM, largely determined by the off-rate of the antibody. The lowest affinity we observe in our dataset is K_D = 2000 nM. For most antibodies, the $k_{on,b}$ is about 100-fold faster than k_{off}, suggesting that a monovalent antibody/antigen complex is more likely to bind to another antigen within reach (provided one is available) rather than dissociate. The average reach is 35 nm, confirming our previous reach measurement of 38 nm, but we also identified antibodies with molecular reach values as low as 20 nm.

Analysing the correlation between parameters using the Pearson correlation coefficient showed a strong correlation between K_D and molecular reach (Fig. 5.12). This is consistent with previous work suggesting that antibodies with higher affinity can accommodate larger antigen distances when binding bivalently[171].

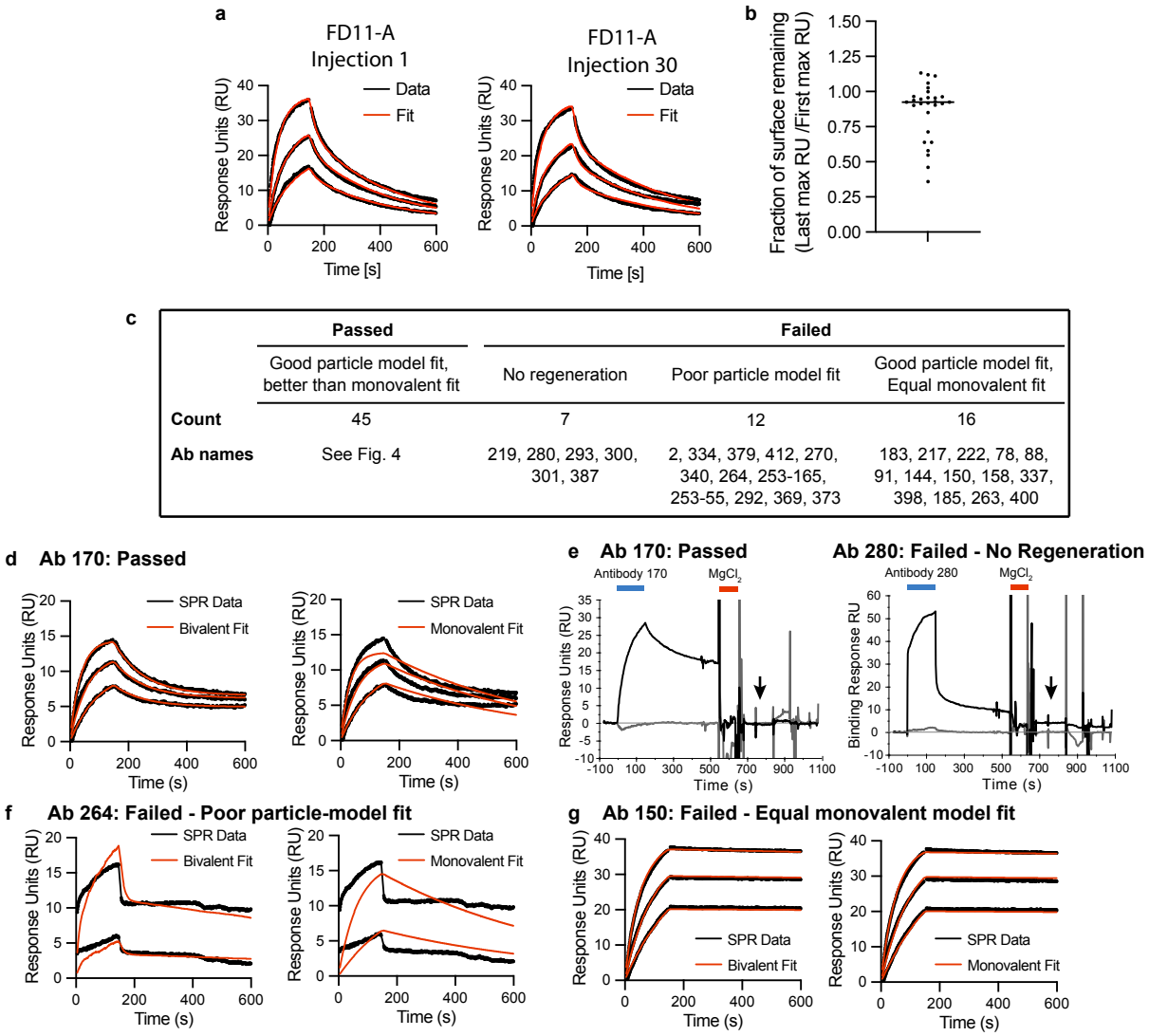

Figure 5.10: Quality controls for high throughput analysis of 80 RBD antibodies using bivalent SPR. (A-B) Surface stability of RBD was assessed by injecting FD-11A at the beginning and end of each experiment. Representative SPR traces of the first and last injection of FD-11A (A) and fraction of FD-11A binding at the end of the experiment (B). The fraction is calculated as the RU at 150 s after injection of the highest concentration in the first divided by the last injection. **(C)** A summary of the antibodies that passed or failed quality control and hence included or excluded from the analysis, respectively. **(D-G)** Examples of antibodies representing the four possible quality control outcomes. **(D)** The antibody 170 was included because the particle model produced a good fit and the monovalent model produced a poor fit. **(E)** The antibody 170 displays complete regeneration (included) whereas antibody 280 shows only partial regeneration (excluded). Partial regeneration can be observed by residual RU after the injection of 3 M $MgCl_2$ for 90 s at the end of each SPR cycle (see arrow). **(F)** The antibody 264 was excluded because the particle model produced a poor fit. **(G)** The antibody 150 was excluded because the particle-based model (left) and the ODE-based monovalent model (right) produced an equally good fit.

5.2.6 *Bivalent binding parameters and epitope distance explain neutralisation potency*

Previous reports have found no or low correlation between neutralisation potency and antibody affinity. We also observed only a weak correlation between neutralisation IC_{50} and monovalent

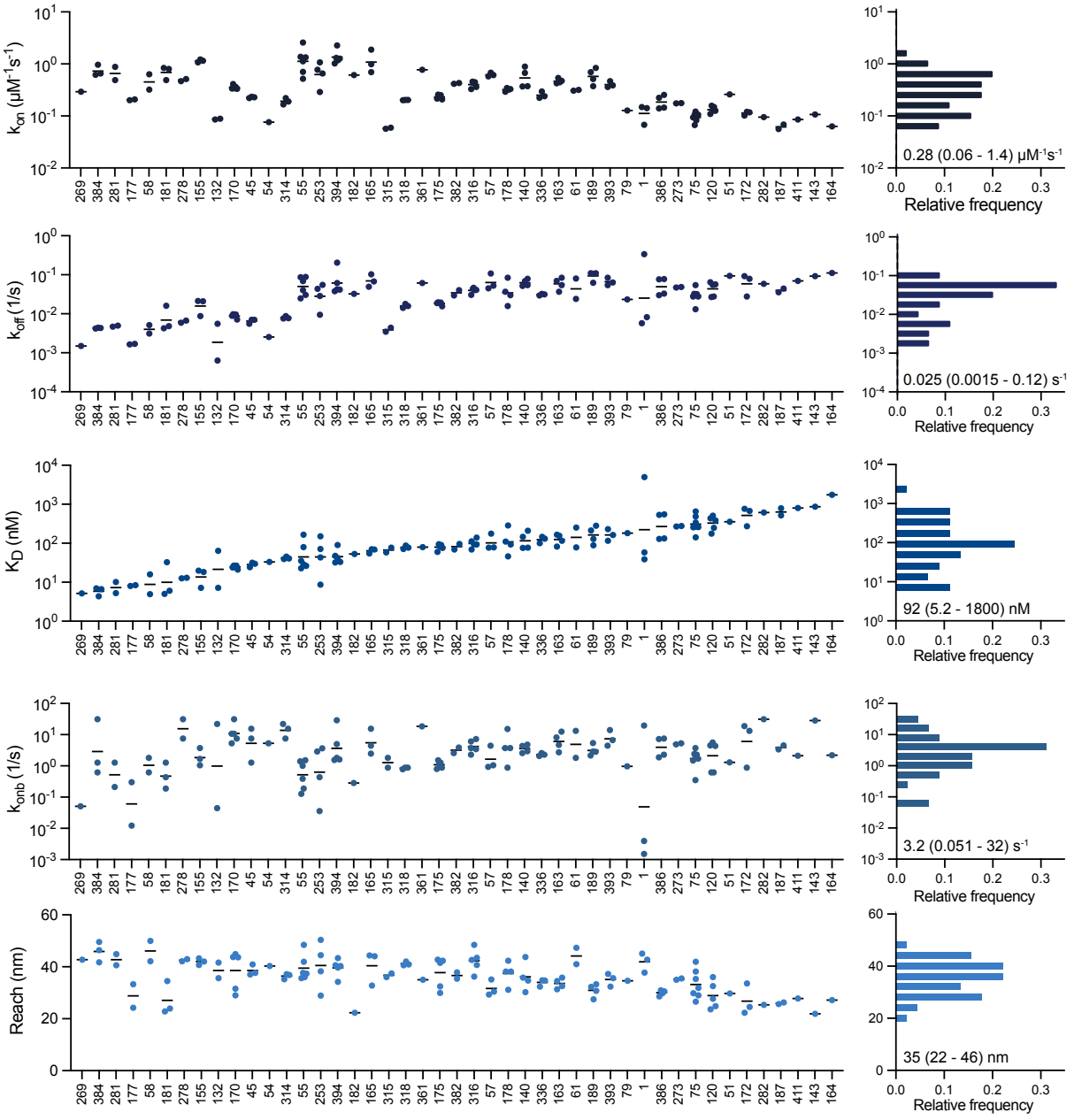

Figure 5.11: Antibody parameters obtained from high throughput screen. Complete set of parameters from 45 antibodies, ordered by affinity. The distribution of parameters is displayed on the right, with mean parameter value and range of parameters indicated.

parameters k_{on} and K_D and no correlation with k_{off} (Fig. 5.13A-C). Considering that the binding parameters likely independently contribute to neutralisation, we conducted a multi-linear regression incorporating k_{on}, k_{off}, and K_D to assess if these monovalent parameters collectively predict neutralization IC_{50} (Fig. 5.13D). The correlation remained weak, suggesting that monovalent binding parameters alone inadequately explain neutralization potency.

Next, we explored whether the bivalent binding parameters $k_{on,b}$ and molecular reach can improve the correlation with neutralization IC_{50}. While $k_{on,b}$ did not correlate with IC_{50},

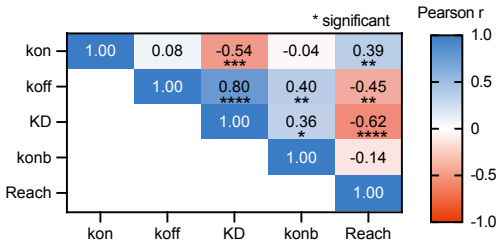

Figure 5.12: Correlations between binding parameters obtained from high-throughput screen. Correlation measured by Pearson index.

(Fig. 5.13E), the molecular reach showed the best correlation among all parameters (Fig. 5.13F). Antibodies with a longer reach tend to be better at neutralising SARS-CoV-2. This correlation was further improved by including $k_{on,b}$ and molecular reach into the multi-linear regression (Fig. 5.13G). This model significantly outperformed the one using solely monovalent parameters. This underscores the pivotal role of the bivalent binding ability of antibodies for neutralisation.

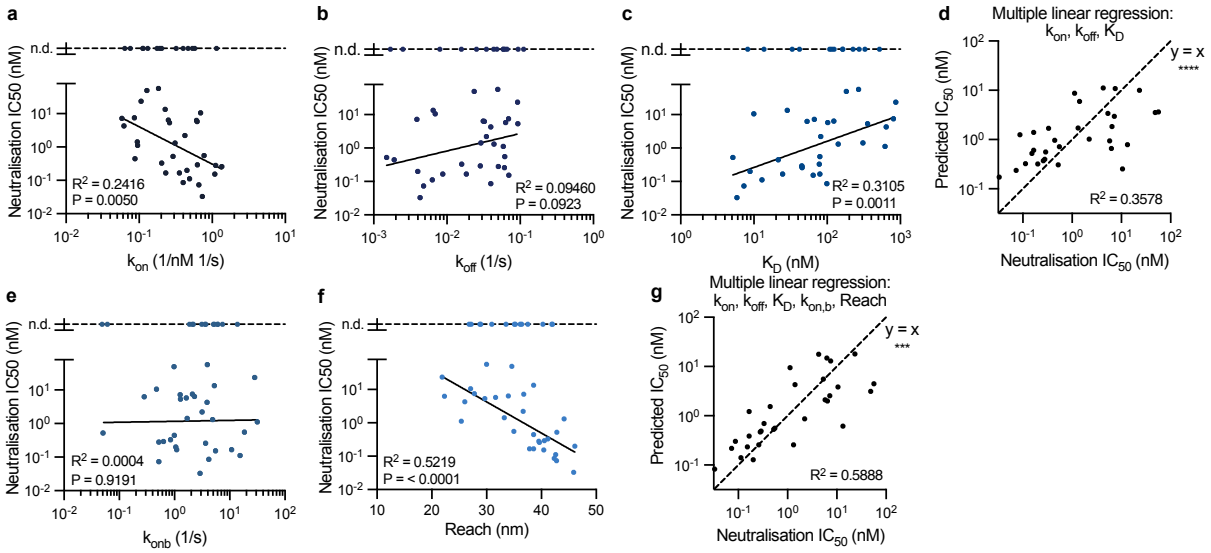

Figure 5.13: Correlations between binding parameters and neutralisation potency. (A-G) Single and multiple linear correlations between the indicated parameters of 45 antibodies (individual data points) and their neutralisation potency (IC_{50}), the concentration of antibody required to reduce *in vitro* SARS-CoV-2 infection by 50%. The 13 antibodies whose potency was not determined (n.d) were excluded from the fit (top dashed line).

While bivalent parameters improve the correlation, they do not offer a complete explanation for neutralisation. Another factor that determines neutralisation potency is the location of the epitope on the antigen. Dejnirattisai et al.[286] showed that anti-RBD antibodies were better at neutralising the closer their epitope was to the ACE2 binding epitope because they can

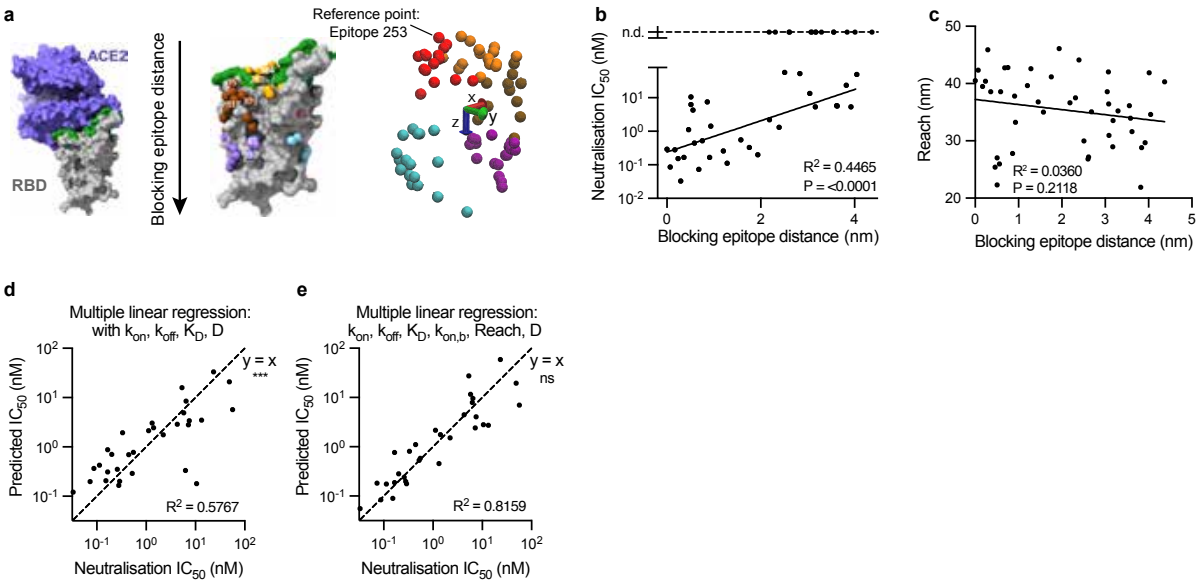

Figure 5.14: Binding parameters and epitope binding distance determine neutralisation potency. **(A)** Structure of RBD binding to ACE2 (left), location antibody binding epitopes on RBD (middle) and in empty space (right). To determine the epitope distance from ACE2 binding site (green surface), the distance in Z direction between reference epitope 253, located furthest to the top of RBD, and each epitope was measured. Images are taken from [286]. Correlation of Blocking epitope distance with **(B)** Neutralisation IC_{50} and **(C)** molecular reach. Multiple linear regression including blocking epitope distance and **D)** only monovalent binding parameters or **E)** all binding parameters.

sterically block ACE2 binding. Because the epitope coordinates on RBD of all these antibodies are known, we could quantify the distance antibody binding and the ACE2 blocking epitope (named blocking epitope distance, D). ACE2 binds to the top of RBD, thus we took the epitope furthest to the top of RBD, which is the binding to antibody 253, as our reference epitope and set it to D = 0.0 (Fig. 5.14A). Then we calculated the difference in Z direction between the baseline epitope and all other epitopes. This gives us distance values ranging from 0 to 4.37 nm. As expected, blocking epitope distance correlates with neutralisation potency (Fig. 5.14B), with antibodies binding in the lower region of RBD are less likely to neutralise SARS-CoV-2. No correlation is observed for reach and blocking epitope distance, suggesting that they are independent measures (Fig. 5.14C), and reach is not determined by epitope location. Including distance with monovalent parameters improves the multi-linear regression fit (Fig. 5.14D). We obtain the best correlation with an R^2 of 0.82 if monovalent and bivalent parameters as well as blocking epitope distance are all included in the multiple linear regression (Fig. 5.14E). This indicates that the binding parameters together with the epitope location of an antibody fully determine its neutralisation potency.

5.2.7 *Particle model can predict neutralisation potency*

Next, we want to use the particle model to predict neutralisation potency directly from the binding parameters measured by SPR.

For predicting neutralisation, the particle model was adapted to simulate antibody binding on a 2D surface. Antigens are distributed randomly on a 2D surface (Fig. 5.15 right). The general workflow for predicting neutralisation is as follows: First, the model uses the binding parameters k_{on}, k_{off} $k_{on,b}$ and reach, as well as the antigen density as inputs and simulates antibody binding over time. The fraction of unbound antigen is recorded over time. This simulation is repeated for a range of antibody concentrations. We then take the fraction of unbound antigen at a specified time T and plot it over antibody concentration. From the resulting dose-response curve we can calculate the predicted binding potency (Fig. 5.15 left), which is the antibody concentration that blocks 50% of all antigens on the surface.

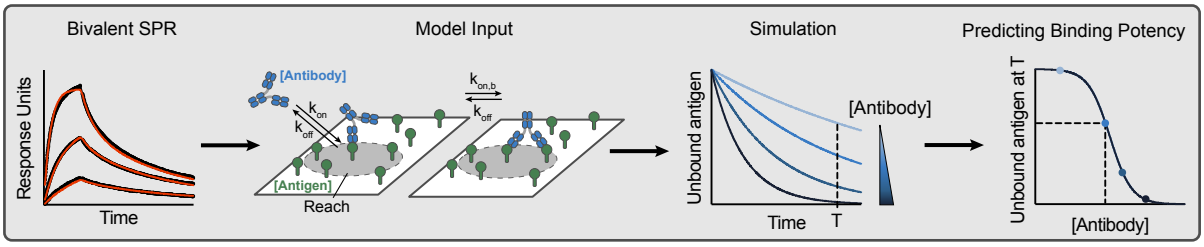

Figure 5.15: Workflow to determine antibody potency using the particle model. The particle model takes binding parameters determined by SPR, antigen density and antibody concentration as input to simulate antibody binding to antigens randomly distributed on a two-dimensional surface. Simulating the model at a range of antibody concentrations allows us to plot the fraction of unbound antigen at a timepoint T over antibody concentration. IC_{50}, antibody concentration that results in 50% of antigen bound, can be determined from this plot and directly compared to experimental neutralisation potency

First, we tested the model with the FD-11A antibody. Using the binding parameters obtained from bivalent SPR, we simulated FD-11A binding to RBD for 60 min for antigen densities between $1 \times 10^{-7}\,nm^{-2}$-$0.04\,nm^{-2}$ (Fig. 5.16A). We reasoned that in the low antigen density regime, almost all interactions are monovalent as antigens are too sparse for antibodies to be able to reach. On the other hand, in the regime of very high antigen density, all antibodies, even those with small reach, will be able to bind bivalently.

The neutralisation IC_{50} of FD-11A was measured by incubating the antibody with SARS-CoV-2 virions for 60 min (Fig. 5.16B). Afterwards, the mixture was added to Vero cells and the infection rate was recorded. We compared the predicted binding potency with the experimental

neutralisation IC_{50}. At a low antigen density of $1 \times 10^{-7}\,nm^{-2}$ the algorithm predicts the IC_{50} to be 600 nM. At a high antigen density of $0.04\,nm^{-2}$ where the antibody can bind bivalently, the predicted binding potency is 1.8 nM, 340-fold lower compared to the low-density regime (Fig. 5.16 C). Comparing the simulated IC_{50} with the experimental IC_{50}, we see that the IC_{50} from the high-density regime is similar to the absolute experimental IC_{50} measured with the full IgG antibody. The predicted potency at the low-density regime is closer to the IC_{50} measured for the monovalent binding Fab domain. This suggests that bivalent binding is essential for the high potency of antibodies.

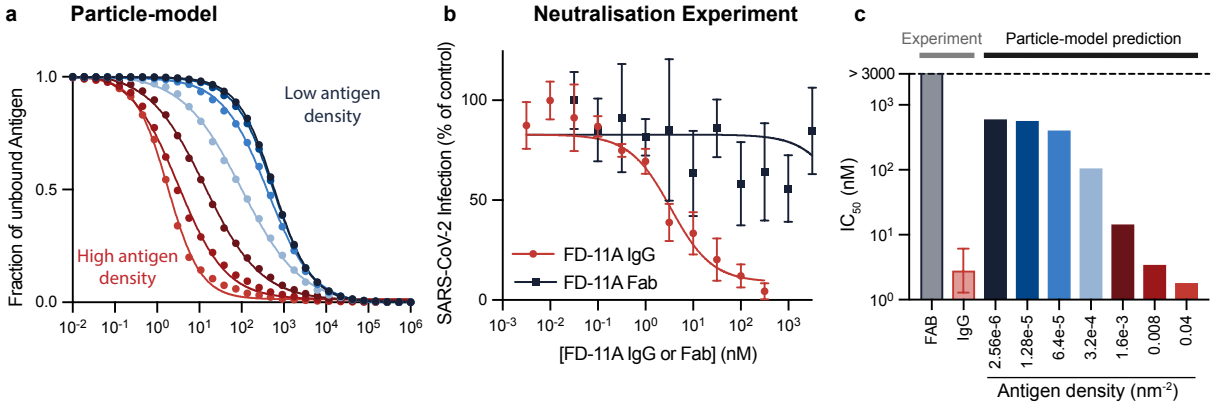

Figure 5.16: Prediction of FD-11A neutralisation potency. **A)** Simulation of the fraction of free antigen over antibody concentration after 60 minutes for surfaces with varying antigen densities. The binding parameters are those determined for FD-11A. **B)** Experimental neutralisation of SARS-Cov-2 by FD-11A IgG (red) and Fab (black) determined by the ability of the virus to infect cells after incubation with antibody for 60 min. IC_{50} is defined as antibody concentration resulting in 50% of infected cells, **C)** Potency values (IC_{50}) from experiment in (B) and mode; prediction in (A).

To generalise this conclusion, we predicted the potency of the 45 antibodies from the antibody screen. The predicted neutralisation potency at a range of antigen densities was plotted against the experimental neutralisation IC_{50}. This was done by including either all 45 antibodies for which we have binding data (Fig. 5.17A-J), or, to limit the effect of epitope location dependencies, by including only antibodies that bind to the top of RBD, selected by an epitope blocking distance of smaller than D <2.37 nm. This limits the number of antibodies to 25. The low-density antigen regime yields IC_{50} values that are excessively high for strongly neutralising antibodies. On the other hand in high-density regime yields IC_{50} values disproportionately low for poorly neutralising antibodies. Only when binding is simulated at intermediate antigen densities, is the predicted neutralisation IC_{50} equal to the experimental neutralisation for all antibodies.

We fitted a linear line to the log-transformed values and plotted the slope and the Y-intercept of the plots over antigen densities (Fig. 5.17J and T). The slope is smaller than 1 for both low and high antigen density regimes, while the Y-intercept decreases with increasing antigen density. Only at intermediate antigen densities ($0.5 \times 10^{-3}\,nm^{-2}$-$1.0 \times 10^{-3}\,nm^{-2}$) we find that the linear fit is not significantly different from the perfect correlation, with a slope close to 1 and a y-intercept equal to zero. This correlation improves even more when antibodies binding to the bottom of RBDs are removed.

The spike protein density on SARS-CoV-2 virions has been estimated to be $1 \times 10^{-3}\,nm^{-2}$ from electron microscopy analysis[293] (Fig. 5.18A). The optimal antigen density from simulations, which predicts accurate potency values, is similar to the actual spike density (Fig. 5.18B).

Why does the prediction accuracy of the model depend on antigen density? At low antigen densities, antigens are spaced far apart (for example for 2.56e-6: $\sim$ 600 nm), and the antibodies will bind mostly monovalently. Their binding strength is solely determined by k_{on} and k_{off}. At very high densities, the antigens are very close (0.04 nm-2.5 nm apart), which allows every antibody even those with a short reach to bind. However, at intermediate densities ($0.0005\,nm^{-2}$-$0.001\,nm^{-2}$) the spacing is around 30-40 nm. Antibodies with a long reach will be able to bind bivalently, while antibodies with a short reach will still bind monovalently. To illustrate this we simulated binding for two antibodies: Ab181 with a low neutralisation IC_{50} and AB394 with a 20-fold higher neutralisation IC_{50}. The two antibodies bind the same epitope on RBD with a very similar affinity. However, Ab394 has a reach of 40 nm while Ab181 only has a reach of 22 nm. At low and high densities, their simulated IC_{50} is similar. Only at intermediate density, we can replicate the 20-fold difference in IC_{50} observed experimentally. This suggests that there is an antigen density regime in which only antibodies with a large reach can effectively utilize bivalent binding, leading to a wide range of neutralisation potencies.

Figure 5.17 ***(following page)*****: The predicted antibody binding potency produces absolute agreement with the experimental neutralisation potency at intermediate antigen densities.** The particle-based model was used to predict the concentration of antibody required to bind 50% of antigen (Predicted IC_{50}) to surfaces randomly distributed with the indicated density of antigen for **(A-I)** all antibodies or **(K-S)** the subset of antibodies that bound within 2.37 nm of the blocking epitope. A linear fit to the log-transformed IC_{50} values (solid line) is compared to a line of absolute agreement (dashed black line - slope 1, y-intercept 0) using an F-test for the null hypothesis that the two lines have the same slope and intercept. A Bonferroni multiple-comparison correction is applied by multiplying each p-value by 11 (number of antigen densities test). **(J,T)** Display the slope (top) and intercept (bottom) of the fitted line for the 11 different antigen densities tested.

Including all measured antibodies

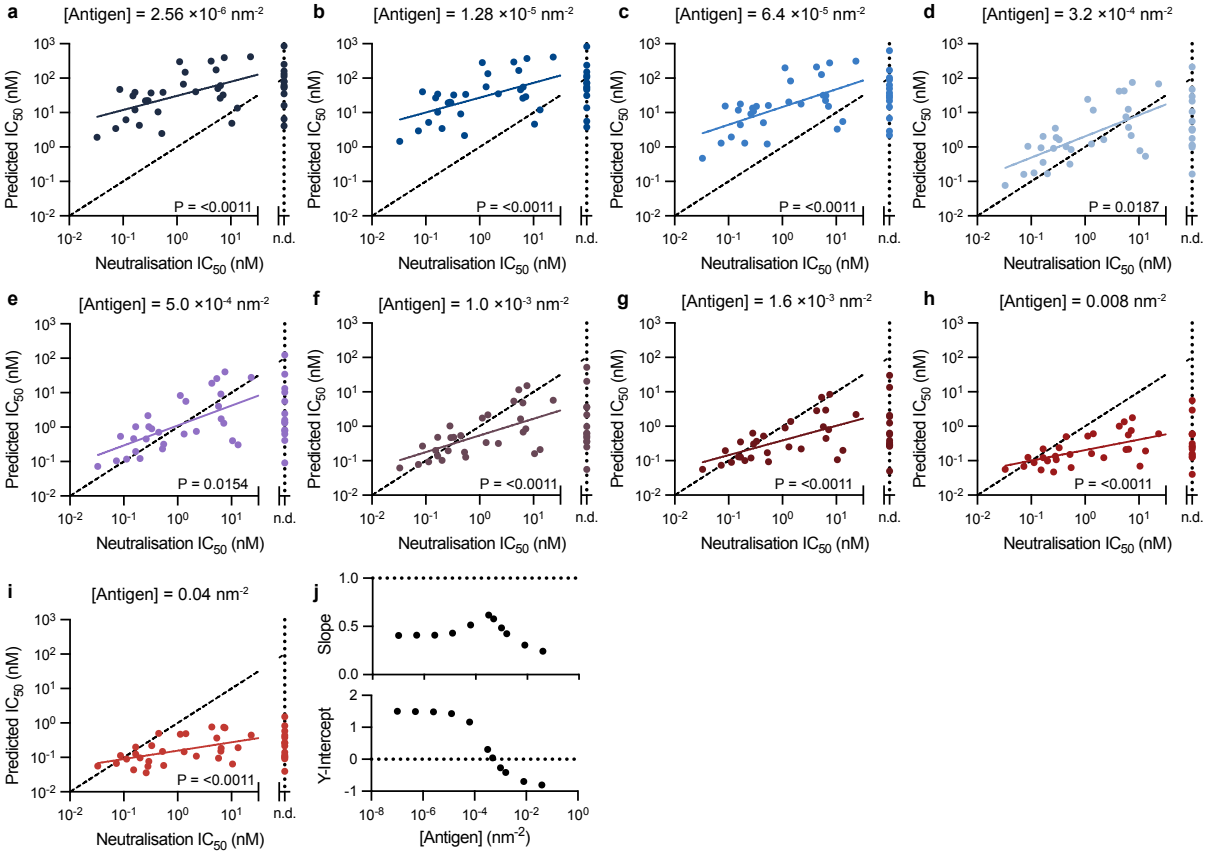

Including antibodies with a epitope blocking distance < 2.37 nm

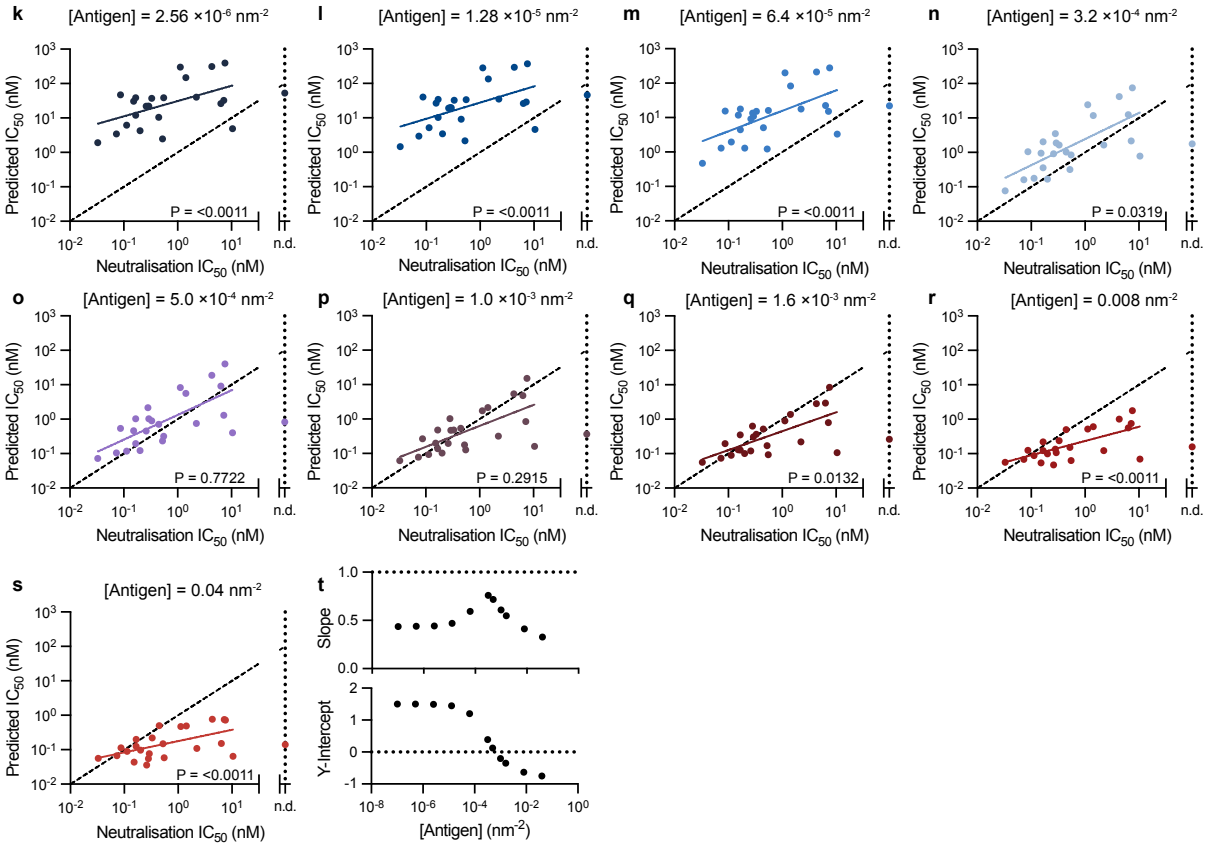

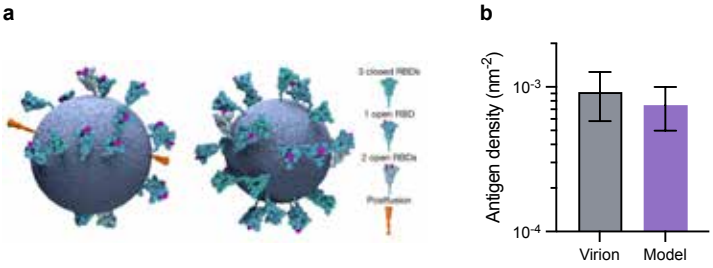

Figure 5.18: Antigen density that produces agreement between predicted and experimental potency matches spike density on virus. **(A)** Cryo-electron microscopy of SARS-CoV-2 virus particle allows estimation of Spike density (graphic taken from [293]). Comparison of Spike density with intermediate antigen density which produces absolute agreement between particle model prediction (Fig 5.17) and experimental IC_{50} (0.00075 nm^{-2} [0.0005, 0.001])

In summary, the particle model allows accurate prediction of neutralisation potency for RBD antibodies when the antigen density and the antibody monovalent/bivalent parameters are known. Neutralisation potency is strongly affected by reach and it is therefore not possible to predict neutralisation from the monovalent parameters alone.

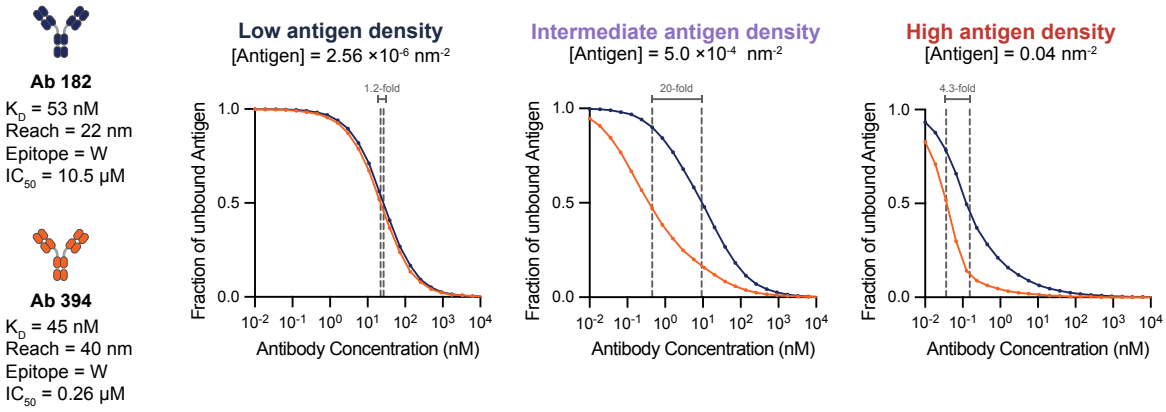

Figure 5.19: Molecular reach can explain the difference in antibody potency. **(A)** Two antibodies were chosen that have very similar monovalent affinity (50nM) and bind the same RBD epitope (Neck), but have very different molecular reach and neutralisation potency. **(B)** Simulation of the fraction of free antigen over antibody concentration for antibodies 181 and 394 after 60 minutes for surfaces with different concentrations of antigen. IC_{50} values are indicated by dotted lines. Intermediate antigen density shows the largest difference in IC_{50} between the two antibodies. **(C)** Comparison of experimental IC_{50} values with predicted IC_{50} values obtained from dose-response curves in (B). Only simulations at intermediate antigen density replicate the difference observed in experimental IC_{50} values.

5.3 Discussion

Prediction of antibody function from binding parameters has been challenging. The function of antibodies critically depends on their ability to bind two antigens bivalently to achieve high-affinity binding. However, previous attempts at quantifying bivalent binding using ordinary differential equations (ODEs) have been unsuccessful, due to the complex stochastic and spatial nature of bivalent binding.

To overcome this challenge, we developed a stochastic and spatially resolved particle-based model for bivalent antibody binding and applied it to antibodies binding RBD of SARS-CoV-2. The model correctly determines the monovalent binding parameters k_{on}, k_{off} and K_D, as well as the bivalent binding parameters $k_{on,b}$ and molecular reach. Importantly, measurements can be performed in a high-throughput fashion, allowing us to measure up to 30 antibodies at a time, as long as the surface antigen stays stable throughout the entire experiment. This method does not require complicated antigen surface preparation as previous approaches using DNA origami[171,288,289], and there is no limitation on the size of the antigen that can be immobilised. This allows the measurement of binding to large viral proteins, rather than small peptide sequences as previously used.

We successfully obtained reliable binding parameters for 45 out of the 80 antibodies tested. Unfortunately, we had to exclude some antibodies due to issues with low binding or incomplete surface regeneration. Additionally, certain antibodies were excluded because they did not exhibit dissociation, making it impossible to determine unambiguous parameters with the bivalent particle model. This exclusion is particularly unfortunate as these antibodies are among the strongest binders and may have a high potency.

What determines the molecular reach?

The RBD-specific antibodies had an average reach of 40 nm, which means that an antibody can bind antigens that are spaced up to 40 nm apart. Previous studies, through structural analysis and binding experiments with defined surfaces, have measured the reach of an antibody to be 16 nm. Through SPR experiments with antigens of different sizes and molecular dynamic simulations, we showed that the size of the antigen contributes to the overall reach of the

antigen. This is due to the antigen contributing to the reach, the molecular reach measures from the antigen anchor points. Defining the molecular reach from antigen anchor point to anchor point, instead of from binding site to binding site, is more than merely a difference in where we set the reference point. Antibodies binding HIV spike proteins can be used as an example to illustrate this. HIV expresses a low density of surface proteins. It is estimated that they are on average spaced 23 nm apart, which was believed to be far beyond the span of an antibody[287]. The assumption of a maximum reach of 16 nm has been used to argue that antibodies are unable to bind HIV bivalently. The HIV spike is of similar size to the SARS-CoV-2 spike protein and presents at a similar density on the virions. Our measurements reveal that antibodies are likely to also bind HIV bivalently.

We also see a large variation in reach within antibodies binding the same epitope (20 to 40 nm for RBD antibodies). We do not fully understand what determines the difference in reach between antibodies binding the same antigen. Antibodies binding to the top of RBD, as measured by the blocking epitope distance, did not show a larger reach than antibodies binding towards the bottom of RBD. Other factors determining the reach could be the binding orientation of the antibody. Furthermore, the length and flexibility of variable loops could contribute to the reach. Also, it has been shown that antibodies with a stronger affinity tolerate larger antigen spacing[171], consistent with the correlation between K_D and reach we found in our dataset. Additional molecular dynamic simulations could shine a light on this.

The reach measured in SPR may differ from the reach experienced directly on the pathogen surface. On the SPR chip, RBD is bound via a linker to Streptavidin on a 3D dextran surface. We assume it can pivot and rotate freely in all directions and is accessible from all sides. On the virus, RBD is part of the trimeric spike protein, which is a much larger antigen than RBD. Given that reach depends on antigen size, we would predict the reach to be larger than measured by SPR. On the other hand, the spike protein is firmly anchored in the membrane with a transmembrane domain. While the spike protein has a flexible stalk region and can bend in multiple directions[294,295], it might have less rotational flexibility than RBD on the SPR chip, reducing the reach of the antibodies. The good correlation between the predicted neutralisation IC_{50} and the experimental IC_{50} at the virus antigen density suggest that the reach measured by SPR is very close to the *in vivo* reach.

Prediction of antibody potency

We found that the molecular reach of an antibody is the strongest correlate of SARS-CoV-2 viral neutralisation. Bivalent binding parameters are essential in determining the neutralisation potency of an antibody. We showed that the binding parameters together with epitope location fully explain neutralisation potency, which sheds light on the longstanding questions regarding what properties of an antibody potency determine its functional potency.

Using the particle model, we simulated antigen binding to the surface of a pathogen and identified how binding is influenced by changes in antigen density. The higher the density, the lower the predicted binding potency. At intermediate antigen densities, the model accurately predicted the experimentally determined concentration of antibody required for virus neutralisation. We reasoned that the reach determines the ability of an antibody to bind bivalently. Antibodies with large reach are more effective at binding bivalently which leads to an overall stronger binding and hence better neutralisation potency. A similar effect was shown in the early studies studying the binding of bivalent ligands to opioid receptors[296]. Only a ligand with a sufficiently long linker was able to bind bivalently. This opens up the possibility to optimise antibody neutralisation by engineering them with a larger reach. Furthermore, it raises the question of whether there is an evolutionary pressure for viruses to prevent bivalent antibody binding, as well as for antibodies to improve bivalent binding. Low antigen density on HIV has been suggested to decrease bivalent antibody binding[287].

The prediction of antibody potency with the particle model is not perfect. One main reason for this is that epitope location is not taken into consideration. Removing antibodies that bind to epitopes at the bottom of the RBD antigen away from the ACE2 binding site improves the model predictions. While steric blocking of ACE2 binding is important for neutralisations, antibodies binding strongly to the bottom regions of RBD may still have important functions *in vivo* via the complement system and immune cell activation. Furthermore, due to the spike protein being a trimer, it contains three RBD domains. Antibodies could potentially bind two RBDs within the same spike protein (intraspike) instead of two antigens on separate spike proteins (interspike). Intraspike binding would allow even antibodies with a short reach to bind bivalently. While binding of antibodies to spike has been imaged using cryo-EM suggesting intraspike binding[297], due to the variability of the heavy chain, the presence of intraspike binding *in vivo* cannot be conclusively determined. Also, RBD can either be in an open and

accessible conformation, or in a closed conformation. Therefore there might not be two RBD domains within one spike protein accessible for an antibody to bind. It has been shown that antibodies cannot bind the HIV spike intraspike[287]. Given that potency correlates with reach in our data, we suggest that the main mode of binding is interspike. Finally, diffusion of antigens in the virus membrane might allow even antibodies with a small reach to bind. We have not found a study quantifying the diffusion coefficient of Spike proteins. The presence of envelope and membrane proteins and their interaction with the viral RNA might limit diffusion. It would be useful to confirm the ability of the model to accurately predict neutralisation potency with another antigen, such as the spike protein of Influenza.

Future implications

By deepening our mechanistic understanding of how antibodies bind to antigens, this project carries significant implications for both basic research as well as clinical applications of antibodies. It would be interesting to investigate whether the bivalent binding parameters impact antigen recognition by the BCR and if these parameters are optimised during affinity maturation. Examining how bivalent interactions change under force is particularly relevant, as B cells apply pulling forces to the BCR-antigen complex during antigen internalisation. Understanding these dynamics could provide insights into the mechanics of BCR-antigen interactions within the immune synapse. Furthermore, the ability to quantify the bivalent binding of antibodies may advance antibody engineering strategies and pave the way for more effective vaccine designs. The data generated will be valuable for machine learning predictions regarding antibody binding and function, providing a useful tool for the scientific and medical communities. The ability to predict the absolute neutralisation potencies may allow for a better determination of the necessary dose when administering antibodies as therapeutics. Furthermore *in vitro* neutralisation assays require live viruses, which necessitates work in a biosafety level 3 for pathogenic viruses. Furthermore, only focusing on neutralisation might overlook non-neutralising antibodies with strong binding that may be very good at activating the immune system.

The current particle model only works for monomeric, randomly distributed antigens. However, in real biological systems, antigens are often not monomeric. Many viral glycoproteins occur as trimers, such as influenza hemagglutinin, i.e. containing several identical epitopes

the antibody can bind to. Secondly, our model was developed for bivalent IgG antibodies, but other antibodies are of interest, such as IgA, which plays an important role in protecting the mucosal surface against bacteria. There are also increasing therapeutic applications for bispecific antibodies, where each binding site of the antibody binds a different antigen. In the future, we would like to extend our current model to include these applications by developing a more comprehensive model that can be applied to a wider range of biological systems and a wider range of antibodies.

6

EXPLOITING BIVALENT BINDING TO STUDY ULTRA-LOW TCR/PMHC INTERACTIONS

6.1 Introduction

As demonstrated in Chapter 4, TCR interactions exhibit exceptionally fast kinetics. While we successfully measured the kinetics of the cognate OT-I/N_4 pMHC with a half-life of $\sim$0.2 s using an SPR instrument with a sampling rate of 40 Hertz, interactions involving lower affinity pMHCs occur so rapidly that we cannot obtain sufficient data points from the SPR curves to fit a binding model. Consequently, for these interactions, we can only derive the K_D from equilibrium dynamics. This limits our ability to test mechanistic models for T-cell activation. For instance, in the kinetic proofreading model, k_{off}, rather than K_D, determines T cell activation.

Previously, higher valency TCRs or pMHCs were used to increase binding in SPR or on cells with many applications. Through the effects of avidity, bivalent binding can increase the apparent affinity of a ligand for its binding site. This leads to a slower dissociation from its target compared to its monomer. For instance, pMHC tetramers serve as a common tool for detecting and staining antigen-specific T cells. By binding to multiple TCRs on the surface of T cells, pMHC tetramers increase binding strength and slow down dissociation[298]. Furthermore, pMHC dimers have been used to enhance the binding of the OTI-TCR to self-pMHCs[113]. In this study, pMHC dimers were created using peptide-based cross-linking reagents, that react with a free cysteine at the C terminus of the H-2Kb molecule[62]. In addition to pMHC, TCR tetramers have been developed for the detection of specific APCs[299]. TCR tetramers exhibit a 500 to 1000-fold prolonged dissociation time compared to monomeric TCRs. Beyond TCR-pMHC interactions, bivalent ligands have been designed for GPCRs to enhance signalling[300],

while dimeric aptamers have shown success in increasing target binding affinity[301]. However, while these examples demonstrate enhanced binding strength through increased valency, they do not allow for accurate quantification of binding parameters.

Here, we aim to utilize this enhanced avidity of bivalent binding to measure the rapid kinetics of low-affinity interactions between TCR and pMHC, utilising the particle-based model developed in Chapter 5 to obtain the monovalent parameters of the TCR/pMHC interaction from bivalent binding curves. If we dimerise the TCR, it will bind bivalently to pMHC. Although the affinity of each TCR subunit remains unchanged, the dimer will bind for a longer duration due to engaging with two pMHC complexes simultaneously (Fig. 6.1). Consequently, dissociation occurs more slowly, which would provide us with an increased number of data points for fitting a binding model. By fitting the particle-based model to the data we can obtain accurate monovalent values for k_{on} and k_{off}. Furthermore, pMHCs with extremely low affinity, such as self-pMHCs, elicit minimal binding responses that approach the sensitivity threshold of the SPR. By leveraging bivalent binding, we could amplify the overall binding response, potentially allowing a measurement of low-affinity K_D values that is less affected by non-specific binding. This could allow us to validate the K_D values measured in Chapter 4.

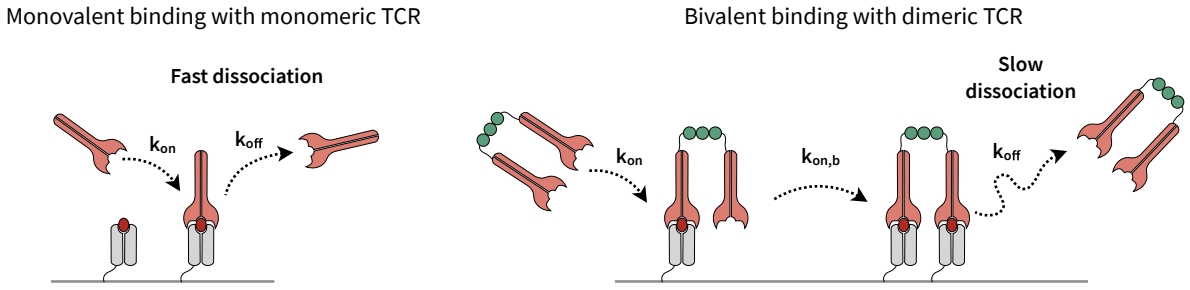

Figure 6.1: Quantifying fast binding rates with dimeric TCR. Schematic showing how bivalent binding of a dimeric TCR improves binding to ligands.

In this chapter, we will focus on the development and validation of a dimeric TCR using the modular SpyTag/SpyCatcher system, which allows the covalent conjugation of two proteins. This chapter aims to provide a detailed description of the process of creating the TCR dimer and to evaluate its effectiveness in measuring the kinetics of very fast interactions. First, we will use the human 1G4 TCR interacting with high-affinity pMHC for which we have kinetic measurements to validate the system and to determine the bivalent binding parameters of the TCR dimer. The 1G4 TCR binds a peptide derived from the tumour-specific antigen NY–ESO-1.

Next, we are applying this method to study low-affinity OT-I interactions. Finally, we are using simulation of binding to understand the limitations and potential optimisations of this method.

6.2 Results

6.2.1 Dimeric TCR production

To create a TCR dimer we made use of the recently published SpyCombinator system[302]. Driscoll et al.[302] developed a recombinant protein termed DoubleCatcher (DC), that contains two SpyCatcher domains joined by a peptide linker. SpyCatcher forms a spontaneous covalent bond with the complementary SpyTag upon binding[303]. This protein thus allows the covalent dimerisation of any two SpyTag fused recombinant proteins (Fig. 6.2). We added a SpyTag to the C-terminus of the TCRβ chain in plasmids for *E. coli* expression of both the OT-I and 1G4 TCR. We are testing two versions of the DoubleCatcher. The first links the SpyCatcher domains with a flexible linker with three glycine-serine-glycine repeats ($[GSG]_3$), and another where the linker is a rigid α helix (αH) taken from the *Bacillus stearothermophilus* ribosomal protein L9[302] (Fig. 6.2B). We wanted to test if the linker length and flexibility impact bivalent binding.

For dimerisation, DC was incubated with refolded monomeric TCR after purification with anion-exchange chromatography. A 3-fold excess of OT-I or 1G4 TCR was added compared to DoubleCatcher and the incubation was carried out for 1 hour at room temperature to allow complete dimerisation. Full dimerisation for both OT-I and 1G4 is confirmed by performing a SDS-PAGE (Fig. 6.3). The full dimer has a molecular weight of 130 kDa, consisting of 2×50 kDa TCR and 30 kDa DoubleCatcher. The successful dimerisation can be observed on protein gel as the disappearance of the band running at the height of the monomeric TCR as well as the DoubleCatcher band and the occurrence of a higher molecular band. The OT-I construct has an engineered cysteine bond between the α and β chains. Under non-denaturing conditions, the two chains run together at 50 kDa for the monomer and 130 kDa as a dimer (Fig. 6.3A). When a denaturing gel is used, α and β chains separate. After dimerisation, we observe a band for the dimerised β chain, while the α chain runs at the same height as for the monomer. The 1G4 used here does not have extra cysteine bonds and separates into α and β chains even in a non-denaturing gel (Fig. 6.3B).

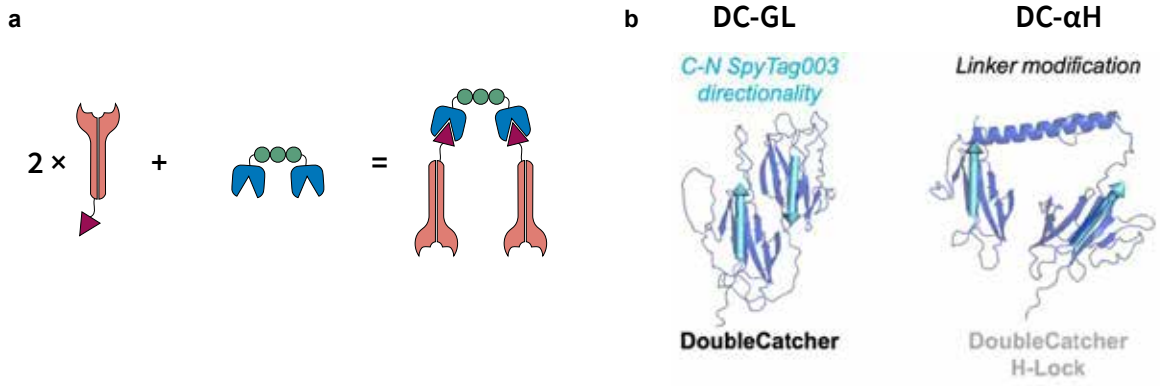

Figure 6.2: The generation of dimeric TCR using the SpyCatcher-SpyTag system. **(A)** Schematic of reaction of DoubleCatcher (DC) with TCR to produce a dimeric TCR. SpyCatcher domains (blue) on DC react with SpyTags (purple) on TCRs and produce a covalent bond. **(B)** AlphaFold2-predicted structure for DoubleCatcher (DC). The DC consists of two SpyCatcher proteins connected by a linker. Cyan vectors indicate the position and orientation of the SpyTag binding sites. The linker can be a sequence of glycine-serine amino acids (DC-GL) or a rigid α helix (DC-αH). Image taken from Driscoll et al.[302].

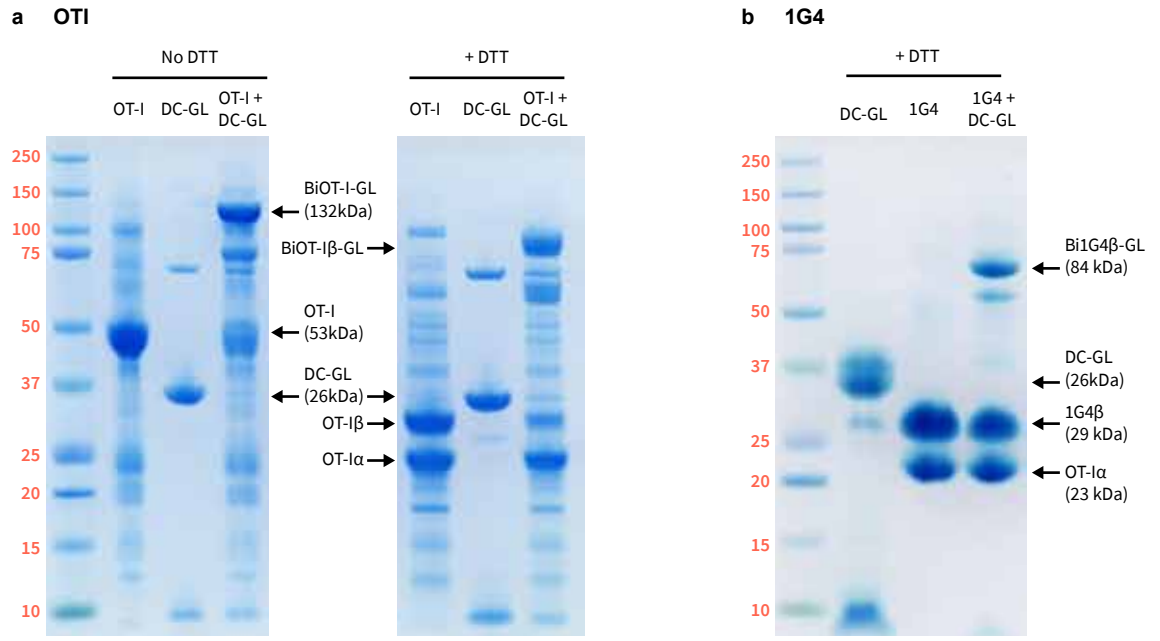

Figure 6.3: DoubleCatcher reacts with TCR to create dimeric TCR. SDS page showing the reaction of OT-I (**(A)**) and 1G4 (**(B)**) TCR with DoubleCatcher (DC). No DTT = non-denatured gel; + DTT = denatured gel, proteins boiled and reduced by the presence of DTT. DoubleCatcher was incubated with a 3-fold excess of TCR for 1 h at room temperature.

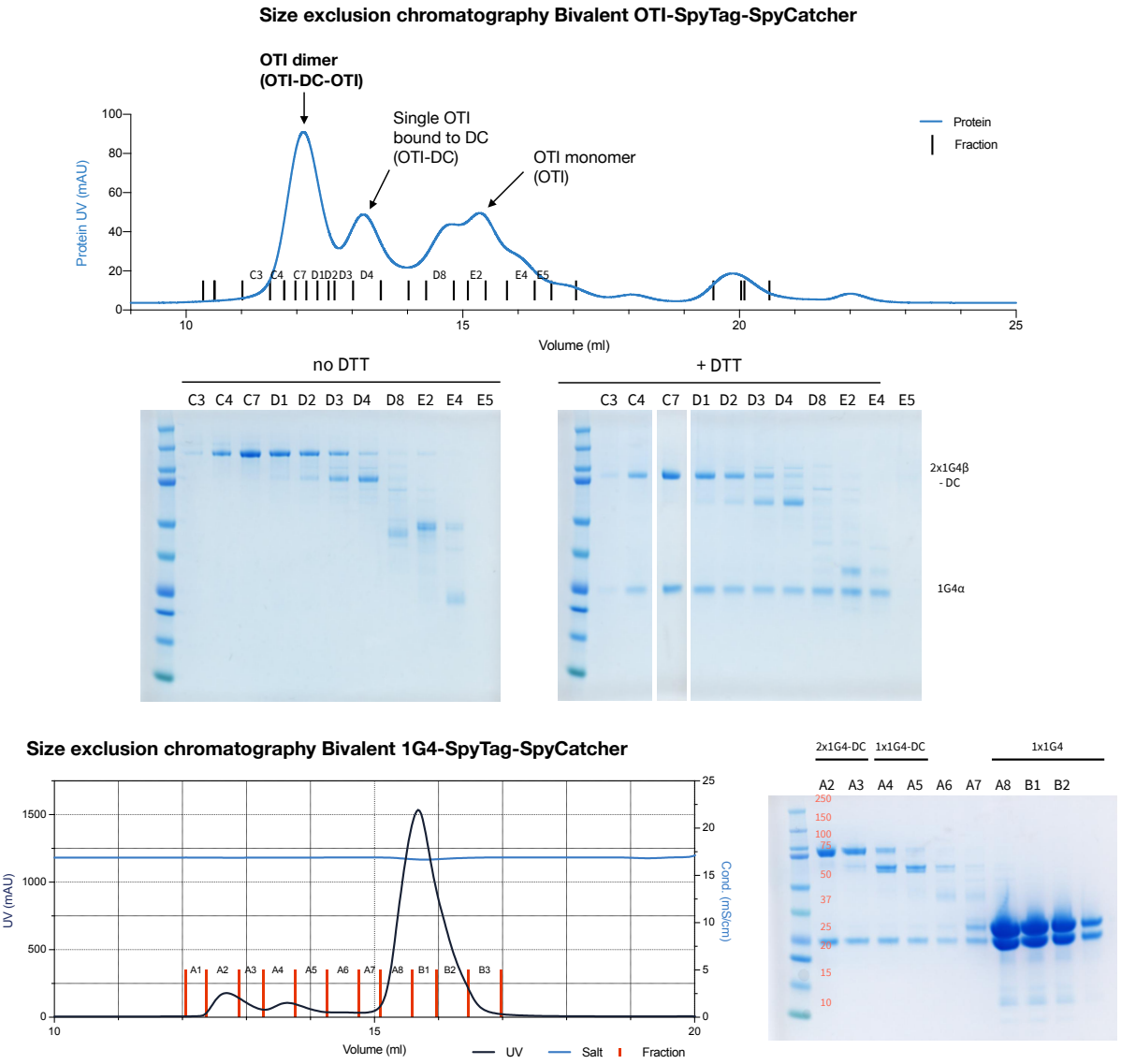

Figure 6.4: Purification of dimeric TCR. Sensogram and protein gel after size exclusion chromatography on S200 column for OT-I (top) and 1G4 (bottom). The TCR dimer elutes after 12 ml, the monomer after 16 ml.

After dimerisation, the TCR dimer was purified using size exclusion chromatography (SEC) (Fig.6.4). Both the OT-I and 1G4 dimer elute after 12 ml, 3 ml before the monomer. A small fraction of single TCR-Double Catcher also elutes, likely due to incomplete cleavage of masked SpyTag with TEV protease. The purity of the fraction was confirmed by SDS page (Fig. 6.4). Only pure fractions were used for SPR experiments. Concentration was measured by nanodrop using an extinction coefficient calculated from the protein sequence.

6.2.2 *Bivalent SPR with dimeric 1G4 TCR*

First, we tested the method using the human 1G4 TCR, that binds to the NY–ESO-$1_{157-165}$ peptide (SLLMWITQC)[304]. We used the 9V variant of this peptide, which has the cysteine in position 9 replaced by a valine for improved stability on the MHC. The 1G4 TCR has a high affinity for the 9V-pMHC, and the kinetic parameters of this interaction have been measured previously[149].

pMHC was immobilised between 500 and 1000 RU. Bivalent 1G4 was injected in a two-fold dilution series with the highest concentration between 1 µM-5 µM. We tested 1G4 dimerised with the DC with the glycine-serine linker (Bi1G4-GL) and with the α helix linker (Bi1G4-αH). As anticipated, the dimeric 1G4 exhibited markedly slower dissociation compared to its monomeric counterpart injected over the same pMHC surface (Fig. 6.5A). Specifically, the half-life of dimer dissociation was found to be eight times longer than that of the monomer, extending to 16 s compared to 2 s, respectively. Bivalent SPR curves were fitted with the particle-based model to derive the monovalent and bivalent interaction parameters, including the association rate (k_{on}), dissociation rate (k_{off}), bivalent association rate ($k_{on,b}$), and molecular reach. The monovalent parameters k_{on}, k_{off}, and K_D obtained from bivalent SPR experiments with the Bi1G4-GL TCR dimer show no significant difference to the published parameters obtained with the monomeric 1G4 (Fig. 6.5B). This suggests that the dimeric 1G4 demonstrates a comparable affinity per binding site as the monomeric 1G4, with the enhanced binding strength occurring due to bivalent binding. For 1G4-αH, similar parameter values were observed, although further repeats are needed to confirm their significance. Regarding the bivalent parameters of the 1G4 dimer, we find a mean $k_{on,b}$ of 1.0 s^{-1} and a mean molecular reach of 15 nm.

The same experiment was performed with the 3A peptide, which exhibits a comparable affinity to the 1G4 TCR as the 9V peptide. As for the 9V peptide, the SPR curves show clear bivalent binding behaviour, characterised by an extended dissociation phase relative to monomeric binding (Fig. 6.6A). While the k_{off} values obtained from the bivalent SPR were consistent with published values, the k_{on} values for Bi1G4-GL binding 3A were significantly lower than those reported, consequently yielding a higher K_D (Fig. 6.6B). Similar to the findings for the 9V peptide, the average values for the bivalent parameters $k_{on,b}$ and molecular reach were 1.0 s^{-1}, and 15 nm, respectively (Fig. 6.6C).

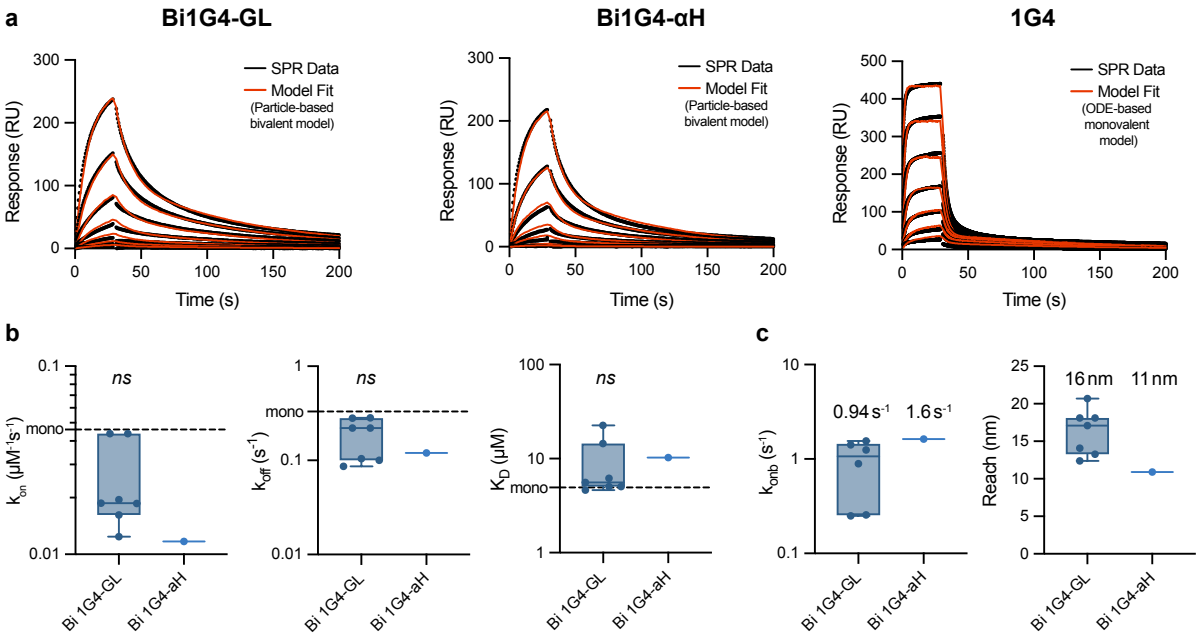

Figure 6.5: Dimeric 1G4 returns the same binding parameters as monomeric 1G4 binding to 9V peptide. **(A)** Representative SPR sensograms of dimeric 1G4, dimerised with DC-GL (Bi1G4-GL) (left), 1G4 dimerised with DC-αH (Bi1G4-αH) (centre) and monomeric 1G4 (right), binding pMHC 9V immobilised at 740 RU. The TCR is injected as a dilution series with increasing concentrations, the highest concentration was 0.96 µM, 0.92 µM and 62 µM for Bi1G4-GL, Bi1G4-αH and 1G4, respectively. The data was fit with either the bivalent particle model for dimeric 1G4, or a monovalent binding model for monomeric 1G4. **(B)** Binding parameters k_{on}, k_{off} and K_D measured for Bi1G4-GL and Bi1G4-αH in comparison to published parameters obtained from monovalent interaction (N= 7 for Bi1G4-GL and N= 1 for Bi1G4-αH). **(C)** Bivalent binding parameters $k_{on,b}$ and reach measured for Bi1G4-GL and Bi1G4-αH. (N= 7 for Bi1G4-GL and N= 1 for Bi1G4-αH) A t-test with Dunnett's multiple comparison correction on log-transformed values was used to determine p-values.

Following the SPR experiments with the high-affinity peptides 9V and 3A, we measured the binding of dimeric 1G4 TCR to lower affinity peptides 6V, 3Y, 6T and 4D, with K_D values ranging between 20 and 160 µM. For all these peptides, kinetic parameters k_{on} and k_{off} are available[149]. Prolonged dissociation can be observed for these peptides in bivalent SPR assays with dimeric 1G4 compared to monomeric 1G4 (Fig. 6.7A and B), particularly notable for peptides 6V and 3Y with affinities of 22 µM and 47 µM, respectively. However, for the lower affinity peptides 4D and 6T with affinities of 140 µM and 162 µM, respectively, the difference in dissociation becomes very small. While the fits demonstrated good agreement during the dissociation phase, the algorithm struggled to fit the steady-state phases, as evidenced by noisy fits.

When plotting the parameters measured for all six peptides, including 9V and 3A, against the published monovalent parameters, we observed that the k_{off} values correlate well (Fig. 6.7C). However, the k_{on} values returned from the bivalent SPR are significantly lower than the

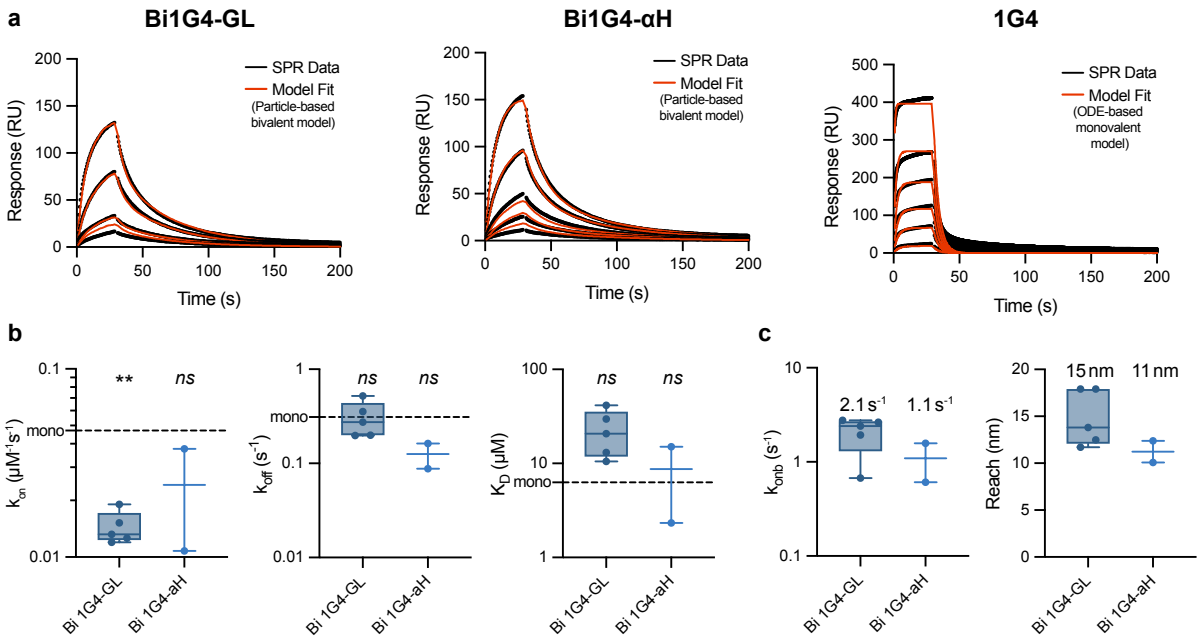

Figure 6.6: Dimeric 1G4 binding to 3A peptide returns the same k_{off} values as monomeric 1G4. **(A)** Representative SPR sensograms of dimeric 1G4, dimerised with DC-GL (Bi1G4-GL) (left), 1G4 dimerised with DC-αH (Bi1G4-αH) (centre) and monomeric 1G4 (right), binding pMHC 3A immobilised at 750 RU. The TCR is injected as a dilution series with increasing concentrations, the highest concentration was 0.76 µM, 0.77 µM and 65 µM for Bi1G4-GL, Bi1G4-αH and 1G4, respectively. The data was fit with either the bivalent particle model for dimeric 1G4, or a monovalent binding model for monomeric 1G4. **(B)** Binding parameters k_{on}, k_{off} and K_D measured for Bi1G4-GL and Bi1G4-αH in comparison to published parameters obtained from monovalent interaction (N= 5 for Bi1G4-GL and N= 2 for Bi1G4-αH). **(C)** Bivalent binding parameters $k_{on,b}$ and reach measured for Bi1G4-GL and Bi1G4-αH. (N= 5 for Bi1G4-GL and N= 2 for Bi1G4-αH). A t-test with Dunnett's multiple comparison correction on log-transformed values was used to determine p-values.

published k_{on} values. The discrepancy is higher for lower k_{on} values, with up to a 30-fold difference.

The algorithm performs a global fit, simultaneously fitting all curves. Precise determination of TCR concentration is crucial for accurately fitting the steady-state response and k_{on} values. The observed failure to fit the steady-state response adequately, alongside the observed low k_{on} values, points to discrepancies in estimating the concentration of Bi1G4 TCR among different injections. This discrepancy persists across multiple experiments and TCR preparation batches, suggesting that it is unlikely to be experimental errors in SPR or the subsequent data fitting. The discrepancies may arise due to the presence of protein aggregates in the sample, which could change the amount of active protein present in each dilution.

For all peptides tested, $k_{on,b}$ and reach were not significantly different between peptides (Fig. 6.7D), implying that these parameters are dictated by the Bi1G4 TCR structure and are independent of the pMHC. However, pMHCs with affinities exceeding 40 µM show substantial

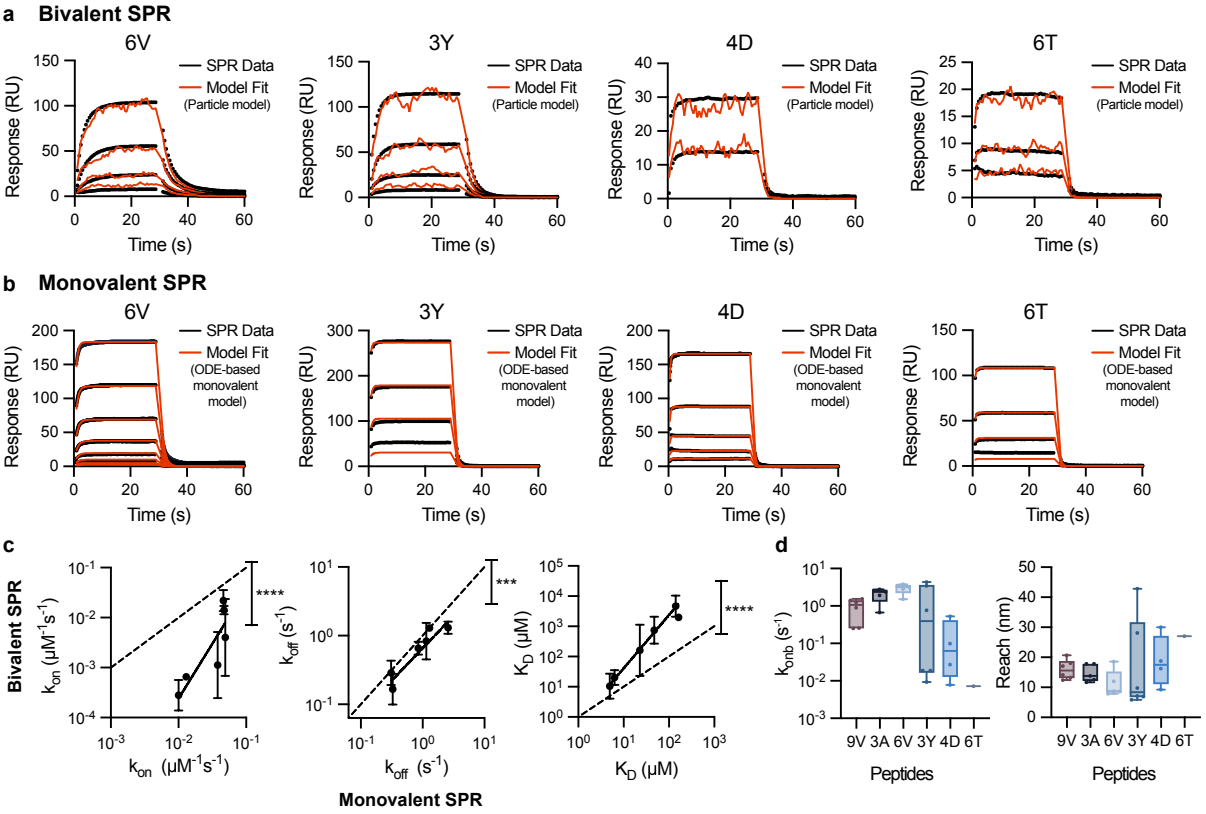

Figure 6.7: Dimeric 1G4 returns correct k_{off} values but not k_{on} values. **(A)** Representative bivalent SPR traces produced by injecting Bi1G4-GL over immobilised pMHC with indicated immobilisation levels. TCR was injected using a 2-fold dilution series. **(B)** Representative monovalent SPR traces produced by injecting monomeric 1G4 over same pMHC surface as in (A). **(C)** Comparison of binding parameters k_{on}, k_{off} and K_D for six peptides obtained with dimeric 1G4 with published values from monovalent 1G4 taken from Aleksic et al.[149]. The dashed line displays perfect agreement (y=x). An F-test was used to determine a p-value for the null hypothesis that the dashed line and the fitted line to log-transformed binding parameters were equal. **(D)** The bivalent binding parameters $k_{on,b}$ and reach for Bi1G4-GL binding to six different peptides. Abbreviations: ns = $p > 0.05$, * = $p \leq 0.05$, ** = $p \leq 0.01$, *** = $p \leq 0.001$, **** = $p \leq 0.0001$.

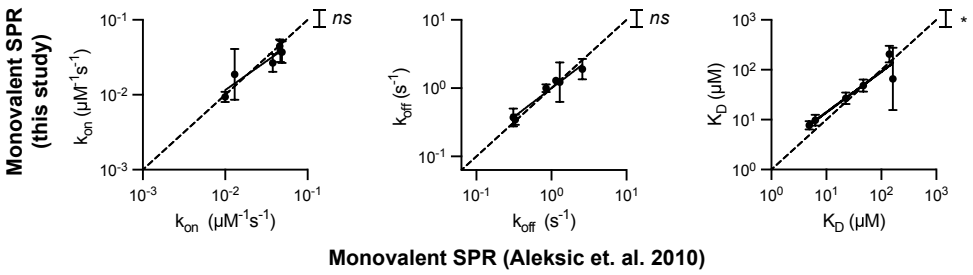

Figure 6.8: Monomeric 1G4 returns correct binding parameters. Comparison of binding parameters k_{on}, k_{off} and K_D for six peptides obtained with monomeric 1G4 (representative data shown in Fig. 6.7B) with published values taken from Aleksic et al.[149]. The dashed line displays perfect agreement (y=x). An F-test was used to determine a p-value for the null hypothesis that the dashed line and the fitted line to log-transformed binding parameters were equal. Abbreviations: ns = $p > 0.05$, * = $p \leq 0.05$, ** = $p \leq 0.01$, *** = $p \leq 0.001$, **** = $p \leq 0.0001$.

variability in the bivalent binding parameters. This variability suggests that the algorithm struggles to uniquely identify parameters that allow the model to accurately fit the data, possibly due to limited data points in the association and dissociation phases. Using the fitted parameters from the 9V, 3A, and 6V pMHCs, each with an affinity below 22 µM, we derived an average $k_{on,b}$ of $1.0\,s^{-1}$ and a reach of 15 nm.

In each SPR experiment, we injected the 1G4 monomer after the Bi1G4 dimer, allowing us to derive k_{on}, k_{off}, and K_D values from the 1G4 monomer by fitting a monovalent model to the data. The monovalent data yielded precise k_{on}, k_{off}, and K_D values, even for peptides exhibiting rapid dissociation (Fig. 6.8).

Overall, while the bivalent method effectively yields accurate k_{off} values, it provides estimates of k_{on} that differ from those measured using monovalent TCR. The fast kinetics of these interactions means that for interactions with a monovalent K_D larger than approximately 160 µM (with k_{off} values larger than approximately $3\,s^{-1}$) the limited number of data points during association and dissociation phases reduces the ability of even bivalent SPR to accurately estimate kinetics. However, for interactions with K_D values below approximately 160 µM, the monomeric 1G4 suffices for measuring kinetic parameters, rendering the bivalent SPR method unnecessary.

6.2.3 *Bivalent SPR with dimeric OT-I TCR*

We next applied the bivalent SPR method to study the interaction between dimeric OT-I TCR and its target peptide, N4-pMHC. Dimeric BiOT-I-GL dimerised using the DC-GL displayed a visibly prolonged dissociation rate, with a half-life of 0.7 s compared to <0.3 s for the OT-I monomer (Fig. 6.9A). When fitting the data with the particle-based model, we obtained the same k_{on} as previously determined for monomeric OT-I (see Fig. 4.2), whereas k_{off} was threefold lower than measured for monomeric OT-I (Fig. 6.9B). This results in a corresponding threefold reduction in K_D. Notably, a $k_{on,b}$ of 8.17 was observed, alongside a reach of 9.2 nm (Fig. 6.9C). The reach measured with the BiOT-I-GL was notably lower than for dimeric Bi1G4-GL, dimerised with the same DoubleCatcher. A possible explanation is that $k_{on,b}$ and reach were not identifiable so many combinations of different values for these parameters led to a similar quality in the fit.

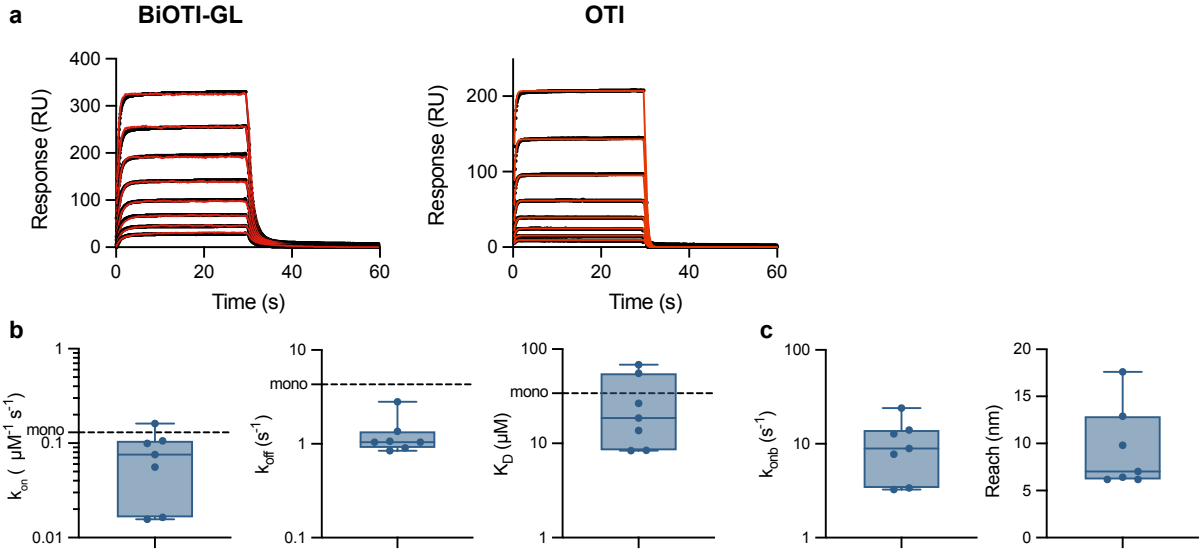

Figure 6.9: Dimeric OT-I TCR binding its cognate peptide N4. **(A)** Representative SPR sensograms of dimeric OT-I, dimerised with DC-GL (BiOTI-GL) (left), and monomeric OT-I (right), binding to pMHC N4 immobilised at 1000 RU. The TCR is injected as a dilution series with increasing concentrations, the highest concentration for was 10 µM and 17 µM for BiOT-GL, and 1G4, respectively. The data was fit with either the bivalent particle model for dimeric OT-I, or a monovalent binding model for monomeric OTI. **(B** Binding parameters k_{on}, k_{off}, K_D returned from biavalent SPR compared to parameters obtained from monomeric OT-I in Chapter 3 (see Fig. 4.1 and 4.2) **(C)** Bivalent binding parameters $k_{on,b}$ and reach for dimeric OT-I binding N4 peptide.

We generated bivalent binding curves for further interactions between OT-I and pMHCs (Fig. 6.10A). For low-affinity peptides, association and dissociation even with the dimeric OT-I TCR were too rapid to be observed. The steady-state binding response was plotted against

TCR concentration, with molar concentrations converted to mass concentration to adjust for differences in protein mass between dimer and monomer (Fig. 6.10B). Dimeric OT-I exhibited enhanced binding for peptides A2, Q4, and Q4R7, all having K_D values below 250 µM, whereas no enhanced binding was evident for the Catnb peptide with a K_D of 1400 µM. Next, we fitted the curves with the particle model. Given that the dimeric 1G4 TCR exhibited higher binding and that the particle model produced excellent fits to the bivalent SPR, we decided to fix the bivalent parameters (reach, $k_{on,b}$) to the values obtained with this TCR when fitting the OT-I data. The rapid kinetics for the OT-I TCR means that even for the dimeric OT-I, we expected no accurate determination of k_{on} and k_{off}. Nonetheless, we reasoned that we would still be able to estimate the value of K_D. However, the fitted K_D values from the bivalent SPR do not align with K_D values from monovalent experiments (Fig. 6.10C).

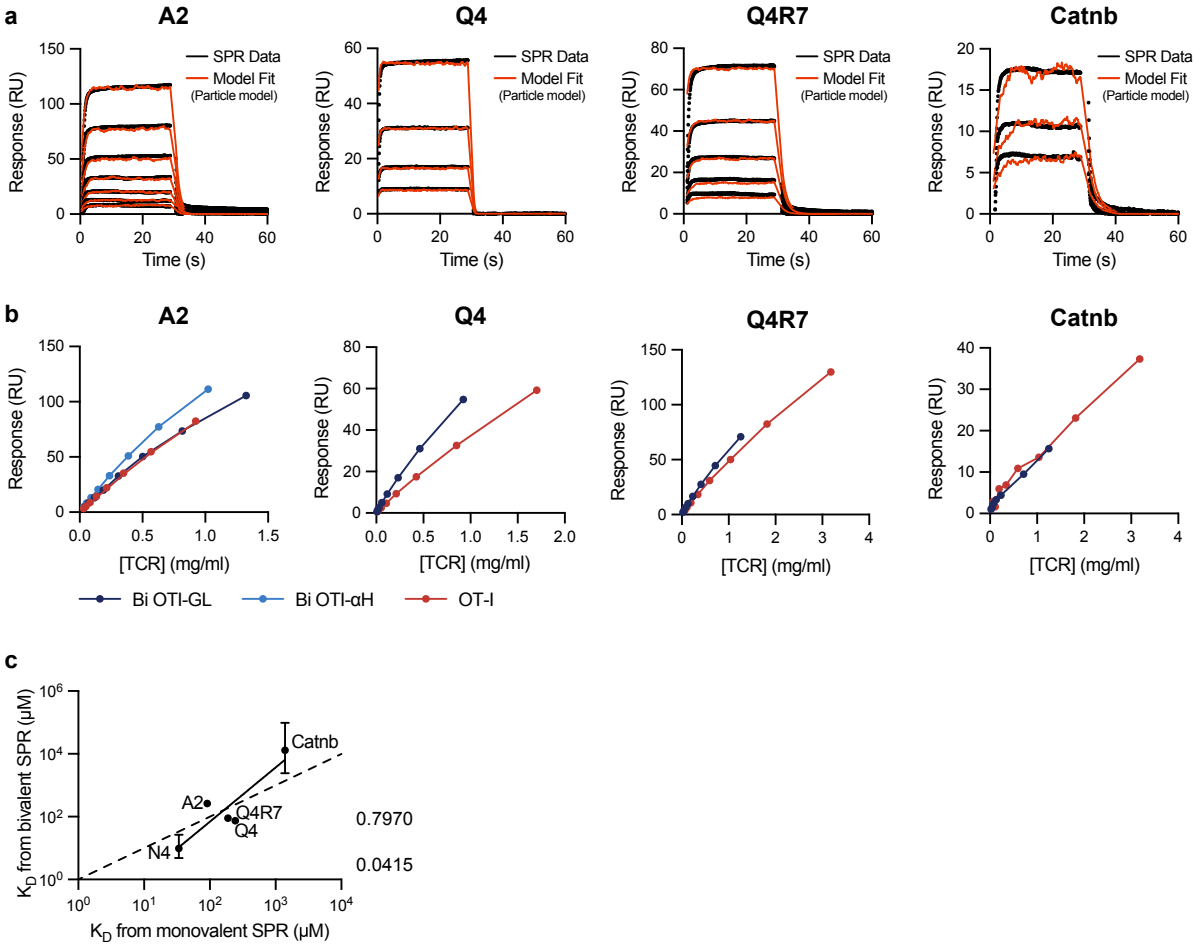

Figure 6.10: Dimeric OT-I binding low-affinity peptides. Representative SPR curves of dimeric OT-I (**(A)**) and corresponding equilibrium binding values over TCR concentration (**(B)**) for peptides A2, Q4, Q4R7 and Catnb. **(C)** Comparison of K_D values obtained from bivalent SPR with K_D values from monovalent SPR (see Fig. 4.5).

6.2.4 *Simulation of possibilities of the dimeric TCR approach*

Dimeric OT-I binding experiments revealed that at lower affinities, the dimer does not exhibit stronger binding compared to the monomer, suggesting that it binds predominantly monovalently. Calculating the theoretical probability of bivalent binding for the dimeric TCR provides insight into behaviour at lower affinities and enables us to explore the limitations and future optimisations of this method (Fig. 6.11).

When a dimeric TCR (or any homodimeric molecule), in the following equations denoted as A, is bound with one arm to one ligand, it can either unbind with the dissociation rate k_{off} or bind a second ligand within reach with the bivalent association rate $k_{on,b}$. The probability of each of these reactions to occur is determined by the rate and the concentration of available free ligands within reach $[L]_{avail}$.

$$AL \rightarrow A + L : \qquad k_{off} \tag{6.1}$$

$$AL + L_{avail} \rightarrow ALL : \qquad k_{onb} \times [L]_{avail} \tag{6.2}$$

The theoretical probability of bivalent binding for the dimeric TCR, i.e. for the second of the above reactions to occur, can be calculated by dividing the probability of the reaction by the sum of probabilities for all possible reactions. The probability of bivalent binding is then given by the following equation:

$$P = \frac{k_{on,b}[L]_{avail}}{k_{off} + k_{on,b}[L]_{avail}} \tag{6.3}$$

$[L]_{avail}$ is calculated as the average number of ligands within reach at a given antigen density:

$$[L]_{avail} = [L] \times \frac{4}{3}\pi \text{Reach}^3. \tag{6.4}$$

We first calculated the theoretical probability of bivalent binding for the dimeric TCR with a reach of 15 nm for a range of k_{off} values (Fig. 6.11 left). This probability is influenced by k_{off}, $k_{on,b}$, reach and antigen density. When k_{off} is small, indicating a high-affinity interaction, the probability of bivalent binding approaches 1. However, as ligand affinity decreases, the probability decreases accordingly, with $k_{off} = 10\,s^{-1}$ failing to reach even 0.5 probability at high antigen densities. Conversely, at low affinities, where k_{off} greatly exceeds $k_{on,b}$ x $[L]_{avail}$, the

probability approaches zero (see k_{off} = 100 s^{-1}), indicating predominant monovalent binding behaviour for low-affinity peptides.

The experimentally observed reach of 15 nm for the dimeric TCR is relatively small. To increase bivalent binding, one solution is to increase reach which would increase the number of nearby antigens. We simulated the binding of dimeric TCR with a larger reach of 35 nm, akin to that of an antibody (Fig. 6.11 right). A larger reach substantially increases the probability of bivalent binding, enabling even ligands with very low affinity (k_{off} = 100 s^{-1}) to exhibit some probability of bivalent binding.

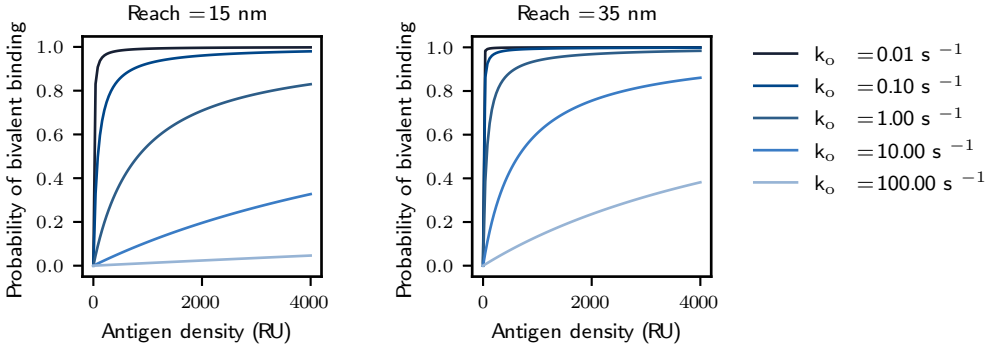

Figure 6.11: Probability of bivalent binding varies with k_{off}, reach and antigen density. Probability of an analyte to bind bivalently according to our particle model over ligand density. Curves show the behaviour of analytes with different k_{off} values and with a reach of 15 nm and 35 nm. The value for $k_{on,b}$ was fixed to 1.0 s^{-1}

To illustrate this visually, we simulated SPR curves for monovalent TCR, bivalent TCR with a reach of 15 nm, and bivalent TCR with a reach of 35 nm. Additionally, we plotted equilibrium binding over concentration to evaluate the influence of bivalent binding on the overall response (Fig. 6.12). The simulations reveal that a TCR dimer with a reach of 35 nm displays a prolonged dissociation compared to a dimer with a reach of 15 nm for k_{off} values smaller than 10 s^{-1}. However, even with an extended reach, the kinetics of interactions cannot be resolved for $k_{off} \geq 10\,s^{-1}$. Nevertheless, at this k_{off} value, there is a noticeable increase in the amount of bound protein compared to the monomer, while no additional binding is observed with the dimer with a smaller reach of 15 nm. A slight enhancement in binding is also observable at k_{off} = 100 s^{-1}.

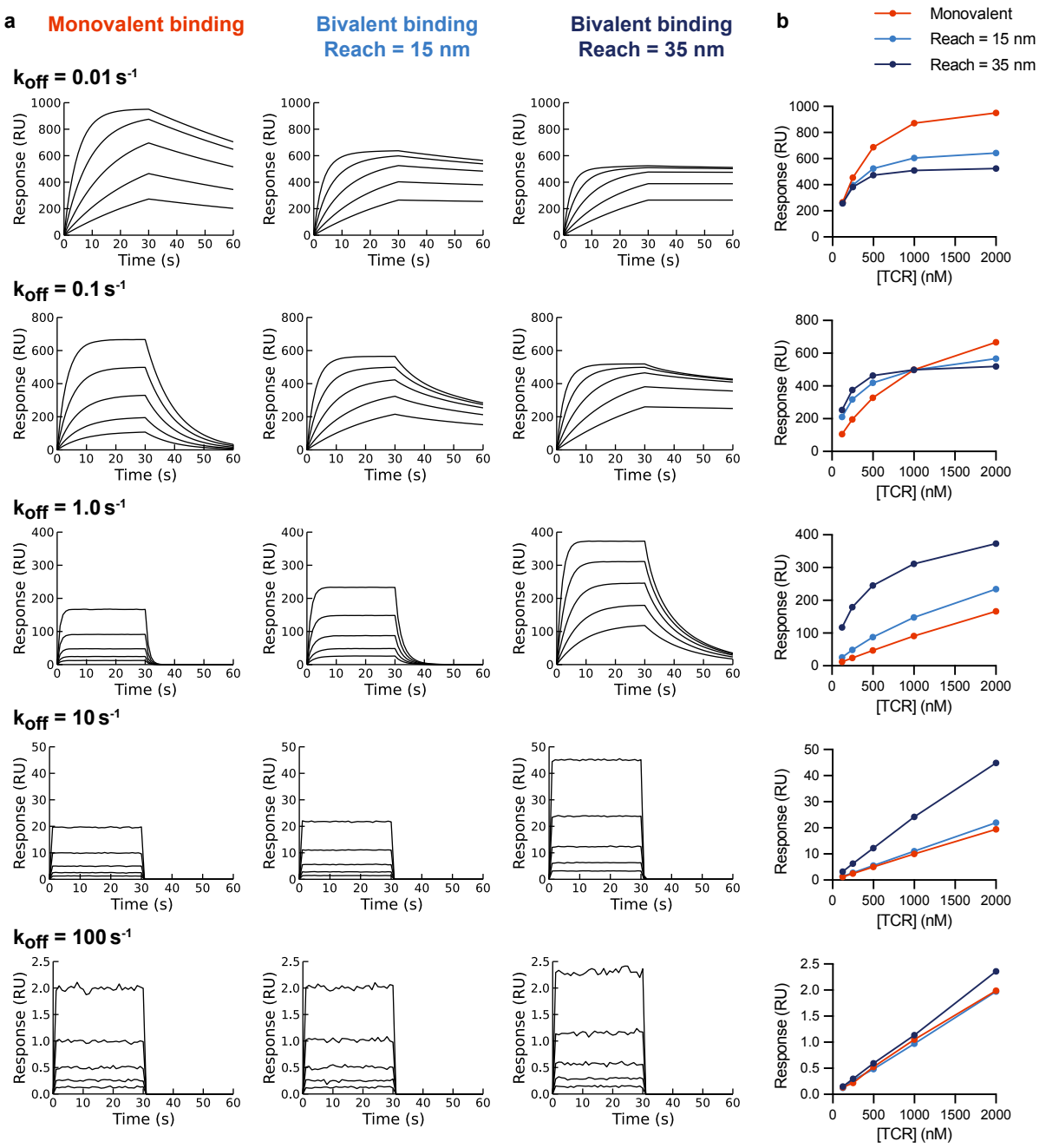

Figure 6.12: Simulated SPR curves show improvement of binding only for high-affinity peptides. **(A)** Simulated SPR binding curves for analytes with different k_{off} values with the particle model. Reach was set to 0.01 nm to simulate monovalent binding (left). Bivalent SPR curves were simulated for an analyte with a reach of 15 nm (centre) and 35 nm (right). **(B)** Equilibrium binding values over analyte concentration from the respective binding curves in (A) for bivalent and monovalent analytes.

6.3 *Discussion*

In this chapter, efforts were made to implement a method that uses dimeric TCR for measuring rapid TCR/pMHC binding kinetics. We showed that this method accurately determines k_{off}

values for interactions between the 1G4 TCR and pMHC with an off-rate less than $3\,s^{-1}$, yet it produced estimates of k_{on} that differed from those measured using a monovalent TCR. In this high-affinity regime, the dimeric TCR method performed similarly to the monovalent measurements. Applying the method to OT-I interactions, we found that we could not determine the dissociation rate for any peptides apart from N4, as a result of fast kinetics. Additionally, the fitted K_D values for the low-affinity OT-I interactions did not replicate the previously measured K_D values using the ultra-low affinity SPR method in Chapter 4.

The steady-state binding values revealed that the dimer TCR does not show improved binding for self pMHCs with $K_D > 1000\,\mu M$, suggesting that the dimeric TCR primarily engages in monovalent binding. Calculations of the theoretical probability of bivalent binding show that the probability of bivalent binding for off-rates $>10\,s^{-1}$ is almost zero. Simulations of SPR curves further demonstrated that a TCR dimer with an extended reach has a higher probability of bivalent binding and exhibits prolonged dissociation times compared to one with a shorter reach for lower k_{off} values. However, this also cannot resolve interaction kinetics when k_{off} is $>10\,s^{-1}$. However, a dimer with a larger reach still shows improved steady-state binding for k_{off} values up to $100\,s^{-1}$ compared to the monomer.

When fitting binding curves of interactions between the 1G4 TCR and pMHCs with affinities greater than $10\,\mu M$, the particle model struggled to fit the association and steady-state phases of the binding curves. This problem may be caused by an incorrect concentration ratio, possibly due to protein aggregation. Although no obvious aggregation was visible on SDS-PAGE, it could potentially be below the detection limits of this method. Due to the large size of the TCR dimer, it elutes early during the SEC, possibly along with aggregates of similar size. To improve the purity of the dimer, one approach could involve first purifying the 1G4 monomer using SEC, followed by dimerisation and another round of purification with SEC. Furthermore, the 1G4 TCR used did not contain any disulfide bonds between the α and β chain. Its stability could be improved by introducing engineered disulfide bonds.

For interactions with fast kinetics, measurement of k_{off} and k_{on} could be improved by using the Creoptix WAVEsystem, as done for the kinetic measurements in Fig. 4.2. The increased sample rate of 40 Hertz and parallel flow cells of the WAVEsytem instrument increases the amount of data points in the association and dissociation phase

The molecular reach of the dimeric TCR

The particle model measured the reach of the TCR dimer to be approximately 15 nm. Driscoll et al.[302] estimated the average distance between the reactive lysine residues of each SpyCatcher domain for different versions of their DoubleCatcher protein using the AlphaFold structure. For the DoubleCatcher with the $[GSG]_3$ linker, the distance is approximately (3.6 ± 0.7) nm, for the DoubleCatcher with a α Helix linker, the distance is (2.7 ± 0.4) nm[302]. Together with the length of the TCR/pMHC complex ($\sim$14 nm)[24] we can estimate the theoretical reach of the TCR dimer to be approximately 31 nm ($2 \times 14\,\text{nm} + 3.6\,\text{nm} = 31.6; 2 \times 14\,\text{nm} + 2.7\,\text{nm} = 30.7$). The length of the pMHC was included in this calculation as we saw in Chapter 5 that the size of the antigen contributes to the molecular reach. There is a large discrepancy between the theoretical reach and the measured reach of 10 nm-15 nm. The TCR dimer may be in a conformation that does not allow it to stretch out fully to maximise its reach. Driscoll et al.[302] have developed further variants of the DoubleCatcher with different distances, rigidity and orientations of the SpyCatcher domains. Using other DoubleCatcher versions might improve the bivalent binding of the TCR dimer.

Further improvements

Simulations of binding showed that a TCR dimer with a larger reach has a higher probability of bivalent binding, consequently increasing the binding response even for low-affinity pMHCs. A TCR with a larger reach, similar to an antibody, could for example be achieved by by fusing the TCR onto an IgG antibody. For this, the variable domains of the antibody would be replaced by the TCR variable and constant domains. TCR fusion proteins have already been successfully engineered, and have shown increased expression and binding affinity[305,306]. Another strategy to increase the binding of TCR to pMHC could involve increasing the valency, such as by generating TCR tetramers. However, this approach could only be employed if the bivalent particle model is adapted for tetrameric interactions. Undoubtedly, further refinement and optimization of this dimeric TCR binding method are needed. This method is only useful if it outperforms binding measurements performed with the monomer, especially when off-rates exceed $5\,s^{-1}$.

The work presented in this chapter shows that the bivalent particle-based model opens up new opportunities for studying biomolecular interactions beyond antibody interactions. Beyond its application in TCR-pMHC interactions, the bivalent SPR holds promise for studying various low-affinity protein interactions. These could include interactions between the Notch receptor and its ligands, which can have a K_D of up to 130 μM[307,308], or the GPCR interaction with metabolic molecules that have been difficult to study so far due to their low affinity[309].

7

CONCLUSION AND FURTHER IMPLICATIONS

The central theme of this thesis was to understand how antigen binding affects the functional response of lymphocyte antigen receptors. The thesis focused on two particular questions: How the TCR discriminates between foreign and self-antigens, and how antigen-antibody interaction drives the effectiveness of antibodies. To address these questions, more sensitive SPR methods and improved binding models were developed in this thesis, allowing the systematic and quantitative study of antigen-receptor interactions.

As for the first question, T cells use their TCRs to discriminate between lower-affinity self and higher-affinity foreign antigens. Early studies on murine TCRs originally showed that T-cell discrimination is perfect, meaning a small decrease in antigen affinity can abolish T-cell responses completely. However, the strength of this discrimination had not yet been quantitatively determined. In Chapter 3 of this thesis, the discrimination strength for a range of TCR systems was investigated by conducting a systematic literature analysis. In most of the studied systems functional response correlated with affinity; this allowed us to introduce a new quantitative measure of discrimination called discriminatory power alpha. Going through two decades of published work, we found that the mean discriminatory power is $\alpha = 2$. This means that a decrease in affinity can be compensated with an increase in concentration that is squared the fold-change in affinity. For example, a decrease in affinity by 5-fold can be compensated by a 25-fold increase in antigen concentration. This demonstrated that contrary to the original experiments, the antigen discrimination is imperfect. This level of discrimination can be explained with the standard kinetic proofreading model. While the discrimination was found to be imperfect, TCR was shown to have enhanced discrimination abilities when compared to other ligand receptors, which showed baseline discrimination ($\alpha \leq 1$).

This result was further validated in Chapter 4 by measuring the affinities between the OT-I TCR and a wide range of variant peptides at physiological temperatures. This included naturally occurring self-peptides and revealed that their affinity is 40 to 100 times lower than the cognate peptide. While these results confirmed an enhanced but imperfect discrimination, fitting the kinetic proofreading model to the data revelead in a notably faster proofreading time of 0.17s compared to other TCRs. This questions whether the OT-I should be used as a standard TCR for experiments.

To help understand this discrepancy, we decided to examine the kinetics of the OT-I/pMHC interaction. However, obtaining precise kinetic data of the interaction is hindered by its rapid kinetics that cannot be resolved with our current methods. Chapter 6 therefore focused on the development of a bivalent SPR method to measure ultra-fast kinetics of interactions. It drew inspiration from the bivalent antigen binding of antibodies. By dimerizing two TCR proteins, bivalent binding could be utilized to slow down the binding kinetics for accurate measurement of the kinetic rates. The method proved effective for high-affinity interactions but further improvements in the structure of the TCR dimer are necessary to make the method useful for low-affinity interactions.

In conclusion, this work disproved the longstanding belief of perfect TCR discrimination. It shows the need to revisit scientific data and conclusions drawn thereof when discrepancies arise, even when these conclusions are widely accepted in the scientific community.

The second question of this thesis focused on how antibodies bind to and neutralize pathogens. While their binding strength is believed to be an essential determinant of their function, so far no consistent correlation with affinity of the interaction and function had been established. In order to figure out what intrinsic property of their antigen-binding interaction determines their functional efficiency, Chapter 5 presented a particle-based bivalent model for obtaining monovalent and bivalent binding parameters from SPR bivalent data. The new model accurately quantified the bivalent interaction of 45 IgG1 antibodies binding the RBD of the SARS-CoV-2 spike protein. The interaction is guided by the monovalent binding rates (k_{on} and k_{off}) which describe the interaction of each binding site, and the bivalent parameters ($k_{on,b}$ and molecular reach) that quantify the ability for bivalent binding. We found that molecular reach plays a fundamental role in determining the neutralization potency of antibodies. Overall, the neutralization potency can be fully explained by a combination of monovalent and bivalent

parameters and epitope location. Using the particle-based bivalent model, it was then possible to predict the absolute neutralization potency of antibodies. This has been a hugely collaborative project between researchers from mathematics, biochemistry, and virology. Our work provides a method for the scientific community that may improve the design of antibodies and vaccines.

Overall, the work presented in this thesis plays a part in advancing our understanding of how the biophysical properties of an interaction directly inform the functional response. This thesis provides a link between the structure of antigens and lymphocyte antigen receptors and their function, which was not readily observable before. Furthermore, this thesis demonstrates that improved methods and more precise quantification of binding interaction are required to identify the link and understand the mechanism of molecular recognition.

7.1 Future implications

The results presented in this thesis have future implications for other unresolved questions in the field, as discussed below.

How can precise characterisations of TCR/antigen interactions improve our understanding of T-cell activation?

Despite the TCR's ability to sense and respond to interactions with self-antigens, our current techniques for measuring protein interaction are not sensitive enough to resolve the fast kinetics of this interaction. Our ability to measure dissociation kinetics is particularly limited, with a maximum of $10\,s^{-1}$ [275], leaving many low-affinity interactions beyond our detection threshold. There are various models proposed for antigen discrimination which rely on different biophysical properties of the TCR-antigen interaction. Occupancy models emphasize affinity, while standard kinetic proofreading models focus on bond lifetime (k_{off}). Other models have suggested the importance of k_{on} by introducing a confinement time or sequential triggering [94,149,310]. In order to test which of these models recapitulate what is happening in the cell, we need to know the affinity as well as the kinetic parameters k_{on} and k_{off} of the

TCR/antigen interaction. To address this, further optimisation of protein binding measurement methods is essential to accurately measure ultrafast kinetics[311].

Beyond antigen discrimination, obtaining more quantitative data on TCR-antigen interactions can further help in understanding the dynamics of signal integration in the TCR signalling pathway. During activation T-cells integrate multiple signals from antigen recognition, such as interaction affinity and antigen concentration, alongside signals from co-signalling receptors and cytokines. Questions remain about how the signalling pathway achieves a switch-like response and how signals from co-signalling receptors such as CD28 and PD1 are integrated[312,313]. The complexity of the signalling pathway makes it challenging to intuitively comprehend the dynamic processes and it is difficult to experimentally measure the protein dynamics. Hence we need mechanistic models that we can test against experimentally observable data. For this, we need precise data on antigen affinity and T-cell response, which will help us create a model to accurately predict the immune response.

Which protein dynamics give rise to kinetic proofreading?

This thesis presented evidence that enhanced antigen discrimination is not an intrinsic feature of the TCR, but rather that it is encoded by the proximal signalling pathway. Furthermore, the discrimination can be explained using the kinetic proofreading model. This leads to the question of which signalling proteins are responsible for antigen discrimination. The phosphorylation of ITAMs as well as the recruitment and activation of signalling proteins Lck, ZAP70 and LAT have been suggested as individual proofreading steps[148,240,248,314]. Proteins in the signalling cascade can be a starting point for improving immunotherapies. Modifying enzymes within the TCR signalling pathway to increase antigen discrimination strength presents an opportunity to decrease off-target toxicity in TCR/CAR T-cell therapies. Off-target recognition is a major concern in these therapies. This is demonstrated by a clinical trial involving MAGE-A3 specific TCR-engineered T-cells, which caused fatal cardiac toxicity due to cross-reactivity with an unrelated epitope from the Titin protein presented on cardiac tissue[315,316]. Current strategies to reduce off-target toxicities focus on identifying potential off-targets through *in vitro* experiments before the therapy is moved to clinical trials. In these methods, the response of T cells carrying a specific TCR is tested against a peptide library including peptides where the amino acids of the target peptide are individually mutated to alanine (alanine scanning), or a combination

of all possible amino acid sequences (combinatorial peptide library scanning). This allows the identification of amino acid positions that are important for peptide recognition, which can be used to identify self-protein derived peptide sequences with this motif[317]. However, these methods may not identify all possible cross-reactivities. In contrast, increasing the discriminatory strength of T cells through signalling pathway modification can prevent them from responding to any potential self-antigen.

The kinetic proofreading may also exist in other proteins of the NTR family that the TCR belongs to. For example, BCRs and Fc Receptors have a similar downstream signalling pathway as the TCR. Both use ITAM phosphorylation for receptor triggering and rely on the phosphorylation of scaffold protein to recruit downstream signalling molecules (protein BLNK in the BCR pathway, and LAT in the Fc receptor pathway). It may be of interest whether BCRs and Fc receptors exhibit a similar enhanced antigen discrimination strength as the TCR. Kinetic proofreading has been proposed for both the BCR and the Fc receptor[311,318,319]. This thesis showed that the discriminatory power of the BCR is greater than 1, indicating enhanced discrimination; however, this conclusion is based on only very few data points. Understanding antigen discrimination by BCRs and Fc receptors could provide insights into shared signaling motifs and mechanisms involved in this process which are also found with the TCR. Kinetic proofreading reduces error rates in various cellular processes that require decision-making, such as ensuring the correct loading of tRNAs with their respective amino acids and in homologous recombination for DNA damage repair. It is likely that this mechanism is employed in other cellular pathways to enhance accuracy. Understanding the dynamics underlying the kinetic proofreading motif in the TCR may help identify similar motifs in other cellular processes. One area of potential investigation could be the cell cycle checkpoints that serve to ensure the accurate progression of cellular division. These checkpoints are critical in upholding genomic stability and preventing aberrant cell proliferation. One example of kinetic proofreading may be the checkpoint signalling linked to microtubule-kinetochore attachment, which has recently been shown to involve multiple rounds of phosphorylation and dephosphorylation, resembling ITAM phosphorylations on the TCR[320].

What are the implications for imperfect discrimination in autoimmune diseases?

Understanding the link between antigen binding and functional response of T cells, B cells and antibodies may be important in understanding the causes of autoimmune diseases. Autoimmune diseases are a diverse group of conditions characterized by a disturbance of immune tolerance that causes T and B cells to mistakenly target endogenous tissues of the host. The underlying causes can be varied and are far from understood[321]. Research heavily focuses on the dysregulation of T and B cell reactivity, often associated with genetic predispositions affecting various immune processes such as chemotaxis, cytokine production, and complement activity. Additionally, disruptions in thymic selection and the development of regulatory T cells can contribute to immune tolerance breakdown and the onset of autoimmune reactions. There is also a strong genetic association of certain MHC alleles with autoimmune diseases, likely because of the role of MHC molecules in presenting self-antigens for T-cell recognition[322]. Further causes of autoimmune reactions involve mutations that lead to the presentation of immunogenic self-peptides, this also includes changes in the post-translational modifications of proteins or the production of misfolded proteins[321]. Infections are believed to trigger autoimmune responses through mechanisms such as non-specific inflammation or molecular mimicry, where structural similarities between self and foreign molecules lead to cross-reactivity with self-peptides[126,323,324].

This thesis showed that antigen discrimination by TCRs is not perfect. Small changes in affinity can be compensated by an increase in the concentration of ligand, which introduces another possibility for the onset of autoimmune reactions; self-antigens that are expressed at higher than normal concentrations could lead to T cell activation. Higher than normal self-antigen expression could also lead to antibody recognition. This thesis explained how antigen density affects antibody function due to the bivalent binding ability of antibodies. This can be applied to autoimmune reactions; at low antigen density, antibodies bind monovalently and are not able to induce an immune response. However, when the density of self-peptides increases, antibodies may be able to bind bivalently and therefore have an increased binding strength which could trigger an immune response. If elevated self-antigen presentation can trigger T cells and antibodies, it could explain autoimmune reactions without a clear connection between the antigen specificity and the target location of the autoimmune reaction[321], for example when the autoantigen is widely expressed in many tissues, but the autoimmune

reaction only occurs in a specific tissue. In such cases, it may be important to search not only for the specific autoantigens but also for an increased expression of the antigen in the targeted tissues.

Additionally, T cell response to elevated self-antigen levels may be crucial in explaining the "autoimmune surveillance of hypersecreting mutants" (ASHM) hypothesis regarding the onset of autoimmune diseases[234]. The hypothesis proposes that self-reactive T cells play an important functional role in healthy individuals. According to this hypothesis, self-reactive T cells detect and eliminate hypersecreting cells in endocrine organs that could threaten organismal homeostasis. This can result in a vulnerability to autoimmune disease and it would be only selected when the cost of hypersecretion exceeds the cost of autoimmunity. Imperfect discriminations would allow T cells to respond to hypersecreting cells that present large amounts of self-antigens derived from proteins in the secretion pathway.

How can we optimise the effector function of antibodies?

The characterisation of bivalent antibody binding opens up new opportunities for identifying and optimising antibodies for therapeutic applications. Depending on the application, different binding properties may need to be optimized. For instance, neutralising antibodies raised against the malaria parasite surface protein PfRH5 need to have a very fast on-rate because the protein is only accessible for a few minutes before the parasite infects blood cells[325]. Another example is the development of bispecific antibodies, where the length and flexibility of the interchain linker have important consequences on the effector function[326–328].The bivalent binding ability should also be considered when selecting an epitope for antibody binding, because, as shown here, the antigen contributes to the overall reach. The thesis has revealed the significant impact of molecular reach on the function of an antibody. This finding raises interesting questions about the optimisation of antibody reach during evolution and whether there are evolutionary selection pressures that limit the size of the reach.

Can we predict receptor antigen interactions?

There is a growing interest in predicting the specificities of lymphocyte antigen receptors computationally, specifically the prediction of TCR/antigen interactions and antibody/epitope interactions. These predictions have significant potential for advancing the fields of immunotherapy and drug design, offering a more targeted approach to disease treatment and prevention. For example, the ability to predict TCR antigen interactions has promising applications in personalized cancer immunotherapy, identifying antigens of autoreactive T cells in autoimmune diseases, reducing graft rejection in organ transplantation, and as a diagnostic tool. Similarly, predicting antibody epitope interactions could assist in the development of therapeutic or diagnostic antibodies, by identifying and optimizing specific antibodies, identifying autoantigens in autoimmune diseases, and may inform vaccine design[329,330]. Recent improvements in machine learning algorithms have led to significant progress in epitope prediction[331]. However, predicting epitopes that have not been encountered in the training set remains challenging due to the high diversity of interacting protein structures and the limited amount of available training data[332]. The existing data are obtained through assays that do not cover a broad range of epitopes and cannot accurately capture differences in affinity of the different receptor/epitope interactions.

This thesis provides some initial ideas for obtaining better data on receptor/epitope interactions that could improve the predictive power of the algorithms. Firstly, TCR/pMHC affinities could be measured using an ultralow-affinity SPR method. This approach provides data for interactions across a wide range of affinities, including low-affinity interactions such as self-peptide interactions, which are not observable with less sensitive methods commonly used for generating epitope prediction datasets. The BiaCore SPR instrument used to generate most of the affinity measurements presented in this thesis allows the measurement of only three interactions at a time. Therefore generating affinity data on enough interactions for a machine learning training dataset would take a long time. However, other SPR techniques such as the Carterra LSA instrument allow the measurement of up to 384 ligands at once[333], making it a more efficient option. In addition, this thesis proposes a second improvement, which is obtaining antibody/antigen binding parameters from bivalent SPR data. This approach allows for high-throughput screening of antibodies while obtaining both monovalent and bivalent affinity parameters of the interaction.

8

MATERIALS AND METHODS

8.1 Materials

Table 8.1: Antibodies used for SPR

Target	Clone	Supplier	RRID
H-2K (mouse MHC Class I)	Y-3	Leinco Technologies	AB_2737575
Human beta2m	B2M-01	Thermo Fisher Scientific	AB_1070702

Table 8.2: Plasmids

Name	Source	Note
pGMT7-OT1a-HC	David Cole	Expression of soluble OT-I α chain with human constant domain
pGMT7-OT1b-HC-His	David Cole	Expression of soluble OT1β chain with human constant domain and 6xHis Tag
pGMT7-OT1b-HC-ST3	David Cole	Expression of soluble OT1 β chain with human constant domain and SpyTag 003
pET-1G4-sTCRa	Johannes Pettmann	Expression of soluble 1G4 α chain
pET-s1G4b-ST3	Johannes Pettmann	Expression of soluble 1G4 β chain with SpyTag003
pET14b-H2Kb-AviTag	Vincenzo Cerundolo	Expression of soluble mouse MHC $H2K^b$ heavy chain with AviTag at C terminus
pTO-N-human-beta2m	Markus Bridge	Expression of soluble human β_2m domain

Table 8.4: General reagents

Name	Company	Catalog number
4PCP sensor chip	Creoptix	N/A
Amine coupling kit	Cytiva	BR100050
Amplicilin		
BirA biotin-protein ligase bulk reaction kit	Avidity	N/A
BugBuster Protein Extraction Reagent	Millipore	70584-M
Series S Sensor Chip CM5	Cytiva	3E+07
DMSO		
HBS-EP	Cytiva	BR100669
IPTG		
LB		
QIAprep Spin Miniprep Kit	Qiagen	27104
NIH pMHC		
PBS		
Q5 Site-Directed Mutagenesis Kit	NEB	E0554S
TEV protease	NEB	P8112S
Tris buffer		
Urea		

Table 8.5: Buffers

Name	Content
Lysis buffer	10% BugBuster Protein Extraction Reagent 20 mM Tris-HCl (pH 8.0) 150 mM NaCl 1% Triton X-100 0.1 mM PMSF 25 µl of 100 mg/ml lysozyme a pinch of DNAse I
Wash buffer	10% BugBuster Protein Extraction Reagent
Urea buffer	100 mM Tris-HCl (pH 8.0) 8 M Urea 2 mM DTT
TCR refolding buffer	150 mM Tris-HCl (pH 8.0) 3 M Urea 200 mM Arg-HCl 0.5 mM EDTA 0.1 mM PMSF
Dialysis buffer	10 mM Tris-HCl (pH 8.0)
HiTrapQ buffer (Low Salt)	10 mM Tris-HCl (pH 8.5) 10 mM NaCl
HiTrapQ buffer (High Salt)	10 mM Tris-HCl (pH 8.5) 1 M NaCl
HBS-EP	0.01 M HEPES (pH 7.4) 0.15 M NaCl 3 mM EDTA 0.005% v/v Tween20
pMHC Refolding Buffer	100 mM Tris-HCl, pH 8.0 400 mM L-Arg·HCl 2 mM EDTA 5 mM Reduced glutathione 0.5 mM Oxidised glutathione 0.1 mM PMSF

Table 8.7: Instruments and equipment

Name	Company
Äkta pure FPLC	Cytiva
HiTrap Q HP column	Cytiva
Superdex 200 increase 10/300 GL column	Cytiva
Sonicator	Sanyo
Biacore T200 SPR system	Cytiva
Biacore S200 SPR system	Cytiva
WAVEsystem	Creoptix

Table 8.8: Software

Name	Version	Company
Graph Pad Prism	v9-10	GraphPad Software
SnapGene	v4	GSL Biotech LLC
BiaEvaluation	v4.1	Cytiva
WAVEcontrol		Creoptix
Python	3.7.4	N/A
Julia	1.7.2	N/A

8.1.1 Sequences

Sequence 1: Soluble OTI α for expression in *E. coli*. Murine constant domain was replaced with human constant domain with additional cysteine (T159C) for improved refolding and stability.

```
MQQQVRQSPQ SLTVWEGETA ILNCSYEDST FNYFPWYQQF PGEGPALLIS IRSVSDKKED GRFTIFFNKR
EKKLSLHITD SQPGDSATYF CAASDNYQLI WGSGTKLIIK PDIQNPDPAV YQLRDSKSSD KSVCLFTDFD
SQTNVSQSKD SDVYITDKCV LDMRSMDFKS NSAVAWSNKS DFACANAFNN SIIPEDTFFP SPESS
```

Sequence 2: Soluble OT-I β chain with 6x His Tag on C terminus for expression in *E. coli*. Murine constant domain was replaced with human constant domain with additional cysteine (S169C) for improved refolding and stability.

```
MDSGVVQSPR HIIKEKGGRS VLTCIPISGH SNVVWYQQTL GKELKFLIQH YEKVERDKGF LPSRFSVQQF
DDYHSEMNMS ALELEDSAMY FCASSRANYE QYFGPGTRLT VLEDLRNVFP PEVAVFEPSE AEISHTQKAT
```

```
LVCLATGFYP DHVELSWWVN GKEVHSGVCT DPQPLKEQPA LNDSRYALSS RLRVSATFWQ DPRNHFRCQV
QFYGLSENDE WTQDRAKPVT QIVSAEAWGR ADHHHHHH
```

Sequence 3: Soluble OT-I β chain with SpyTag 003 on C terminus for expression in *E. coli*. Murine constant domain was replaced with human constant domain with additional cysteine (S169C) for improved refolding and stability.

```
MDSGVVQSPR HIIKEKGGRS VLTCIPISGH SNVVWYQQTL GKELKFLIQH YEKVERDKGF LPSRFSVQQF
DDYHSEMNMS ALELEDSAMY FCASSRANYE QYFGPGTRLT VLEDLRNVFP PEVAVFEPSE AEISHTQKAT
LVCLATGFYP DHVELSWWVN GKEVHSGVCT DPQPLKEQPA LNDSRYALSS RLRVSATFWQ DPRNHFRCQV
QFYGLSENDE WTQDRAKPVT QIVSAEAWGR ADGGSRGVPH IVMVDAYKRY K
```

Sequence 4: Soluble $H2K^b$ heavy chain with AviTag on C terminus for expression in *E. coli*.

```
MGPHSLRYFV TAVSRPGLGE PRYMEVGYVD DTEFVRFDSD AENPRYEPRA RWMEQEGPEY WERETQKAKG
NEQSFRVDLR TLLGYYNQSK GGSHTIQVIS GCEVGSDGRL LRGYQQYAYD GCDYIALNED LKTWTAADMA
ALITKHKWEQ AGEAERLRAY LEGTCVEWLR RYLKNGNATL LRTDSPKAHV THHSRPEDKV TLRCWALGFY
PADITLTWQL NGEELIQDME LVETRPAGDG TFQKWASVVV PLGKEQYYTC HVYHQGLPEP LTLRWEPPPS
GSLHHILDAQ KMVWNHRGLN DIFEAQKIEW HE
```

Sequence 5: Human β_2m for expression in *E. coli*.

```
MIQRTPKIQV YSRHPAENGK SNFLNCYVSG FHPSDIEVDL LKNGERIEKV EHSDLSFSKDW SFYLLYYTEF
TPTEKDEYAC RVNHVTLSQP KIVKWDRDM
```

Sequence 6: Soluble 1G4 α chain for expression in *E. coli*. No engineered cysteines.

```
MQEVTQIPAA LSVPEGENLV LNCSFTDSAI YNLQWFRQDP GKGLTSLLLI QSSQREQTSG RLNASLDKSS
GRSTLYIAAS QPGDSATYLC AVRPTSGGSY IPTFGRGTSL IVHPYIQNPD PAVYQLRDSK SSDKSVCLFT
DFDSQTNVSQ SKDSDVYITD KTVLDMRSMD FKSNSAVAWS NKSDFACANA FNNSIIPEDT FFPSPESS
```

Sequence 7: Soluble OT-I β chain with SpyTag 003 on C terminus for expression in *E. coli*. No engineered cysteines.

```
MGVTQTPKFQ VLKTGQSMTL QCAQDMNHEY MSWYRQDPGM GLRLIHYSVG AGITDQGEVP NGYNVSRSTT
EDFPLRLLSA APSQTSVYFC ASSYVGNTGE LFFGEGSRLT VLEDLKNVFP PEVAVFEPSE AEISHTQKAT
LVCLATGFYP DHVELSWWVN GKEVHSGVST DPQPLKEQPA LNDSRYALSS RLRVSATFWQ DPRNHFRCQV
QFYGLSENDE WTQDRAKPVT QIVSAEAWGR ADGGSRGVPH IVMVDAYKRY K
```

Sequence 8: DoubleCatcher with $(GLG)_3$ linker.

```
GGAMVTTLSG LSGEQGPSGD MTTEEDSATH IKFSKRDEDG RELAGATMEL RDSSGKTIST WISDGHVKDF
YLYPGKYTFV ETAAPDGYEV ATPIEFTVNE DGQVTVDGEA TEGDAHTGSG GSGGSGVTTL SGLSGEQGPS
GDMTTEEDSA THIKFSKRDE DGRELAGATM ELRDSSGKTI STWISDGHVK DFYLYPGKYT FVETAAPDGY
EVATPIEFTV NEDGQVTVDG EATEGDAGSS GSENLYFQ
```

Sequence 9: DoubleCatcher with α Helix linker.

```
GGAMVTTLSG LSGEQGPSGD MTTEEDSATH IKFSKRDEDG RELAGATMEL RDSSGKTIST WISDGHVKDF
YLYPGKYTFV ETAAPDGYEV ATPIEFTVNE DGQVTVDGEA TEGDAHTGSG GSGGSGVTTL SGLSGEQGPS
GDMTTEEDSA THIKFSKRDE DGRELAGATM ELRDSSGKTI STWISDGHVK DFYLYPGKYT FVETAAPDGY
EVATPIEFTV NEDGQVTVDG EATEGDAGSS GSENLYFQ
```

8.2 Methods

8.2.1 Meta-analysis

Supplementary tables that contain information on each calculation of α for TCRs (Table SA.1) and non-TCR receptors (Table SA.2) are provided.

The broad method was to obtain a measure of ligand potency from each study. If provided by the study, this was often an EC_{50}, which is the concentration of ligand eliciting 50% of the maximum response. If not explicitly provided, we estimated ligand potency as P_X, which was defined by the concentration of ligand that produced X response. To do this, we drew a horizontal line at X on a provided dose-response graph and estimated the ligand concentration where the data intercepted the horizontal line. The disadvantage of this method is that ligand potency was estimated based on the single representative graph provided in the study.

Each study contained estimates of K_D or k_{off} for the specific TCR/pMHC interactions used. We only included studies where monomeric SPR binding data was available to avoid multimeric binding parameters (e.g. when using tetramers). However, when analysing discrimination by other non-TCR receptors, we included binding data from various methods (e.g. SPR, radiolabelled ligands) provided they were monomeric measurements.

The plot of potency over K_D or k_{off} was fitted using linear regression on log-transformed axes. We reported the slope of the fit (i.e. the discrimination power, α), the goodness-of-fit measure (R^2), and the P-value for the null hypothesis that the slope is zero (i.e. $\alpha = 0$). We defined significance using the threshold of p=0.05.

A subset of the data relied on engineered high-affinity TCR/pMHC interactions. It has been observed that increasing the affinity beyond a threshold does not improve ligand potency[239,334]. To avoid underestimating the discrimination power, we found that globally removing data where $K_D < 1$ μM avoided entering this saturation regime (with a single exception, see ID 58-61 in Supplementary Information). Similarly, to avoid over-estimating α, we did not include data where the potency was extrapolated (i.e. when EC_{50} values were larger than the highest ligand concentration tested). Some studies provided multiple measures of T-cell responses

and in this case, we produced potency plots for each response and hence were able to obtain multiple estimates of α.

Only significant discrimination powers ($p < 0.05$) were included in the final comparisons (Fig. 3.4) except for the original and revised mouse TCR data (Fig. 3.4B) because only a few datasets were available. We found more studies that performed functional experiments on the original mouse TCRs compared to those that measured binding and therefore, to avoid introducing a potential bias in the analysis, we included only a single calculated α for each independent SPR measurement. In the case of the original mouse TCR data, we included 4 calculations of α (Table SA.1, ID 1, 2, 11, 14) and in the case of the revised mouse TCR data, we included 6 calculations of α (Table SA.1, ID 5, 13, 15, 17, 18, 19). However, we explicitly include all α values we calculated in Table SA.1 where it is clear that including them would not impact any conclusions. However, discrimination powers obtained using artificial conditions, when antigen was presented on plates as recombinant protein or when presented on APCs but co-receptor was blocked, were *not* included in aggregated analyses (Fig. 3.4B, Fig. 3.5A-B).

All statistical analyses of α were performed using parametric 1-way ANOVA and/or multiple t-tests (with the stated correction for multiple comparisons) on log-transformed data.

8.2.2 *Plasmids and cloning*

The OT-I TCR construct used in this thesis consists of the murine variable OT-I domain and the human constant domain truncated above the transmembrane domain with an artificial interchain disulphide.The pGMT7 plasmids containing OT-I α chain and OTI β chain with human constant domains were obtained from David Cole (University of Cardiff). The plasmid contains a T7 promoter for *E.coli* protein expression. A 5x His Tag and a SpyTag 003 were cloned to the C terminus of the OT-I β chain using site-directed mutagenesis (Q Site-Directed Mutagenesis Kit. NEB). The plasmid was amplified with primers which had the desired tag incorporated into their 5´ ends. The pET plasmids containing the soluble 1G4 α and β chains were obtained from Johannes Pettmann. The plasmids have a T7 promoter for expression. As for the OT-I, a SpyTag was added to the C terminus end of the 1G4 β chain site-directed mutagenesis. The pET14b plasmid for soluble H2K^b expression was obtained from Vincenzo Cerundolo (University of Oxford). An AviTag was added to the C terminus end using site-directed mutagenesis. All plasmids were cloned into Top10 or D5alpha *E.coli* cells using chemical transformation. Plasmids were purified via QIAprep Spin Miniprep Kit (Qiagen). Sequences were confirmed via Sanger sequencing (Source Bioscience). For expression, plasmids were transformed into Bl21 (DE3) or NiCo21 cells.

8.2.3 *Protein expression and purification*

TCR For soluble TCR production (OT-I or 1G4), TCR α and β chains were expressed in BL21 *Escherichia coli* cells overnight at 37°C following induction with 0.15 mM IPTG. Cells were harvested and lysed using sonication and the BugBuster Protein Extraction Reagent (Millipore). Next, denatured proteins were isolated from inclusion bodies using 8 M Urea

Buffer. Proteins were stored at -80°C until use. OT-I-TCR was refolded by adding 15 mg of each chain dropwise in 1 L refolding buffer, followed by dialysis for 3 days in 10 L Tris buffer, with a buffer change after 1 day. After dialysis, the protein was filtered and purified using ion-exchange chromatography (HiTrap Q column) with a NaCl gradient. Next, the protein solution was concentrated and purified again by size exclusion chromatography (Superdex 200 Increase column [GE Healthcare]) in HBS-EP (0.01 M HEPES pH 7.4, 0.15 M NaCl, 3 mM EDTA, 0.005 % v/v Tween20). See Fig. 8.1A, B for SDS page of OT-I after anion exchange and size exclusion chromatography. Purified TCR was used for SPR measurements for no longer then 24 hours after purification to avoid aggregation. TCR concentration was determined by NanoDrop Spectrophotometer. The accuracy of concentration measurements was confirmed with a Bradford assay, using ovalbumin as a standard (Fig. 8.1C).

PMHC For pMHC production in *E.coli*, soluble MHC Class I heavy chain (murine $H2K^b$ or human HLA-A*02:01) and human β_2m were expressed separately in BL21 DE3 *Escherichia coli*. Cell lysis and inclusion bodies purification was done identically to TCR production. MHC heavy chain, β_2m and peptide were added dropwise to pMHC refolding buffer at a concentration of 2 µM, 1 µM, 10 µM, respectively. The protein solution was kept under constant stirring for more than 40 h at 4°C. Afterwards, the refold was filtered through a 0.45 µL filter and concentrated. If required, pMHC were biotinylated overnight at room temperature using the BirA Biotin-protein ligase reaction kit (Avidity LLC). Next, pMHCs were purified in HBS-EP Buffer by Size exclusion chromatography using the Superdex 75 column. Class I pMHCs from HEK cells were purchased from the NIH protein facility. pMHC were produced as described[335]. pMHCs were aliquoted and stored at -80°C until use.

PEPTIDES Peptides were synthesised at a purity of >95% (Peptide Protein Research, UK). The OT-I cognate peptide N4 is an 8 amino acid peptide class I peptide derived from ovalbumin ($OVA_{257-264}$)[273]. The peptide variants used here were described previously[112,114,128]. The cognate peptide for the 1G4 TCR is a 9 amino acid, class I peptide derived from the NYE-ESO protein ($NYE_{157-165}$). Here we use the 9V peptide, where the ninth amino acid was altered into a Valine for improved stability[304]. See Table 4.1 for a list of peptides and their sequences.

DOUBLECATCHER DoubleCatcher was produced by collaborators as described previously[302]. Masked SpyTag was cleaved using TEV protease (NEB) with a TEV protease to protein ratio of 0.5 (units/µg protein). The reaction was performed at 4°C overnight.

TCR DIMERISATION The TCR after anion exchange chromatography or SEC was mixed with DoubleCatcher in a 3:1 ratio. The excess in TCR is to make sure the DoubleCatcher is saturated. The reaction mix was incubated at room temperature for 1 h.

ANTIBODIES Anti-RBD IgG1 antibodies were produced by collaborators as described previously[336].

(a)

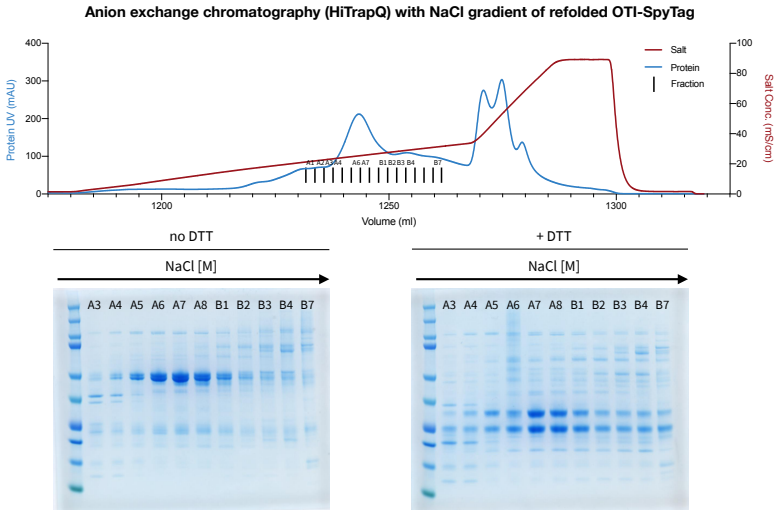

(b)

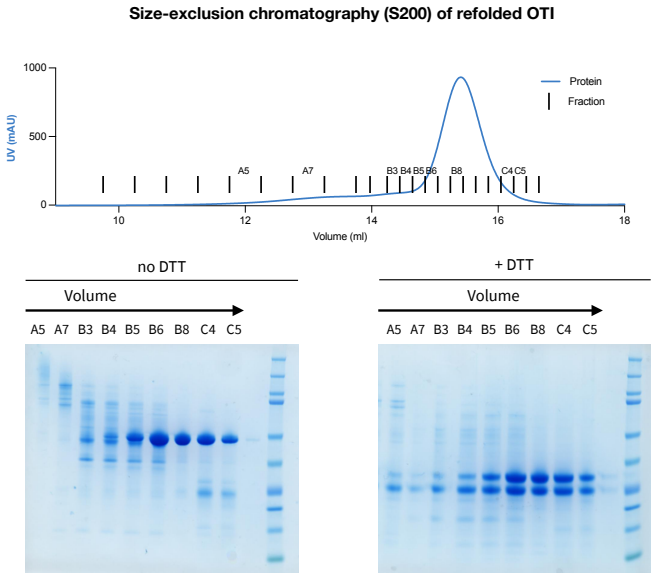

(c)

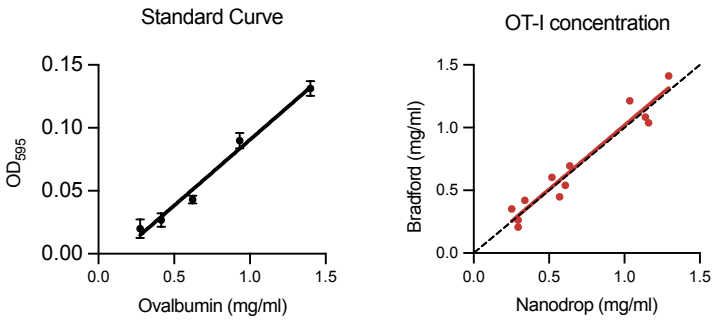

Figure 8.1: OTI refold and concentration measurement. **(A)** Sensogram (top) and SDS page (bottom) of OTI purification with anion exchange chromatography **(B** Sensogram (top) and SDS page (bottom) of OTI purification with size exclusion chromatography **(C)** Concentration measurement with Bradford assay and nanodrop.

8.2.4 SPR experiments

TCR SPR equilibrium binding analysis of TCR-pMHC interaction was measured by SPR on a Biacore T200 or S200 instrument (GE Healthcare Life Sciences) with a CM5 sensor chip. HBS-EP was used as running buffer and all K_D measurements were performed at 37°C. For protein immobilisation, the sensor chip was saturated with streptavidin using an amine coupling kit (GE Healthcare Life Sciences). Biotinylated pMHCs were injected into experimental flow cells (FC) for different time lengths to immobilise 400 to 1500 RU pMHC. Matching levels of CD86 were immobilised in FC1 as a reference. Next, excess streptavidin was blocked with two 40 s injections of 500 μM biotin (Avidity) and the sensor was conditioned with 8 injections of running buffer. TCR was injected at increasing concentrations at a flow rate of 30 ml/min. HBS-EP Buffer from the same batch that was used for TCR purification was injected after every 2-3 TCR injections as reference. Following TCR injections, Y3 or anti-β2m antibody was injected for 8 min.

K_D values were analysed by fitting a 1:1 Langmuir binding ($B_{eq} = B_{\max} \cdot [A]/(K_D + [A])$) function to double-referenced equilibrium RU values. Maximum binding of the B2M antibody to pMHC was used to generate the empirical standard curve and to relate the B_{max} of TCRs to B_{max} of antibody binding. For low-affinity peptides, B_{max} was constricted to B_{max} calculated from the standard curve.

For kinetic measurements by SPR, we used a Biacore S200. Different TCR concentrations were injected at a flow rate of 30 µL/min. To minimize diffusion artifacts, TCR was injected separately in flow paths 1–2 and 3–4. We obtained k_{off} by fitting a mono-exponential to double-referenced dissociation curves.

For kinetic measurements by grating-coupled interferometry (GCI), we used a Creoptix waveRAPID. pMHC was immobilised to 150-350 RU on a 4PCP sensor chip. For determining kinetic parameters with the WAVERapid method, a single TCR concentration was injected multiple times using different length pulses for a total duration of 5 s, followed by a 50 s dissociation phase. To calibrate how the analyte (TCR) concentration changes over time during pulse injection, 0.5% DMSO is injected. The flow rate was set to 100 µL/min per flow cell. We obtained k_{off} by fitting a mono-exponential to double-referenced dissociation curves.

BIVALENT SPR FOR RBD ANTIBODIES A BIAcore T200 instrument (GE Healthcare Life Sciences) at 37°C and and a flow rate of 100 μl/min. The running buffer was HBS-EP. Monovalent Streptavidin-SpyCatcher was coupled to CM5 sensor chips using an amino coupling kit (GE Healthcare Life Sciences) to near saturation, typically around 7000 - 8000 RU. Antigens, either biotinylated (RBD) or containing a SpyTag (CD19), were injected into the experimental flow cells (FCs) for different lengths of time to produce desired immobilisation levels (typically 20 - 70 RU). The concentration of immobilised antigen was calculated using an empirical factor to convert the immobilisation level to a molar concentration. We used the formula: molar conc. = immobilisation level / (conversion factor $\times$ molecular weight). The conversion factor was previously determined to be 149 RU per g/liter[337]. Usually, FC1 was kept blank as a reference for FC2, FC3, and FC4. Excess streptavidin was blocked with two 40 s injections of

250 µM biotin (Avidity). Before antibody injections, the chip surface was conditioned with 2 injections of the running buffer. A dilution series of antibodies was injected simultaneously in all FCs, starting with the lowest concentration. Antibodies were injected for 150s followed by a buffer injection of 450s at a flow rate of 100 µl/min. After each cycle, the chip surface is regenerated with 3M MgCl (Cytiva) for 90 s at 30 µl/min to remove all remaining bound antibodies. A buffer injection was included after every 2 or 3 antibody injections; all binding data were double-referenced by subtracting the response of the control flow cell and the closest buffer injection. Before running the high-throughput SPR experiment, we conducted an initial screen to determine whether the surface could be regenerated after each antibody injection. For this, each antibody was injected at a concentration of 50 nM with an association phase of 150 sec followed by a dissociation phase of 475 sec before injecting 3M MgCl (Cytiva) for 90 sec at a flow rate of 30 µl/min followed by a buffer injection. For the high-throughput SPR experiments, up to 32 antibodies at 3 concentrations (typically between 30 and 100 nM) each were injected in sequence over the SPR chip surface. Buffer was injected after every third cycle.

8.2.5 Functional T cell experiments

MICE OT-I mice (JAX stock no.: 003831) were purchased from Jackson Laboratory and CD45.1 mice from Charles River. Mice were bred and maintained in the University of Oxford specific pathogen-free (SPF) animal facilities. Mice were routinely screened for the absence of pathogens and were kept in individually ventilated cages with environmental enrichment at 20–24°C, 45–65% humidity with a 12 h light/dark cycle (7am–7pm) with half an hour dawn and dusk period. Mice were euthanized by CO_2 asphyxiation followed by cervical dissociation. Breeding was conducted in agreement with the United Kingdom Animal Scientific Procedures Act of 1986 and performed under approved experimental procedures by the Home Office and the Local Ethics Reviews Committee (University of Oxford) under UK project licenses P4BEAEBB5 and PP3609558.

T CELL ACTIVATION ASSAY OT-I T-cells were isolated from lymph nodes and spleen of 6-12 week old OT-I mice. Selection was carried out with a MojoSortTM CD8+ T-cell negative isolation kit and magnets (Biolegend, #480008 and #480019). Isolated OT-I T-cells were resuspended in complete RPMI (RPMI 1640 [Gibco, #21870-076] supplemented with 2% FCS and 100x Penicillin-Streptomycin [Gibco, #10378-016]). Naive OT-I T-cells (50,000) were seeded in 96-well U-bottom together with splenocytes (100,000) from CD45.1 mice loaded with the indicated dose of the following peptides: N4 (SIINFEKL), A2 (SAINFEKL), Q4 (SIIQFEKL), T4 (SIITFEKL), Q7 (SIINFEQL), Q4H7 (SIIQFEHL), G4 (SIIGFEKL), E1 (EIINFEKL). Cells were harvested after 24 hours.

FLOW CYTOMETRY Single-cell suspensions obtained from spleen or cultured CD8+ T-cells were stained in V-bottom 96-well plates in flow cytometry buffer (2% FCS, 2 mM EDTA, and 0.02% sodium azide in 1x PBS). Live dead staining and surface staining was performed using Zombie NIR Fixable Viability Kit (Biolegend, #423106/423105), TruStain FcXTM (anti-mouse

CD16/32, Biolegend, #101319) and fluorochrome-conjugated the primary antibodies against CD45.1 (Biolegend, clone: A20), CD8 (Biolegend, clone: 53-6.7), CD69 (Biolegend, clone: H1.2F3), and CD44 (Biolegend, clone: IM7). Cells were fixed using 4% PFA for 30 minutes at 4°C. Flow cytometry data were recorded on BD LSRII or FortessaX20 using BDFACSDiva (v8.0) software and analyzed using FlowJoTM software (v10.4.2, Tree Star).

DATA ANALYSIS All data fitting and statistical analysis were carried out in GraphPad Prism 10. EC_{50} values were obtained by fitting the dose-response data with a 4-parameter sigmoidal model on a linear scale using the following equation:

$$R(x) = R_0 + (x^n) * (R_{\max} - R_0)/(x^n + \mathrm{EC}_{50}^n)\,, \tag{8.1}$$

where x is the peptide concentration used to pulse the target cells (in µM), R_0 and $R_{\max}$ refer to the response at $x = 0$ and maximum response, respectively, and n denotes the Hill coefficient. The EC_{50} values were used as peptide potency.

The log-transformed potency over affinity data was fit to the kinetic proofreading model using the following equation[246]:

$$Y = A + N\log_{10}(1 + (k_{\mathrm{on}}10^{X})/k_{\mathrm{p}})\,, \tag{8.2}$$

where Y is the log-transformed potency, X is the log-transformed affinity K_D, k_{on} is the on-rate, k_{p} is the proofreading rate, N is the number of proofreading steps, and A is the maximum potency (y-intercept). Given that on-rates produce only modest variation between pMHCs, k_{on} was fixed to the value measured for the OT-I/N4 interaction (0.13 $\mu\mathrm{M}^{-1}\mathrm{s}^{-1}$).

8.2.6 *SARS-CoV-2 neutralisation assay*

Neutralisation potency for anti-RBD antibodies against SARS-CoV-2 was measured by collaborators as previously described[286,336].

8.2.7 *Data analysis for bivalent SPR*

DATA FITTING WORKFLOW The Particle-based model was developed by collaborators and the model and fitting process was described in detail previously[336].

In this section we explain the detailed workflow for analysis of the high-throughput bivalent SPR experiments.

After double referencing the SPR curves for each antibody concentration, we aligned them to the start of the dissociation phase (setting it to $t_s = 150$s) to improve curve alignment. To eliminate artefacts arising from the start and end of the association phase (generally large spikes in RU arising from needle motion), the first 5 seconds of the association phase, the last 4 seconds of the association phase, and the first 5 seconds of the dissociation phase were excluded from the data. We also excluded all SPR curves where the maximum response across the entire injection was smaller than 6 RU because this minimal binding is within the

systematic error for SPR experiments (typically 1 RU per 100 seconds of injection or 6 RU for our 600-second experiments). Finally, to produce more manageable file sizes we reduced the temporal resolution from 10 Hz to 1 Hz and this did not impact our results because the kinetics of the SPR traces were much slower than 1 Hz.

We then fitted the processed data for each antibody using the bivalent Particle-based model (see Particle-model data fitting section). The antigen and antibody concentrations for each SPR curve were provided as input parameters for the fitting process. The surrogate model used in fitting contained the following parameter ranges: $\log_{10}(\mathrm{k_{on}}) \in [-5.0, 2.0]$ with $M_1 = 42$, $\log_{10}(\mathrm{k_{off}}) \in [-4.0, 0.0]$ with $M_2 = 40$, $\log_{10}(\mathrm{k_{on,b}}) \in [-3.0, 1.5]$ with $M_3 = 30$, and reach $\in [2, 35]$ with $M_4 = 30$. During the fitting of the surrogate to SPR data, a box constraint that $\log_{10}(C_p) \in [1.0, 4.0]$ was used. The fitting process was repeated 100 times, and the parameters yielding the lowest fitness were recorded. The estimated bivalent model parameters from the fitting process were converted into the corresponding biophysical parameters using the experimental antigen concentration. In addition, the bivalent SPR curves were fit with an ODE-based monovalent model.

Finally, a quality control procedure was introduced to ensure the accuracy of the bivalent binding parameters. First, we checked that the antigen surface could be regenerated after each antibody injection (7 out of 80 antibodies did not unbind after regeneration). Second, we only included data where the particle model produces a close fit to the data (12 out of 80 antibodies could not be fit). Third, we only included data where the particle model produced a fit that was better than the ODE-based monovalent model. We reasoned that SPR data that could accurately be fit by the ODE-based monovalent model did not contain information that could accurately determine bivalent binding (bivalent binding parameters of 16 out of 80 antibodies could not be determined).

Bivalent SPR data that passed all quality control measures for each antibody were averaged across SPR experiments. We report the geometric mean for parameters that varied on a logarithmic range in the model (k_{on}, k_{off}, $\mathrm{K_D}$, $k_{\mathrm{on,b}}$) and the mean for the molecular reach that varied on a linear range in the model.

MULTIPLE LINEAR REGRESSION We fit a one-way multiple linear model in Prism (v 9.5.1) with the following formula:

$$y = \beta_0 + \beta_1 x_1 + ... + \beta_n x_n$$

where y is the predicted neutralisation $\mathrm{IC_{50}}$ for each antibody, β_0 is the y-intercept to fit, $(x_1, \ldots, x_n)$ are the values for $\log_{10}(\mathrm{k_{on}})$, $\log_{10}(\mathrm{k_{off}})$, $\log_{10}(K_{\mathrm{D}})$, $\log_{10}(\mathrm{k_{on,b}})$, reach, and the blocking epitope distance respectively, and $(\beta_1, \ldots, \beta_n)$ are the corresponding regression coefficients for each variable. Models contain either all variables or a subset. A Least Squares regression type was used and models were compared using an Extra-Sum-of-Squares F test.

A

APPENDIX

Supplementary Tables

Table A.1: Overview of discrimination powers for TCRs. Each row is associated with an experimental ID that is linked to detailed information on how the data was extracted (see Supplementary Information text) and the potency plots (Fig. SA.1,SA.2,SA.3,SA.4).

	Receptor and Ligand			Potency Assay			References		Fitting Result					
ID	TCR	Peptide	Species	Assay	**Coreceptor**	Output	Ref SPR measurement	Ref Potency measurement	Power	Std Error	R squared	P-value	signf	n
1	OT-I	OVA (257-264)	Mouse	Cellular	Yes	Lysis	Alam 1996[112]	Hogquist 1995[127]	12.	Perfect line	1.0		ns	2
2	OT-I	OVA (257-264)	Mouse	Cellular	Yes	Lysis	Alam 1999[128]	Hogquist 1995[127]	10.	2.4	0.95	0.14	ns	3
3	OT-I	OVA (257-264)	Mouse	Plate	Yes	CD69	Rosette 2001[238]	Rosette 2001[238]	18.13	Perfect line	1.0		ns	2
4	OT-I	OVA (257-264)	Mouse	Cellular	Yes	pERK	Alam 1999[128]	Altan-Bonnet 2005[96]	>5.1	1.9	0.88	0.23	ns	1(3)
5	OT-I	OVA (257-264)	Mouse	Cellular	Yes	CD69	Stepanek 2014[240]	Daniels 2006[114]	2.1	0.33	0.93	0.0084	sig	5
6	OT-I	OVA (257-264)	Mouse	Cellular	Yes	IFNγ	Stepanek 2014[240]	Zehn 2009[114]	2.0	Perfect line	1		ns	2
7	OT-I	OVA (257-264)	Mouse	Cellular	Yes	CD69	Stepanek 2014[240]	Lo 2019[243]	1.1	0.27	0.89	0.055	ns	4
8	OT-I	OVA (257-264)	Mouse	Cellular	No	CD69	Stepanek 2014[240]	Lo 2019[243]	0.37	0.12	0.84	0.084	ns	4
9	OT-I	OVA (257-264)	Mouse	Cellular	Yes	CD69	Stepanek 2014[240]	Lo 2019[243] (G131D)	1.1	0.12	0.98	0.010	sig	4
10	OT-I	OVA (257-264)	Mouse	Cellular	No	CD69	Stepanek 2014[240]	Lo 2019[243] (G131D)	1.4	0.19	0.96	0.020	sig	4
11	3.L2	Hb (64-76)	Mouse	Cellular	Yes	Lysis	Kersh 1998[338] (k_{off})	Kersh 1996[129]	6.8	0.61	0.98	0.008	sig	4
12	3.L2	Hb (64-76)	Mouse	Cellular	Yes	Lysis	Persaud 2010[339]	Persaud 2010[339]	0.37	0.37	0.25	0.39	ns	5
13	3.L2	Hb (64-76)	Mouse	Cellular	Yes	Lysis	Hong 2015[241]	Kersh 1996[129]	3.2	0.37	0.97	0.013	sig	4
14	2B4	MCC (88-103)	Mouse	Cellular	Yes	IL-2	Lyons 1996[131]	Lyons 1996[131]	6.7	Perfect line	1		ns	2
15	2B4	MCC (88-103)	Mouse	Cellular	Yes	IL-2	Krogsgaard 2003[340]	Lyons 1996[131]	2.19	Perfect line	1		ns	2
16	2B4	MCC (88-103)	Mouse	Plate	Yes	IL-2	Krogsgaard 2003[340]	Krogsgaard 2003[340]	1.2	0.41	0.65	0.030	sig	7
17	2B4	MCC (88-103)	Mouse	Cellular	Yes	IL-2	Wu 2002[242]	Lyons 1996[131]	2.8	Perfect line	1		ns	
18	2B4	MCC (88-103)	Mouse	Cellular	Yes	IL-2	Newell 2011[341]	Newell 2011[341]	2.3	0.30	0.97	0.017	sig	4
19	2B4	MCC (88-103)	Mouse	Cellular	Yes	IL-2	Birnbaum 2014[136]	Birnbaum 2014[136]	0.95	0.24	0.84	0.029	sig	5
20	5cc7	MCC (88-103)	Mouse	Cellular	Yes	IL-2	Birnbaum 2014[136]	Birnbaum 2014[136]	0.74	0.99	0.16	0.51	ns	5
21	P14	gp33 (33–41)	Mouse	Plate	Yes	IFNγ	Tian 2007[342]	Tian 2007[342]	1.3	0.29	0.67	0.0011	sig	12
22	P14	gp33 (33–41)	Mouse	Cellular	Yes	Lysis	Tian 2007[342]	Tian 2007[342]	2.1	0.87	0.49	0.054	ns	12
23	B3K506	3K	Mouse	Cellular	Yes	Proliferation	Govern 2010[343]	Govern 2010[343]	2.9	0.32	0.92	<0.0001	sig	9
24	B3K506	3K	Mouse	Cellular	Yes	TNFα	Govern 2010[343]	Govern 2010[343]	2.4	0.22	0.95	<0.0001	sig	8
25	B3K508	3K	Mouse	Cellular	Yes	Proliferation	Govern 2010[343]	Govern 2010[343]	2.9	0.17	1.0	0.036	sig	3
26	B3K508	3K	Mouse	Cellular	Yes	TNFα	Govern 2010[343]	Govern 2010[343]	2.5	0.14	1.0	0.037	sig	3
27	2C	SIYR	Mouse	Plate	No	IL-2	Chervin 2009[344]	Chervin 2009[344]	0.12	0.19	0.17	0.59	ns	4
28	2C	SIYR	Mouse	Cellular	No	IL-2	Chervin 2009[344]	Chervin 2009[344]	Too few points				ns	0
29	2C	SIYR	Mouse	Cellular	Yes	IL-2	Chervin 2009[344]	Chervin 2009[344]	0.66	1.7	0.069	0.74	ns	4
30	2C	QL9	Mouse	Cellular	Yes	IL-2	Bowerman 2009[345]	Bowerman 2009[345]	2.7	1.3	0.82	0.28	ns	2
31	2C	QL9 and SIYR	Mouse	Cellular	Yes	IL-2	Jones 2008[346]	Jones 2008[346]	4.7	1.4	0.92	0.18	ns	3
32	2C	QL9 and SIYR	Mouse	Cellular	No	IL-2	Jones 2008[346]	Jones 2008[346]	6.5	Perfect line	1		ns	2
33	42F3	QL9	Mouse	Cellular	Yes	IL-2	Adams 2016[347]	Adams 2016[347]	0.15	0.65	0.010	0.83	ns	8
34	AH1 specific	AH1 (gp70 423–431)	Mouse	Cellular	Yes	IFNγ	McMahan 2006[348]	McMahan 2006[348]	5.1	1.2	0.79	0.0072	sig	7
35	1G4	NY-ESO-1 (157-165)	Human	Cellular	Yes	Lysis	Irving 2012[334]	Irving 2012[334]	0.67	0.043	0.99	0.0041	sig	4
36	1G4	NY-ESO-1 (157-165)	Human	Cellular	Yes	Lysis	Schmid 2010[349]	Schmid 2010[349]	0.69	0.20	0.75	0.026	sig	7
37	1G4	NY-ESO-1 (157-165)	Human	Plate	Yes	IFNγ	Aleksic 2010[149]	Aleksic 2010[149]	0.60	0.12	0.63	0.0001	sig	17
38	1G4	NY-ESO-1 (157-165)	Human	Cellular	Yes	Lysis	Aleksic 2010[149]	Aleksic 2010[149]	1.6	0.21	0.89	0.0001	sig	9
39	1G4	NY-ESO-1 (157-165)	Human	Plate	Yes	IFNγ	Dushek 2011[350]	Dushek 2011[350]	0.55	0.17	0.63	0.019	sig	8
40	G10	gag p17	Human	Plate	Yes	IFNγ	Dushek 2011[350]	Dushek 2011[350]	0.95	0.16	0.79	0.0003	sig	9
41	1E6	INS	Human	Cellular	Yes	Lysis	Cole 2016[265] (25°C)	Cole 2016[265]	1.1	0.85	0.62	0.037	sig	7
42	1E6	INS	Human	Cellular	Yes	Lysis	Cole 2016[265] (37°C)	Cole 2016[265]	1.2	0.29	0.85	0.026	sig	5
43	A6	Tax (11-19)	Human	Cellular	Yes	CD107	Thomas 2011[351]	Thomas 2011[351]	2.0	0.38	0.97	0.12	ns	3
44	A6	Tax (11-19)	Human	Cellular	Yes	IFNγ	Thomas 2011[351]	Thomas 2011[351]	2.2	0.42	0.97	0.12	ns	2
45	gp209 TCR	gp100 (209–217)	Human	Cellular	Yes	IFNγ	Zhong 2013[352]	Zhong 2013[352]	1.3	0.54	0.74	0.14	ns	6
46	gp209 TCR	gp100 (209–217)	Human	Cellular	Yes	ppERK	Zhong 2013[352]	Zhong 2013[352]	1.2	0.84	0.41	0.25	ns	6
47	gp100 TCR	gp100 (280–288)	Human	Cellular	Yes	Lysis	Bianchi 2016[353]	Bianchi 2016[353]	2.3	0.73	0.71	0.036	sig	6
48	gp100 TCR	gp100 (280–288)	Human	Cellular	Yes	MIP-1β	Bianchi 2016[353]	Bianchi 2016[353]	3.6	0.54	0.92	0.0026	sig	6
49	14.3.d	SEC3	Human	Plate	No	NFAT	Andersen 2001[354]	Andersen 2001[355]	0.81	0.22	0.93	0.17	ns	3
50	14.3.d	F23.1	Human	Plate	No	NFAT	Andersen 2001[354]	Andersen 2001[355]	0.66	0.83	0.24	0.51	ns	4
51	TCR55	HIV Pol(448-456)	Human	Cellular	Yes	CD69	Sibener 2018[155]	Sibener 2018[155]	0.19	0.22	0.10	0.41	ns	9
52	ILA1	ILA	Human	Cellular	Yes	Degranulation	Laugel 2007[244]	Laugel 2007[244]	1.0	0.38	0.70	0.076	ns	4
53	ILA1	ILA	Human	Cellular	No	Degranulation	Laugel 2007[244]	Laugel 2007[244]	0.19	1.2	0.025	0.90	ns	4
54	ILA1	ILA	Human	Cellular	Yes	CD107a	Laugel 2007[244]	Laugel 2007[244]	2.2	0.30	0.96	0.018	sig	4
55	ILA1	ILA	Human	Cellular	No	CD107a	Laugel 2007[244]	Laugel 2007[244]	3.6	0.27	0.99	0.0055	sig	4
56	ILA1	ILA	Human	Cellular	Yes	IFNγ	Laugel 2007[244]	Laugel 2007[244]	2.2	0.39	0.94	0.03	sig	4
57	ILA1	ILA	Human	Cellular	No	IFNγ	Laugel 2007[244]	Laugel 2007[244]	3.2	0.41	0.97	0.015	sig	4
58	ILA1	ILA	Human	Cellular	Yes	MIP-1β	Tan 2015[356]	Tan 2015[356]	1.4	0.54	0.76	0.13	ns	5
59	ILA1	ILA	Human	Cellular	Yes	IFNγ	Tan 2015[356]	Tan 2015[356]	0.77	0.057	0.99	0.0054	sig	5
60	ILA1	ILA	Human	Cellular	Yes	TNFα	Tan 2015[356]	Tan 2015[356]	0.97	0.24	0.89	0.054	ns	5
61	ILA1	ILA	Human	Cellular	Yes	IL-2	Tan 2015[356]	Tan 2015[356]	1.1	0.084	0.99	0.0058	sig	5
62	KFJ	NY-ESO-1 (60-72)	Human	Cellular	Yes	TNFα	Chan 2018[357]	Chan 2018[357]	-0.59	0.99	0.15	0.61	ns	4
63	Gliadin TCR	Gliadin	Human	Cellular	Yes	Proliferation	Broughton 2012[358]	Broughton 2012[358]	0.83	0.027	1.0	0.021	sig	4
64	LC13	FLR	Human	Cellular	Yes	CD69	Burrows 2010[245]	Burrows 2010[245]	1.9	0.16	0.99	0.0075	sig	5
65	LC13	FLR	Human	Cellular	No	CD69	Burrows 2010[245]	Burrows 2010[245]	7.8	0.040	1	0.0033	sig	3
66	LC13	FLR	Human	Cellular	Yes	Lysis	Burrows 2010[245]	Burrows 2010[245]	4.1	2.1	0.80	0.30	ns	3
67	SB27	LPEP	Human	Cellular	Yes	Lysis	Burrows 2010[245]	Burrows 2010[245]	0.11	0.19	0.10	0.60	ns	5
68	gag TCR	Gag293 (HIV)	Human	Cellular	Yes	CD69	Benati 2016[359]	Benati 2016[359]	1.0	0.29	0.72	0.016	sig	7
69	MEL5	MART-1 (27-35)	Human	Cellular	Yes	MIP-1β	Ekeruche-Makinde 2012[360]	Ekeruche-Makinde 2012[360]	2.3	0.42	0.81	0.001	sig	6
70	MEL5	MART-1 (27-35)	Human	Cellular	Yes	MIP-1β	Madura 2019[361]	Madura 2019[361]	4.5	2.6	0.51	0.18	ns	6

Table A.2: Overview of discrimination powers for non-TCR receptors. Each row is associated with an experimental ID that is linked to detailed information on how the data was extracted (see Supplementary Information text) and the potency plots (Fig. SA.5,SA.6).

	Family	Receptor	Output	Ref Affinity measurement	Ref Potency measurement	Power	Std Error	R squared	P value	sig.	n
1	Cytokine	IL-2Rβ	pSTAT5 (NK cells)	Levin 2012[249]	Levin 2012[249]	0.55	0.031	0.99	0.0032	sig	4
2	Cytokine	IL-2Rβ	%pSTAT5 (T cells)	Levin 2012[249]	Levin 2012[249]	0.74	0.047	0.99	0.0039	sig	4
3	Cytokine	IL-13Rα1	pSTAT6	Moraga 2015[250]	Moraga 2015[250]	0.47	0.065	0.80	<0.0001	sig	9
4	Cytokine	IL-13Rα2	Proliferation	Moraga 2015[250]	Moraga 2015[250]	0.39	0.24	0.27	0.15	ns	9
5	Cytokine	IL-13Rα2	CD86	Moraga 2015[250]	Moraga 2015[250]	0.44	0.085	0.90	0.0139	sig	5
6	Cytokine	IL-13Rα1	CD205	Moraga 2015[250]	Moraga 2015[250]	0.42	0.048	0.96	0.0031	sig	9
7	Cytokine	IFNAR1/IFNAR2	antiviral	Thomas 2011[251]	Thomas 2011[251]	0.71	0.11	0.79	<0.0001	sig	13
8	Cytokine	IFNAR1/IFNAR2	antiproliferation	Thomas 2011[251]	Thomas 2011[251]	1.3	0.11	0.93	<0.0001	sig	13
9	Cytokine	IFN-γ R1-IL-10Rβ	pSTAT1	Mendoza 2017[252]	Mendoza 2017[252]	0.024	0.046	0.030	0.61	ns	11
10	Cytokine	IFN-γ R1-IL-10Rβ	antiviral	Mendoza 2017[252]	Mendoza 2017[252]	0.034	0.063	0.032	0.60	ns	11
11	Cytokine	IFN-γ R1-IL-10Rβ	antiproliferation	Mendoza 2017[252]	Mendoza 2017[252]	0.50	0.14	0.60	0.0054	sig	11
12	Cytokine	gp130 (and IL6Rα)	pSTAT1	Martinez-Fabregas 2019[253]	Martinez-Fabregas 2019[253]	0.54	0.24	0.84	0.26	ns	3
13	Cytokine	gp130 (and IL6Rα)	pSTAT3	Martinez-Fabregas 2019[253]	Martinez-Fabregas 2019[253]	0.52	0.32	0.57	0.24	ns	4
14	RTK	EGFR	growth rate	Reddy 1996[255]	Reddy 1996[255]	0.55	0.10	0.97	0.12	ns	3
15	RTK	c-Kit	pERK	Ho 2017[254]	Ho 2017[254]	0.83	0.14	0.95	0.028	sig	4
16	RTK	c-Kit	pAKT	Ho 2017[254]	Ho 2017[254]	0.88	0.14	0.96	0.023	sig	4
17	GPCR	A2A receptor	whole cell	Guo 2012[257]	Guo 2012[257]	0.29	0.20	0.22	0.19	ns	10
18	GPCR	A2A receptor	cAMP	Guo 2012[257]	Guo 2012[257]	0.71	0.29	0.42	0.041	sig	10
19	GPCR	M3 muscarinic receptor	Calcium	Sykes 2009[256]	Sykes 2009[256]	0.77	0.53	0.29	0.21	ns	7
20	GPCR	M3 muscarinic receptor	GTPγS Binding	Sykes 2009[256]	Sykes 2009[256]	0.55	0.18	0.65	0.029	sig	7
21	GPCR	CXCR4	Voltage	Guyon 2013[258]	Guyon 2013[258]	0.57	0.40	0.40	0.25	ns	5
22	GPCR	CXCR3	Calcium mobilization	Heise 2005[259]	Heise 2005[259]	0.73	0.033	1.0	0.029	sig	3
23	GPCR	CXCR3	GTPγS Binding	Heise 2005[259]	Heise 2005[259]	1.1	0.0039	1	0.0024	sig	3
24	GPCR	CXCR3	Migrated Cells	Heise 2005[259]	Heise 2005[259]	0.56	Perfect line	1		ns	2
25	CAR	C6.5 (scFc against ErbB2)	INFγ	Chmielewski 2004[260]	Chmielewski 2004[260]	0.52	0.028	0.99	0.0003	sig	5
26	CAR	ErB2	CD107	Liu 2015[261]	Liu 2015[261]	1.1	0.14	0.97	0.017	sig	4
27	CAR	ErB2	Proliferation	Liu 2015[261]	Liu 2015[261]	0.64	0.18	0.87	0.068	ns	4
28	CAR	DNA-CAR	pERK	Taylor 2017[78]	Taylor 2017[78]	1.2	0.17	0.96	0.019	sig	4
29	BCR	D1.3	IL2	Batista 1998[262]	Batista 1998[262]	1.4	0.18	0.94	0.0014	sig	
30	BCR	HyHEL10	IL2	Batista 1998[262]	6 Batista 1998[262]	1.3	0.12	0.98	0.0088	sig	4

Supplementary Figures

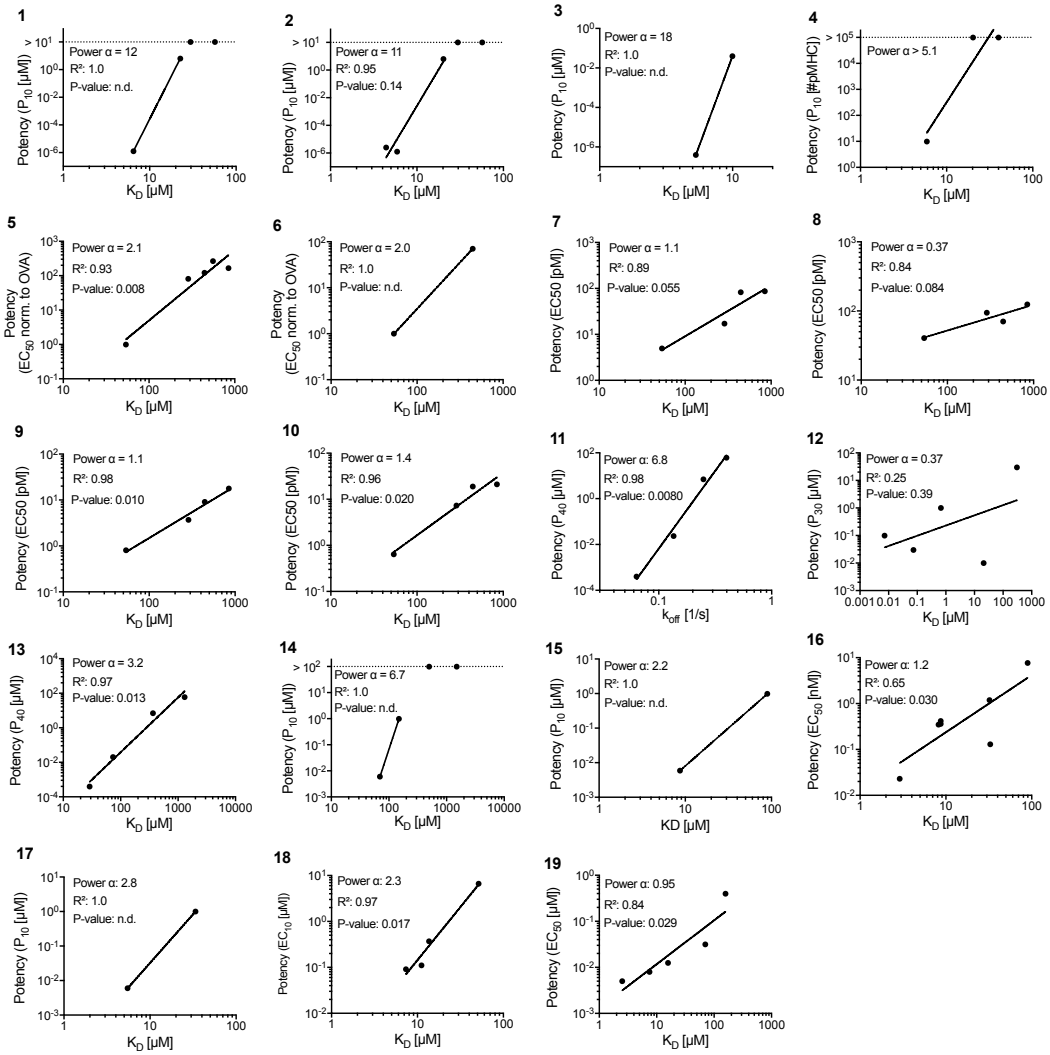

Figure A.1: Potency over K_D data for the original mouse TCRs with original and revised K_D values The fitted discrimination power (α), coefficient of determination (R^2), and p-value for the null hypothesis of a horizontal line (P-value) are indicated. Each panel is linked by an ID to a paragraph in the supplementary information.

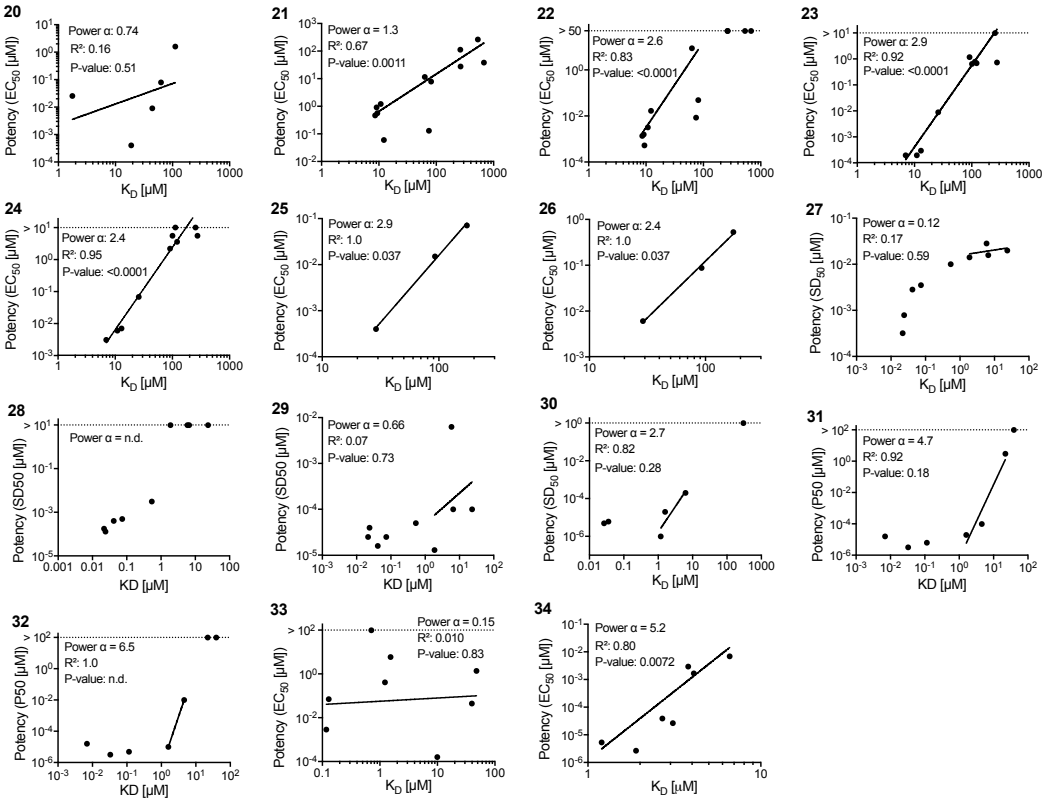

Figure A.2: Potency over K_D data for other mouse TCRs The fitted discrimination power (α), coefficient of determination (R^2), and p-value for the null hypothesis of a horizontal line (P-value) are indicated. Each panel is linked by an ID to a paragraph in the supplementary information.

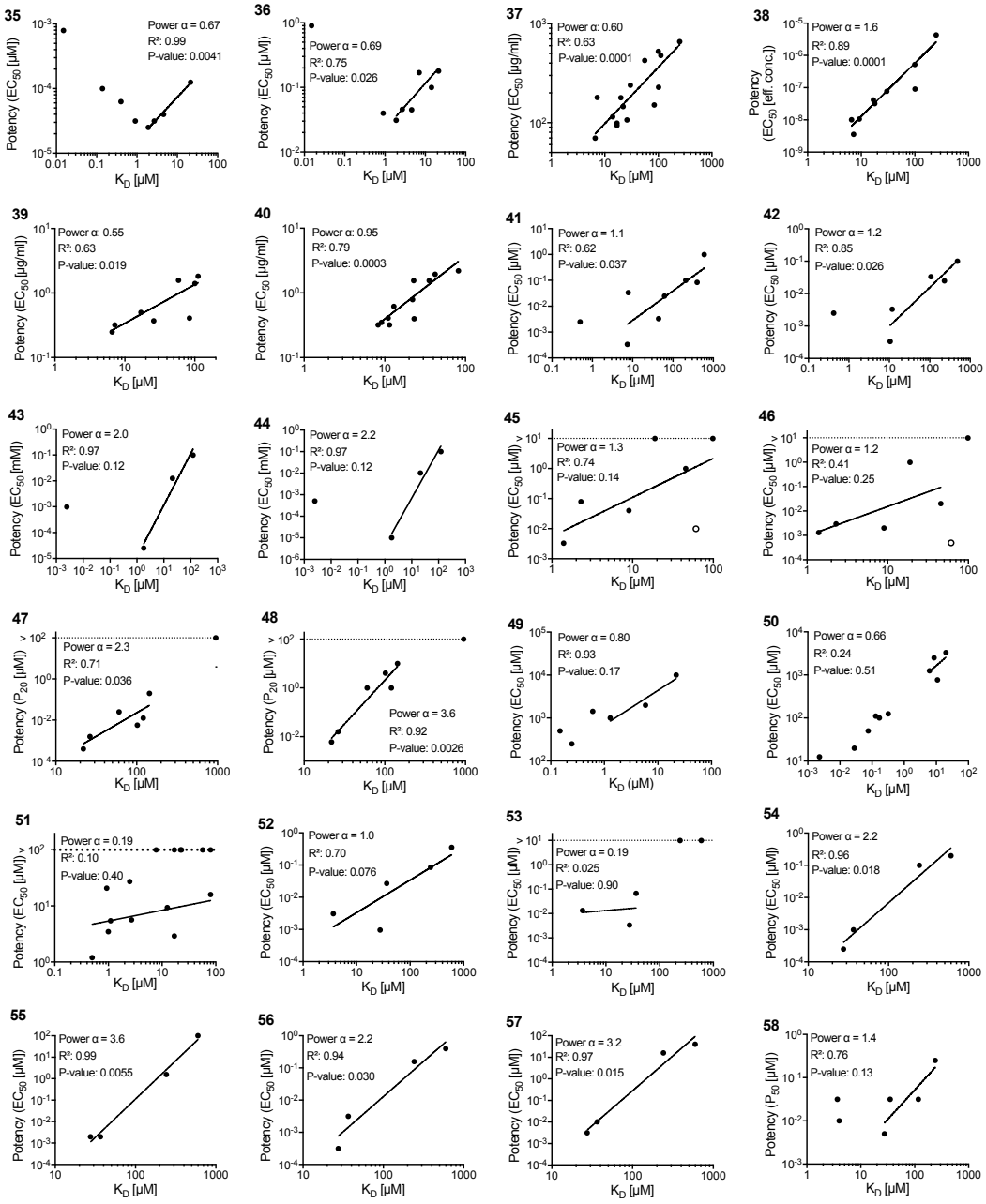

Figure A.3: Potency over K_D data for other human TCRs The fitted discrimination power (α), coefficient of determination (R^2), and p-value for the null hypothesis of a horizontal line (P-value) are indicated. Each panel is linked by an ID to a paragraph in the supplementary information.

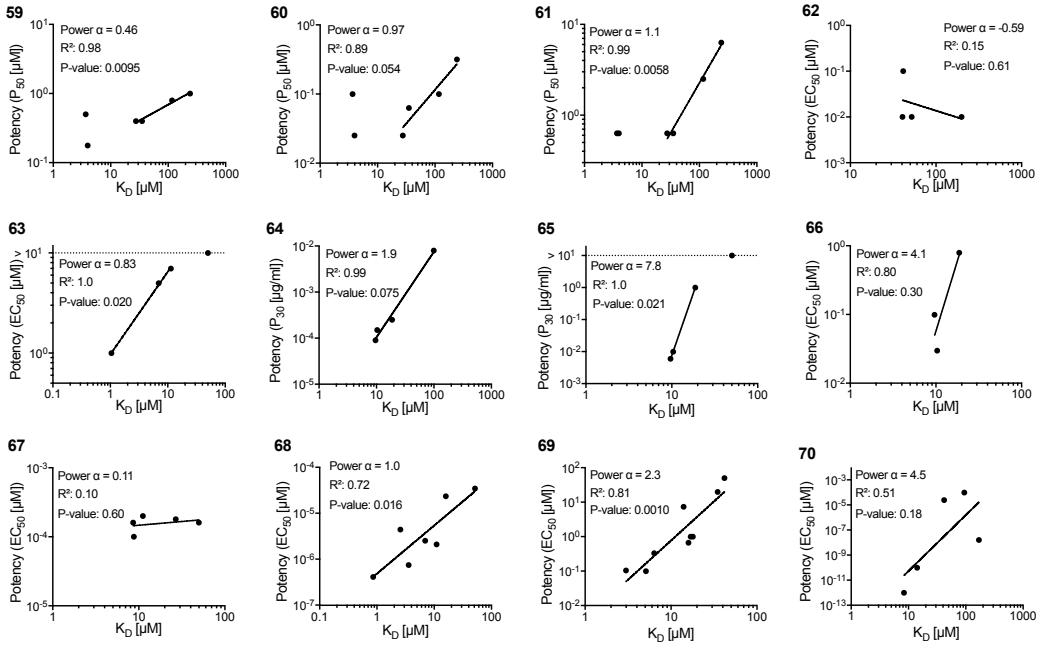

Figure A.4: Potency over K_D data for other human TCRs The fitted discrimination power (α), coefficient of determination (R^2), and p-value for the null hypothesis of a horizontal line (P-value) are indicated. Each panel is linked by an ID to a paragraph in the supplementary information.

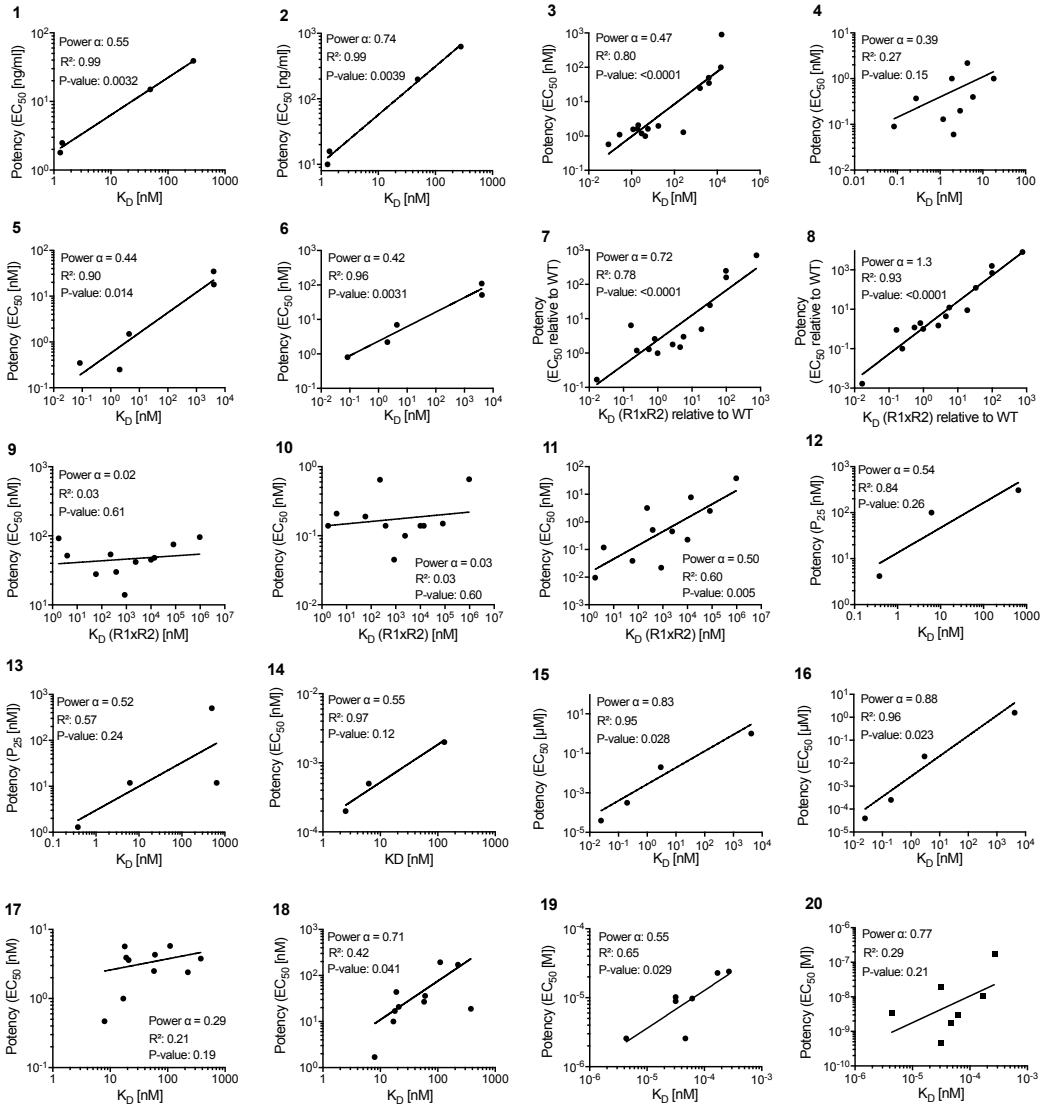

Figure A.5: Potency over K_D data for other (non-TCR) receptors The fitted discrimination power (α), coefficient of determination (R^2), and p-value for the null hypothesis of a horizontal line (P-value) are indicated. Each panel is linked by an ID to a paragraph in the supplementary information.

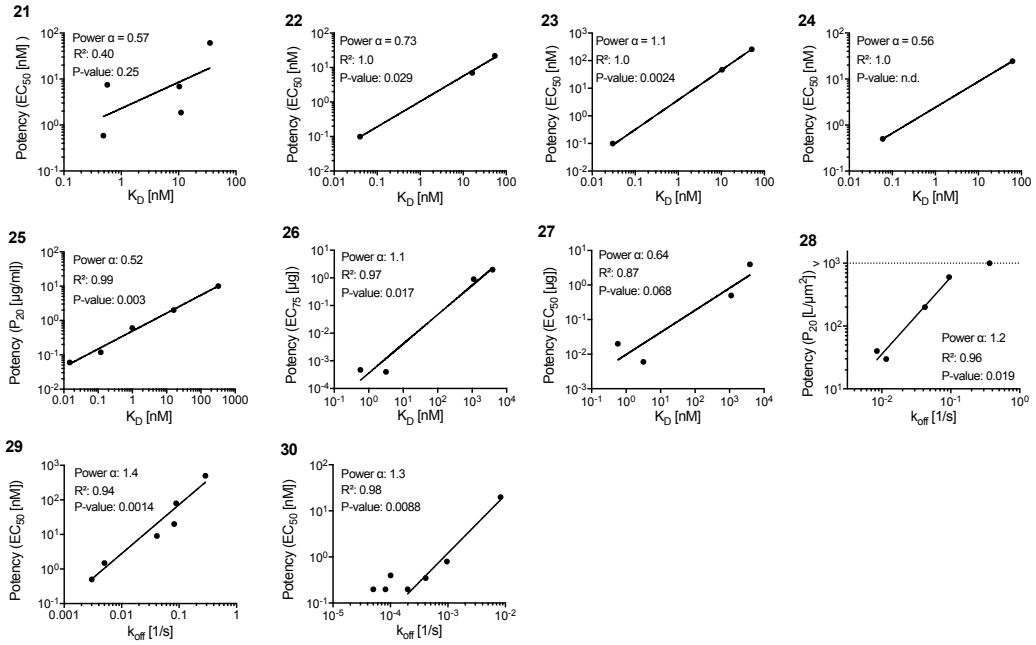

Figure A.6: Potency over K_D data for other (non-TCR) receptors The fitted discrimination power (α), coefficient of determination (R^2), and p-value for the null hypothesis of a horizontal line (P-value) are indicated. Each panel is linked by an ID to a paragraph in the supplementary information.

Supplementary Text

Studies included in the analysis

We provide information on each potency plot we generated in the sections that follow, including the location of the potency and K_D data within each study. References to Figures and Tables are to those in the cited manuscript not to those in the present study. We provide the value of α produced and additional information, including R^2 and p-values are provided in Table A.1 and A.2.

Original mouse TCR data

OT-I

ID 1 [112] Experiments were performed with the murine transgenic TCR OT-I that binds to a peptide from ovalbumin (OVA) presented on H2Kb. Affinity was measured by SPR at 25°C. Affinity values were taken from Table 1 and Figure 3f. For the power analysis, we used K_D values estimated from the binding kinetics (kinetic K_D values). Potency measures for the OVA peptide and peptide variants were previously measured by Hogquist et al[127]. OT-I T cell responses to OVA and single amino acid peptide variants (A2 and E1) were measured in a cell lysis assay. For the power analysis, we extracted the potency of the peptides by reading the P_{10} (peptide concentration producing 10% specific lysis) from the dose-response curve in Figure 2. We excluded peptides that did not result in any response. We were able to include two data points with potency and affinity values for the power analysis producing $\alpha = 12$ (ID 1).

ID 2 [128] The OT-I TCR binding to the peptides derived from OVA were used with affinity and kinetics measured by SPR at 6, 25 and 37°C. Unusual biphasic binding was observed at 37°C for some peptides with two k_{on} and two k_{off} values reported based on a slow first and fast second step binding. Affinity values were provided in Table 1. To avoid picking the fast or slow phase parameters, we used the monophasic affinity data measured at 25°C for the power analysis. Potency data was taken from Hogquist et al[127]. Three data points were included in the analysis producing $\alpha = 10$ (ID 2).

ID 3 [238] OT-I TCR affinity and functional activity was measured when binding its wild type ligand OVA or single amino acid variants (G4). Affinity values of TCR-pMHC interaction, measured by SPR at 25 and 37°C, were provided in Table 1. Similar to Alam et al.[128], TCR binding to MHC loaded with OVA showed biphasic binding at 37°C. As before, we used the data measured at 25 °C for the power analysis. Functional data was generated with T cells isolated from OT-I transgenic mice. T cells were then stimulated with peptide-MHC complexes immobilised on plates. We read off potency data from dose response curves in Figure 1. Only two data points were available for calculating the discrimination power α producing $\alpha = 18$ (ID 3)

ID 4[96] In this study, the OT-I T cell response when stimulated with OVA and was determined by phosphorylation of the kinase ERK in the MAPK pathway. Responses to OVA peptide as well as two peptide variants were studied. Potency values were extracted as P_{10} from dose response curves in Figure 1C. Only the OVA peptide could activate T cells above background. Potency for unresponsive peptides was set to the highest concentration used in assay. Therefore, the discrimination power α calculated with these data points gives a lower bound on the actual value for α. Using the affinity data from Alam et al[128] produced $\alpha > 5.1$ (ID 4).

3.L2

ID 11[338] This paper contains affinity and kinetic data for 3.L2 TCR which recognises murine haemoglobin (Hb 64-76) measured by SPR at 25 °C. We used k_{off} values for the power analysis as K_D values did not correlate (see main text). The D73 peptide was excluded from power analysis because this mutation impacted peptide loading to MHC. Potency data for this TCR was taken from Kersh et al[129]. In the functional experiments, 3.L2 T cell hybridoma cells were incubated with antigen presenting cells pulsed with peptides. Activation was measured by lysis of target cells. P_{40} values (ligand concentration at 40% lysis) of T cell response were given in Figure 4, the corresponding dose response curve was shown in Figure 5. Four data points were included in the analysis and produced $\alpha = 6.8$ (ID 11).

2B4

ID 14[131] The 2B4 TCR used in this study recognises a moth cytochrome c (MCC) peptide bound to MHC class II molecule I-Ek. Table 2 provides K_D values using SPR at 25°C. The potency of the peptides was determined with T cell hybridomas, stimulated by peptide-pulsed APCs, with activation determined by IL-2 production. For the power analysis we extracted the P_{10} from the dose response curve in Figure 1A. Two data points were available for the power analysis producing an $\alpha = 6.7$ (ID 14).

Revised data for the original mouse TCRs

OT-I

ID 5 [114,240] Revised affinity data for OT-I TCR was published by Stepanek et al[240]. The K_D values were taken from the Table in Figure S1D. Potency data for the same set of peptide variants was measured by Daniels et al[114]. Functional experiments were done with pre-selection OT-I double-positive thymocytes. T cell activation was measured by expression of CD69 after incubation with peptide-pulsed antigen presenting cells. EC_{50} values, corrected for small differences in peptide affinity for MHC and normalised to OVA, were given in Figure 1a. Together, these papers provide 5 data points producing α = 2.1 (ID 5).

ID 6 [240,278] Zehn et al[278] provided additional functional data for OT-I TCR. Potency data is measured by intracellular IFNγ production by OT-I T cells stimulated with peptide pulsed antigen presenting cell. The EC_{50} values, given in table in Supplementary Figure 2C, were normalised to OVA. To calculate the discrimination power, we used K_D values from Stepanek et al[240]. The two data points available produced a power of α = 2.0 (ID 6).

ID 7 - 10 [240,243] Lo et al.[243] generated additional functional data for the OT-I TCR. The functional response of $CD8^+$ or $CD8^-$ Jurkat cells expressing the OT-I TCR after stimulation with peptide-pulsed antigen-presenting cells was measured by CD69 upregulation. The EC_{50} values were provided in Supplementary Figure 7C. K_D values were previously measured by Stepanek et al[240]. The study included affinity and potency data for when one of the phosphorylation sites of LAT was mutated. The calculated discrimination power was the same (α = 1.1 for both wild-type LAT (ID 7) and mutated LAT (ID 9) unless CD8 was not present, in which case α= 0.37 (ID 8) or α = 1.4 (ID 10) using Jurkats expressing wild-type or mutated LAT, respectively.

3.L2

ID 12 [339] In this study, the 3.L2 TCR as well as the M15 TCR, a high-affinity TCR engineered from the 3.L2 TCR system, were used, both TCRs bind to murine haemoglobin (Hb 64-76). Table 1 provides K_D values using SPR at 25°C. Functional data was generated by incubating T hybridoma cells with peptide-pulsed APCs and measuring IL-2 production. We extracted potency values from dose-response curves in Figure 1b and c. Potency values from both TCR systems produce α = 0.37 (ID 12).

ID 13 [241] This paper contains binding and potency data for the 3.L2 TCR interacting with the WT haemoglobin peptide and a panel of altered peptide ligands. Table 2 provides K_D values using SPR at 25°C. The paper does not contain new potency measurements and therefore, we used potency values measured by Kersh and Allen[129] for the power analysis. This dataset produces α = 3.2 (ID 13).

2B4

ID 17[242] This paper contains affinity data for 2B4 TCR binding to its cognate MCC antigen and a set of variant peptides. Table 1 contains K_D values determined by SPR at 25°C. To compare with the original discrimination power, we used the original potency data[131] to produce α = 2.8 (ID 17).

ID 15 - 16[340] Revised data for 2B4 TCR is provided by Krogsgaard[340]. Table 1 provides K_D values measured by SPR at 25°C. For potency measurement, T cells from transgenic 2B4 mice were incubated peptide MHC molecules immobilised on plates, activation was measured by IL-2 production (EC_{50} values were given in Table 1). All ligands were included in the analysis, including those initially labelled as outliers in the publication. The resulting α is 1.2 (ID 16). We also calculated α with affinity data from this study and potency data from Lyons et al[131] (α = 2.2, ID 15).

ID 18[341] Newell et al.[341] studied the 2B4 and the 226 TCRs that bind to MCC. The K_D values were measured by SPR at 25°C and provided in Figure 5D (2B4) and 6B (266). T-cell hybridomas were incubated with peptide-pulsed cells and T-cell activation was measured by IL-2 production. P_{10} (concentration at 10% maximal IL-2 produced by wild-type 2B4) values given in Figure 5C (2B4) and 6 (266). Data for 2B4 produces α = 2.3 (ID 18). The 266 TCR was not included in the analysis, because not enough data points were available.

ID 19- 20[362] The affinity and potency of the 2B4 and the related 5cc7 TCR, which both interact with MCC, were reported. As before, SPR was used to report K_D values. Functional assays were done with blasted transgenic T cell incubated with peptide pulsed cells. To determine potency, IL-2 production was measured. We extracted both K_D values and EC_{50} values from Figure 4C. Data for 2B4 produced $\alpha = 0.95$ (ID 19) and for 5cc7 produced α = 0.74 (ID 20).

Other mouse TCRs

P14

ID 21 - 22[342] The mouse P14 TCR that recognises a set of altered peptides from the lymphocytic choriomeningitis virus epitope gp33–41 on murine class I MHC Db. All binding parameters were measured by SPR at 25°C. In functional assays, T cell cytotoxicity, and IFN-γ production of blasted splenocytes from P14 TCR transgenic mice was measured when binding peptide-MHC. Cytotoxicity was measured in a cellular assay, IFNγ production in a plate assay. The EC_{50} is used as potency measurement. All affinity and potency data were provided in Table 2. The α value for this TCR system is 2.1 for cytotoxicity assay (ID 21) and 1.3 for IFNγ assay (ID 22).

B3K506 and B3K508

ID 23 - 26[343] The MHC-II restricted B3K506 and B3K508 TCRs that recognise the 3K peptide were studied. The K_D values were measured by SPR at 25°C. T cell response was measured by T cell proliferation and cytokine production after stimulation with peptide-pulsed APCs. All K_D and EC_{50} values were given in Table S1. The B3K506 system produced α = 2.9 (ID 23) and α = 2.4 (ID 24) and the B3K508 system produced α = 2.9 (ID 25) and α = 2.5 (ID 26) for proliferation and TNFα production, respectively.

2C

ID 27 - 29[344] A panel of TCRs, derived from the murine 2C TCR, that differed in their affinity to the SIYR peptide presented on H-2Kb were used. The K_D values were measured by SPR at 25°C and provided in Table 1. Functional experiments were done with T cell hybridomas with or without CD8 expression. T cells were either incubated with peptides immobilised on plates or with antigen presenting cells pulsed with peptides. For cellular experiments EC_{50} values are given in Figure 3B and D (with and without CD8 respectively), for plate assays in Figure 4B (only CD8 negative data). Most of the ligands have a $K_D < 1$ μM, hence the data points were excluded from the analysis (see inclusion/exclusion criteria in Methods) and therefore, only few data points remained for the power analysis. CD8 negative T cell expressing TCRs stimulated in a plate assay produced $\alpha = 0.12$ (ID 27), however in the cellular assay TCRs binding to the antigen with a $K_D > 1$ were not activated in CD8 negative T cells (no data points to calculate α) (ID 28). TCRs in CD8 positive T cells stimulated in the cellular assay produce $\alpha = 0.66$ (ID 29).

ID 30[345] The 2C high affinity TCR and variants thereof binding to the QL9 and the altered QL9 peptide F5R were studied. The K_D values were measured by SPR at 25°C. Functional data was generated with T cell hybridomas stimulated by peptide-pulsed APCs with T cell activation assessed by IL-2 production. K_D and EC_{50} values were taken from Table 1. K_D values below 1μM were excluded from our power analysis. This data produces α = 2.7 (ID 30).

ID 31-32[346] The authors report binding and functional responses of high-affinity 2C TCR variants interacting with SIY peptide on MHC Kb and QL9 peptide on Ld. In total, 8 different TCR/pMHC ligand pairs were included. The K_D values were measured by SPR at 25°C and provided in Table 1. K_D values lower than 1 μM were excluded from the analysis. Functional assays were done with T cell hybridoma with and without CD8 expression with T cell activation assessed by IL-2 production in response to peptide-pulsed APCs. We extracted potency values as P_{50} from dose response curves in Figure 3. TCR variants m6 and m13 when binding to SIY-Kb showed no activation ($P_{50} > 100\mu$M). The calculated discrimination power is α = 4.7 for CD8 positive (ID 31) and α = 6.5 for CD8 negative T cells (ID 32).

NOT INCLUDED[85] This study provided binding and affinity data for the 2C TCR with and without CD8. However, when applying our inclusion/exclusion criteria only a single data

point was available and therefore, we were unable to calculate α. The reason is that only few interactions were measured by SPR and the majority of these produced K_D values below 1 μM.

42F3

ID 33 [347] The 42F3 TCR recognises the class I MHC molecule H2-Ld presenting the peptide p2Ca. The K_D values for a panel of peptide variants were measured by SPR at 25°C and potency data (EC_{50} of of IL2 production after cellular stimulation) were taken from Table 1 and Supplementary Figure 3C. The resulting α is 0.15 (ID 33).

Gp70 (AH1)-specific TCR

ID 34 [348] The TCR used in this study recognises the AH1 peptide which is derived from the endogenous retroviral protein gp70(423-431), a MHC class I restricted tumor-associated antigen. The authors used a set of AH1 variants with optimised affinities. The K_D values were measured by SPR at 25°C and provided in Figure 1B. Functional data was generated with a T cell line incubated with peptide-pulsed APCs. EC_{50} values of a proliferation assay are provided in Figure 2B. The calculated discrimination power was $\alpha = 5.2$ (ID 34).

Other human TCRs

1G4

ID 35 [334] The 1G4 TCR used in this study binds the NY-ESO-1 (157-165) peptide loaded on MHC class I HLA-A2. The authors generated a panel of TCRs derived from the human 1G4 TCR that bind with higher affinity than the wild-type TCR. The K_D values were measured by SPR at 25°C and provided in a table in Figure 1A. Potency was measured with a cytotoxicity assay and we extracted the mean EC_{50} values from Figure 5E. A decrease in potency was observed for TCRs with an affinity of $K_D < 1$ μM, which were excluded as per our exclusion criteria (see Methods). This data produced $\alpha = 0.67$ (ID 35).

ID 36 [349] Here, TCR/peptide–MHC binding parameters and T cell function were investigated with a panel of 1G4 TCR variants binding to the the NY-ESO-1 peptide. The K_D values were measured by SPR and provided in Table 1. The functional response of T cells was determined in a cytotoxic T cell assay. We extracted the mean EC_{50} values from Figure 4B. Data points with $K_D < 1\mu$M are excluded from the power analysis. The resulting α is 0.69 (ID 36).

ID 37 - 38 [149] Here, the interaction between 1G4 TCR binding a set of variant NY-ESO-1 (157-165) peptides on MHC class I was studied. The K_D values were measured by SPR at 37°C. The potency was determined by IFNγ production of T cell after stimulation by plate-immobilised pMHC or cytotoxicity by peptide-pulsed T2 APCs. The 1G4 TCR clone was used for both experiments. All affinity and EC_{50} values were given in Table S1. Discrimination power α for the 1G4 system is 0.6 (IFNγ, ID 37) and 1.6 (Cytotoxicity assay, ID 38).

1G4 and G10

ID 39 - 40[350] Experimental data was generated with the 1G4 and G10 TCR clones binding to a panel of peptide variants. The 1G4 TCR recognises the NY-ESO-1 antigen and the G10 TCR recognises the HIV gag p17 antigen in the context of MHC class I HLA-A2. The K_D values were measured by SPR at 37°C. Potency was determined by measuring IFNγ production in response to plate-immobilised recomvbinant pMHC. All K_D and EC_{50} values were given in Table S1 and S2. For the 1G4 system we found α = 0.55 (ID 39) and for the G10 system we found α = 0.95 (ID 40).

1E6

ID 41-42[265] The MHC-I-restricted 1E6 TCR reactive to preproinsulin (INS) was studied. The K_D values for a panel of variant peptides were measured by SPR at 25 and 37°C and provided in Figure 2. All K_D values lower than 1μM were excluded from the power analysis (see Methods). Functional assays were done with primary T cells responding to peptide-pulsed APCs and target cell lysis was measured for T cell activation. The EC_{50} was determined from the data in Figure 2K. We calculated α = 1.1 for K_D values measured at 25°C (ID 41) and α = 1.2 for K_D values measured at 37°C (ID 42).

A6

ID 43 -44[351] The A6 and engineered variants recognising the Tax or HuD peptides were used. The K_D values were measured by SPR at 25°C and provided in Figure 1A. T cell activation in response to peptide-pulsed APCs was assessed by CD107a expression and IFNγ production. Potency data was extracted as P_{20} for CD107a assay from dose-response curve in Figure 4C and as P_{10} for IFNγ assay from dose-response curve in Figure 5A. Data points with $K_D < 1\mu$M were not included in the power analysis. The resulting α is 2.0 (ID 43) and 2.2 (ID 44) for CD107 and IFNγ readout, respectively.

Gp100-specific TCR (Melanoma)

ID 45-46[352] Seven TCRs specific to human melanoma gp209–2M epitope (modified from gp100 (209-217)) were isolated from patients vaccinated with gp209– 2M. The K_D values of these TCRs measured by SPR at 25°C was provided in Table 1. Functional activity was determined by IFNγ production and ERK phosphorylation of transduced $CD8^+$ splenocytes mixed with peptide-pulsed APCs. Potency values were extracted from Figure S3A and C as P_{10}. The L2G2 TCR, which appeared as an extreme outlier showing the highest potency despite having the lowest affinity, was excluded from the analysis. This data point is shown in the plots as an open circle and including it would have further reduced the estimates α. The calculated powers were α = 1.3 for IFNγ production (ID 45) and α = 1.2 for ERK phosphorylation assay (ID 46).

ID 47 -48[353] T cell responses of a TCR specific to melanoma epitope gp100(280–288) were studied using a set of altered peptides. The K_D values were measured by SPR at 25°C and provided in Table 2. Functional assays used gp100 TCR-transduced CD8+ T-cells stimulated by

peptide-pulsed APCs with T cell activation assessed by cytotoxic lysis and MIP-1β production. We extracted the potency data as P_{10} from dose response curves in Figure 6. The resulting α values were 2.3 (lysis assay, ID 47) and 3.6 (MIP-1β production, ID 48).

14.3.d

ID 49 - 50[355] T-cell responses were measured using variants of the Staphylococcus enterotoxin C3 (SEC3) super antigen. In addition, the binding of a panel of mutated variants of the antibody F23.1 were also used. The K_D values of SEC3 were measured by SPR and provided in Table 1. The K_D values of the antibodies were provided in Table 1 of a different publication[354]. T-cell hybridomas, containing an NFAT-GFP expression cassette, were stimulated with SEC3 or antibody molecules immobilised onto plate surfaces to observe functional responses. We extracted all potency values as EC20 from Figure 4. According to our exclusion criteria (see Methods), we did not include any data point where $K_D < 1$ μM. The remaining data points generated with the SEC3 variants produced $\alpha = 0.81$ (ID 49) and with the F23.1 antibody variants produced $\alpha = 0.66$ (ID50).

TCR55

ID 51[155] This study used the TCR55 specific for HLA-B35-HIV(Pol448–456) binding to a set of variant peptides. The K_D values were measured by SPR at 25°C. T cell activation after stimulation with peptides pulsed on APCs was measured by CD69 expression. All K_D and EC_{50} values were given in Figure S5C. We calculated $\alpha = 0.19$ (ID 51).

ILA1

ID 52 - 57[244] The MHC-class I restricted ILA1 TCR is specific for the human telomerase reverse transcriptase (hTERT) epitope ILAKFLHWL (hTERT540-548). The K_D values of ligand variants were measured by SPR at 25°C and provided in Table 1. Three different assays were used to measure T cell activation: Degranulation assay, CD107a expression, and IFNγ production. Each assay was performed using APCs expressing either WT MHC or CD8-null MHC which cannot bind CD8. Potency values for degranulation were given in Table 1, CD107a and IFNγ potency data were extracted from dose-response curves in Figure 7. For potency data measured with wild-type (WT) and CD8 null MHC respectively, we calculated an α of 1.5 (WT, ID 52) and 2.5 (CD8 neg., ID 53) for degranulation, 2.2 (WT, ID 54) and 3.6 (CD8 neg., ID 55) for CD107a, and 2.2 (WT, ID 56) and 3.2 (CD8 neg., ID 57) for IFNγ production.

ID 58 - 61[356] The ILA1 TCR interaction with peptide variants was studied. The K_D values were measured by SPR at 25°C and provided in Table 1. T cell activation was measured by peptide-pulsed APCs and determined by MIP-1β, IFNγ, TNFα, and IL-2 production using intracellular cytokine staining. The potency values were read off as P_{50} from the dose-response curves in Figure 2. Authors suggested that the TCR shows a plateau at K_D values < 5 μM. Therefore we decided to exclude K_D values < 5 μM from the power analysis to avoid

underestimating the discrimination power α. The data produces α = 1.4 (ID 58), 0.77 (ID 59), 0.97 (ID 60) and 1.1 (ID 61) for MIP-1β, IFNγ, TNFα and IL-2 production respectively.

NY-ESO-1(60-72)-specific TCR

ID 62 [357] Four TCRs binding to the tumorigenic antigen NY-ESO-1(60-72) were obtained from patients with melanomas expressing NY-ESO-1. The K_D values were measured by SPR 25°C and given in Figure 2C. The functional response of TCRs to exogenous peptide stimulation was assessed by measuring IFNγ production of T cells incubated with NY-ESO-1-expressing melanoma cells. We extracted EC_{50} values from dose-response curves in Figure 1F. We calculated $\alpha = -0.59$ (ID 62).

Gliadin-specific TCRs (Celiac disease)

ID 63 [358] Seven DQ8-glia-a1-restricted T cell receptors isolated from celiac disease patients were characterised for their binding affinity to a-I- gliadin and their functional response. The K_D values were measured by SPR at 25°C and provided in Figure 2 and S5. T-cell activation was assessed by proliferation in response to peptide-pulsed APCs. We extracted P_{20} values from the dose-response curves in Figure 1 (Black curve Q-Q). We calculated an α = 0.83 (ID 63).

LC13

ID 64 - 67 [245] The LC13 and SB27 TCRs were studied using an alanine scan. The K_D values were measured by SPR and provided in Table S2. T-cell activation was measured using Jurkat T cells expressing the TCR with CD69 and cytoxicity assessed in response to peptide-pulsed APCs. Figure 1C and 1D showed the dose-response curves for CD69 upregulation for either CD8 positive or CD8 negative cells. We extracted the P_{30} as potency measure. EC_{50} of cytotoxicity assay was given in Figure 2 for LC13 and Figure S2 for SB27. Potency values from CD69 produced α = 1.9 (ID 64) for CD8 positive cells and α =7.8 (ID 65) for CD8 negative cells. Lysis assays produced α = 4.1 (ID 66) for the LC13 and α = 0.11 (ID 67) for SB27 TCR.

HIV-Gag293-specific TCRs

ID 68 [359] TCRs specific to HIV Gag293 protein were isolated from patients infected with HIV. The K_D values were measured by SPR and provided in Table 3. T-cell activation was assessed using TCR-transduced J76 cells measuring CD69 expression in response to peptide-pulsed APCs. We extracted the mean EC_{50} values from Figure 6D. We calculated $\alpha = 1.0$ (ID 68).

MEL5

ID 69 [360] The MEL5 and MEL187.c5 TCRs were studied that bind the MART-1 antigen and variants thereof. The K_D values were measured by SPR at 25°C and provided in Table 1. T cell activation was measured by MIP-1β production in response to peptide-pulsed APCs. We extracted potency values as P_{50} from dose response curves in Figure 2 and S1. Because

responses to peptides were measured in separate experiments, potency data is normalised to wild type peptide. This produced $\alpha = 2.3$ (ID 69).

ID 70[361] The MEL5, MEL187.c5, DMF4, and DMF5 were studied that recognise the MART-1 antigen. Two overlapping peptides were used: nonapeptide MART-1(27-35) and decapeptide MART-1(26-35). The K_D values were measured by SPR at 25°C and provided in Table 1. T cell activation was assessed using primary human T cells responding to peptide-pulsed APCs with MIP-1β used as a marker of T cell activation. We determined P_{30} directly form does response curves in Figure 1A. Data produced $\alpha = 4.5$ (ID 70)

Other (non-TCR) surface receptors

Cytokine receptors

ID 1-2[249] Engineered IL-2 variants with increased binding affinity for the interleukin-2 (IL-2) receptor subunit β (IL-2Rb) were studied. The K_D values for IL-2 variants to IL-2Rβ are given in Supplementary Figure 3 and determined by SPR at 25°C. As only the affinities to a single subunit were varied between ligands, potency was plotted over these K_D values. Functional experiments were performed with either CD25 negative human Natural Killer cells or CD25 negative murine T cells. We extracted the EC_{50} values as a measure of potency from dose-response curves in Figure 3a and 3e. We calculated α = 0.55 (ID 1) for experiments done with Natural Killer cells and α = 0.74 (ID 2) for T cells.

ID 3-6[250] The relationship between the interaction of interleukin 13 (IL-13) with its cytokine receptor and the resulting downstream cellular responses was investigated. A panel of IL-13 variants with a range of binding affinities for the receptor subunit IL-13Ra1 was generated. The binding affinities of these ligands were given in a table in Figure 2C in the paper. Here, only the affinity for the α subunit of the receptor dimer was varied and therefore, we plotted potency over these K_D values. Functional responses of binding were determined by measuring STAT6 phosphorylation, CD86 and CD209 production, and proliferation after receptor stimulation in the IL-13-responsive cell line A549. We extracted EC_{50} values for pSTAT6 from Figure 5B. To avoid extrapolating potencies, ligands with EC_{50} larger than the highest concentration plotted in the dose-response curve (in Figure 5A) were excluded. The mean proliferation EC_{50} values were taken from Figure 5G. CD86 EC_{50} values were extracted from the dose response curve in Figure 5H, CD209 EC_{50} values from the dose-response curve in Figure S7C. EC_{50} values for CD86 and CD209 extracted from the dose response curves did not exactly match EC_{50} values given in Figure S7 D and E, but both values resulted in similar α values. The α values calculated for the IL-13 receptor are 0.47 (ID 3), 0.39 (ID 4), 0.44 (ID 5), and 0.42 (ID 6) for potency values from pSTAT6, proliferation, CD86, and CD205 assays, respectively.

ID 7-8[251] Study uses a set of mutated cytokines derived from IFNα2 and IFNω, binding cytokine receptors IFNAR1 and IFNAR2. All binding affinities of mutants normalised to WT are provided in Supplemental Table 2. Because mutations change the affinities to both IFNAR1

and IFNAR2 we calculated an effective binding affinity by multiplying K_D of IFNAR1 with K_D of IFNAR2 (R1xR2). Functional response of cells to cytokine mutants was determined by their antiviral activity in a Hepatitis C Virus Replication Assay, their antiproliferation activity on WISH cells. Mean EC_{50} values normalised to WT obtained from Figure 7A. We calculated $\alpha = 0.71$ (ID 7) for antiviral potency and $\alpha = 1.3$ (ID 8) for antiproliferation potency.

ID 9-11[252] Study of IFN1 receptor activation with engineered higher-affinity type I IFNs. Affinity constants for peptides to each receptor subunit were measured by SPR. To get the effective K_D we multiplied K_D of IFN- αR1 binding with K_D of IFN- αR2 binding (R1xR2) Ligand activity was measured by STAT phosphorylation, antiviral activity and antiproliferation activity. All affinity and EC_{50} values were provided in Table S2. The data produced $\alpha = 0.024$ for STAT1 phosphorylation (ID 9), $\alpha = 0.034$ for antiviral activity (ID 10), and α = 0.50 (ID 11) for the anti-proliferation assay.

ID 12-13[253] In this study, the authors engineered IL-6 variants with different affinities to the IL-6 receptor subunit gp130. Cytokine gp130 binding kinetics were measured with a switchSENSE chip, binding parameters were given in Supplementary Figure 1D. The influence of IL-6 variants on the functional activity of the receptor was determined by the amount of STAT1 and STAT3 phosphorylation at different ligand concentrations. We read off the potency of each ligand as P_{25} directly from dose-response curves in Figure 2A and B. We calculated α = 0.54 for pSTAT1 (ID 12) and α = 0.52 for pSTAT 3 (ID 13).

Receptor Tyrosine Kinase (RTK)

ID 14[255] In this study, the effect of three mutated epidermal growth factors on epidermal growth factor receptor (EGFR) was studied. Affinity values of growth factor to receptor were measured with radioactively labelled ligands binding to receptors on cells. Data are given in Table 1. The functional response of cells to ligands was determined by measuring the specific growth rate after stimulation. We extracted the EC_{50} values from dose-response curves in Figure 4. This produced $\alpha = 0.55$ (ID 14).

ID 15 - 16[254] Paper contains data on the c-Kit receptor tyrosine kinase which is activated by the Stem cell factor (SCF). Affinity and functional response of the receptor to SCF variants was studied. Binding parameters were measured by SPR and provided in Figure 1F. Cell activation after stimulation with ligands was determined by the amount of ERK and AKT phosphorylation (pERK and pAKT). We extracted the potency data for each variant as EC_{50} from dose response curves in Figure 2D and 2E. We calculated α = 0.83 (ID 15) and α = 0.88 (ID 16) for pERK and pAKT measurements respectively.

GPCRs

ID 17 -18[257] The binding parameters of the GPCR adenosine A2A receptor to various agoinist and their functional effects were studied. Association and dissociation rates, and hence K_D values, were determined with a kinetic radioligand binding assay. Functional activity

of HEK293 expressing the A2A receptor was measured by detecting cAMP production and changes in cell morphology. The binding data was provided in Table 3 and EC_{50} values from functional experiments were given in Table 4. The discrimination power calculated with cell morphology data is $\alpha = 0.29$(ID 17) and with the cAMP assay produced α = 0.71 (ID 18).

ID 19-20[256] The M3 muscarinic receptor was studied using a set of agonists. The binding kinetics were determined with competition binding assay and were provided in Table 1. Agonist potency was measured by guanosine 5'-O- (3-[35S]thio) triphosphate (GTPγS) binding to GαD subunits, and by intracellular calcium levels after receptor stimulation. Potency data measured as EC_{50} values were provided in Table 2. The resulting power was $\alpha = 0.77$ (ID 19) and $\alpha = 0.55$ (ID 20) for calcium response and GTPγS binding assay, respectively.

ID 21[258] The CXCR4 receptor is activated by the chemokine CXCL12. In this paper, the interactions of Baclofen and other GABA ligands were tested on their abilities to activate CXCR4. The affinity of ligands to the receptor was measured by back-scattering interferometry and K_D values given in Figure 7. The functional response of oocytes expressing CXCR4 to ligands was determined by measuring the inward currents at different ligand concentrations. EC_{50} values were provided in Table 1. We calculated αD = 0.57 for this system (ID 21).

ID 22 -24[259] Characterisation of binding properties and potencies of CXC chemokine receptor 3 antagonists. The binding properties of the antagonist were determined using a kinetic radioligand binding assay. Affinity values were in Table 1 measured for different cell lines. Functional responses after ligand binding were measured by guanosine 5'-O-(3-[35S]thio)triphosphate (GTPyS) binding, calcium release, and cellular chemotaxis. All EC_{50} values of assays were given in the text. We calculated αD = 0.72 (ID 22) , 1.1 (ID 23), and 0.56 (ID 24) for calcium release, GTPyS binding, and chemotaxis assays respectively.

CARs

ID 25[260] This study contains affinity and potency data for a CAR binding the ErbB2 surface antigen. The authors generated a series of anti-ErB2 single-chain variable fragments fused to the CD3ζ cytoplasmic domain. The K_D values are reported in Table 1. Functional experiments were done in a plate assay, with ErbB2 immobilised to a surface. The potency of receptors was measured by IFNγ production of T cells after stimulation. We extracted P_{20} values from the dose-response curve in Figure 4A. The resulting α is 0.52 (ID 25).

ID 26-27[261] This study characterised a panel of CARs that bind to the ErbB2 surface protein. CARs were constructed by linking the various anti-ErB2 single-chain variable fragments to the CD8αD hinge and transmembrane domain followed by the 4-1BB and CD3ζ intracellular signalling domains. The K_D values were measured by SPR and provided in Table S1. We obtained potency data by using CD107a expression and proliferation assay data in Figures 2A and C to the respective plot dose-response curves. P_{50} values were extracted from these plots. The resulting α values are 1.1 for CD107 (ID 26) and 0.64 for proliferation assay (ID 27).

ID 28[78] Taylor et al.[78] developed a synthetic CAR signalling system in which the extracellular domains of the CAR and its ligand antigen were exchanged with short hybridizing strands of DNA. The DNA-CARζ consist of an ssDNA covalently attached to a SNAP tag protein which was fused to a transmembrane domain and the CD3ζ chain. DNA strands of different lengths and sequences were designed to vary the affinity of the CAR to the ligand. Binding was measured as the lifetime (τ_{corr}) of single ligand-CAR interactions using microscopy and corrected for photobleaching and provided in Figure 2D. The dissociation rate k_off was calculated from the lifetimes with $k_{\text{off}} = ln(2)/\tau$. To measure T cell responses, ligands, consisting of the complimentary strand of ssDNA, were anchored in planar supported lipid bilayer where they can freely diffuse. The DNA-CARζ was expressed in TCR-negative Jurkat cells. Cell activation after incubation with ligands was measured by phosphorylation of ERK. Potency data was extracted as P_{20} from dose-response curves in Figure 2C. This CAR system produced α = 1.2 (ID 28).

BCRs

ID 29-30[262] The study used the HyHEL10 and D1.3 BCRs, which have a high affinity to the hen egg lysozyme (HEL) and variants thereof. The K_D values were measured by SPR at 25°C and dissociation rates were provided in Table 1. For functional experiments, the ability of B cells to mediate HEL presentation to T cell hybridomas after stimulation with mutant lysozymes was determined by measuring IL-2 production of T cells specific to HEL. We extracted the potency data from dose-response curves in Figures 3 and 4 as EC_{50}. The authors described an affinity floor for the B cell receptor when the dissociation rate was below 10^{-4} s^{-1} so that potency did not longer decrease for these interactions. To avoid underestimating α, we did not include these higher affinity ligands in the power analysis. The resulting α values were α = 1.4 for the D1.3 BCR (ID 29) and α = 1.3 for the HyHEL10 BCR (ID 30).

REFERENCES

1. Rang HP. The receptor concept: pharmacology's big idea. *British Journal of Pharmacology* **147** (2006) S9. doi:10.1038/SJ.BJP.0706457.

2. Janeway CA, Medzhitov R. Innate immune recognition. *Annual review of immunology* **20** (2002) 197–216. doi:10.1146/ANNUREV.IMMUNOL.20.083001.084359.

3. Davis MM, Chien Y, Gascoigne NRJ, Hedrick SM. A Murine T Cell Receptor Gene Complex: Isolation, Structure and Rearrangement. *Immunological Reviews* **81** (1984) 235–258. doi:10.1111/j.1600-065X.1984.tb01113.x.

4. Weiss A, Littman DR. Signal transduction by lymphocyte antigen receptors. *Cell* **76** (1994) 263–274. doi:10.1016/0092-8674(94)90334-4.

5. Flajnik MF, Kasahara M. Origin and evolution of the adaptive immune system: genetic events and selective pressures. *Nature reviews. Genetics* **11** (2010) 47. doi:10.1038/NRG2703.

6. Burnet FM. A Modification of Jerne's Theory of Antibody Production using the Concept of Clonal Selection. *Australian Journal of Science* **20** (1957) 67–69. doi:10.3322/canjclin.26.2.119.

7. Moticka EJ. The Clonal Selection Theory of Antibody Formation. *A Historical Perspective on Evidence-Based Immunology*, chap. 6 (2016), 47–54. doi:10.1016/B978-0-12-398381-7.00006-X.

8. Matzinger P, Bevan MJ. Why do so many lymphocytes respond to major histocompatibility antigens? *Cellular Immunology* **29** (1977) 1–5. doi:10.1016/0008-8749(77)90269-6.

9. Murphey K. *Janeway's Immunobiology* (New York: Garland Science), 8 edn. (2012).

10. Robinson J, Barker DJ, Marsh SG. 25years of the IPD-IMGT/HLA Database. *HLA* **103** (2024) e15549. doi:10.1111/TAN.15549.

11. Barker DJ, Maccari G, Georgiou X, Cooper MA, Flicek P, Robinson J, et al. The IPD-IMGT/HLA Database. *Nucleic Acids Research* **51** (2023) D1053–D1060. doi:10.1093/nar/gkac1011.

12. Rudolph MG, Stanfield RL, Wilson IA. How TCRs Bind MHCs, Peptides, and Coreceptors. *Annual Review of Immunology* **24** (2006) 419–466. doi:10.1146/annurev.immunol.23.021704.115658.

13. Roche PA, Furuta K. The ins and outs of MHC class II-mediated antigen processing and presentation. *Nature Reviews Immunology* **15** (2015) 203–216. doi:10.1038/nri3818.

14. Rock KL, Gramm C, Rothstein L, Clark K, Stein R, Dick L, et al. Inhibitors of the proteasome block the degradation of most cell proteins and the generation of peptides presented on MHC class I molecules. *Cell* **78** (1994) 761–771. doi:10.1016/S0092-8674(94)90462-6.

15. Bard JA, Goodall EA, Greene ER, Jonsson E, Dong KC, Martin A. Structure and Function of the 26S Proteasome. *Annual Review of Biochemistry* **87** (2018) 697–724. doi:10.1146/annurev-biochem-062917-011931.

16. Reits EA, Vos JC, Grammé M, Neefjes J. The major substrates for TAP in vivo are derived from newly synthesized proteins. *Nature* **404** (2000) 774–778. doi:10.1038/35008103.

17. Blees A, Januliene D, Hofmann T, Koller N, Schmidt C, Trowitzsch S, et al. Structure of the human MHC-I peptide-loading complex. *Nature* **551** (2017) 525–528. doi:10.1038/nature24627.

18. Fisette O, Wingbermühle S, Tampé R, Schäfer LV. Molecular mechanism of peptide editing in the tapasin-MHC I complex. *Scientific reports* **6** (2016). doi:10.1038/SREP19085.

19. Pishesha N, Harmand TJ, Ploegh HL. A guide to antigen processing and presentation. *Nature Reviews Immunology 2022 22:12* **22** (2022) 751–764. doi:10.1038/s41577-022-00707-2.

20. Riese RJ, Wolf PR, Brömme D, Natkin LR, Villadangos JA, Ploegh HL, et al. Essential Role for Cathepsin S in MHC Class II–Associated Invariant Chain Processing and Peptide Loading. *Immunity* **4** (1996) 357–366. doi:10.1016/S1074-7613(00)80249-6.

21. Pos W, Sethi DK, Wucherpfennig KW. Mechanisms of peptide repertoire selection by HLA-DM. *Trends in Immunology* **34** (2013) 495–501. doi:10.1016/j.it.2013.06.002.

22. Yang H, Buisson S, Bossi G, Wallace Z, Hancock G, So C, et al. Elimination of latently HIV-infected cells from antiretroviral therapy-suppressed subjects by engineered immune-mobilizing T-cell receptors. *Molecular Therapy* **24** (2016) 1913–1925.

23. Labrecque N, Whitfield LS, Obst R, Waltzinger C, Benoist C, Mathis D. How much TCR does a T cell need? *Immunity* **15** (2001) 71–82. doi:10.1016/S1074-7613(01)00170-4.

24. Sušac L, Vuong MT, Thomas C, von Bülow S, O'Brien-Ball C, Santos AM, et al. Structure of a fully assembled tumor-specific T cell receptor ligated by pMHC. *Cell* **185** (2022) 3201–3213.e19. doi:10.1016/J.CELL.2022.07.010.

25. Cabaniols JP, Fazilleau N, Casrouge A, Kourilsky P, Kanellopoulos JM. Most α/β T Cell Receptor Diversity Is Due to Terminal Deoxynucleotidyl Transferase. *The Journal of Experimental Medicine* **194** (2001) 1385. doi:10.1084/JEM.194.9.1385.

26. Rossjohn J, Gras S, Miles JJ, Turner SJ, Godfrey DI, McCluskey J. T cell antigen receptor recognition of antigen-presenting molecules. *Annual Review of Immunology* **33** (2015) 169–200. doi:10.1146/annurev-immunol-032414-112334.

27. van der Merwe PA, Davis SJ. Molecular Interactions Mediating T Cell Antigen Recognition. *Annual Review of Immunology* **21** (2003) 659–684. doi:10.1146/annurev.immunol.21.120601.141036.

28. Stone JD, Chervin AS, Kranz DM. T-cell receptor binding affinities and kinetics: impact on T-cell activity and specificity. *Immunology* **126** (2009) 165–176. doi:10.1111/j.1365-2567.2008.03015.x.

29. Garcia KC, Degano M, Stanfield RL, Brunmark A, Jackson MR, Peterson PA, et al. An $\alpha\beta$ T Cell Receptor Structure at 2.5 Å and Its Orientation in the TCR-MHC Complex. *Science* **185** (1996) 209–219. doi:10.1126/SCIENCE.274.5285.209.

30. Brown JH, Jardetzky TS, Gorga JC, Stern LJ, Urban RG, Strominger JL, et al. Three-dimensional structure of the human class II histocompatibility antigen HLA-DR1. *Nature* **364** (1993) 33–39. doi:10.1038/364033A0.

31. Chang VT, Fernandes RA, Ganzinger KA, Lee SF, Siebold C, McColl J, et al. Initiation of T cell signaling by CD45 segregation at 'close contacts'. *Nature Immunology* **17** (2016) 574–582. doi:10.1038/ni.3392.

32. Notti RQ, Yi F, Heissel S, Molina H, Klebanoff CA, Walz T. The resting state of the human T-cell receptor. *bioRxiv* (2023) 2023.08.22.554360. doi:10.1101/2023.08.22.554360.

33. Punt JA, Roberts JL, Kearse KP, Singer A. Stoichiometry of the T cell antigen receptor (TCR) complex: Each TCR/CD3 complex contains one TCR α, one TCR β, and two CD3epsilon chains. *Journal of Experimental Medicine* **180** (1994) 587–593.

34. Reth M. Antigen receptor tail clue. *Nature* **338** (1989) 383–384. doi:10.1038/338383B0.

35. Underhill DM, Goodridge HS. The many faces of ITAMs. *Trends in Immunology* **28** (2007) 66–73. doi:10.1016/J.IT.2006.12.004.

36. Dong D, Zheng L, Lin J, Zhang B, Zhu Y, Li N, et al. Structural basis of assembly of the human T cell receptor–CD3 complex. *Nature* **573** (2019) 546–552. doi:10.1038/s41586-019-1537-0.

37. Saotome K, Dudgeon D, Colotti K, Moore MJ, Jones J, Zhou Y, et al. Structural analysis of cancer-relevant TCR-CD3 and peptide-MHC complexes by cryoEM. *Nature Communications* **14** (2023) 2401. doi:10.1038/s41467-023-37532-7.

38. Aivazian D, Stern LJ. Phosphorylation of T cell receptor zeta is regulated by a lipid dependent folding transition. *Nature structural biology* **7** (2000) 1023–1026. doi:10.1038/80930.

39. Xu C, Gagnon E, Call ME, Schnell JR, Schwieters CD, Carman CV, et al. Regulation of T cell receptor activation by dynamic membrane binding of the CD3epsilon cytoplasmic tyrosine-based motif. *Cell* **135** (2008) 702–713. doi:10.1016/j.cell.2008.09.044.

40. Zhang H, Cordoba SP, Dushek O, Anton van der Merwe P. Basic residues in the T-cell receptor ζ cytoplasmic domain mediate membrane association and modulate signaling. *Proceedings of the National Academy of Sciences* **108** (2011) 19323–19328. doi:10.1073/pnas.1108052108.

41. Weinbaum S, Tarbell JM, Damiano ER. The Structure and Function of the Endothelial Glycocalyx Layer. *Annual Review of Biomedical Engineering* **9** (2007) 121–167. doi:10.1146/annurev.bioeng.9.060906.151959.

42. Reitsma S, Slaaf DW, Vink H, van Zandvoort MAMJ, oude Egbrink MGA. The endothelial glycocalyx: composition, functions, and visualization. *Pflügers Archiv - European Journal of Physiology* **454** (2007) 345–359. doi:10.1007/s00424-007-0212-8.

43. Jenkins E, Körbel M, O'Brien-Ball C, McColl J, Chen KY, Kotowski M, et al. Antigen discrimination by T cells relies on size-constrained microvillar contact. *Nature Communications* **14** (2023) 1611. doi:10.1038/s41467-023-36855-9.

44. Polliack A, de Harven E. Surface features of normal and leukemic lymphocytes as seen by scanning electron microscopy. *Clinical Immunology and Immunopathology* **3** (1975) 412–430. doi:10.1016/0090-1229(75)90029-X.

45. Jung Y, Riven I, Feigelson SW, Kartvelishvily E, Tohya K, Miyasaka M, et al. Three-dimensional localization of T-cell receptors in relation to microvilli using a combination of superresolution microscopies. *Proceedings of the National Academy of Sciences* **113** (2016) 201605399. doi:10.1073/pnas.1605399113.

46. Majstoravich S, Zhang J, Nicholson-Dykstra S, Linder S, Friedrich W, Siminovitch KA, et al. Lymphocyte microvilli are dynamic, actin-dependent structures that do not require Wiskott-Aldrich syndrome protein (WASp) for their morphology. *Blood* **104** (2004) 1396–1403. doi:10.1182/blood-2004-02-0437.

47. Cai E, Marchuk K, Beemiller P, Beppler C, Rubashkin MG, Weaver VM, et al. Visualizing dynamic microvillar search and stabilization during ligand detection by T cells. *Science* **356** (2017) eaal3118. doi:10.1126/science.aal3118.

48. Barclay AN, Brown MH, Law SKA, McKnight AJ, Tomlinson MG, van der Merwe PA. *The Leucocyte Antigen FactsBook* (Elsevier), second edn. (1997).

49. Samelson LE, Patel MD, Weissman AM, Harford JB, Klausner RD. Antigen activation of murine T cells induces tyrosine phosphorylation of a polypeptide associated with the T cell antigen receptor. *Cell* **46** (1986) 1083–1090. doi:10.1016/0092-8674(86)90708-7.

50. Qian D, Weiss A. T cell antigen receptor signal transduction. *Current Opinion in Cell Biology* **9** (1997) 205–212.

51. Chan C, Irving B, Fraser JD, Weiss A. The zeta chain is associated with a tyrosine kinase and upon T-cell antigen receptor stimulation associates with ZAP-70, a 70-kDa tyrosine phosphoprotein. *Proceedings of the National Academy of Sciences of the United States of America* **88** (1991) 9166–9170.

52. Farrell MV, Nunez AC, Yang Z, Pérez-Ferreros P, Gaus K, Goyette J. Protein-PAINT: Superresolution microscopy with signaling proteins. *Science Signaling* **15** (2022) 9782. doi:10.1126/SCISIGNAL.ABG9782.

53. Nika K, Soldani C, Salek M, Paster W, Gray A, Etzensperger R, et al. Constitutively Active Lck Kinase in T Cells Drives Antigen Receptor Signal Transduction. *Immunity* **32** (2010) 766–777. doi:10.1016/j.immuni.2010.05.011.

54. Stirnweiss A, Hartig R, Gieseler S, Lindquist JA, Reichardt P, Philipsen L, et al. T Cell Activation Results in Conformational Changes in the Src Family Kinase Lck to Induce Its Activation. *Science Signaling* **6** (2013) ra13–ra13. doi:10.1126/scisignal.2003607.

55. van der Merwe PA, Dushek O. Mechanisms for T cell receptor triggering. *Nature Reviews Immunology* **11** (2011) 47–55. doi:10.1038/nri2887.

56. Davis SJ, Van Der Merwe PA. The kinetic-segregation model: TCR triggering and beyond. *Nature immunology* **7** (2006) 803–809.

57. Secrist JP, Burns LA, Karnitz L, Koretzky GA, Abraham RT. Stimulatory effects of the protein tyrosine phosphatase inhibitor, pervanadate, on T-cell activation events. *Journal of Biological Chemistry* **268** (1993) 5886–5893. doi:10.1016/S0021-9258(18)53403-7.

58. Cordoba SP, Choudhuri K, Zhang H, Bridge M, Basat AB, Dustin ML, et al. The large ectodomains of CD45 and CD148 regulate their segregation from and inhibition of ligated T-cell receptor. *Blood* **121** (2013) 4295–4302. doi:10.1182/blood-2012-07-442251.

59. Irles C, Symons A, Michel F, Bakker TR, van der Merwe PA, Acuto O. CD45 ectodomain controls interaction with GEMs and Lck activity for optimal TCR signaling. *Nature immunology* **4** (2003) 189–197. doi:10.1038/ni877.

60. Boniface JJ, Rabinowitz JD, Wülfing C, Hampl J, Reich Z, Altman JD, et al. Initiation of signal transduction through the T cell receptor requires the multivalent engagement of peptide/MHC ligands [corrected]. *Immunity* **9** (1998) 459–466. doi:10.1016/S1074-7613(00)80629-9.

61. Germain RN. T-cell signaling: the importance of receptor clustering. *Current biology* **7** (1997) R640–4. doi:10.1016/S0960-9822(06)00323-X.

62. Cochran JR, Cameron TO, Stern LJ. The relationship of MHC-peptide binding and T cell activation probed using chemically defined MHC class II oligomers. *Immunity* **12** (2000) 241–250. doi:10.1016/S1074-7613(00)80177-6.

63. Krogsgaard M, Li QJ, Sumen C, Huppa JB, Huse M, Davis MM. Agonist/endogenous peptide-MHC heterodimers drive T cell activation and sensitivity. *Nature* **434** (2005) 238–243. doi:10.1038/NATURE03391.

64. Yokosuka T, Sakata-Sogawa K, Kobayashi W, Hiroshima M, Hashimoto-Tane A, Tokunaga M, et al. Newly generated T cell receptor microclusters initiate and sustain T cell

activation by recruitment of Zap70 and SLP-76. *Nature immunology* **6** (2005) 1253–1262. doi:10.1038/NI1272.

65. Trautmann A. Microclusters initiate and sustain T cell signaling. *Nature Immunology* **6** (2005) 1213–1214. doi:10.1038/ni1205-1213.

66. Ma Y, Pandzic E, Nicovich PR, Yamamoto Y, Kwiatek J, Pageon SV, et al. An intermolecular FRET sensor detects the dynamics of T cell receptor clustering. *Nature Communications* **8** (2017) 15100. doi:10.1038/ncomms15100.

67. Li HL, Davis W, Puré E. Suboptimal cross-linking of antigen receptor induces Syk-dependent activation of p70S6 kinase through protein kinase C and phosphoinositol 3-kinase. *Journal of Biological Chemistry* **274** (1999) 9812–9820. doi:10.1074/jbc.274.14.9812.

68. Ma CY, Marioni JC, Griffiths GM, Richard AC. Stimulation strength controls the rate of initiation but not the molecular organization of tcr-induced signalling. *eLife* **9** (2020) 1–57. doi:10.7554/eLife.53948.

69. Brameshuber M, Kellner F, Rossboth BK, Ta H, Alge K, Sevcsik E, et al. Monomeric TCRs drive T cell antigen recognition. *Nature Immunology* **19** (2018) 487–496. doi:10.1038/s41590-018-0092-4.

70. Guo X, Yan C, Li H, Huang W, Shi X, Huang M, et al. Lipid-dependent conformational dynamics underlie the functional versatility of T-cell receptor. *Cell Research* **27** (2017) 505–525. doi:10.1038/cr.2017.42.

71. Rangarajan S, He Y, Chen Y, Kerzic MC, Ma B, Gowthaman R, et al. Peptide-MHC (pMHC) binding to a human antiviral T cell receptor induces long-range allosteric communication between pMHC-and CD3-binding sites. *Journal of Biological Chemistry* **293** (2018) 15991–16005. doi:10.1074/JBC.RA118.003832/ATTACHMENT/DF6A9EF7-D6C0-4BD4-B1DE-CEC02D880B69/MMC1.DOCX.

72. Alba J, D'abramo M. The Full Model of the pMHC-TCR-CD3 Complex: A Structural and Dynamical Characterization of Bound and Unbound States. *Cells* **11** (2022) 668. doi:10.3390/CELLS11040668/S1.

73. Gil D, Schamel WWA, Montoya M, Sánchez-Madrid F, Alarcón B. Recruitment of Nck by CD3epsilon Reveals a Ligand-Induced Conformational Change Essential for T Cell Receptor Signaling and Synapse Formation. *Cell* **109** (2002) 901–912. doi:10.1016/S0092-8674(02)00799-7.

74. Yiemwattana I, Ngoenkam J, Paensuwan P, Kriangkrai R, Chuenjitkuntaworn B, Pongcharoen S. Essential role of the adaptor protein Nck1 in Jurkat T cell activation and function. *Clinical and Experimental Immunology* **167** (2011) 99–107. doi:10.1111/j.1365-2249.2011.04494.x.

75. Szymczak AL, Workman CJ, Gil D, Dilioglou S, Vignali KM, Palmer E, et al. The CD3ϵ Proline-Rich Sequence, and Its Interaction with Nck, Is Not Required for T Cell

Development and Function. *The Journal of Immunology* **175** (2005) 270–275. doi:10.4049/jimmunol.175.1.270.

76. Fernandes RA, Yu C, Carmo AM, Evans EJ, van der Merwe PA, Davis SJ. What Controls T Cell Receptor Phosphorylation? *Cell* **142** (2010) 668–669. doi:10.1016/j.cell.2010.08.018.

77. Yousefi OS, Günther M, Hörner M, Chalupsky J, Wess M, Brandl SM, et al. Optogenetic control shows that kinetic proofreading regulates the activity of the T cell receptor. *eLife* **8** (2019) 1–33. doi:10.7554/elife.42475.

78. Taylor MJ, Husain K, Gartner ZJ, Mayor S, Vale RD. A DNA-based T cell receptor reveals a role for receptor clustering in ligand discrimination. *Cell* **169** (2017) 108–119. doi:10.1016/j.cell.2017.03.006.

79. Denham EM, Barton MI, Black SM, Bridge MJ, de Wet B, Paterson RL, et al. A generic cell surface ligand system for studying cell–cell recognition. *PLoS Biology* **17** (2019) 1–30. doi:10.1371/journal.pbio.3000549.

80. Kim ST, Takeuchi K, Sun ZYJ, Touma M, Castro CE, Fahmy A, et al. The $\alpha\beta$ T cell receptor is an anisotropic mechanosensor. *Journal of Biological Chemistry* **284** (2009) 31028–31037. doi:10.1074/jbc.M109.052712.

81. Wang Jh. T cell receptors, mechanosensors, catch bonds and immunotherapy. *Progress in Biophysics and Molecular Biology* **153** (2020) 23–27. doi:10.1016/j.pbiomolbio.2020.01.001.

82. Göhring J, Schrangl L, Schütz GJ, Huppa JB. Mechanosurveillance: Tiptoeing T Cells. *Frontiers in Immunology* **13** (2022) 886328. doi:10.3389/FIMMU.2022.886328/BIBTEX.

83. Göhring J, Kellner F, Schrangl L, Platzer R, Klotzsch E, Stockinger H, et al. Temporal analysis of T-cell receptor-imposed forces via quantitative single molecule FRET measurements. *Nature Communications* **12** (2021) 2502. doi:10.1038/s41467-021-22775-z.

84. Mørch AM, Schneider F, Jenkins E, Santos AM, Fraser SE, Davis SJ, et al. The kinase occupancy of T cell coreceptors reconsidered. *Proceedings of the National Academy of Sciences of the United States of America* **119** (2022). doi:10.1073/PNAS.2213538119.

85. Holler PD, Kranz DM. Quantitative analysis of the contribution of TCR/pepMHC affinity and CD8 to T cell activation. *Immunity* **18** (2003) 255–264. doi:10.1016/S1074-7613(03)00019-0.

86. Wooldridge L, Van Den Berg HA, Glick M, Gostick E, Laugel B, Hutchinson SL, et al. Interaction between the CD8 Coreceptor and Major Histocompatibility Complex Class I Stabilizes T Cell Receptor-Antigen Complexes at the Cell Surface. *The Journal of biological chemistry* **280** (2005) 27491. doi:10.1074/JBC.M500555200.

87. Li QJJ, Dinner AR, Qi S, Irvine DJ, Huppa JB, Davis MM, et al. CD4 enhances T cell sensitivity to antigen by coordinating Lck accumulation at the immunological synapse. *Nature immunology* **5** (2004) 791–799. doi:10.1038/NI1095.

88. Laugel B, Price DA, Milicic A, Sewell AK. CD8 experts differential effects on the deployment of cytotoxic T lymphocyte effector functions. *European Journal of Immunology* **37** (2007) 905–913. doi:10.1002/eji.200636718.

89. Artyomov MN, Lis M, Devadas S, Davis MM, Chakraborty AK. CD4 and CD8 binding to MHC molecules primarily acts to enhance Lck delivery. *Proceedings of the National Academy of Sciences* **107** (2010) 16916–16921. doi:10.1073/pnas.1010568107.

90. Horkova V, Drobek A, Paprckova D, Niederlova V, Prasai A, Uleri V, et al. Unique roles of co-receptor-bound LCK in helper and cytotoxic T cells. *Nature Immunology* **24** (2023) 174–185. doi:10.1038/s41590-022-01366-0.

91. Huse M, Klein LO, Girvin AT, Faraj JM, Li QJ, Kuhns MS, et al. Spatial and temporal dynamics of T cell receptor signaling with a photoactivatable agonist. *Immunity* **27** (2007) 76–88. doi:10.1016/j.immuni.2007.05.017.

92. Balagopalan L, Kortum RL, Coussens NP, Barr VA, Samelson LE. The linker for activation of T cells (LAT) signaling hub: from signaling complexes to microclusters. *The Journal of biological chemistry* **290** (2015) 26422–26429. doi:10.1074/JBC.R115.665869.

93. Hellmeier J, Platzer R, Eklund AS, Schlichthaerle T, Karner A, Motsch V, et al. DNA origami demonstrate the unique stimulatory power of single pMHCs as T cell antigens. *Proceedings of the National Academy of Sciences* **118** (2021) e2016857118. doi:10.1073/PNAS.2016857118/SUPPL_FILE/PNAS.2016857118.SD03.XLSX.

94. Rachmilewitz J. Serial triggering model. *Advances in experimental medicine and biology* **640** (2008) 95–102. doi:10.1007/978-0-387-09789-3_9.

95. Valitutti S, Muller S, Cella M, Padovan E, Lanzavecchia A. Serial triggering of many T-cell receptors by a few peptide MHC complexes. *Nature* **375** (1995).

96. Altan-Bonnet G, Germain RN. Modeling T cell antigen discrimination based on feedback control of digital ERK responses. *PLoS Biology* **3** (2005) 1925–1938. doi:10.1371/journal.pbio.0030356.

97. Zikherman J, Au-Yeung B. The role of T cell receptor signaling thresholds in guiding T cell fate decisions. *Current Opinion in Immunology* **33** (2015) 43–48. doi:10.1016/j.coi.2015.01.012.

98. Kellogg RA, Tian C, Lipniacki T, Quake SR, Tay SS. Digital signaling decouples activation probability and population heterogeneity. *eLife* **4** (2015) e08931. doi:10.7554/ELIFE.08931.

99. Miller JFAP. IMMUNOLOGICAL FUNCTION OF THE THYMUS. *The Lancet* **278** (1961) 748–749. doi:10.1016/S0140-6736(61)90693-6.

100. von Boehmer H, Teh HS, Kisielow P. The thymus selects the useful, neglects the useless and destroys the harmful. *Immunology today* **10** (1989) 57–61. doi:10.1016/0167-5699(89)90307-1.

101. Takada K, Takahama Y. Positive-Selection-Inducing Self-Peptides Displayed by Cortical Thymic Epithelial Cells. *Advances in Immunology* **125** (2015) 87–110. doi:10.1016/BS.AI.2014.09.003.

102. Murata S, Sasaki K, Kishimoto T, Niwa SI, Hayashi H, Takahama Y, et al. Regulation of CD8+ T cell development by thymus-specific proteasomes. *Science* **316** (2007) 1349–1353. doi:10.1126/SCIENCE.1141915.

103. Sasaki K, Takada K, Ohte Y, Kondo H, Sorimachi H, Tanaka K, et al. Thymoproteasomes produce unique peptide motifs for positive selection of CD8+ T cells. *Nature Communications* **6** (2015) 1–10. doi:10.1038/ncomms8484.

104. Nitta T, Murata S, Sasaki K, Fujii H, Ripen AM, Ishimaru N, et al. Thymoproteasome Shapes Immunocompetent Repertoire of CD8+ T Cells. *Immunity* **32** (2010) 29–40. doi:10.1016/J.IMMUNI.2009.10.009.

105. Santori FR, Kieper WC, Brown SM, Lu Y, Neubert TA, Johnson KL, et al. Rare, Structurally Homologous Self-Peptides Promote Thymocyte Positive Selection . *Immunity* **17** (2002) 131–142.

106. Hogquist KA, Tomlinson AJ, Kieper WC, McGargill MA, Hart MC, Naylor S, et al. Identification of a Naturally Occurring Ligand for Thymic Positive Selection. *Immunity* **6** (1997) 389–399. doi:10.1016/S1074-7613(00)80282-4.

107. Singer A, Adoro S, Park JH. Lineage fate and intense debate: myths, models and mechanisms of CD4- versus CD8-lineage choice. *Nature Reviews Immunology* **8** (2008) 788–801. doi:10.1038/nri2416.

108. Brugnera E, Bhandoola A, Cibotti R, Yu Q, Guinter TI, Yamashita Y, et al. Coreceptor Reversal in the Thymus. *Immunity* **13** (2000) 59–71. doi:10.1016/S1074-7613(00)00008-X.

109. Cibotti R, Bhandoola A, Guinter TI, Sharrow SO, Singer A. CD8 Coreceptor Extinction in Signaled CD4 + CD8 + Thymocytes: Coordinate Roles for Both Transcriptional and Posttranscriptional Regulatory Mechanisms in Developing Thymocytes. *Molecular and Cellular Biology* **20** (2000) 3852–3859. doi:10.1128/MCB.20.11.3852-3859.2000.

110. Shinzawa M, Moseman EA, Gossa S, Mano Y, Bhattacharya A, Guinter T, et al. Reversal of the T cell immune system reveals the molecular basis for T cell lineage fate determination in the thymus. *Nature Immunology* **23** (2022) 731–742. doi:10.1038/s41590-022-01187-1.

111. Yates AJ. Theories and quantification of thymic selection. *Frontiers in Immunology* **5** (2014) 68254. doi:10.3389/FIMMU.2014.00013/BIBTEX.

112. Alam SM, Travers PJ, Wung JL, Nasholds W, Redpath S, Jameson SC, et al. T cell-receptor affinity and thymocyte positive selection. *Nature* **381** (1996) 616–620. doi:10.1038/381616a0.

113. Juang J, Ebert PJR, Feng D, Garcia KC, Krogsgaard M, Davis MM. Peptide-MHC heterodimers show that thymic positive selection requires a more restricted set of self-peptides than negative selection. *Journal of Experimental Medicine* **207** (2010) 1223–1234. doi:10.1084/jem.20092170.

114. Daniels MA, Teixeiro E, Gill J, Hausmann B, Roubaty D, Holmberg K, et al. Thymic selection threshold defined by compartmentalization of Ras/MAPK signalling. *Nature* **444** (2006) 724–729. doi:10.1038/nature05269.

115. Kurd N, Robey EA. T cell selection in the thymus: a spatial and temporal perspective. *Immunological reviews* **271** (2016) 114. doi:10.1111/IMR.12398.

116. Goldrath AW, Bevan MJ. Low-Affinity Ligands for the TCR Drive Proliferation of Mature CD8+ T Cells in Lymphopenic Hosts. *Immunity* **11** (1999) 183–190. doi:10.1016/S1074-7613(00)80093-X.

117. Lo WL, Felix NJ, Walters JJ, Rohrs H, Gross ML, Allen PM. An endogenous peptide positively selects and augments the activation and survival of peripheral CD4 + T cells. *Nature Immunology* **10** (2009) 1155–1162. doi:10.1038/ni.1796.

118. Ebert PJR, Jiang S, Xie J, Li QJ, Davis MM. An endogenous positively selecting peptide enhances mature T cell responses and becomes an autoantigen in the absence of microRNA miR-181a. *Nature Immunology* **10** (2009) 1162–1169. doi:10.1038/ni.1797.

119. Stefanová I, Dorfman JR, Germain RN. Self-recognition promotes the foreign antigen sensitivity of naive T lymphocytes. *Nature* **420** (2002) 429–434. doi:10.1038/nature01146.

120. Dembic Z. Introduction—Common Features About Cytokines. *The Cytokines of the Immune System* (2015) 1–16. doi:10.1016/B978-0-12-419998-9.00001-8.

121. Harding CV, Unanue ER. Quantitation of antigen-presenting cell MHC class II/peptide complexes necessary for T-cell stimulation. *Nature* **346** (1990) 574–576. doi:10.1038/346574A0.

122. Irvine DJ, Purbhoo MA, Krogsgaard M, Davis MM. Direct observation of ligand recognition by T cells. *Nature* **419** (2002) 845–849. doi:10.1038/nature01076.

123. Huang J, Brameshuber M, Zeng X, Xie J, Li Qj, Chien Yh, et al. A single peptide-major histocompatibility complex ligand triggers digital cytokine secretion in CD4+ T cells. *Immunity* **39** (2013) 846–857. doi:10.1038/jid.2014.371.

124. Siller-Farfán JA, Dushek O. Molecular mechanisms of T cell sensitivity to antigen. *Immunological Reviews* **285** (2018) 194–205. doi:10.1111/imr.12690.

125. Fujinami RS, Oldstone MB. Amino acid homology between the encephalitogenic site of myelin basic protein and virus: mechanism for autoimmunity. *Science* **230** (1985) 1043–1045. doi:10.1126/SCIENCE.2414848.

126. Cusick MF, Libbey JE, Fujinami RS. Molecular mimicry as a mechanism of autoimmune disease. *Clinical Reviews in Allergy and Immunology* **42** (2012) 102–111. doi:10.1007/S12016-011-8294-7/TABLES/2.

127. Hogquist KA, Jameson SC, Bevan MJ. Strong agonist ligands for the T cell receptor do not mediate positive selection of functional CD8+ T cells. *Immunity* **3** (1995) 79–86. doi:10.1016/1074-7613(95)90160-4.

128. Alam SM, Davies GM, Lin CM, Zal T, Nasholds W, Jameson SC, et al. Qualitative and Quantitative Differences in T Cell Receptor Binding of Agonist and Antagonist Ligands. *Immunity* **10** (1999) 227–237. doi:10.1016/S1074-7613(00)80023-0.

129. Kersh GJ, Allen PM. Structural basis for T cell recognition of altered peptide ligands: a single T cell receptor can productively recognize a large continuum of related ligands. *The Journal of experimental medicine* **184** (1996) 1259–1268. doi:10.1084/jem.184.4.1259.

130. Kersh GJ, Kersh EN, Fremont DH, Allen PM. High-and low-potency ligands with similar affinities for the TCR: the importance of kinetics in TCR signaling. *Immunity* **9** (1998) 817–826. doi:10.1016/S1074-7613(00)80647-0.

131. Lyons DS, Lieberman SA, Hampl J, Boniface JJ, Chien Yh, Berg LJ, et al. A TCR binds to antagonist ligands with lower affinities and faster dissociation rates than to agonists. *Immunity* **5** (1996) 53–61. doi:10.1016/S1074-7613(00)80309-X.

132. Mason D. A very high level of crossreactivity is an essential feature of the T-cell receptor. *Immunology today* **19** (1998) 395–404. doi:10.1016/S0167-5699(98)01299-7.

133. Sender R, Weiss Y, Navon Y, Milo I, Azulay N, Keren L, et al. The total mass, number, and distribution of immune cells in the human body. *Proceedings of the National Academy of Sciences of the United States of America* **120** (2023). doi:10.1073/PNAS.2308511120.

134. Wooldridge L, Ekeruche-Makinde J, Berg HAVD, Skowera A, Miles JJ, Tan MP, et al. A single autoimmune T cell receptor recognizes more than a million different peptides. *Journal of Biological Chemistry* **287** (2012) 1168–1177. doi:10.1074/jbc.M111.289488.

135. Ishizuka J, Grebe K, Shenderov E, Peters B, Chen Q, Peng Y, et al. Quantitating T Cell Cross-Reactivity for Unrelated Peptide Antigens. *Journal of immunology (Baltimore, Md. : 1950)* **183** (2009) 4337. doi:10.4049/JIMMUNOL.0901607.

136. Birnbaum ME, Mendoza JL, Sethi DK, Dong S, Glanville J, Dobbins J, et al. Deconstructing the peptide-MHC specificity of T cell recognition. *Cell* **157** (2014) 1073–1087. doi:10.1016/j.cell.2014.03.047.

137. Housset D, Malissen B. What do TCR-pMHC crystal structures teach us about MHC restriction and alloreactivity? *TRENDS in Immunology* **24** (2003) 429. doi:10.1016/S1471-4906(03)00180-7.

138. Stoll S, Delon J, Brotz TM, Germain RN. Dynamic imaging of T cell-dendritic cell interactions in lymph nodes. *Science* **296** (2002) 1873–1876.

139. Feinerman O, Germain RN, Altan-Bonnet G. Quantitative challenges in understanding ligand discrimination by $\alpha\beta$ T cells. *Molecular immunology* **45** (2008) 619. doi:10.1016/j.molimm.2007.03.028.

140. Gascoigne NRJ, Zal T, Alam SM. T-cell receptor binding kinetics in T-cell development and activation. *Expert Reviews in Molecular Medicine* **3** (2001) 1–17. doi:10.1017/S1462399401002502.

141. Coombs D, Dushek O, van der Merwe PA. A Review of Mathematical Models for T Cell Receptor Triggering and Antigen Discrimination. *Mathematical Models and Immune Cell Biology* (2011) 25–45. doi:10.1007/978-1-4419-7725-0_2.

142. Chakraborty AK, Weiss A. Insights into the initiation of TCR signaling. *Nature immunology* **15** (2014) 798. doi:10.1038/ni.2940.

143. Clark AJ. The reaction between acetyl choline and muscle cells. *The Journal of Physiology* **61** (1926) 530. doi:10.1113/JPHYSIOL.1926.SP002314.

144. Colquhoun D. Binding, gating, affinity and efficacy: The interpretation of structure-activity relationships for agonists and of the effects of mutating receptors. *British Journal of Pharmacology* **125** (1998) 923. doi:10.1038/SJ.BJP.0702164.

145. Lowe ES, Lertora JJL. Dose–Effect and Concentration–Effect Analysis. *Principles of Clinical Pharmacology* (Academic Press). 3 edn. (2012), 343–356. doi:10.1016/B978-0-12-385471-1.00020-9.

146. Hopfield JJ. Kinetic proofreading: a new mechanism for reducing errors in biosynthetic processes requiring high specificity. *Proc Natl Acad Sci USA* **71** (1974) 4135–4139. doi:10.1073/pnas.71.10.4135.

147. McKeithan TW. Kinetic proofreading in T-cell receptor signal transduction. *Proceedings of the national academy of sciences* **92** (1995) 5042–5046. doi:10.1073/pnas.92.11.5042.

148. Tischer DK, Weiner OD. Light-based tuning of ligand half-life supports kinetic proofreading model of T cell signaling. *eLife* **8** (2019) 1–25. doi:10.7554/eLife.42498.

149. Aleksic M, Dushek O, Zhang H, Shenderov E, Chen JLL, Cerundolo V, et al. Dependence of T Cell Antigen Recognition on T Cell Receptor-Peptide MHC Confinement Time. *Immunity* **32** (2010) 163–174. doi:10.1016/j.immuni.2009.11.013.

150. François P, Voisinne G, Siggia ED, Altan-Bonnet G, Vergassola M, Francois P, et al. Phenotypic model for early T-cell activation displaying sensitivity, specificity, and antagonism. *Proceedings of the National Academy of Sciences* **110** (2013) E888—-E897. doi:10.1073/pnas.1300752110.

151. Dushek O, Van der Merwe PA. An induced rebinding model of antigen discrimination. *Trends in Immunology* **35** (2014) 153–158. doi:10.1016/j.it.2014.02.002.

152. Gudipati V, Rydzek J, Perez ID, Scharf L, Königsberger S, Einsele H, et al. Inefficient ZAP70-Signaling Blunts Antigen Detection by CAR-T-Cells. *bioRxiv* (2019) 720417. doi:10.1101/720417.

153. Huang J, Zarnitsyna VI, Liu B, Edwards LJ, Jiang N, Evavold BD, et al. The kinetics of two-dimensional TCR and pMHC interactions determine T-cell responsiveness. *Nature* **464** (2010) 932–936. doi:10.1038/nature08944.

154. Liu B, Chen W, Evavold BD, Zhu C. Accumulation of dynamic catch bonds between TCR and agonist peptide-MHC triggers T cell signaling. *Cell* **157** (2014) 357–368. doi:10.1016/j.cell.2014.02.053.

155. Sibener LV, Fernandes RA, Kolawole EM, Carbone CB, Liu F, McAffee D, et al. Isolation of a structural mechanism for uncoupling T cell receptor signaling from peptide-MHC binding. *Cell* **174** (2018) 672–687. doi:10.1016/j.cell.2018.06.017.

156. Robert P, Aleksic M, Dushek O, Cerundolo V, Bongrand P, Anton van der Merwe P, et al. Kinetics and Mechanics of Two-Dimensional Interactions between T Cell Receptors and Different Activating Ligands. *Biophysical Journal* **102** (2012) 248–257. doi:10.1016/j.bpj.2011.11.4018.

157. Pettmann J, Awada L, Różycki B, Huhn A, Faour S, Kutuzov M, et al. Mechanical forces impair antigen discrimination by reducing differences in T-cell receptor/peptide–MHC off-rates. *The EMBO Journal* **42** (2023). doi:10.15252/embj.2022111841.

158. Janeway CA, Travers P, Walport M, Shlomchik MJ. The interaction of the antibody molecule with specific antigen. *The Immune System in Health and Disease.* (Garland Science). 5 edn. (2001).

159. Murin CD, Wilson IA, Ward AB. Antibody responses to viral infections: a structural perspective across three different enveloped viruses. *Nature Microbiology* **4** (2019) 734–747. doi:10.1038/s41564-019-0392-y.

160. Kappler K, Hennet T. Emergence and significance of carbohydrate-specific antibodies. *Genes & Immunity* **21** (2020) 224–239. doi:10.1038/s41435-020-0105-9.

161. Soliman C, Pier GB, Ramsland PA. Antibody recognition of bacterial surfaces and extracellular polysaccharides. *Current Opinion in Structural Biology* **62** (2020) 48–55. doi:10.1016/J.SBI.2019.12.001.

162. Belete TM. Novel targets to develop new antibacterial agents and novel alternatives to antibacterial agents. *Human Microbiome Journal* **11** (2019) 100052. doi:10.1016/J.HUMIC.2019.01.001.

163. Grönwall C, Vas J, Silverman GJ. Protective Roles of Natural IgM Antibodies. *Frontiers in Immunology* **3** (2012). doi:10.3389/fimmu.2012.00066.

164. Chou MY, Fogelstrand L, Hartvigsen K, Hansen LF, Woelkers D, Shaw PX, et al. Oxidation-specific epitopes are dominant targets of innate natural antibodies in mice and humans. *Journal of Clinical Investigation* **119** (2009) 1335–1349. doi:10.1172/JCI36800.

165. Bajénoff M, Germain RN. Seeing is believing: A focus on the contribution of microscopic imaging to our understanding of immune system function. *European Journal of Immunology* **37** (2007) S18–S33. doi:10.1002/EJI.200737663.

166. Sarma VR, Silverton EW, Davies DR, Terry WD. The Three-Dimensional Structure at 6 A Resolution of a Human γG1 Immunoglobulin Molecule. *Journal of Biological Chemistry* **246** (1971) 3753–3759. doi:10.1016/S0021-9258(18)62192-1.

167. Poljak RJ, Amzel LM, Avey HP, Becka LN, Nisonoff A. Structure of Fab New at 6 Å Resolution. *Nature New Biology* **235** (1972) 137–140. doi:10.1038/newbio235137a0.

168. Phillips ML, Oi VT, Schumaker VN. Electron microscopic study of ring-shaped, bivalent hapten, bivalent antidansyl monoclonal antibody complexes with identical variable domains but IgG1, IgG2a and IgG2b constant domains. *Molecular Immunology* **27** (1990) 181–190. doi:10.1016/0161-5890(90)90113-E.

169. Bennett WS, Huber R, Engel J. Structural and functional aspects of domain motions in protein. *Critical Reviews in Biochemistry and Molecular Biology* **15** (1984) 291–384. doi:10.3109/10409238409117796.

170. Lesk AM, Chothia C. Elbow motion in the immunoglobulins involves a molecular ball-and-socket joint. *Nature 1988 335:6186* **335** (1988) 188–190. doi:10.1038/335188a0.

171. Shaw A, Hoffecker IT, Smyrlaki I, Rosa J, Grevys A, Bratlie D, et al. Binding to nanopatterned antigens is dominated by the spatial tolerance of antibodies. *Nature Nanotechnology* **14** (2019) 184–190. doi:10.1038/s41565-018-0336-3.

172. Jay J, Bray B, Qi Y, Igbinigie E, Wu H, Li J, et al. IgG Antibody 3D Structures and Dynamics. *Antibodies* **7** (2018) 18. doi:10.3390/antib7020018.

173. Deng Y, Efremov AK, Yan J. Modulating binding affinity, specificity, and configurations by multivalent interactions. *Biophysical Journal* **121** (2022) 1868–1880. doi:10.1016/J.BPJ.2022.04.017.

174. Xie W, Wucherpfennig K, Patel DJ. A structural platform for B cell receptor signaling. *Cell Research* **33** (2022) 95–96. doi:10.1038/s41422-022-00724-9.

175. Su Q, Chen M, Shi Y, Zhang X, Huang G, Huang B, et al. Cryo-EM structure of the human IgM B cell receptor. *Science* **377** (2022) 875–880. doi:10.1126/SCIENCE.ABO3923/SUPPL_FILE/SCIENCE.ABO3923_SM.PDF.

176. Forthal DN. Functions of Antibodies. *Antibodies for Infectious Diseases* (Washington, DC, USA: ASM Press), vol. 2 (2015), 23–48. doi:10.1128/9781555817411.ch2.

177. Mancardi D, Daëron M. Fc Receptors in Immune Responses. *Reference Module in Biomedical Sciences* (Elsevier) (2014). doi:10.1016/B978-0-12-801238-3.00119-7.

178. Vivier E, Tomasello E, Baratin M, Walzer T, Ugolini S. Functions of natural killer cells. *Nature Immunology 2008 9:5* **9** (2008) 503–510. doi:10.1038/ni1582.

179. Junker F, Gordon J, Qureshi O. Fc Gamma Receptors and Their Role in Antigen Uptake, Presentation, and T Cell Activation. *Frontiers in Immunology* **11** (2020) 547589. doi:10.3389/FIMMU.2020.01393/BIBTEX.

180. Cyster JG. B cell follicles and antigen encounters of the third kind. *Nature Immunology* **11** (2010) 989–996. doi:10.1038/ni.1946.

181. Zou YR, Grimaldi C, Diamond B. B Cells. *Kelley and Firestein's Textbook of Rheumatology: Volumes 1-2, Tenth Edition* **1** (2017) 207–230.e3. doi:10.1016/B978-0-323-31696-5.00013-9.

182. Ferapontov A, Omer M, Baudrexel I, Nielsen JS, Dupont DM, Juul-Madsen K, et al. Antigen footprint governs activation of the B cell receptor. *Nature Communications* **14** (2023) 976. doi:10.1038/s41467-023-36672-0.

183. Minguet S, Dopfer EP, Schamel WW. Low-valency, but not monovalent, antigens trigger the B-cell antigen receptor (BCR). *International Immunology* **22** (2010) 205–212. doi:10.1093/INTIMM/DXP129.

184. Pierce SK, Liu W. The tipping points in the initiation of B cell signalling: how small changes make big differences. *Nature Reviews Immunology* **10** (2010) 767–777. doi:10.1038/nri2853.

185. Lee J, Sengupta P, Brzostowski J, Lippincott-Schwartz J, Pierce SK. The nanoscale spatial organization of B-cell receptors on immunoglobulin M– and G–expressing human B-cells. *Molecular Biology of the Cell* **28** (2017) 511–523. doi:10.1091/mbc.e16-06-0452.

186. Depoil D, Fleire S, Treanor BL, Weber M, Harwood NE, Marchbank KL, et al. CD19 is essential for B cell activation by promoting B cell receptor–antigen microcluster formation in response to membrane-bound ligand. *Nature Immunology* **9** (2008) 63–72. doi:10.1038/ni1547.

187. Tolar P, Hanna J, Krueger PD, Pierce SK. The Constant Region of the Membrane Immunoglobulin Mediates B Cell-Receptor Clustering and Signaling in Response to Membrane Antigens. *Immunity* **30** (2009) 44–55. doi:10.1016/j.immuni.2008.11.007.

188. Fleire SJ, Goldman JP, Carrasco YR, Weber M, Bray D, Batista FD. B Cell Ligand Discrimination Through a Spreading and Contraction Response. *Science* **312** (2006) 738–741. doi:10.1126/science.1123940.

189. Natkanski E, Lee WYY, Mistry B, Casal A, Molloy JE, Tolar P. B cells use mechanical energy to discriminate antigen affinities. *Science* **340** (2013) 1587–1590. doi:10.1126/SCIENCE.1237572/SUPPL_FILE/NATKANSKI.SM.PDF.

190. Katletz S, Stroh C, Rankl C, Titulaer UM, Hinterdorfer P. Force-induced lysozyme-HyHEL5 antibody dissociation and its analysis by means of a cooperative binding model. *Biophysical Journal* **99** (2010) 323–332. doi:10.1016/j.bpj.2010.03.060.

191. Morfill J, Neumann J, Blank K, Steinbach U, Puchner EM, Gottschalk KE, et al. Force-based Analysis of Multidimensional Energy Landscapes: Application of Dynamic Force Spectroscopy and Steered Molecular Dynamics Simulations to an Antibody Fragment–Peptide Complex. *Journal of Molecular Biology* **381** (2008) 1253–1266. doi:10.1016/J.JMB.2008.06.065.

192. Liu W, Meckel T, Tolar P, Sohn HW, Pierce SK. Antigen affinity discrimination is an intrinsic function of the B cell receptor. *Journal of Experimental Medicine* **207** (2010) 1095–1111. doi:10.1084/jem.20092123.

193. Batista FD, Iber D, Neuberger MS. B cells acquire antigen from target cells after synapse formation. *Nature* **411** (2001) 489–494. doi:10.1038/35078099.

194. Spillane KM, Tolar P. Mechanics of antigen extraction in the B cell synapse. *Molecular Immunology* **101** (2018) 319–328. doi:10.1016/j.molimm.2018.07.018.

195. Yuseff MI, Reversat A, Lankar D, Diaz J, Fanget I, Pierobon P, et al. Polarized Secretion of Lysosomes at the B Cell Synapse Couples Antigen Extraction to Processing and Presentation. *Immunity* **35** (2011) 361–374. doi:10.1016/j.immuni.2011.07.008.

196. Eisen HN. Affinity Enhancement of Antibodies: How Low-Affinity Antibodies Produced Early in Immune Responses Are Followed by High-Affinity Antibodies Later and in Memory B-Cell Responses. *Cancer Immunology Research* **2** (2014) 381–392. doi:10.1158/2326-6066.CIR-14-0029.

197. Schmidt AG, Xu H, Khan AR, O'Donnell T, Khurana S, King LR, et al. Preconfiguration of the antigen-binding site during affinity maturation of a broadly neutralizing influenza virus antibody. *Proceedings of the National Academy of Sciences of the United States of America* **110** (2013) 264–269. doi:10.1073/PNAS.1218256109/-/DCSUPPLEMENTAL/PNAS.201218256SI.PDF.

198. Velick SF, Parker CW, Eisen HN. EXCITATION ENERGY TRANSFER AND THE QUANTITATIVE STUDY OF THE ANTIBODY HAPTEN REACTION. *Proceedings of the National Academy of Sciences of the United States of America* **46** (1960) 1470–1482. doi:10.1073/PNAS.46.11.1470.

199. James LK. B cells defined by immunoglobulin isotypes. *Clinical and Experimental Immunology* **210** (2022) 230–239. doi:10.1093/CEI/UXAC091.

200. [Dataset] Wikipedia. Antibody Isotypes (2022).

201. Schreiber G, Haran G, Zhou HXX. Fundamental aspects of protein-protein association kinetics. *Chemical reviews* **109** (2009) 839–860. doi:10.1021/cr800373w.

202. Schild HO. pA, a new scale for the measurement of drug antagonism. *British Journal of Pharmacology and Chemotherapy* **2** (1947) 189. doi:10.1111/J.1476-5381.1947.TB00336.X.

203. Adam G, Delbruck M. Reduction of dimensionality in biological diffusion processes. *Structural Chemistry and Molecular Biology* **198** (1968) 198–215.

204. Axelrod D, Wang MD. Reduction-of-Dimensionality Kinetics at Reaction-Limited Cell Surface Receptors. *Biophysical Journal* **66** (1994) 588–600. doi:10.1016/S0006-3495(94)80834-3.

205. Adrien V, Taulier N, Verchère A, Monlezun L, Picard M, Ducruix A, et al. Kinetic study of membrane protein interactions: from three to two dimensions. *Scientific Reports 2024 14:1* **14** (2024) 1–10. doi:10.1038/s41598-023-50827-5.

206. Huppa JB, Axmann M, Mörtelmaier MA, Lillemeier BF, Newell EW, Brameshuber M, et al. TCR-peptide-MHC interactions in situ show accelerated kinetics and increased affinity. *Nature* **463** (2010) 963. doi:10.1038/NATURE08746.

207. Xie ZR, Chen J, Wu Y. Linking 3D and 2D binding kinetics of membrane proteins by multiscale simulations. *Protein Science : A Publication of the Protein Society* **23** (2014) 1789. doi:10.1002/PRO.2574.

208. Dustin ML, Ferguson LM, Chan PY, Springer TA, Golan DE. Visualization of CD2 interaction with LFA-3 and determination of the two-dimensional dissociation constant for adhesion receptors in a contact area. *The Journal of cell biology* **132** (1996) 465–474. doi:10.1083/JCB.132.3.465.

209. Gavutis M, Jaks E, Lamken P, Piehler J. Determination of the two-dimensional interaction rate constants of a cytokine receptor complex. *Biophysical Journal* **90** (2006) 3345–3355. doi:10.1529/biophysj.105.072546.

210. Liedberg BO, Nylander C, Lundstrom I. SURFACE PLASMON RESONANCE FOR GAS DETECTION AND BIOSENSING*. *Sensors and Actuators* **4** (1983) 299–304.

211. Flanagan MT, Pantell RH. Surface plasmon resonance and immunosensors. *Electronics Letters* **20** (1984) 968–970. doi:10.1049/EL:19840660.

212. Cullen DC, Brown RG, Lowe CR. Detection of immuno-complex formation via surface plasmon resonance on gold-coated diffraction gratings. *Biosensors* **3** (1987) 211–225. doi:10.1016/0265-928X(87)85002-2.

213. Corr M, Slanetz AE, Boyd LF, Jelonek MT, Khilko S, Al-Ramadi BK, et al. T cell receptor-MHC class I peptide interactions: affinity, kinetics, and specificity. *Science* **265** (1994) 946–949. doi:10.1126/SCIENCE.8052850.

214. Yanase Y, Hiragun T, Ishii K, Kawaguchi T, Yanase T, Kawai M, et al. Surface Plasmon Resonance for Cell-Based Clinical Diagnosis. *Sensors 2014, Vol. 14, Pages 4948-4959* **14** (2014) 4948–4959. doi:10.3390/S140304948.

215. Nguyen K, Li K, Flores K, Tomaras GD, Dennison SM, McCarthy JM. Parameter estimation and identifiability analysis for a bivalent analyte model of monoclonal antibody-antigen binding. *Analytical biochemistry* **679** (2023). doi:10.1016/J.AB.2023.115263.

216. Daghestani HN, Day BW. Theory and Applications of Surface Plasmon Resonance, Resonant Mirror, Resonant Waveguide Grating, and Dual Polarization Interferometry Biosensors. *Sensors 2010, Vol. 10, Pages 9630-9646* **10** (2010) 9630–9646. doi:10.3390/S101109630.

217. Qi Q, Liu Y, Cheng Y, Glanville J, Zhang D, Lee JY, et al. Diversity and clonal selection in the human T-cell repertoire. *Proceedings of the National Academy of Sciences of the United States of America* **111** (2014) 13139–13144. doi:10.1073/PNAS.1409155111.

218. Chiffelle J, Genolet R, Perez MA, Coukos G, Zoete V, Harari A. T-cell repertoire analysis and metrics of diversity and clonality. *Current Opinion in Biotechnology* **65** (2020) 284–295. doi:10.1016/j.copbio.2020.07.010.

219. Robins HS, Srivastava SK, Campregher PV, Turtle CJ, Andriesen J, Riddell SR, et al. Overlap and effective size of the human CD8+ T cell receptor repertoire. *Science Translational Medicine* **2** (2010). doi:10.1126/SCITRANSLMED.3001442.

220. Lever M, Maini PK, van der Merwe PA, Dushek O. Phenotypic models of T cell activation. *Nature Reviews Immunology* **14** (2014) 619–629. doi:10.1038/nri3728.

221. Rabinowitz JD, Beeson C, Lyons DS, Davis MM, McConnell HM. Kinetic discrimination in T-cell activation. *Proceedings of the National Academy of Sciences* **93** (1996) 1401–1405.

222. Chan C, George AJT, Stark J. Cooperative enhancement of specificity in a lattice of T cell receptors. *Proceedings of the National Academy of Sciences* **98** (2001) 5758–5763. doi:10.1073/pnas.101113698.

223. Chan C, Stark J, George AJT. Feedback control of T-cell receptor activation. *Proceedings of the Royal Society of London. Series B: Biological Sciences* **271** (2004) 931–939. doi:10.1098/rspb.2003.2587.

224. Lalanne JB, François P. Principles of adaptive sorting revealed by in silico evolution. *Physical review letters* **110** (2013) 218102.

225. Ganti RS, Lo WL, McAffee DB, Groves JT, Weiss A, Chakraborty AK. How the T cell signaling network processes information to discriminate between self and agonist ligands. *Proceedings of the National Academy of Sciences* **117** (2020) 26020–26030.

226. Burroughs NJ, Lazic Z, Van Der Merwe PA. Ligand detection and discrimination by spatial relocalization: A kinase-phosphatase segregation model of TCR activation. *Biophysical journal* **91** (2006) 1619–1629. doi:10.1529/BIOPHYSJ.105.080044.

227. Fernandes RA, Ganzinger KA, Tzou JC, Jönsson P, Lee SF, Palayret M, et al. A cell topography-based mechanism for ligand discrimination by the T cell receptor. *Proceedings of the National Academy of Sciences* **116** (2019) 14002–14010. doi:10.1073/pnas.1817255116.

228. Natarajan K, McShan AC, Jiang J, Kumirov VK, Wang R, Zhao H, et al. An allosteric site in the T-cell receptor Cβ domain plays a critical signalling role. *Nature communications* **8** (2017) 1–14.

229. Schamel WWA, Risueño RM, Minguet S, Ort\'\iz AR, Alarcón B, Ortíz AR, et al. A conformation- and avidity-based proofreading mechanism for the TCR-CD3 complex. *Trends in immunology* **27** (2006) 176–182. doi:10.1016/j.it.2006.02.005.

230. Wu P, Zhang T, Liu B, Fei P, Cui L, Qin R, et al. Mechano-regulation of peptide-MHC class I conformations determines TCR antigen recognition. *Molecular cell* **73** (2019) 1015–1027. doi:10.1016/j.molcel.2018.12.018.

231. Klotzsch E, Schütz GJ. Improved ligand discrimination by force-induced unbinding of the T cell receptor from peptide-MHC. *Biophysical Journal* **104** (2013) 1670–1675. doi:10.1016/j.bpj.2013.03.023.

232. Cameron BJ, Gerry AB, Dukes J, Harper JV, Kannan V, Bianchi FC, et al. Identification of a Titin-derived HLA-A1–presented peptide as a cross-reactive target for engineered MAGE A3–directed T cells. *Science translational medicine* **5** (2013) 197ra103—-197ra103.

233. Wang J, Jelcic I, Mühlenbruch L, Haunerdinger V, Toussaint NC, Zhao Y, et al. HLA-DR15 molecules jointly shape an autoreactive T cell repertoire in multiple sclerosis. *Cell* **183** (2020) 1264–1281. doi:10.1016/J.CELL.2020.09.054.

234. Kohanim YK, Tendler A, Mayo A, Friedman N, Alon U, Korem Kohanim Y, et al. Endocrine autoimmune disease as a fragility of immune surveillance against hypersecreting mutants. *Immunity* **52** (2020) 872–884. doi:10.1016/j.immuni.2020.04.022.

235. Min B, Yamane H, Hu-Li J, Paul WE. Spontaneous and homeostatic proliferation of CD4 T cells are regulated by different mechanisms. *The Journal of Immunology* **174** (2005) 6039–6044.

236. Min B. Spontaneous T cell proliferation: a physiologic process to create and maintain homeostatic balance and diversity of the immune system. *Frontiers in immunology* **9** (2018) 547.

237. Sewell AK. Why must T cells be cross-reactive? *Nature Reviews Immunology* **12** (2012) 669–677. doi:10.1038/nri3279.

238. Rosette C, Werlen G, Daniels MA, Holman PO, Alam SM, Travers PJ, et al. The impact of duration versus extent of TCR occupancy on T cell activation: a revision of the kinetic proofreading model. *Immunity* **15** (2001) 59–70. doi:10.1016/s1074-7613(01)00173-x.

239. Lever M, Lim HS, Kruger P, Nguyen J, Trendel N, Abu-Shah E, et al. Architecture of a minimal signaling pathway explains the T-cell response to a 1 million-fold variation in antigen affinity and dose. *Proceedings of the National Academy of Sciences* **113** (2016) E6630—-E6638.

240. Stepanek O, Prabhakar AS, Osswald C, King CG, Bulek A, Naeher D, et al. Coreceptor scanning by the T cell receptor provides a mechanism for T cell tolerance. *Cell* **159** (2014) 333–345. doi:10.1016/j.cell.2014.08.042.

241. Hong J, Persaud SP, Horvath S, Allen PM, Evavold BD, Zhu C. Force-Regulated In Situ TCR–Peptide-Bound MHC Class II Kinetics Determine Functions of CD4 + T Cells. *The Journal of Immunology* **195** (2015) 3557–3564. doi:10.4049/jimmunol.1501407.

242. Wu LC, Tuot DS, Lyons DS, Garcia KC, Davis MM. Two-step binding mechanism for T-cell receptor recognition of peptide-MHC. *Nature* **418** (2002) 552–556.

243. Lo WLL, Shah NH, Rubin SA, Zhang W, Horkova V, Fallahee IR, et al. Slow phosphorylation of a tyrosine residue in LAT optimizes T cell ligand discrimination. *Nature immunology* **20** (2019) 1481–1493. doi:10.1038/s41590-019-0502-2.

244. Laugel B, van den Berg HA, Gostick E, Cole DK, Wooldridge L, Boulter J, et al. Different T cell receptor affinity thresholds and CD8 coreceptor dependence govern cytotoxic T lymphocyte activation and tetramer binding properties. *Journal of Biological Chemistry* **282** (2007) 23799–23810.

245. Burrows SR, Chen Z, Archbold JK, Tynan FE, Beddoe T, Kjer-Nielsen L, et al. Hard wiring of T cell receptor specificity for the major histocompatibility complex is underpinned by TCR adaptability. *Proceedings of the National Academy of Sciences* **107** (2010) 10608–10613.

246. Pettmann J, Huhn A, Shah EA, Kutuzov MA, Wilson DB, Dustin ML, et al. The discriminatory power of the T-cell receptor. *eLife* **10** (2021). doi:10.7554/ELIFE.67092.

247. Shen L, Matloubian M, Kadlecek TA, Weiss A. A disease-associated mutation that weakens ZAP70 autoinhibition enhances responses to weak and self-ligands. *Science Signaling* **14** (2021).

248. Lo WL, Kuhlmann M, Rizzuto G, Ekiz HA, Kolawole EM, Revelo MP, et al. A single-amino acid substitution in the adaptor LAT accelerates TCR proofreading kinetics and alters T-cell selection, maintenance and function. *Nature Immunology* **24** (2023) 676–689. doi:10.1038/s41590-023-01444-x.

249. Levin AM, Bates DL, Ring AM, Krieg C, Lin JT, Su L, et al. Exploiting a natural conformational switch to engineer an interleukin-2 'superkine'. *Nature* **484** (2012) 529–533.

250. Moraga I, Richter D, Wilmes S, Winkelmann H, Jude K, Thomas C, et al. Instructive roles for cytokine-receptor binding parameters in determining signaling and functional potency. *Science signaling* **8** (2015) ra114—-ra114.

251. Thomas C, Moraga I, Levin D, Krutzik PO, Podoplelova Y, Trejo A, et al. Structural linkage between ligand discrimination and receptor activation by type I interferons. *Cell* **146** (2011) 621–632.

252. Mendoza JL, Schneider WM, Hoffmann HHH, Vercauteren K, Jude KM, Xiong A, et al. The IFN-λ-IFN-λR1-IL-10Rβ Complex Reveals Structural Features Underlying Type III IFN Functional Plasticity. *Immunity* **46** (2017) 379–392. doi:10.1016/j.immuni.2017.02.017.

253. Martinez-Fabregas J, Wilmes S, Wang L, Hafer M, Pohler E, Lokau J, et al. Kinetics of cytokine receptor trafficking determine signaling and functional selectivity. *eLife* **8** (2019) e49314.

254. Ho CCM, Chhabra A, Starkl P, Schnorr PJ, Wilmes S, Moraga I, et al. Decoupling the functional pleiotropy of stem cell factor by tuning c-Kit signaling. *Cell* **168** (2017) 1041–1052.

255. Reddy CC, Niyogi SK, Wells A, Wiley HS, Lauffenburger D. Engineering epidermal growth factor for enhanced mitogenic potency. *Nature biotechnology* **14** (1996) 1696–1699.

256. Sykes DA, Dowling MR, Charlton SJ. Exploring the mechanism of agonist efficacy: a relationship between efficacy and agonist dissociation rate at the muscarinic M3 receptor. *Molecular pharmacology* **76** (2009) 543–551.

257. Guo D, Mulder-Krieger T, IJzerman AP, Heitman LH. Functional efficacy of adenosine A2A receptor agonists is positively correlated to their receptor residence time. *British journal of pharmacology* **166** (2012) 1846–1859.

258. Guyon A, Kussrow A, Olmsted IR, Sandoz G, Bornhop DJ, Nahon JL. Baclofen and other GABAB receptor agents are allosteric modulators of the CXCL12 chemokine receptor CXCR4. *Journal of Neuroscience* **33** (2013) 11643–11654.

259. Heise CE, Pahuja A, Hudson SC, Mistry MS, Putnam AL, Gross MM, et al. Pharmacological characterization of CXC chemokine receptor 3 ligands and a small molecule antagonist. *Journal of Pharmacology and Experimental Therapeutics* **313** (2005) 1263–1271.

260. Chmielewski M, Hombach A, Heuser C, Adams GP, Abken H. T cell activation by antibody-like immunoreceptors: increase in affinity of the single-chain fragment domain above threshold does not increase T cell activation against antigen-positive target cells but decreases selectivity. *The Journal of Immunology* **173** (2004) 7647–7653.

261. Liu X, Jiang S, Fang C, Yang S, Olalere D, Pequignot EC, et al. Affinity-tuned ErbB2 or EGFR chimeric antigen receptor T cells exhibit an increased therapeutic index against tumors in mice. *Cancer research* **75** (2015) 3596–3607.

262. Batista FD, Neuberger MS. Affinity dependence of the B cell response to antigen: a threshold, a ceiling, and the importance of off-rate. *Immunity* **8** (1998) 751–759.

263. Fulton RB, Hamilton SE, Xing Y, Best JA, Goldrath AW, Hogquist KA, et al. The TCR's sensitivity to self-peptide–MHC dictates the ability of naïve CD8+ T cells to respond to foreign antigens. *Nature immunology* **16** (2015) 107. doi:10.1038/NI.3043.

264. Adams JJ, Narayanan S, Liu B, Birnbaum ME, Kruse AC, Bowerman NA, et al. T cell receptor signaling is limited by docking geometry to peptide-major histocompatibility complex. *Immunity* **35** (2011) 681–693. doi:10.1016/j.immuni.2011.09.013.

265. Cole DK, Bulek AM, Dolton G, Schauenberg AJ, Szomolay B, Rittase W, et al. Hotspot autoimmune T cell receptor binding underlies pathogen and insulin peptide cross-reactivity. *The Journal of clinical investigation* **126** (2016) 2191–2204. doi:10.1172/JCI85679.

266. André V. *Identifying signalling molecules controlling T cell antigen sensitivity and discrimination*. Ph.D. thesis, University of Oxford, Oxford (2022).

267. Abu-Shah E, Trendel N, Kruger P, Nguyen J, Pettmann J, Kutuzov M, et al. Human CD8+ T cells exhibit a shared antigen threshold for different effector responses. *The Journal of Immunology* **205** (2020) 1503–1512.

268. Dushek O. Elementary Steps in T Cell Receptor Triggering. *Frontiers in Immunology* **2** (2012) 2011–2013. doi:10.3389/fimmu.2011.00091.

269. Barton MI, Paterson RL, Denham EM, Goyette J, van der Merwe PA. Ligand requirements for immunoreceptor triggering. *bioRxiv* (2023) 2023.09.11.557203. doi:10.1101/2023.09.11.557203.

270. Patel A, Andre V, Eguiguren SB, Barton MI, Burton J, Denham EM, et al. Using CombiCells, a platform enabling titration and combinatorial display of cell surface ligands, to study T cell antigen sensitivity by TCRs, CARs, and BiTEs. *bioRxiv* (2023) 2023.06.15.545075. doi:10.1101/2023.06.15.545075.

271. Hogquist KA, Jameson SC, Heath WR, Howard JL, Bevan MJ, Carbone FR. T cell receptor antagonist peptides induce positive selection. *Cell* **76** (1994) 17–27. doi:10.1016/0092-8674(94)90169-4.

272. Jameson SC, Carbone FR, Bevan MJ, Jameson BSC, Carbone FR, Bevan MJ. Clone-specific T Cell Receptor Antagonists of Major Histocompatibility Complex Class I-restricted Cytotoxic T Cells. *Analysis* **177** (1993).

273. Kelly JM, Sterry SJ, Cose S, Turner SJ, Fecondo J, Rodda S, et al. Identification of conserved T cell receptor CDR3 residues contacting known exposed peptide side chains from a major histocompatibility complex class I-bound determinant. *European Journal of Immunology* **23** (1993) 3318–3326. doi:10.1002/eji.1830231239.

274. Fremont DH, Stura EA, Matsumura, Peterson PA, Wilson IA, Kappler JW, et al. Crystal structure of an H-2Kb-ovalbumin peptide complex reveals the interplay of primary and secondary anchor positions in the major histocompatibility complex binding groove (murine major histocompatibility complex class I/allele-specific motifs/x-ray cr. *Immunology* **92** (1995) 2479–2483.

275. Kartal Ö, Andres F, Lai MP, Nehme R, Cottier K. waveRAPID—A Robust Assay for High-Throughput Kinetic Screens with the Creoptix WAVEsystem. *SLAS Discovery* **26** (2021) 995–1003. doi:10.1177/24725552211013827.

276. Cole DK, Pumphrey NJ, Boulter JM, Sami M, Bell JI, Gostick E, et al. Human TCR-Binding Affinity is Governed by MHC Class Restriction. *The Journal of Immunology* **178** (2007) 5727–5734. doi:10.4049/jimmunol.178.9.5727.

277. Pettmann J. *Antigen discrimination in primary human T cells*. Ph.D. thesis, University of Oxford, Oxford (2021).

278. Zehn D, Lee SY, Bevan MJ. Complete but curtailed T cell response to very low affinity antigen. *Nature* **458** (2009) 211–214. doi:10.1038/nature07657.Complete.

279. Lo Wl, Shah NH, Ahsan N, Horkova V, Stepanek O, Salomon AR, et al. Lck promotes Zap70-dependent LAT phosphorylation by bridging Zap70 to LAT. *Nature Immunology* **19** (2018). doi:10.1038/s41590-018-0131-1.

280. Limozin L, Bridge M, Bongrand P, Dushek O, van der Merwe PA, Robert P. TCR–pMHC kinetics under force in a cell-free system show no intrinsic catch bond, but a minimal encounter duration before binding. *Proceedings of the National Academy of Sciences of the United States of America* **116** (2019) 16943–16948. doi:10.1073/pnas.1902141116.

281. Dens C, Laukens K, Bittremieux W, Meysman P. The pitfalls of negative data bias for the T-cell epitope specificity challenge. *Nature Machine Intelligence* **5** (2023) 1060–1062. doi:10.1038/s42256-023-00727-0.

282. Lu RM, Hwang YC, Liu IJ, Lee CC, Tsai HZ, Li HJ, et al. Development of therapeutic antibodies for the treatment of diseases. *Journal of Biomedical Science 2020 27:1* **27** (2020) 1–30. doi:10.1186/S12929-019-0592-Z.

283. Khoury DS, Cromer D, Reynaldi A, Schlub TE, Wheatley AK, Juno JA, et al. Neutralizing antibody levels are highly predictive of immune protection from symptomatic SARS-CoV-2 infection. *Nature Medicine 2021 27:7* **27** (2021) 1205–1211. doi:10.1038/s41591-021-01377-8.

284. Senefeld JW, Franchini M, Mengoli C, Cruciani M, Zani M, Gorman EK, et al. COVID-19 Convalescent Plasma for the Treatment of Immunocompromised Patients: A Systematic Review and Meta-analysis. *JAMA Network Open* **6** (2023) e2250647. doi:10.1001/jamanetworkopen.2022.50647.

285. Scourfield DO, Reed SG, Quastel M, Alderson J, Bart VMT, Teijeira Crespo A, et al. The role and uses of antibodies in COVID-19 infections: a living review. *Oxford Open Immunology* **2** (2021). doi:10.1093/OXFIMM/IQAB003.

286. Dejnirattisai W, Zhou D, Ginn HM, Duyvesteyn HME, Supasa P, Case JB, et al. The antigenic anatomy of SARS-CoV-2 receptor binding domain. *Cell* **184** (2021) 2183–2200.e22. doi:10.1016/J.CELL.2021.02.032.

287. Klein JS, Bjorkman PJ. Few and Far Between: How HIV May Be Evading Antibody Avidity. *PLOS Pathogens* **6** (2010) e1000908. doi:10.1371/JOURNAL.PPAT.1000908.

288. Jendroszek A, Kjaergaard M. Nanoscale spatial dependence of avidity in an IgG1 antibody. *Scientific Reports 2021 11:1* **11** (2021) 1–10. doi:10.1038/s41598-021-92280-2.

289. Zhang P, Liu X, Liu P, Wang F, Ariyama H, Ando T, et al. Capturing transient antibody conformations with DNA origami epitopes. *Nature Communications* **11** (2020) 3114. doi:10.1038/s41467-020-16949-4.

290. Milstein JN, Meiners JC. Worm-Like Chain (WLC) Model. *Encyclopedia of Biophysics* (2013) 2757–2760. doi:10.1007/978-3-642-16712-6_502.

291. Kienberger F, Pastushenko VP, Kada G, Gruber HJ, Riener C, Schindler H, et al. Static and Dynamical Properties of Single Poly(Ethylene Glycol) Molecules Investigated by Force Spectroscopy. *Single Mol* **1** (2000) 123–128. doi:10.1002/1438-5171.

292. Forrey C, Douglas JF, Gilson MK. The Fundamental Role of Flexibility on the Strength of Molecular Binding. *Soft matter* **8** (2012) 6385. doi:10.1039/C2SM25160D.

293. Ke Z, Oton J, Qu K, Cortese M, Zila V, McKeane L, et al. Structures and distributions of SARS-CoV-2 spike proteins on intact virions. *Nature* **588** (2020) 498–502. doi:10.1038/s41586-020-2665-2.

294. Choi YK, Cao Y, Frank M, Woo H, Park SJ, Yeom MS, et al. Structure, Dynamics, Receptor Binding, and Antibody Binding of the Fully Glycosylated Full-Length SARS-CoV-2 Spike Protein in a Viral Membrane. *Journal of Chemical Theory and Computation* **17** (2021) 2479–2487. doi:10.1021/ACS.JCTC.0C01144/SUPPL_FILE/CT0C01144_SI_003.MP4.

295. Turoňová B, Sikora M, Schürmann C, Hagen WJH, Welsch S, Blanc FEC, et al. In situ structural analysis of SARS-CoV-2 spike reveals flexibility mediated by three hinges. *Science* **370** (2020) 203–208. doi:10.1126/SCIENCE.ABD5223/SUPPL_FILE/ABD5223S1.MOV.

296. Erez M, Takemori AE, Portoghese PS. Narcotic Antagonistic Potency of Bivalent Ligands Which Contain θ-Naltrexamine. Evidence for Bridging between Proximal Recognition Sites. *Journal of Medicinal Chemistry* **25** (1982) 847–849. doi:10.1021/JM00349A016/ASSET/JM00349A016.FP.PNG_V03.

297. Callaway HM, Hastie KM, Schendel SL, Li H, Yu X, Shek J, et al. Bivalent intra-spike binding provides durability against emergent Omicron lineages: Results from a global consortium. *Cell Reports* **42** (2023) 112014. doi:10.1016/J.CELREP.2023.112014.

298. Altman JD, Moss PAH, Goulder PJR, Barouch DH, McHeyzer-Williams MG, Bell JI, et al. Phenotypic analysis of antigen-specific T lymphocytes. *Science* **274** (1996) 94–96. doi:10.1126/SCIENCE.274.5284.94.

299. Laugel B, Boulter JM, Lissin N, Vuidepot A, Li Y, Gostick E, et al. Design of soluble recombinant T cell receptors for antigen targeting and T cell inhibition. *Journal of Biological Chemistry* **280** (2005) 1882–1892. doi:10.1074/jbc.M409427200.

300. Carrithers MD, Lerner MR. Synthesis and characterization of bivalent peptide ligands targeted to G-protein-coupled receptors. *Chemistry & biology* **3** (1996) 537–542. doi:10.1016/S1074-5521(96)90144-1.

301. Hasegawa H, Taira KI, Sode K, Ikebukuro K. Improvement of Aptamer Affinity by Dimerization. *Sensors* **8** (2008) 1090–1098. doi:10.3390/S8021090.

302. Driscoll CL, Keeble AH, Howarth MR. SpyMask enables combinatorial assembly of bispecific binders. *Nature Communications* **15** (2024) 2403. doi:10.1038/s41467-024-46599-9.

303. Keeble AH, Howarth M. Power to the protein: enhancing and combining activities using the Spy toolbox. *Chemical Science* **11** (2020) 7281. doi:10.1039/D0SC01878C.

304. Chen JLL, Stewart-Jones G, Bossi G, Lissin NM, Wooldridge L, Choi EML, et al. Structural and kinetic basis for heightened immunogenicity of T cell vaccines. *The Journal of Experimental Medicine* **201** (2005) 1243. doi:10.1084/JEM.20042323.

305. Lunde E, Løset GT, Bogen B, Sandlie I. Stabilizing mutations increase secretion of functional soluble TCR-Ig fusion proteins. *BMC biotechnology* **10** (2010). doi:10.1186/1472-6750-10-61.

306. Wagner EK, Qerqez AN, Stevens CA, Nguyen AW, Delidakis G, Maynard JA. Human cytomegalovirus-specific T-cell receptor engineered for high affinity and soluble expression using mammalian cell display. *Journal of Biological Chemistry* **294** (2019) 5790–5804. doi:10.1074/JBC.RA118.007187/ATTACHMENT/5B1077BE-C456-4793-B3DC-C484DBF0AF26/MMC3.PDF.

307. Gonzalez-Perez D, Das S, Antfolk D, Ahsan HS, Medina E, Dundes CE, et al. Affinity-matured DLL4 ligands as broad-spectrum modulators of Notch signaling. *Nature Chemical Biology* **19** (2023) 9–17. doi:10.1038/s41589-022-01113-4.

308. Cordle J, Redfield C, Stacey M, van der Merwe PA, Willis AC, Champion BR, et al. Localization of the delta-like-1-binding site in human Notch-1 and its modulation by calcium affinity. *The Journal of biological chemistry* **283** (2008) 11785–11793. doi:10.1074/JBC.M708424200.

309. Smith NJ. Low Affinity GPCRs for Metabolic Intermediates: Challenges for Pharmacologists. *Frontiers in Endocrinology* **3** (2012). doi:10.3389/FENDO.2012.00001.

310. Dushek O, Das R, Coombs D. A role for rebinding in rapid and reliable T cell responses to antigen. *PLoS computational biology* **5** (2009) e1000578. doi:10.1371/journal.pcbi.1000578.

311. Goldstein B, Coombs D, Faeder JR, Hlavacek WS. Kinetic Proofreading Model. *Multichain Immune Recognition Receptor Signaling* (New York, NY: Springer New York), vol. 640 (2008), 82–94. doi:10.1007/978-0-387-09789-3_8.

312. Riha P, Rudd CE. CD28 co-signaling in the adaptive immune response. *Self Nonself* **1** (2010) 231. doi:10.4161/SELF.1.3.12968.

313. Arasanz H, Gato-Cañas M, Zuazo M, Ibañez-Vea M, Breckpot K, Kochan G, et al. PD1 signal transduction pathways in T cells. *Oncotarget* **8** (2017) 51936–51945. doi:10.18632/oncotarget.17232.

314. Voisinne G, Locard-Paulet M, Froment C, Maturin E, Menoita MG, Girard L, et al. Kinetic proofreading through the multi-step activation of the ZAP70 kinase underlies early T cell ligand discrimination. *Nature Immunology* **23** (2022) 1355–1364. doi:10.1038/s41590-022-01288-x.

315. Linette GP, Stadtmauer EA, Maus MV, Rapoport AP, Levine BL, Emery L, et al. Cardiovascular toxicity and titin cross-reactivity of affinity-enhanced T cells in myeloma and melanoma. *Blood* **122** (2013) 863–871. doi:10.1182/blood-2013-03-490565.

316. Raman MCC, Rizkallah PJ, Simmons R, Donnellan Z, Dukes J, Bossi G, et al. Direct molecular mimicry enables off-target cardiovascular toxicity by an enhanced affinity TCR designed for cancer immunotherapy. *Scientific Reports* **6** (2016) 18851. doi:10.1038/srep18851.

317. Bijen HM, van der Steen DM, Hagedoorn RS, Wouters AK, Wooldridge L, Falkenburg JF, et al. Preclinical Strategies to Identify Off-Target Toxicity of High-Affinity TCRs. *Molecular Therapy* **26** (2018) 1206–1214. doi:10.1016/j.ymthe.2018.02.017.

318. Torigoe C, Inman JK, Metzger H. An Unusual Mechanism for Ligand Antagonism. *Science* **281** (1998) 568–572. doi:10.1126/science.281.5376.568.

319. Tsourkas PK, Liu W, Das SC, Pierce SK, Raychaudhuri S. Discrimination of membrane antigen affinity by B cells requires dominance of kinetic proofreading over serial engagement. *Cellular and Molecular Immunology* **9** (2012) 62. doi:10.1038/cmi.2011.29.

320. Hayward D, Roberts E, Gruneberg U. MPS1 localizes to end-on microtubule-attached kinetochores to promote microtubule release. *Current Biology* **32** (2022) 5200–5208.e8. doi:10.1016/j.cub.2022.10.047.

321. Pisetsky DS. Pathogenesis of autoimmune disease. *Nature Reviews Nephrology* **19** (2023) 509–524. doi:10.1038/s41581-023-00720-1.

322. Dendrou CA, Petersen J, Rossjohn J, Fugger L. HLA variation and disease. *Nature Reviews Immunology* **18** (2018) 325–339. doi:10.1038/nri.2017.143.

323. Ruff WE, Greiling TM, Kriegel MA. Host–microbiota interactions in immune-mediated diseases. *Nature Reviews Microbiology* **18** (2020) 521–538. doi:10.1038/s41579-020-0367-2.

324. Reynolds CJ, Sim MJW, Quigley KJ, Altmann DM, Boyton RJ. Autoantigen cross-reactive environmental antigen can trigger multiple sclerosis-like disease. *Journal of Neuroinflammation* **12** (2015) 1–5. doi:10.1186/S12974-015-0313-9/FIGURES/2.

325. Jamwal A, Constantin CF, Hirschi S, Henrich S, Bildl W, Fakler B, et al. Erythrocyte invasion-neutralising antibodies prevent Plasmodium falciparum RH5 from binding to basigin-containing membrane protein complexes. *eLife* **12** (2023). doi:10.7554/ELIFE.83681.

326. Le Gall F, Reusch U, Little M, Kipriyanov SM. Effect of linker sequences between the antibody variable domains on the formation, stability and biological activity of a bispecific tandem diabody. *Protein Engineering Design and Selection* **17** (2004) 357–366. doi:10.1093/protein/gzh039.

327. Hao CH, Han QH, Shan ZJ, Hu JT, Zhang N, Zhang XP. Effects of different interchain linkers on biological activity of an anti-prostate cancer single-chain bispecific antibody. *Theoretical Biology and Medical Modelling* **12** (2015) 1–10. doi:10.1186/S12976-015-0010-5/FIGURES/4.

328. Staufer O, Leithner A, Liberta F, Zhou S, Schiele F, Reindl S, et al. Solution structure and synaptic analyses reveal molecular mechanisms of bispecific T cell engagers. *bioRxiv* (2022). doi:10.1101/2022.06.15.496334.

329. Zeng X, Bai G, Sun C, Ma B. Recent Progress in Antibody Epitope Prediction. *Antibodies* **12** (2023). doi:10.3390/ANTIB12030052.

330. Kim J, McFee M, Fang Q, Abdin O, Kim PM. Computational and artificial intelligence-based methods for antibody development. *Trends in Pharmacological Sciences* **44** (2023) 175–189. doi:10.1016/J.TIPS.2022.12.005.

331. Meysman P, Barton J, Bravi B, Cohen-Lavi L, Karnaukhov V, Lilleskov E, et al. Benchmarking solutions to the T-cell receptor epitope prediction problem: IMMREP22 workshop report. *ImmunoInformatics* **9** (2023) 100024. doi:10.1016/j.immuno.2023.100024.

332. Moris P, De Pauw J, Postovskaya A, Gielis S, De Neuter N, Bittremieux W, et al. Current challenges for unseen-epitope TCR interaction prediction and a new perspective derived from image classification. *Briefings in Bioinformatics* **22** (2021). doi:10.1093/bib/bbaa318.

333. Matharu Z, Bee C, Schwarz F, Chen H, Tomlinson M, Wu G, et al. High-Throughput Surface Plasmon Resonance Biosensors for Identifying Diverse Therapeutic Monoclonal Antibodies. *Analytical Chemistry* **93** (2021) 16474–16480. doi:10.1021/acs.analchem.1c03548.

334. Irving M, Zoete V, Hebeisen M, Schmid D, Baumgartner P, Guillaume P, et al. Interplay between T cell receptor binding kinetics and the level of cognate peptide presented by major histocompatibility complexes governs CD8+ T cell responsiveness. *Journal of Biological Chemistry* **287** (2012) 23068–23078. doi:10.1074/jbc.M112.357673.

335. Willis RA, Ramachandiran V, Shires JC, Bai G, Jeter K, Bell DL, et al. Production of Class II MHC Proteins in Lentiviral Vector-Transduced HEK-293T Cells for Tetramer Staining Reagents. *Current Protocols* **1** (2021) 1–55. doi:10.1002/cpz1.36.

336. Huhn A, Nissley D, Wilson DB, Kutuzov M, Donat R, Tan TK, et al. The molecular reach of antibodies determines their SARS-CoV-2 neutralisation potency. *bioRxiv* (2023). doi:10.1101/2023.09.06.556503.

337. Goyette J, Salas CS, Coker-Gordon N, Bridge M, Isaacson SA, Allard J, et al. Biophysical assay for tethered signaling reactions reveals tether-controlled activity for the phosphatase SHP-1. *Science Advances* **3** (2017) e1601692. doi:10.1126/sciadv.1601692.

338. Kersh EN, Shaw S, Allen PM, Shaw AS, Allen PM. Fidelity of T cell activation through multistep T cell receptor zeta phosphorylation. *Science* **281** (1998) 572–575.

339. Persaud SP, Donermeyer DL, Weber KS, Kranz DM, Allen PM. High-affinity T cell receptor differentiates cognate peptide–MHC and altered peptide ligands with distinct kinetics and thermodynamics. *Molecular immunology* **47** (2010) 1793–1801. doi:10.1016/j.molimm.2010.02.013.

340. Krogsgaard M, Prado N, Adams EJ, He XlL, Chow DCC, Wilson DB, et al. Evidence that structural rearrangements and/or flexibility during TCR binding can contribute to T cell activation. *Molecular cell* **12** (2003) 1367–1378. doi:10.1016/S1097-2765(03)00474-X.

341. Newell EW, Ely LK, Kruse AC, Reay PA, Rodriguez SN, Lin AE, et al. Structural Basis of Specificity and Cross-Reactivity in T Cell Receptors Specific for Cytochrome c –I-Ek. *The Journal of Immunology* **186** (2011) 5823–5832. doi:10.4049/jimmunol.1100197.

342. Tian S, Maile R, Collins EJ, Frelinger JA. CD8+ T cell activation is governed by TCR-peptide/MHC affinity, not dissociation rate. *The Journal of Immunology* **179** (2007) 2952–2960. doi:10.4049/jimmunol.179.5.2952.

343. Govern CC, Paczosa MK, Chakraborty AK, Huseby ES. Fast on-rates allow short dwell time ligands to activate T cells. *Proceedings of the National Academy of Sciences* **107** (2010) 8724–8729.

344. Chervin AS, Stone JD, Holler PD, Bai A, Chen J, Eisen HN, et al. The impact of TCR-binding properties and antigen presentation format on T cell responsiveness. *The Journal of Immunology* **183** (2009) 1166–1178.

345. Bowerman NA, Crofts TS, Chlewicki L, Do P, Baker BM, Garcia KC, et al. Engineering the binding properties of the T cell receptor: peptide: MHC ternary complex that governs T cell activity. *Molecular immunology* **46** (2009) 3000–3008.

346. Jones LL, Colf LA, Stone JD, Garcia KC, Kranz DM. Distinct CDR3 conformations in TCRs determine the level of cross-reactivity for diverse antigens, but not the docking orientation. *The Journal of Immunology* **181** (2008) 6255–6264.

347. Adams JJ, Narayanan S, Birnbaum ME, Sidhu SS, Blevins SJ, Gee MH, et al. Structural interplay between germline interactions and adaptive recognition determines the bandwidth of TCR-peptide-MHC cross-reactivity. *Nature immunology* **17** (2015) 87–94. doi:10.1038/ni.3310.

348. McMahan RH, McWilliams JA, Jordan KR, Dow SW, Wilson DB, Slansky JE. Relating TCR-peptide-MHC affinity to immunogenicity for the design of tumor vaccines. *The Journal of clinical investigation* **116** (2006) 2543–2551.

349. Schmid DA, Irving MB, Posevitz V, Hebeisen M, Posevitz-Fejfar A, Sarria JCCF, et al. Evidence for a TCR affinity threshold delimiting maximal CD8 T cell function. *Journal of immunology (Baltimore, Md. : 1950)* **184** (2010) 4936–4946. doi:10.4049/jimmunol.1000173.

350. Dushek O, Aleksic M, Wheeler RJ, Zhang H, Cordoba SP, Peng YC, et al. Antigen potency and maximal efficacy reveal a mechanism of efficient T cell activation. *Science signaling* **4** (2011) 39–39. doi:10.1126/scisignal.2001430.

351. Thomas S, Xue SA, Bangham CRM, Jakobsen BK, Morris EC, Stauss HJ. Human T cells expressing affinity-matured TCR display accelerated responses but fail to recognize low density of MHC-peptide antigen. *Blood* **118** (2011) 319–329.

352. Zhong S, Malecek K, Johnson LA, Yu Z, de Miera EVS, Darvishian F, et al. T-cell receptor affinity and avidity defines antitumor response and autoimmunity in T-cell immunotherapy. *Proceedings of the National Academy of Sciences* **110** (2013) 6973–6978.

353. Bianchi V, Bulek A, Fuller A, Lloyd A, Attaf M, Rizkallah PJ, et al. A molecular switch abrogates glycoprotein 100 (gp100) T-cell receptor (TCR) targeting of a human melanoma antigen. *Journal of Biological Chemistry* **291** (2016) 8951–8959.

354. Andersen PS, Geisler C, Buus S, Mariuzza RA, Karjalainen K. Role of the T cell receptor ligand affinity in T cell activation by bacterial superantigens. *Journal of Biological Chemistry* **276** (2001) 33452–33457.

355. Andersen PS, Menné C, Mariuzza RA, Geisler C, Karjalainen K. A response calculus for immobilized T cell receptor ligands. *Journal of Biological Chemistry* **276** (2001) 49125–49132.

356. Tan MP, Gerry AB, Brewer JE, Melchiori L, Bridgeman JS, Bennett AD, et al. T cell receptor binding affinity governs the functional profile of cancer-specific CD8+ T cells. *Clinical & Experimental Immunology* **180** (2015) 255–270.

357. Chan KF, Gully BS, Gras S, Beringer DX, Kjer-Nielsen L, Cebon J, et al. Divergent T-cell receptor recognition modes of a HLA-I restricted extended tumour-associated peptide. *Nature communications* **9** (2018) 1–13.

358. Broughton SE, Petersen J, Theodossis A, Scally SW, Loh KL, Thompson A, et al. Biased T cell receptor usage directed against human leukocyte antigen DQ8-restricted gliadin peptides is associated with celiac disease. *Immunity* **37** (2012) 611–621.

359. Benati D, Galperin M, Lambotte O, Gras S, Lim A, Mukhopadhyay M, et al. Public T cell receptors confer high-avidity CD4 responses to HIV controllers. *The Journal of clinical investigation* **126** (2016) 2093–2108.

360. Ekeruche-Makinde J, Clement M, Cole DK, Edwards ESJ, Ladell K, Miles JJ, et al. T-cell receptor-optimized peptide skewing of the T-cell repertoire can enhance antigen targeting. *Journal of Biological Chemistry* **287** (2012) 37269–37281.

361. Madura F, Rizkallah PJ, Legut M, Holland CJ, Fuller A, Bulek A, et al. TCR-induced alteration of primary MHC peptide anchor residue. *European journal of immunology* **49** (2019) 1052–1066.

362. Birnbaum ME, Dong S, Garcia KC. Diversity-oriented approaches for interrogating T-cell receptor repertoire, ligand recognition, and function. *Immunological reviews* **250** (2012) 82–101. doi:10.1111/imr.12006.